SCUOLA DI INGEGNERIA
CORSO DI LAUREA MAGISTRALE IN INGEGNERIA CIVILE
ANNO ACCADEMICO 2013/2014

Laboratory experiments on the interaction between waves and a wave energy converter

Relatori:
Prof. Ing. Lorenzo Cappietti
Prof. Ing. Andreas Kortenhaus
Prof. Ing. Pier Luigi Aminti
Ing. Tim Verbrugghe

Candidato:
Alessio Niccolini

Index

1. Introduction

This thesis work is my first important goal; it is the natural conclusion of my academic career, started and motivated by my enthusiasm for the sea and the environment.

It ends with the hope that will not be my last, although small, contribution for a better and more sustainable world; if on one side there is my desire to protect the environment, on the other side it represents also my line of duty. It should be well impressed in each of us that the 11th December 1997 during the COP3 conference of the United Nations Framework Convention on Climate Change (UNFCCC) more than 160 countries met in Japan to sign an agreement concerning the global warming and the climate change; the Kyoto Protocol. It includes all the fields of human activities, like the energy sector, the industrial processes, the use of solvents, the agriculture, the waste management, and more.

The research field is a sector too many times hidden to the students, despite of the students of today are the innovators of tomorrow. For this reason I feel to mention two people, without who this work would not have been possible.

I thank Professor Lorenzo Cappietti for the constant support given to me and for showing me the fascinating world of research. I thank him especially for his friendship and his encouragements in this difficult period.

A special thanks to Professor Andreas Kortenhaus for helping me in the writing of the thesis. Thanks for the opportunity to spent a wonderful experience in a context of high level.

2. Objectives

With the following lines I will explain the aims of my work as the result of my three months spent at the Department of Civil Engineering in Gent. This work is the starting point for a new project that is the following of the FlanSea buoy (see chapter 3.5); in other word laying the foundations for the design of a new point absorber better than the previous device (a buoy moored to the sea bed with a steel cable).

To become a productive wave energy device, the movement of the buoy needs to be more as possible up and down, avoiding the pitching (see chapter 3.9). A better motion will also reduce or avoid some problems that occurred at the Flansea buoy like the failure of the keel, the damage of the steel cable and the scour near the anchorage.

Through the design, the performing and the analysis of a small scale laboratory experiments program the aims of my thesis are:

- Finding out the relations between the buoy's motions, the buoy's geometry and the waves;
- Proposing new solutions regarding the geometry of the buoy;
- Giving advices for the next step in order to concentrate the efforts in the right way.

At last, but not less important, there is my personal objectives: gain experience in the field of the research in a high level context.

The steps to achieve the objectives are seven; within the following flow chart it is described in detail how the aims have been reached and the logical connections between the chapters.

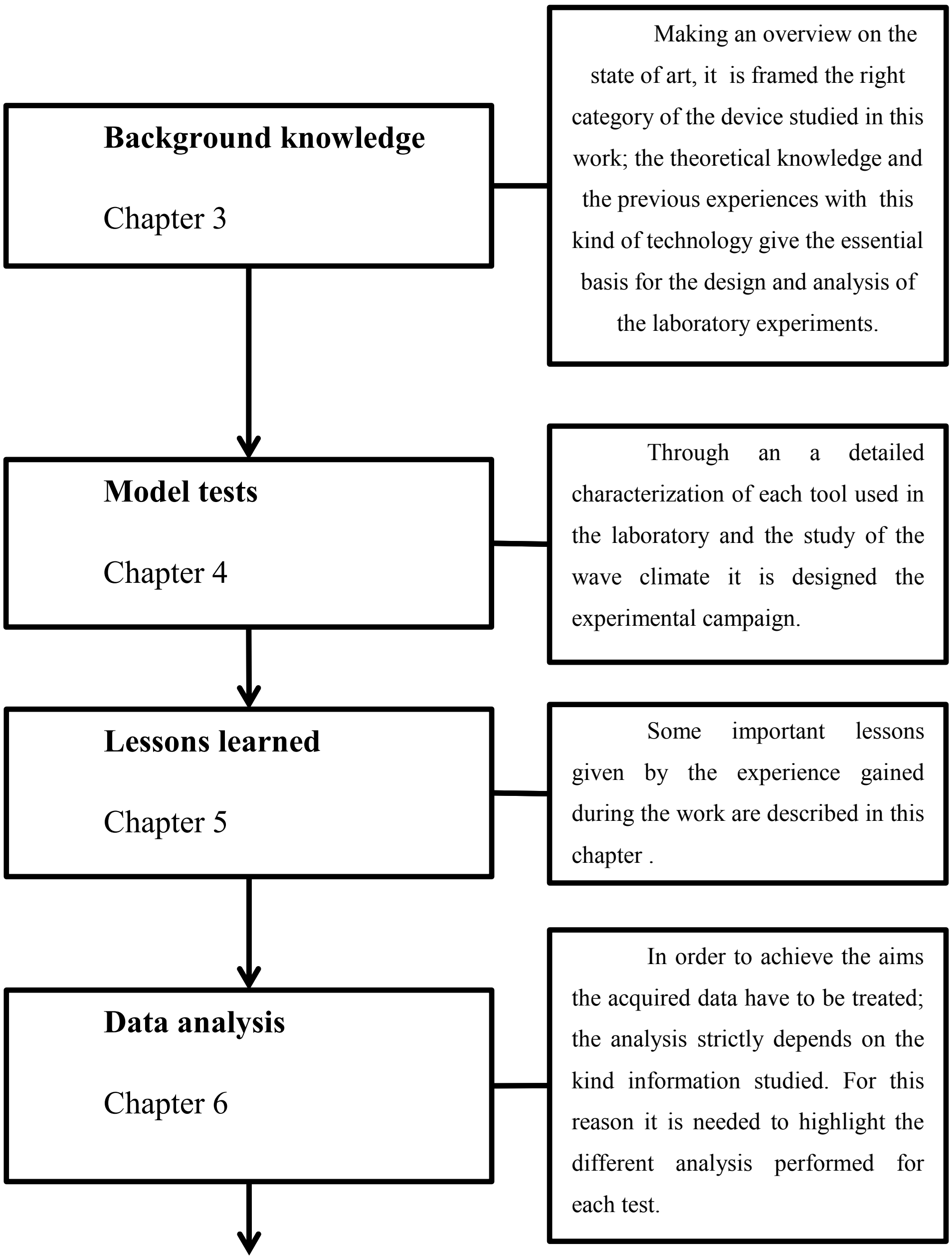
Background knowledge
Chapter 3
Making an overview on the state of art, it is framed the right category of the device studied in this work; the theoretical knowledge and the previous experiences with this kind of technology give the essential basis for the design and analysis of the laboratory experiments.
Model tests
Chapter 4
Through an a detailed characterization of each tool used in the laboratory and the study of the wave climate it is designed the experimental campaign.
Lessons learned
Chapter 5
Some important lessons given by the experience gained during the work are described in this chapter .
Data analysis
Chapter 6
In order to achieve the aims the acquired data have to be treated; the analysis strictly depends on the kind information studied. For this reason it is needed to highlight the different analysis performed for each test.

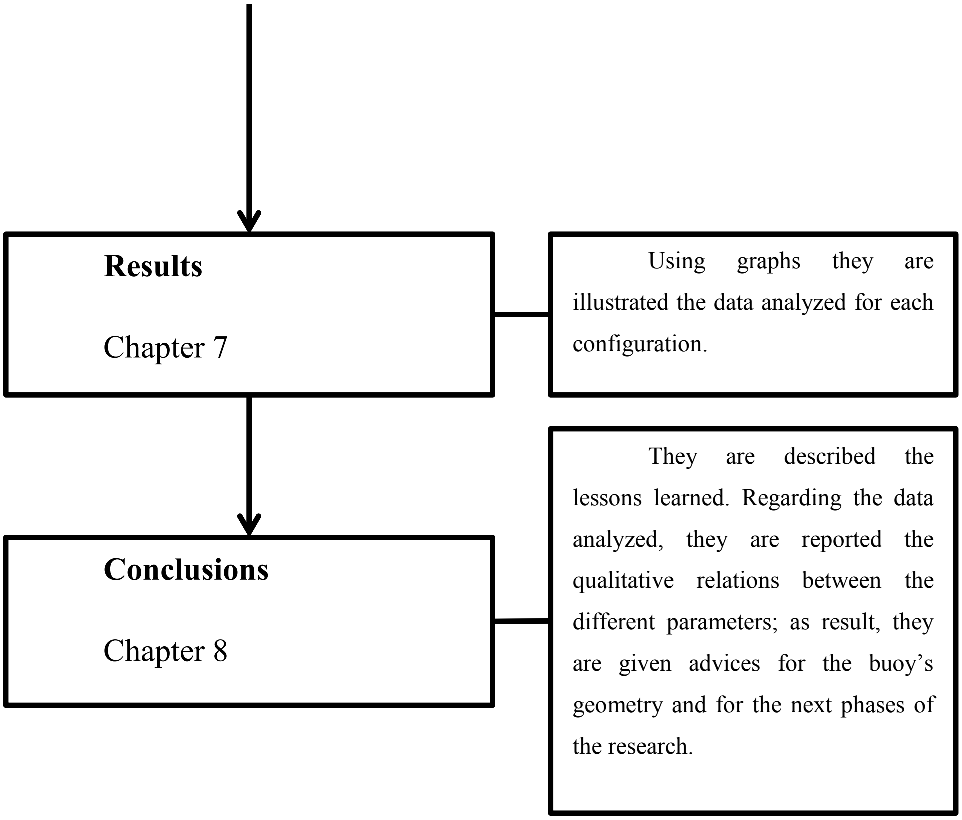

Fig. 2.1 – Flow chart of the chapters

3. Background knowledge

3.1 Introduction

The conventional energy reserves is running out, the climate is changing and the cost of the electricity is rising. How can we maintain the same standard of life?

Solutions to today energy challenges need to be explored through alternative, renewable and clean energy sources to enable a diverse energy resource plan. An extremely abundant and promising source of energy exists in oceans, that cover more than 70 % of the earth. The energy is stored in oceans partly as thermal energy, partly as kinetic energy (waves and currents) and also in chemical and biological products.

We are entering in an era where the energy generated by the Sea could offer an affordable contribution in the coastal States. Numerous techniques for extracting energy from the Oceans are waiting to be installed and start working.

The kinetic energy present in marine and tidal currents can be converted to electricity using relatively conventional turbine technology. To harness the kinetic energy in waves a wide variety of designs have been suggested. Ocean thermal energy conversion is possible in locations with large temperature differences, extracting energy with a heat engine. Salinity gradients can be exploited for energy extraction through the osmotic process.

3.2 Ocean energy types

In this subchapter they are treated some important ocean energy types; however the wind systems are not showed because they harvest energy directly from the wind. Also the hybrid systems that use, for example, both solar and ocean thermal energy are not taken into account. The wave energy is amply described in the next subchapter.

3.2.1 Marine and Tidal energy

As before explained, the seas and the oceans are one of the biggest energy resource for our planet; the expressions of them are various, but the most popular and well accessible is the wave energy and the tidal energy.

Two main types of ocean currents exist: marine currents and tidal currents. Marine currents such as the Gulf Stream in the Atlantic originate from differences in water temperature within the ocean. Huge water masses move to the poles and when they cool down, flow back towards the Equator [Fig. 3.1]:

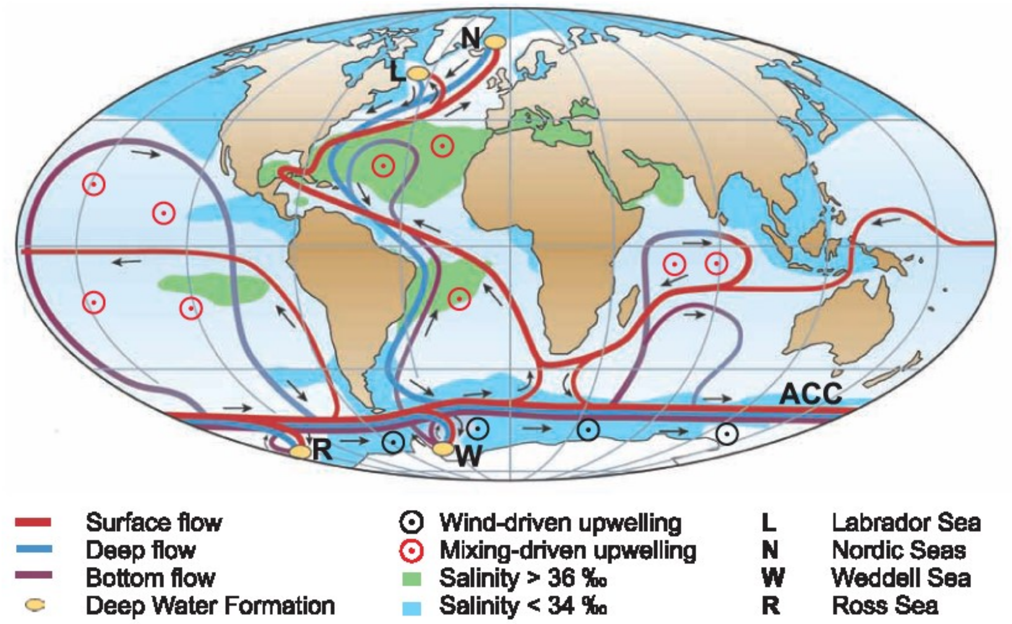

Fig. 3.1 *– Schematic illustration of the marine currents in the Oceans (www.climatestate.com)*

On the other hand the tidal currents represent the huge quantity of water moving by the Moon gravity and the revolution of the Earth around the Sun. The ocean tides are cyclic variations in seawater elevation and flow velocity due to the quantity of water moving by the Moon gravity and the revolution of the Earth around the Sun, representing the interaction of their gravitational forces. The strength of the currents varies, depending on the proximity of the moon and sun relative to earth. The magnitude of the tide-generating force is about 68% moon and 32% sun due to their respective masses and distance from earth; furthermore the effects are emphasized by the irregular coastal morphology where constrained channels augment the water flow and increase the energy density.

Instead of a constant flow in one direction as with marine currents, tidal currents flow in one direction at the beginning of the cycle and reverse directions at the end of the cycle. Depending on location and geography, tidal currents come in half-day (semidiurnal), daily (diurnal), and 14 day cycles. In Figure [3.2] they are illustrated the areas where the tidal resource is plentiful:

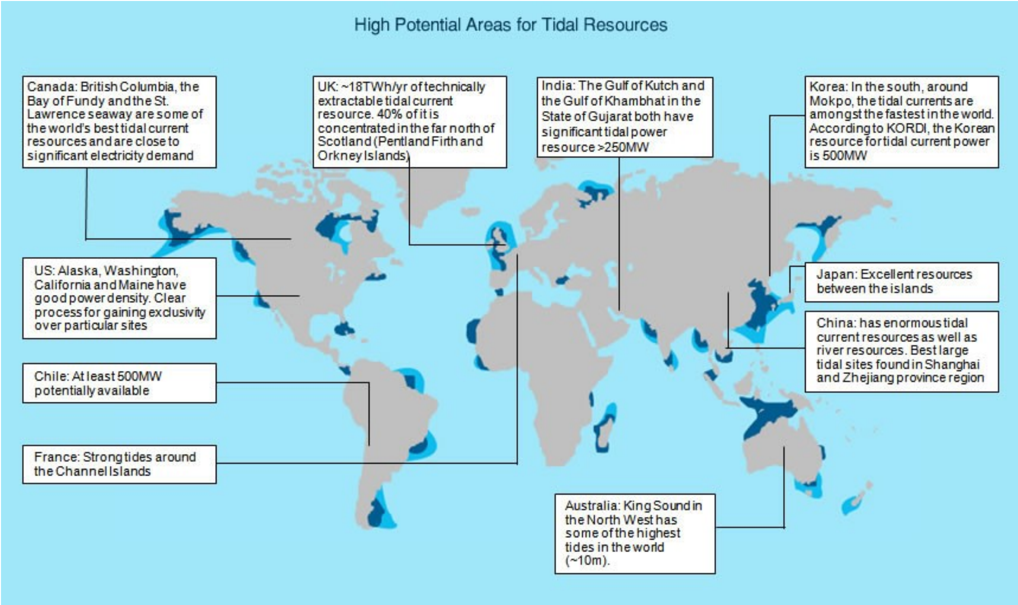

Fig. 3.2 *– Suitable areas for tidal energy plants (www.renewablegreenenergypower.com)*

The total kinetic power in a marine current turbine is governed by the following equation:

$$P_{kin} = \frac{1}{2}\rho A v^3$$

Where:

P [W] is the power,

ρ [kg/m^3] is the fluid density,

v [m/s] is the fluid velocity

A [m^2] is the cross-sectional area of the turbine.

However, the harvesting energy due to losses is lower and an be written as:

$$P = \frac{1}{2}C_p\rho A v^3$$

Where C_p is known as the power coefficient and is the percentage of power that can be extracted from the fluid stream taking into account losses. For marine turbines, C_p is usually in a range around 0.35÷0.5.

The European cost presents some very profitable areas, especially in UK [Fig. 3.3]:

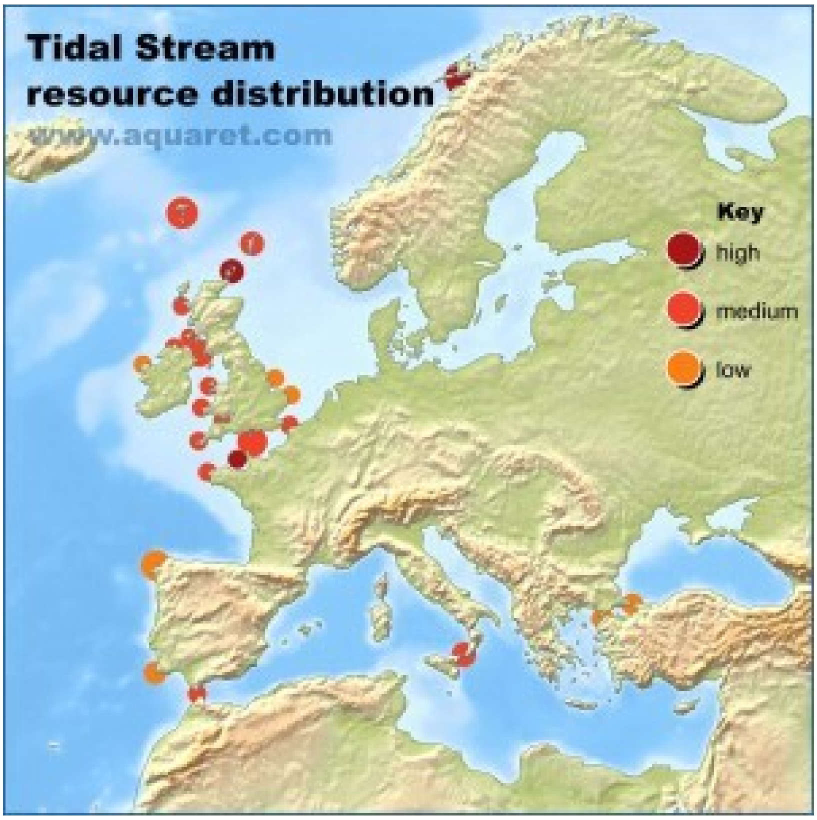

Fig. 3.3 *– Tidal energy distribution in Europe (www.emec.org.uk)*

The technology improved takes advantage by the different energy potential caused by the seaward and inward flow [Fig. 3.4]:

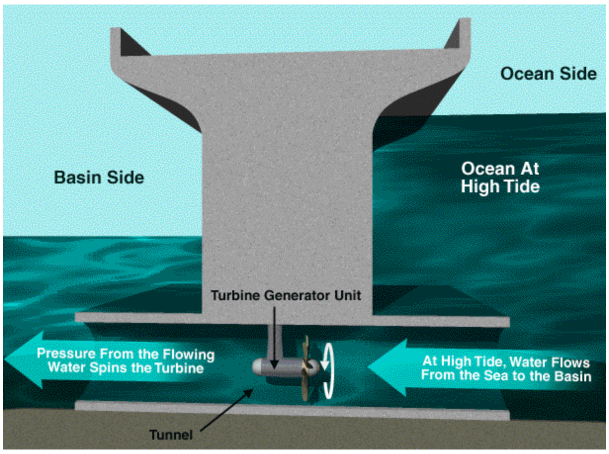

Fig. 3.4 *– Operation principle of the tidal energy plant (www.bigelow.org)*

One of the most important operating tidal facility in the world is La Rance tidal power plant, [Fig. 3.5]; the energy is provided by 24 generator of 10 MW which can run during both incoming and outgoing tides.


Fig. 3.5 *– Photo of the La Rance tidal power plant (www.energystorageexchange.org)*

Prototypes of marine current generators have been deployed in both Europe and the US. The technology used for this type may even be described as looking like underwater wind turbines, especially for the Horizontal Axis Tidal Turbines. Variations in the designs can include the turbine size, number of blades and shape of blades as showed in the figures below [Fig. 3.6, Fig. 3.7, Fig. 3.8]:

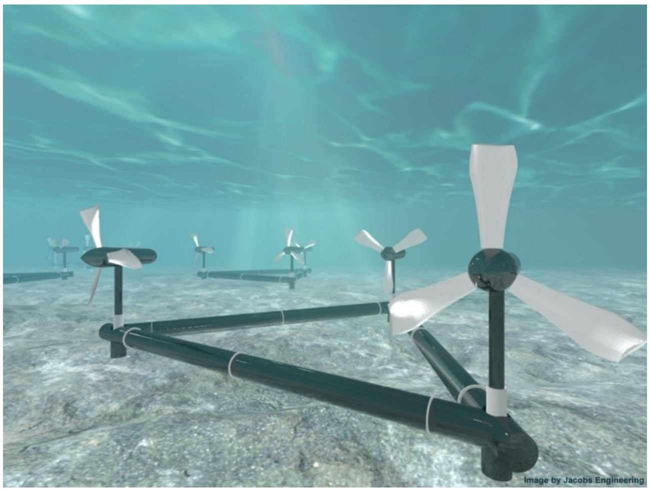

Fig. 3.6 *- Horizontal Axis Tidal Turbines example (www.maritimejournal.com)*

Fig. 3.7 *- Horizontal Axis Tidal Turbines example (www.esru.strath.ac.uk)*

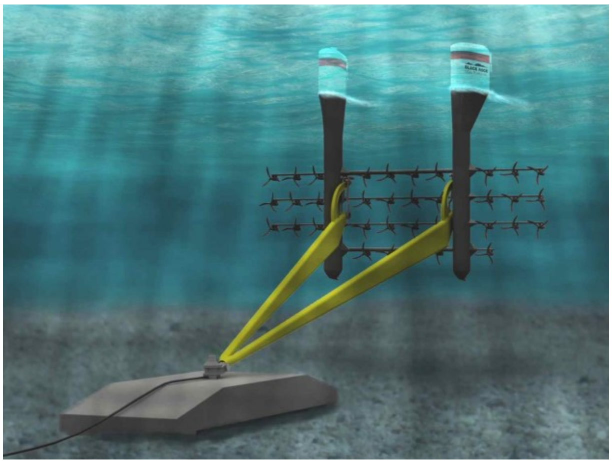

Fig. 3.8 *- Horizontal Axis Tidal Turbines example (www.digbycourier.ca)*

Another type is the Vertical Axis Tidal Turbine. This device works with currents coming from any direction, with the blades that rotate around a vertical axis [Fig. 3.9, Fig. 3.10]:

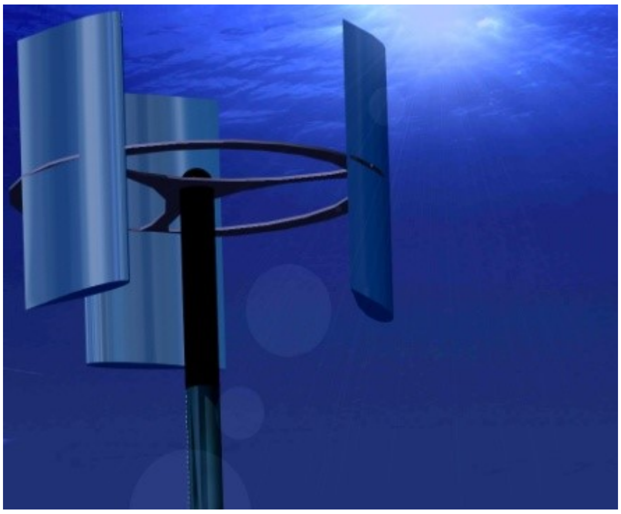

Fig. 3.9 *- Vertical Axis Tidal Turbines example (www.esru.strath.ac.uk)*

Fig. 3.10 *- Vertical Axis Tidal Turbines example (www.teeic.indianaffairs.gov)*

Oscillating Hydrofoil devices [Fig. 3.11] consist in a foil attached to the tip of a mobile arm. Currents will exert pressure on the foil, forcing it to ascend and descend in an oscillating motion. Electricity is produced through an hydraulic system.

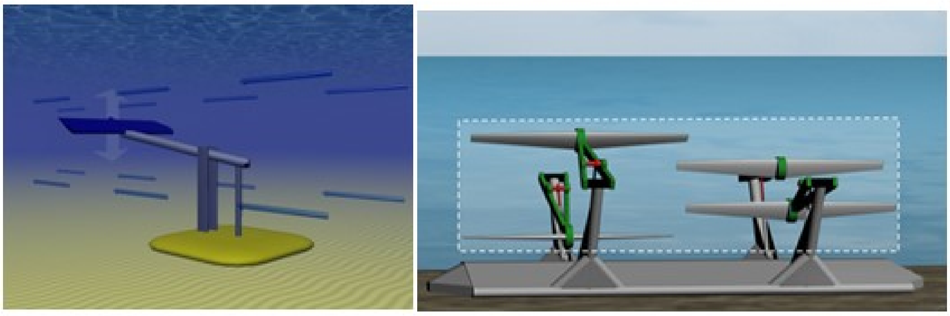

Fig. 3.11 *- Oscillating Hydrofoil examples (crueltyfreelife.wordpress.com)*

3.2.2 Ocean Thermal Energy Conversion

Ocean thermal energy converter uses the temperature difference between the warm surface of the ocean and the colder layers underneath. The warm water from the surface is used to boil a special working fluid, which is then run through a turbine and condensed using cold seawater pumped up from the depths [Fig. 3.12]:

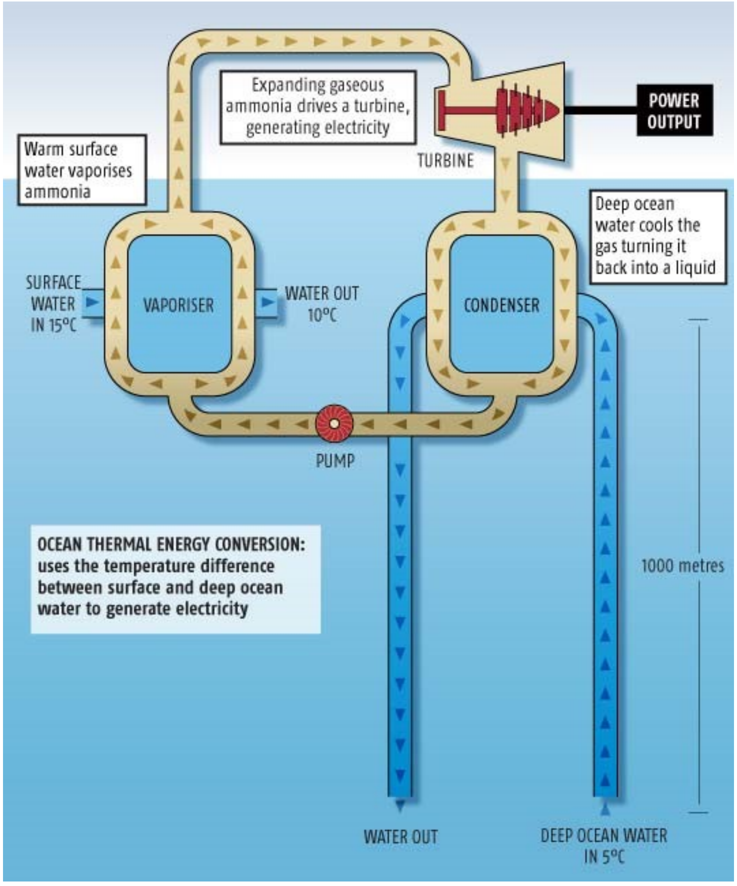

Fig. 3.12 *– Ocean thermal energy power plant (www.vedeni.wordpress.com)*

The areas where the energy harvesting are profitable are the sea's strips around the equator [Fig. 3.13]:

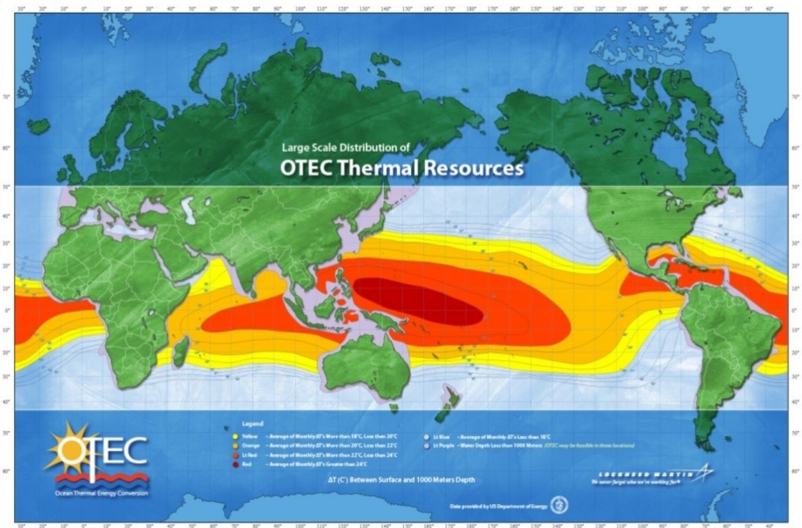

Fig. 3.13 *– Ocean thermal energy distribution (www.lockheedmartin.com)*

3.2.3 Salinity Gradient

The “Pressure Retarded Osmosis” is a process that allows to use the potential energy available when saltwater and freshwater mix. This method exploits the movement of water across an osmotic membrane to run turbines [Fig. 3.14]. The development of this type of energy is still at a very early stage.

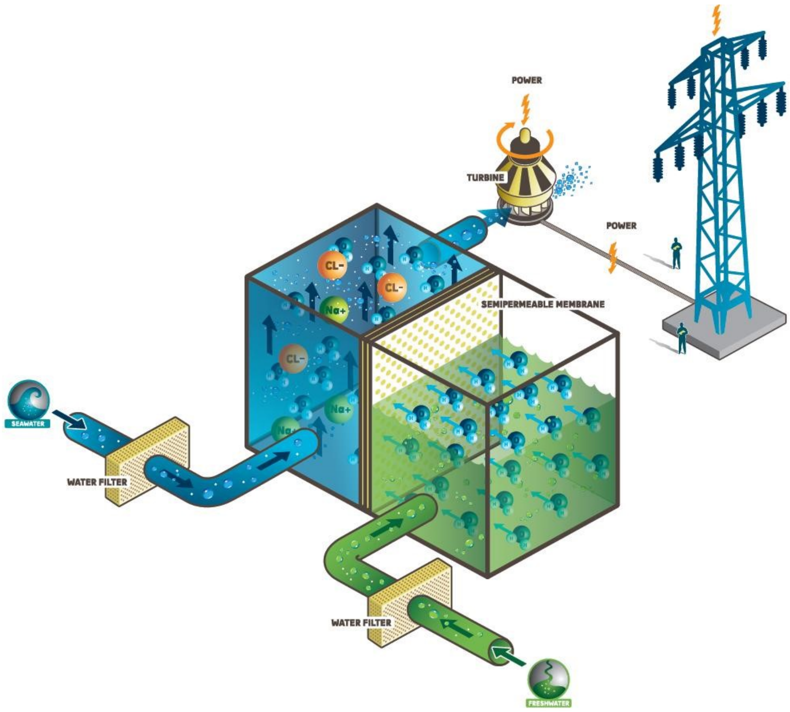

Fig. 3.14 *– Salinity gradient power plant (www.climatetechwiki.org)*

3.3 Wave energy in general

3.3.1 Historic overview

The history of wave power is old; the first patent suggested to use wave energy was presented by Girard and his son in 1799 and before the first patent a lot of ideas were proposed as reported in the following two drafts [Fig. 3.15, Fig. 3.16]:

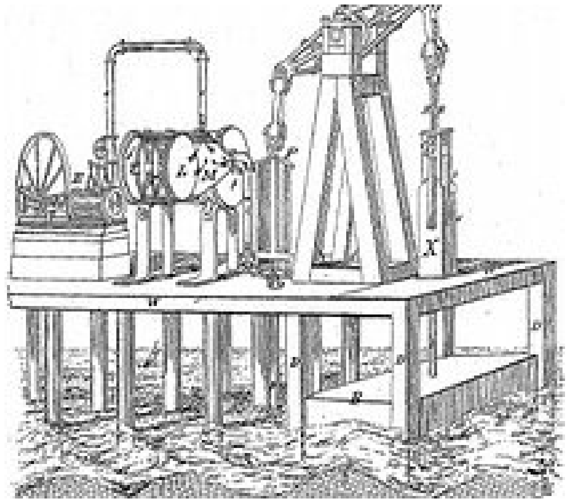

Fig. 3.15 *– Draft on a wave energy convert (www.gizmodo.com)*

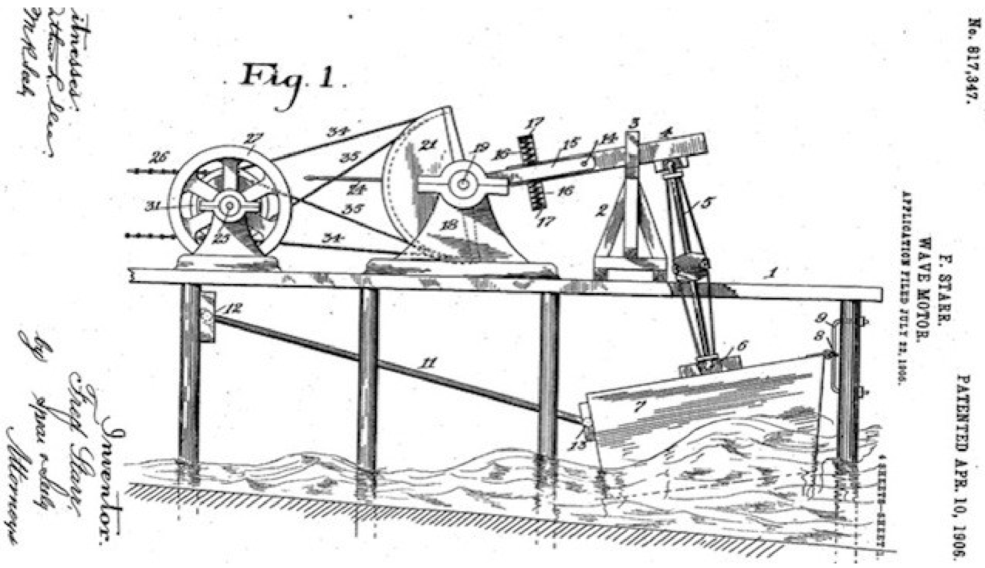

Fig. 3.16 *– Draft on a wave energy convert (www.gizmodo.com)*

The first oscillating water column type of wave energy device was developed in 1910 by Bochaux-Praceique to light and power his house near Royan, near Bordeaux in France.

Despite this, the wave energy is a relatively young field. The modern scientists agreed that the wave energy pioneer was Yoshio Masuda with his experiments in the 1940. He has tested various concepts of wave energy devices at sea, with several hundred units used to power navigation lights. In the figure below is showed a Masuda's patent proposed in 1965 [Fig. 3.17]:

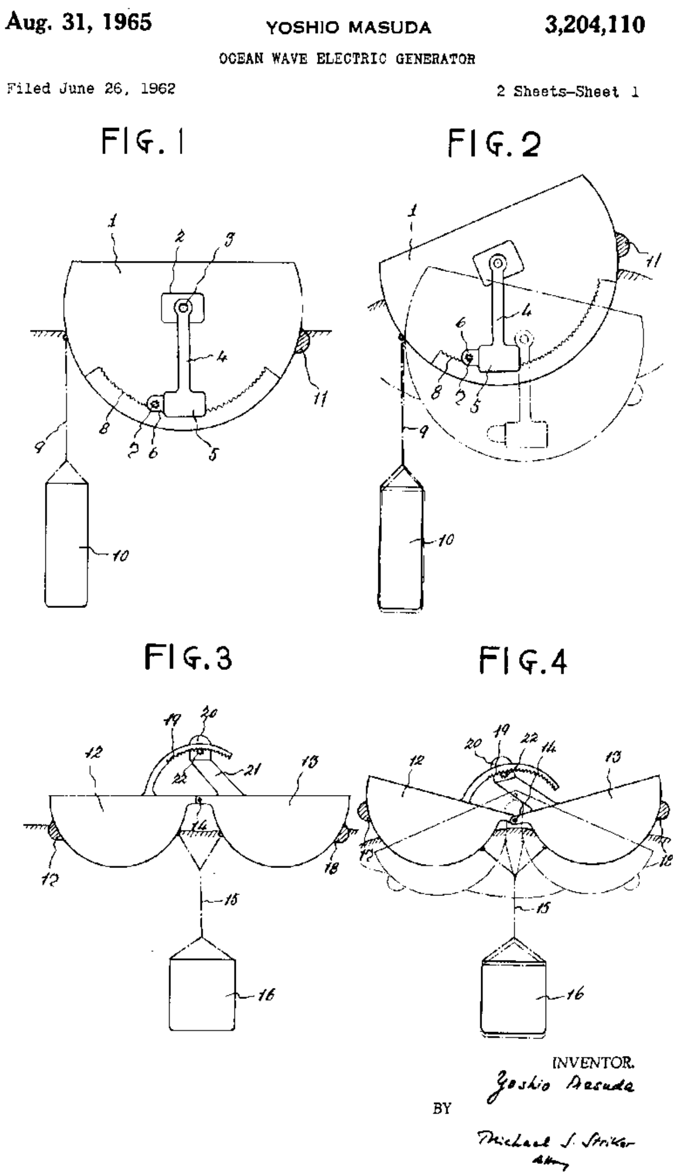

Fig. 3.17 *– One device proposed by Yoshio Masuda (Masuda's patent 1965)*

Scientist really realized the importance of this renewable energy only in 1973 when the growing oil crises arouse the desire to examine the potential to generate energy from ocean waves. Many scientists from renowned universities started working on this project like Stephen Salter from the University of Edinburgh, Kjell Budal and Johannes Falnes from Norwegian Institute of Technology, Michael E. McCormick from U.S. Naval Academy, David Evans from Bristol University, Michael French from University of Lancaster, Nick Newman and C. C. Mei from MIT.

However this development was drastically reduced in 1980 when the problem of oil was resolved due to the fall of the oil price.

Nowadays the wave energy is in its pre commercial phase, and much work is going on the evaluation of the wave energy potential and the detailed characterization of this very important renewable energy resource.

3.3.2 Wave energy available in the Oceans and in the Seas

Several researches have been conducted to quantify the accessible wave energy in the Oceans. The waves are generated by the wind that blow over the water surface; the effects of earth's temperature variation due to solar heating, combined with a multitude of atmospheric phenomena generate wind currents in global scale; therefore the energy in the ocean waves is a form of concentrated solar energy.

The power transmitted by a regular wave per unit crest is[1]:

$$P = \frac{1}{8}\rho g H^2 C_g$$

Where:

ρ is the fluid density [~1,028 kg/m^3],

H [m] is the wave height.

The C_g [m/s] is the group velocity that can be written as:

$$C_g = \frac{1}{2}\left(1 + \frac{2kd}{\sinh(2kd)}\right)\frac{L}{T}$$

[1] Cornett, A. M. (2008). A global wave energy resource assessment. *National Research Council.* Ontario, Canada.

Where

d [m] is the local water depth,

L [m] is the wave length,

T [s] is the wave period,

k= 2π/L is the wave number,

C = L/T [m/s] is the wave celerity.

The dispersion equation relates the wave length, the water depth and the wave period:

$$L = \frac{T^2 g}{2\pi} tanh(kd)$$

In shallow water (L/10 < h < L/2), the following explicit equation for L can be used without noticeable error:

$$L = L_0 \left(\tanh(kd)^{\frac{3}{4}}\right)^{\frac{1}{2}}$$

In deep water (h > L/2), C = L/T = $2C_g$ and L = L_o= $gT^2/2\pi$, therefore:

$$P_0 = \frac{1}{32\pi} \rho g^2 H^2 T \quad \text{(regular wave in depth water)}$$

The real sea states is given as a sum of regular waves with different frequencies, amplitudes and directions. The variance spectral density function or wave spectrum S(f,θ) describes this complex mixing. The power for real sea state is:

$$P = \rho g \int_0^{2\pi} \int_0^{\infty} C_g(f,h)\, S(f,\theta) df\, d\theta$$

With:

$$C_g(f,h) = \frac{1}{2}\left(1 + \frac{2kd}{\sinh(2kd)}\right) \frac{Tg}{2\pi} tanh(kd)$$

A correct wave power approximation per unit width for irregular waves is:

$$P \approx \frac{\rho g}{16} H_s^2 C_g(T_e, h)$$

where T_e[s] is known as the energy period and $C_g(T_e,h)$ is the group velocity of a wave with period T_e in water depth d. The energy period of a sea state is as:

$$T_e = \frac{\int_0^{2\pi}\int_0^{\infty} f^{-1}\, S(f)df\, d\theta}{\int_0^{2\pi}\int_0^{\infty} S(f)df\, d\theta}$$

In deep water (h > L/2), the approximate expression for the wave power can be written as:

$$P_0 \approx \frac{1}{64\pi}\rho g^2 H_s^2 T_e$$

Measured seastates are often specified in terms of significant wave height H_s and

peak period T_p[s] or mean period T_z[s]. The energy period T_e can be estimated asumming:

$$T_e = \alpha T_p$$

Where α=0.86 for a Pierson-Moskowitz spectrum, and α increases towards unity with decreasing spectral width. The assumption that α=0.90 or T_e=0.9T_p, it means to assuming a JONSWAP spectrum with a peak factor of γ=3.3.

At the European level WERATLAS or the European Wave Energy Atlas (Pontes, 1998) describes the deep-water resources off the Atlantic and Mediterranean coasts of Europe. The technical resource is wave power parameter more useful than the theoretical resource because it describes the power that can be harvested in an area by a WEC.

The results show that the global gross theoretical resource is about 3.7 ÷3.5 TW[2], discarding the areas where the P is less than 5 kW/m; the total reduction from gross to

[2] Barstow, S., & Al. (2010). Assessing the global wave energy potential. *Proceedings of OMAE2010*. China.

net resource is about 20% and the net resource is about 3 TW. Globally, the most important reduction is for areas where ice coverage is a problem.

The figure [3.18] shows the global theoretical gross wave power; it is evident that the largest power levels occur where the Coriolis force is more intensive, or rather at the western coasts of the continents.

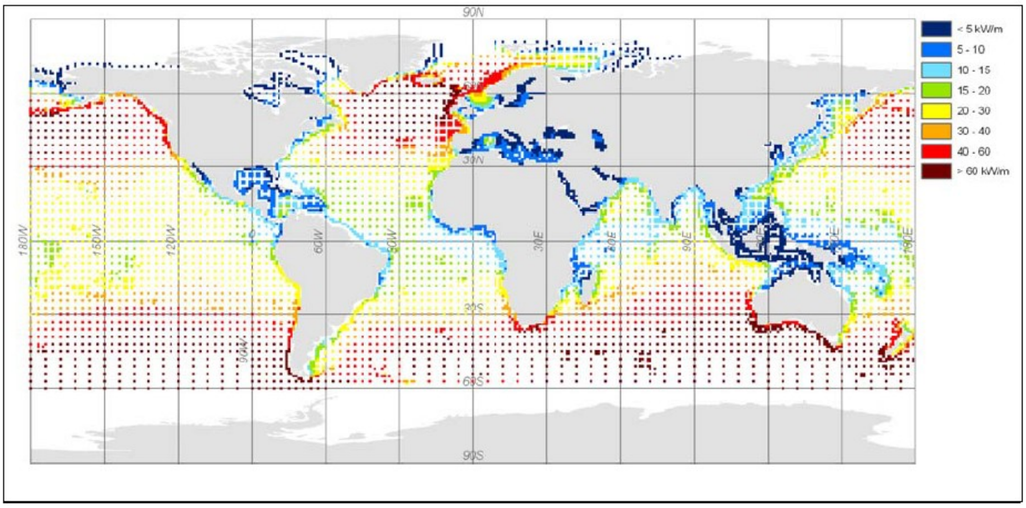

Fig. 3.18 *- Annual global gross theoretical wave power (American Society of Mechanical Engineers, 2010)*

In the figure [3.19] is showed the seasonality of the gross theoretical wave power distribution (ratio of the minimum monthly mean power to annual average) .The seasonality is much higher in the northern hemisphere. The system efficiency decreases significantly when the wave conditions are more variable and so wave resource stability is an important advantage for the southern hemisphere.

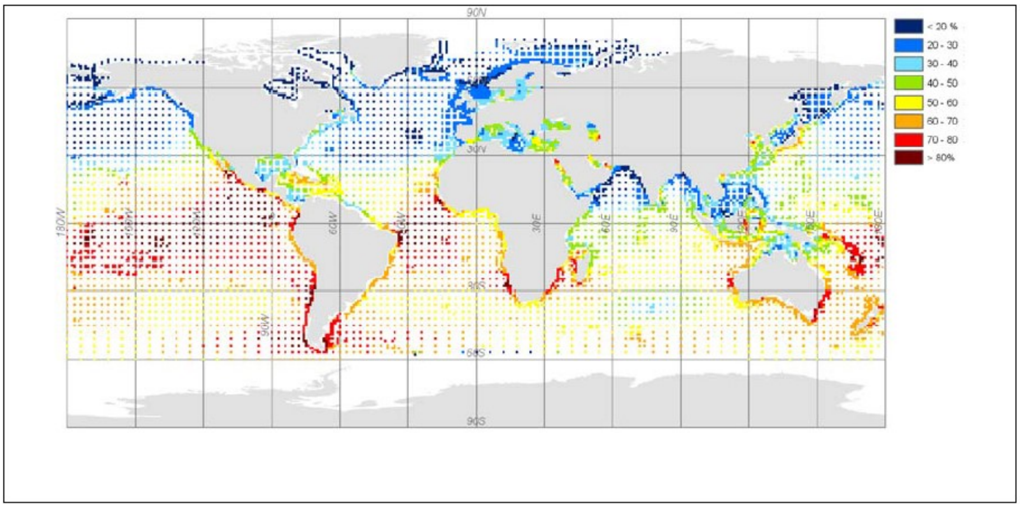

Fig. 3.19 - Seasonality of gross theoretical wave power distribution (American Society of Mechanical Engineers, 2010)

3.4 Wave energy devices

The wave energy devices can be characterized as belonging at three different classes. The shoreline, nearshore and the offshore devices. Each type has the own advantage and they are developing, promising great results in the near future; in the following paragraphs it is explained the most common devices that currently are at the center of many researches.

3.4.1 Shoreline devices

Shoreline devices have the advantage of being close to the utility network, are easy to maintain, and due to the travel through shallow water they have a reduced probability of being damaged in extreme conditions. On the other hand the shallow water leads to lower wave power, but this can be partially compensated by natural energy concentrated locations. Tidal range can also be an issue. In addition, by nature of their location, there are generally site specific requirements including shoreline geometry and geology and preservation of coastal scenery, so devices cannot be designed for mass manufacturing.

Probably the most popular and future profitable shoreline device is the Oscillation Water Column (OWC). As illustrated in the schematic figure in the next page [Fig. 3.20], this device uses wave motion to trap a volume of air and compress it in a closed chamber. The pressure is dissipated through a specialized ducted air turbine device at high velocities. When the wave recedes, the airflow fills the chamber generating a second burst of energy.

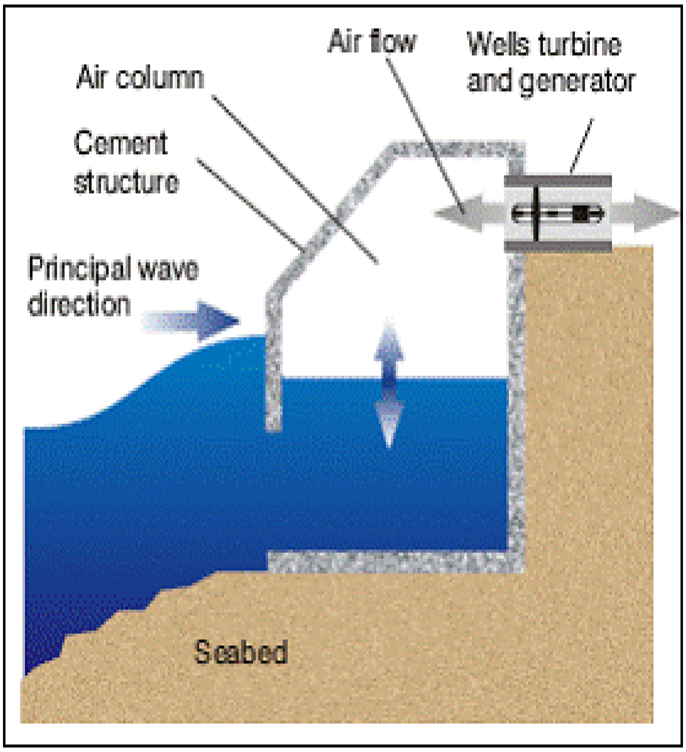

Fig. 3.20 *– Operation principle of a OWC (www.dpenergy.com)*

The turbine used is usually a Well's turbine [Fig. 3.21]; it is a special type of turbine, capable of maintaining constant direction of revolution despite the direction of the air flow passing through it.

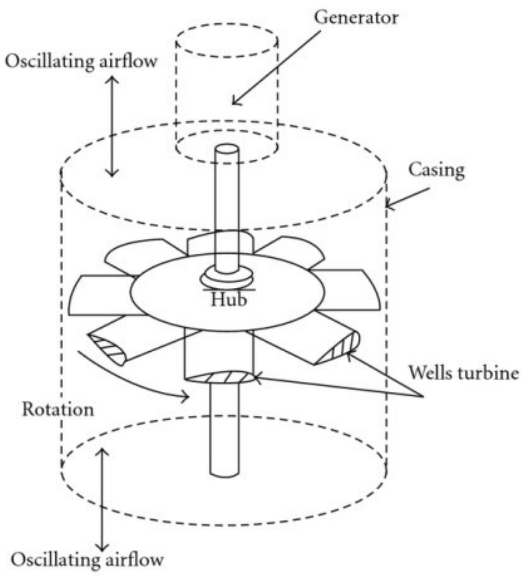

Fig. 3.21 *– Well's turbine (Takao et al., 2012)*

There are two shoreline OWC developed in Europe; the first one is the European Pilot Plant [Fig. 3.22]; located on the Pico Island in the Azores,the plant was designed as full-scale testing facility and it is fully automated; with a power of 400 kW it can supply a sizable part of the island's energy demand.

Fig. 3.22 *– European Pilot Plant (www.wavec.org)*

Limpet [Fig. 3.23], developed by the Queen's University of Belfast and Wavegen Ltd in the United Kingdom, is the follower of a prototype built on the island of Islay.

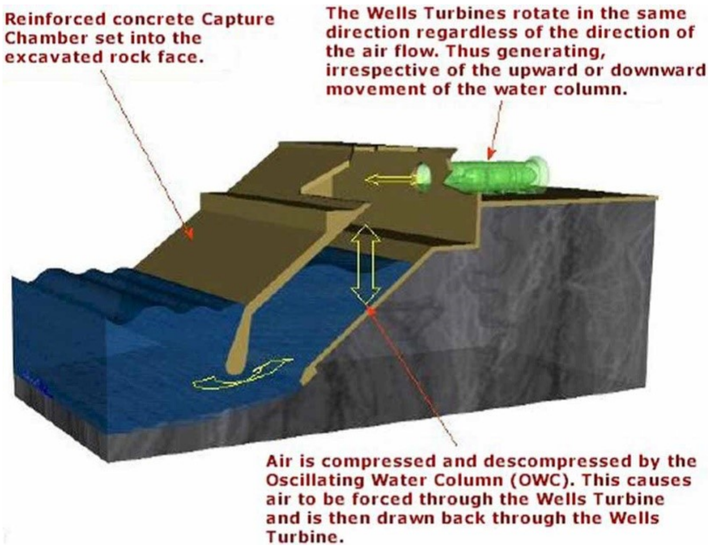

Fig. 3.23 *– Operation principle of the Limpet (source by Wavegen)*

This device was installed by the Wavegen in 2000 and this technology is still operational today [Fig. 3.24]:

Fig. 3.24 *– Limpet OWC (source by Wavegen)*

As it occurs for the tidal energy, it is possible to convey the water in the crest of the wave in artificial reservoir [Fig. 3.25]. Here the water is stored at a level higher than the average water level outside the basin due to the conversion of the kinetic energy in potential energy. The conversion occurs through conventional low head hydraulic turbines. As the OWC, this device can be fixed or not to the coastline (see in the following paragraph).

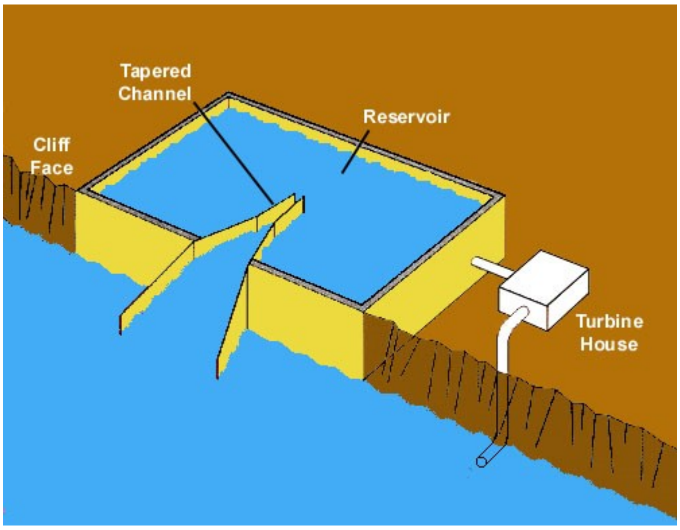

***Fig. 3.25** – Operation principle of the wave overtopping device (Boyle, 1996)*

Probably the most popular wave overtopping device is the Tapchan [Fig. 3.26]; built in Norway in 1980, it consists of a collector that funnels waves into an narrow channel that increases their height.

Since there are few moving parts, the maintenance costs are relatively low, and the reservoir gives energy storage. The output power is also very consistent, in contrast to most wave power devices which give a cyclic output with the cycle of the waves. However, construction costs associated with the reservoir and long channel are high, and so the location must be carefully chosen to include natural features which might form the basis for construction.

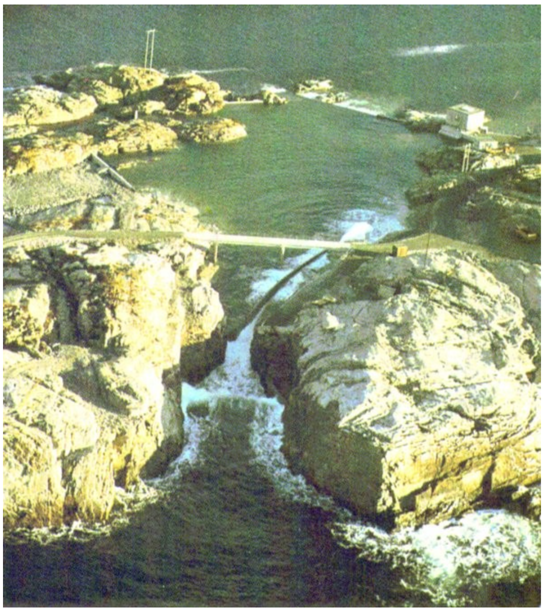

***Fig. 3.26** – Tapchan overtopping device (www.dpenergy.com)*

3.4.2 Nearshore devices

Nearshore devices are defined as devices that are in relatively shallow water, that is usually when the water depth is less than one quarter of the wave length. Devices in this location are often attached to the sea bed, which gives a suitable stationary base against which an oscillating body can work. Like shoreline devices, a disadvantage is that shallow water leads to waves with reduced power, limiting the harvesting potential.

The main and first prototype device for moderate water depths was the Osprey [Fig. 3.27], developed by Wavegen Ltd. in the UK.

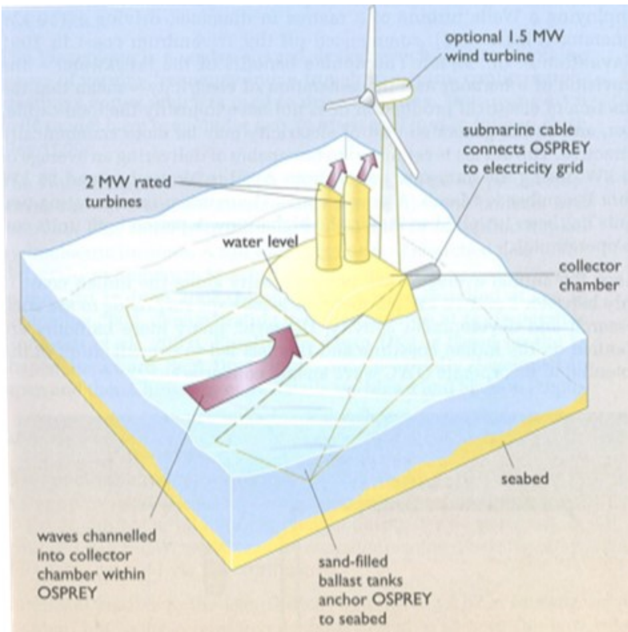

***Fig. 3.27** – Schematic representation of the Osprey WEC (Boyle, 2004)*

Many and different prototypes were designed, and the first device, made in steel, called Osprey 1 [Fig. 3.28] was installed at 100 m off the coast at Dounreay. Taking into account the advantage of larger waves, it was installed relatively faraway the shoreline. However, it means to dare the environment. This was demonstrated in 1995 when the prototype was destroyed in a storm.

***Fig. 3.28** – Osprey 1 (Martin Bond, SCIENCE PHOTO LIBRARY)*

Another type of shoreline device is the Oyster, designed by Aquamarine Power Ltd. The Oyster [Fig. 3.29, Fig. 3.30] is a bottom hinged rigid flap which completely penetrates the water column from above the surface to the sea bed. When waves attach the Oyster, WEC starts to rotate around the horizontal axis, and this motion moves an high pressure water pump. The flow is transferred to the shore through pipeline where the hydraulic pressure is converted into electric power via a Pelton turbine.

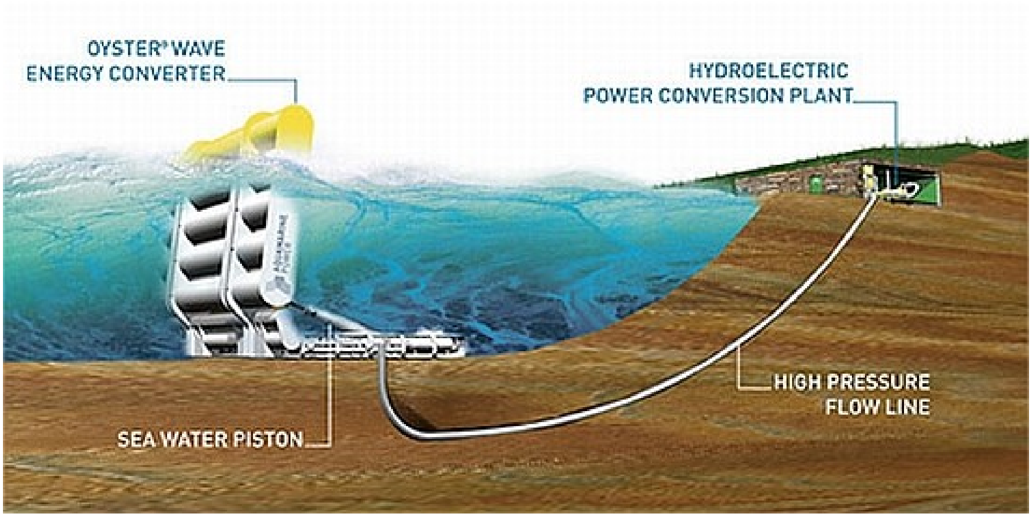

Fig. 3.29 *– Oyster WEC (www.aquamarinepower.com)*

Fig. 3.30 *– Oyster WEC (www.aquamarinepower.com)*

3.4.3 Offshore devices

Offshore devices are generally in deep water. The definition "deep water" can mean "tens of meters" or "a depth exceeding one third of the wavelength" as well. The advantage of siting a WEC in deep water is that it can harvest greater amounts of energy due to the higher energy content in deep water waves, as showed in the figure below taken from a study conducted by the society AW-Energy [Fig.3.31]; however, offshore devices are more difficult to build, to maintain, and need to be designed to survive the more extreme conditions, adding cost to the construction.

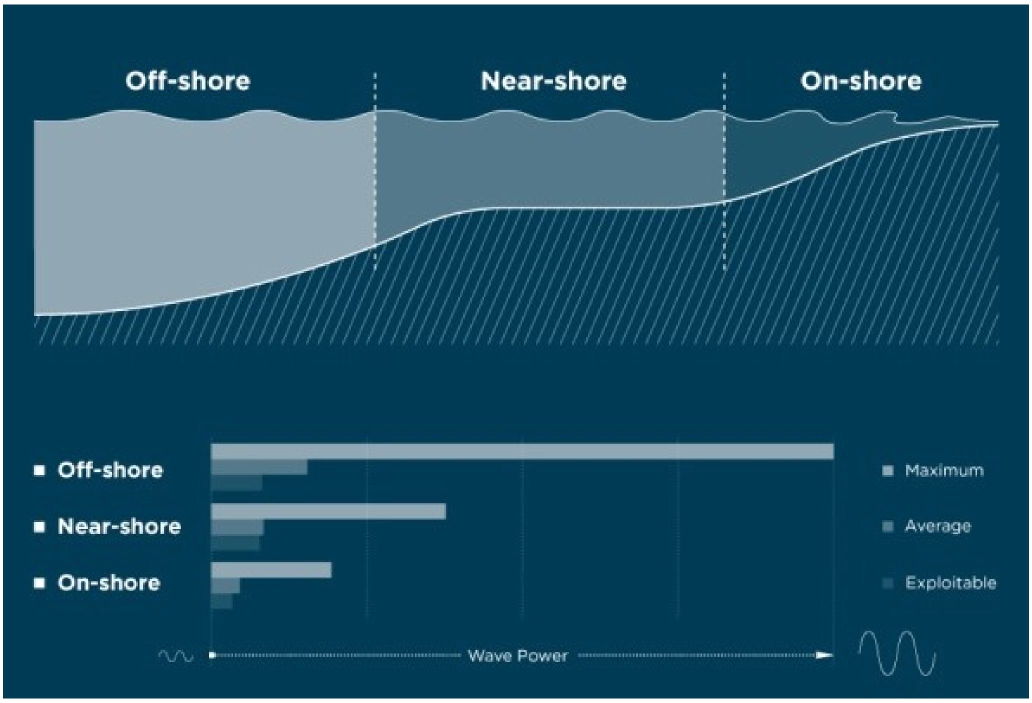

Fig. 3.31 *– Wave energy for the three different kinds of device (www.aw-energy.com)*

Some of the promising offshore WECs developed in Europe are illustrated below.

The Archimedes wave swing is a simple solution. This wave energy converter is a cylindrical shaped buoy which is submerged and tethered to the ocean floor. Moored to the seabed, this generation unit has got only one moving part, the floater unit. The floater unit is an air-filled device which is connected to a lower fixed cylinder. In the fixed cylinder, a uniquely designed linear generator converts the up and down motion into energy.

According to Archimedes principle, when an object is submerged in a fluid, a force acts on the object which forces it upwards. The wave action powers the floater which moves up and down, generating a reciprocating movement [Fig. 3.32].

The power-absorption concept has been proven at full-scale in 2004 in a pilot plant that was installed off the coast of Portugal.

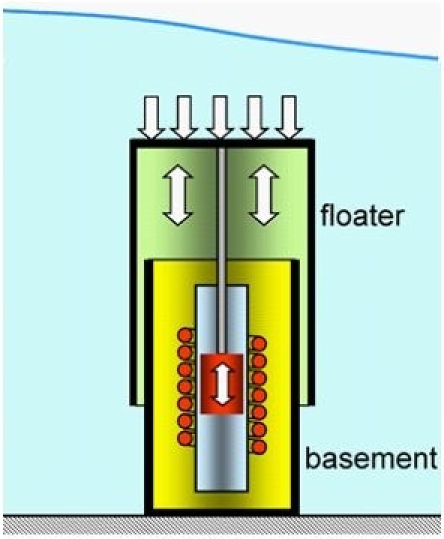

Fig. 3.32 *– Archimedes wave swing operational principle(Cruz, 2008)*

An alternative method of generating power is through so called moving body devices which rely solely on the relative movement of different parts of the device with the waves to generate pressure in a working fluid. The working fluid might be sea water or hydraulic oil held in a sealed tank which is then passed through a turbine to generate electricity.

The McCabe Wave Pump [Fig. 3.33], conceived in 1980 was one of the early exponents of this principle. It consists of three tubular sections or pontoons which face into the wave and pivot as wave fronts move across.

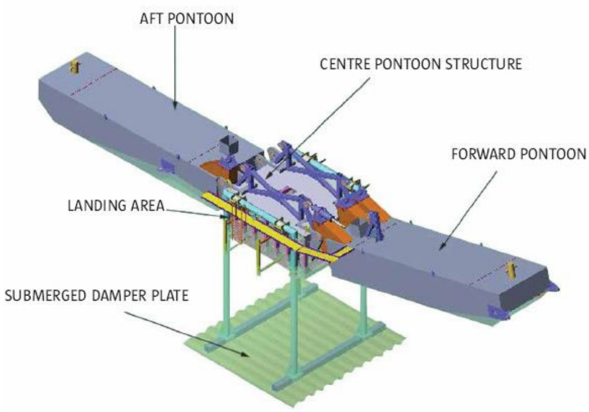

Fig. 3.33 *– The McCabe Wave Pump (Energetech 2006)*

The McCabe Wave Pump currently under development by Hydam Technology Ltd was deployed in 1996 off the coast of Kilbaha, County Clare, Ireland and was installed in the Shannon Estuary off the west coast of Ireland with trials completed in 2004 [Fig. 3.34]:

***Fig. 3.34** – The McCabe Wave Pump (Hydam Technology Ltd)*

The Pelamis [Fig. 3.35] is a device 150 meters long, with a diameter of 3.5 meters and a weight of approximately 700 tons.

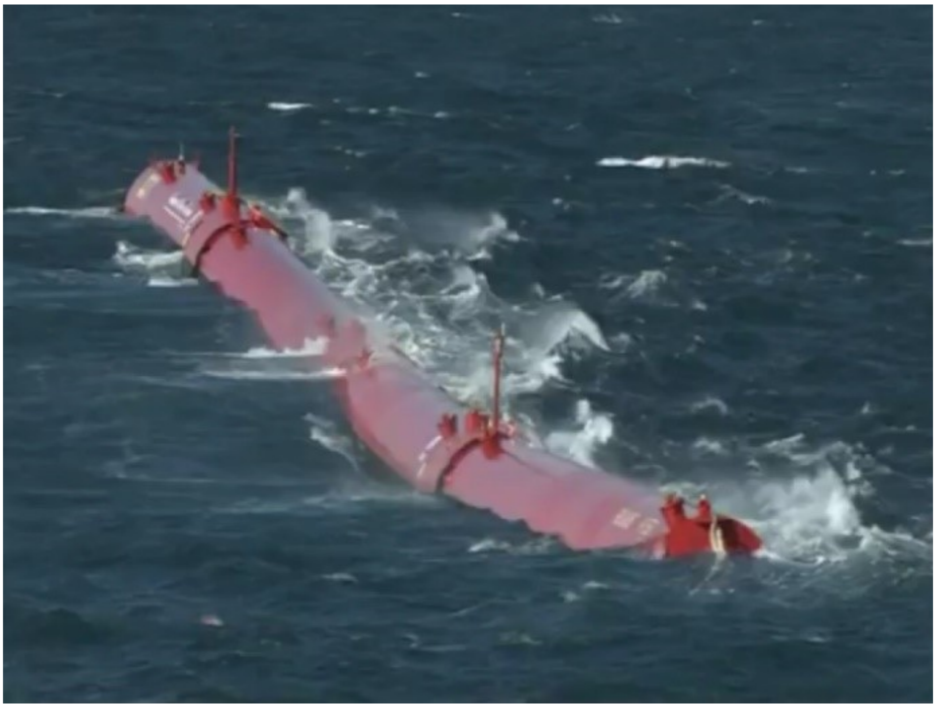

***Fig. 3.35** – Pelamis in function (www.pelamiswave.com)*

As a wave passes the device, the sections are forced to rise and fall relative to one another, causing at the hinges between each section a moment [Fig. 3.36]:

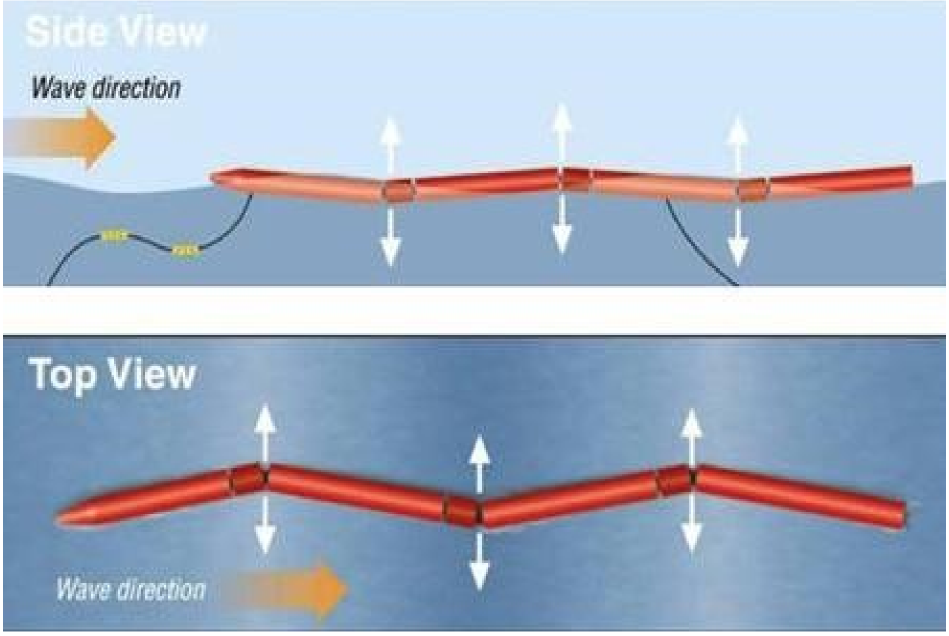

Fig. 3.36 *– Pelamis (http://www.pelamiswave.com)*

Hydraulic rams resist this hinging, and the pressurised fluid then drives turbines, which in turn drive electrical generators, housed in the body of the device [Fig. 3.37]:

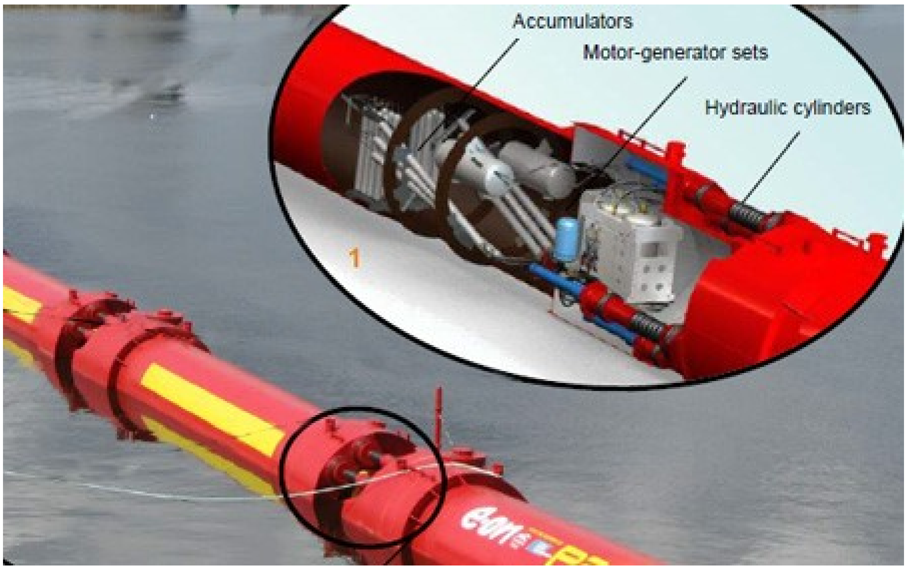

Fig. 3.37 *– Pelamis PTO (www.pelamiswave.com)*

The Pelamis is moored to the sea bed in order to keep it in position [Fig. 3.38], but it is able to turn so it will naturally face the oncoming waves, from whichever direction they arrive.

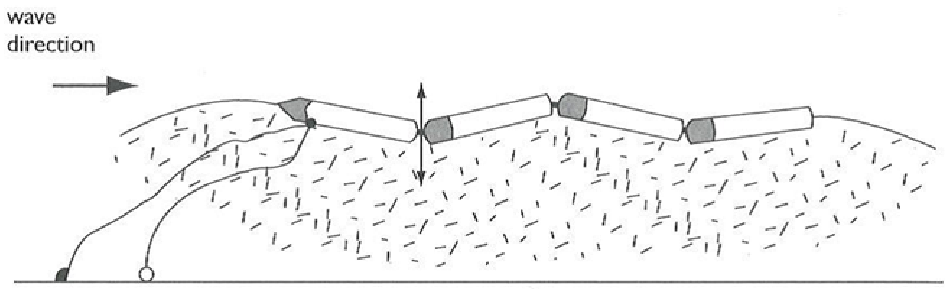

Fig. 3.38 *– Anchorage of Pelamis (www.pelamiswave.com)*

In the 1970 Stephen Salter, a professor at Edinburgh University, designed a wave generation system potentially capable of capturing 90% of the incident wave energy [Fig. 3.39]:

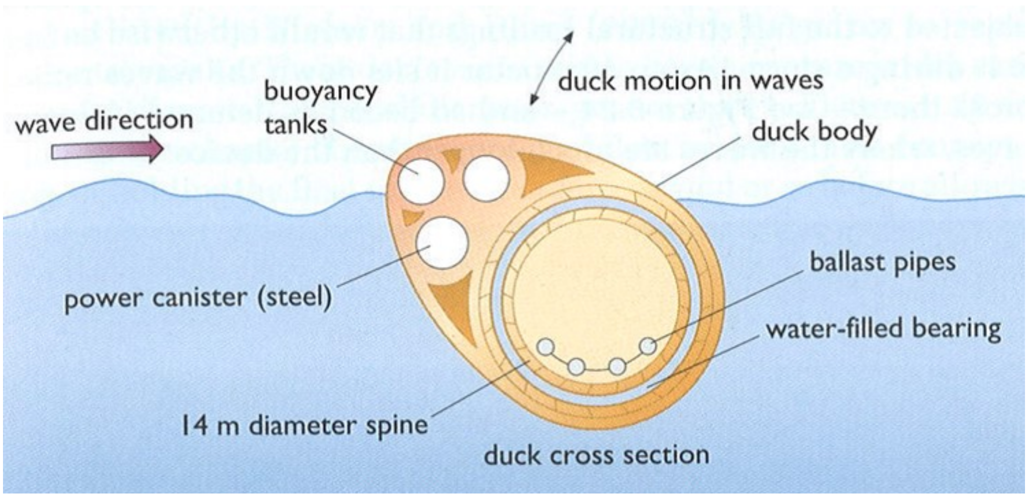

Fig. 3.39 *- Salter's duck section (Thorpe, 1999)*

The leading edge of the duck is shaped such that the pressures exerted on it by the approaching wave force the duck to rotate about a central axis, and the tip bobs in the water. This rotation, relative to fixed moorings at either end, is converted into useful power by an electrical generator housed in the body. This could be done by driving pistons, which force hydraulic fluid to drive a motor powering an electrical generator as illustrated in the following example [Fig. 3.40]:

Fig. 3.40 *- Salter's duck (www.mech.ed.ac.uk)*

The OWC is surely one technology that can be applied in offshore conditions; many prototypes are developing like the examples reported below [Fig. 3.41, Fig. 3.42, Fig. 3.43]:

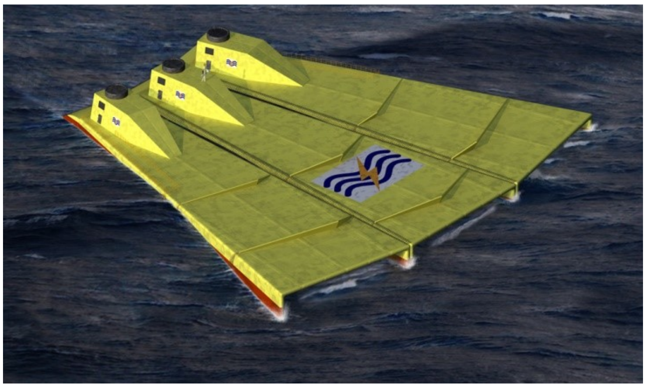

Fig. 3.41 *– Offshore OWC (www.owel.co.uk)*

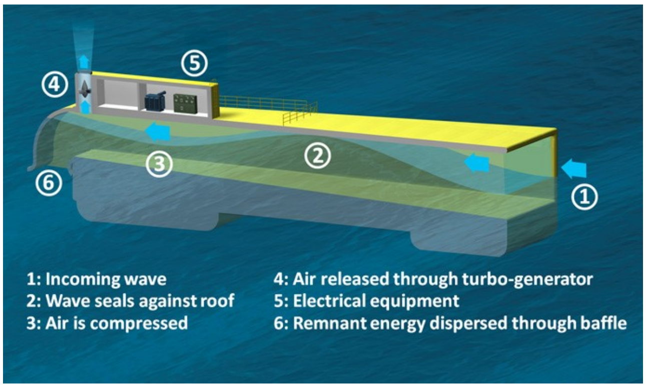

Fig. 3.42 *– Offshore OWC (www.owel.co.uk)*

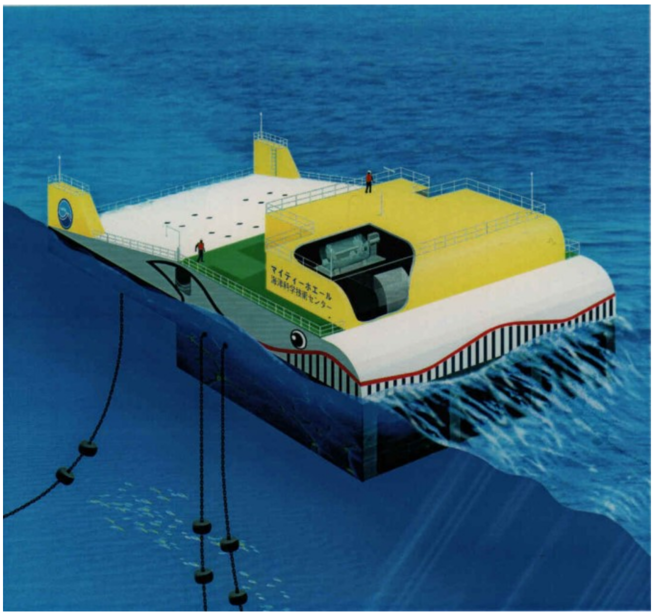

Fig. 3.43 *– Offshore OWC (www.jamstec.go.jp)*

The world's first operational grid-connected offshore wave energy device is the Wave Dragon [Fig. 3.44, Fig. 3.45, Fig. 3.46]. The device, installed in the summer 2003 in Denmark, had an output power of 20 kW, but after initial tests additional turbines were added and the device moved to a new location with more intense waves.

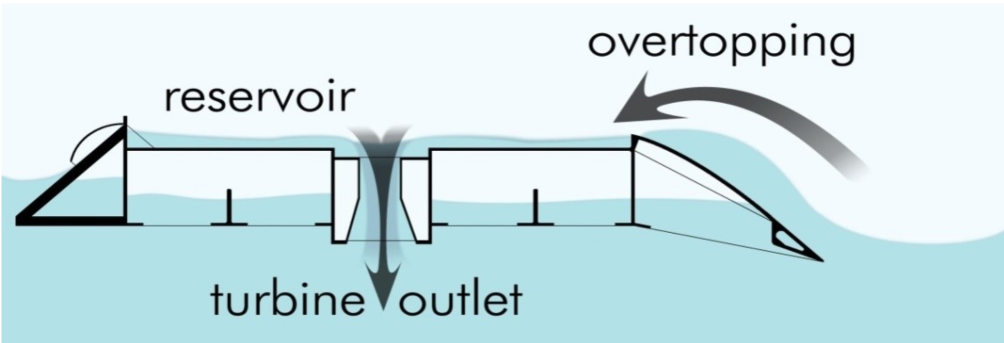

Fig. 3.44 *– Offshore overtopping device (www.wavedragon.net/)*

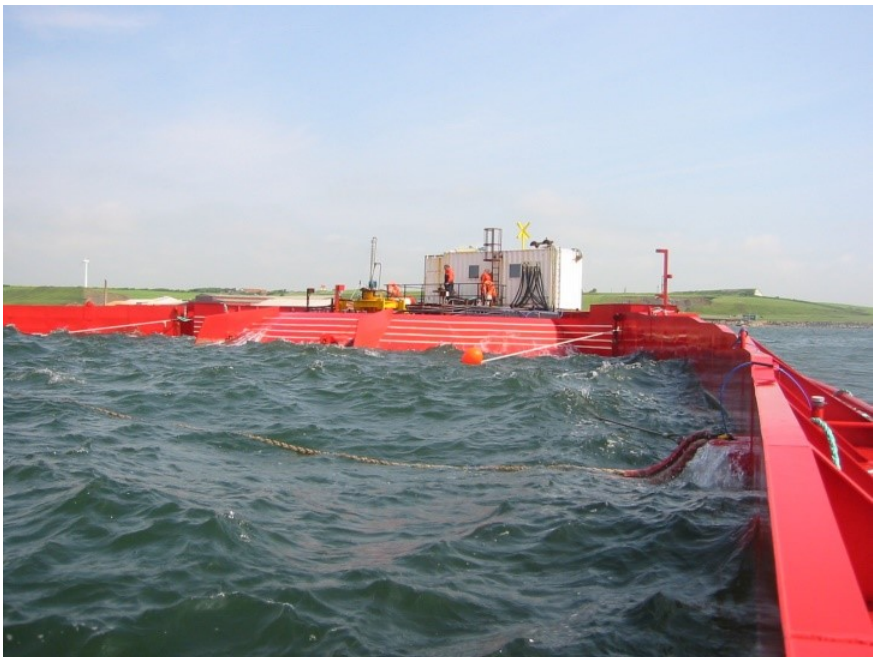

Fig. 3.45 *– Wave dragon WEC (www.wavedragon.net/)*

Fig. 3.46 *– Wave dragon WEC (www.wavedragon.net/)*

The point absorber is a type of wave energy device that, , compared to other technologies, can provide a large amount of power in a relatively small device. Point absorbers are relatively small compared to wave length, and may be bottom mounted or floating structures.

The conversion of power in the system can take many forms and depends on the conformation of the device.

The problems for these devices are related to the water depth, and could be compared with the general issues that can be find in the offshore structures in general: difficult and more expensive maintenance, anchorage in deep water, long cables etc. .

One of the first buoy model developed is the Norwegian buoy. The device was tested 1980 in the Trondheim Fjord. The floating buoy could oscillate along a strut that was connected to a universal joint on an anchor on the sea bed.

The mechanism of working is very simple. The hull is open and sea water can flow into and out from an inner chamber, where the water surface acts as the piston of an air pump.

The three photos show, from left to right, the buoy when it moved near its equilibrium position, when latched in low position and finally when latched in upper position [Fig. 3.47]:

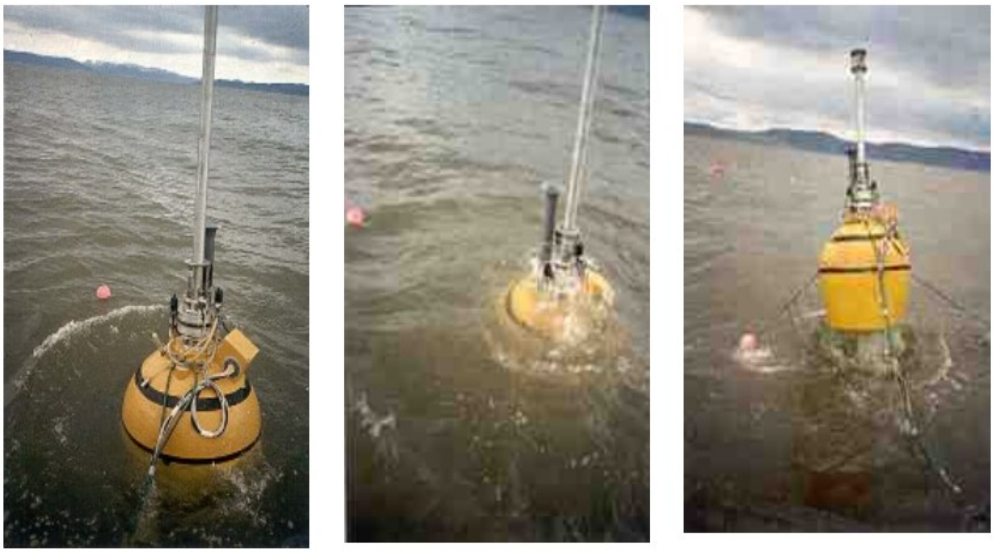

Fig. 3.47 *- Photos of the Norwegian buoy (Budal et al., 1982)*

Another kind of PTO is a linear electric generator that is housed inside a steel hull mounted on a concrete ballast structure and converts linear motion of cable to electric power [Fig. 3.48]:

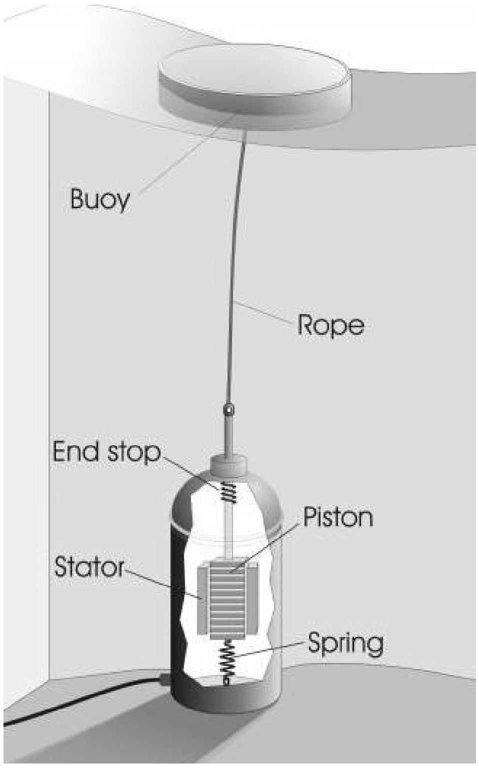

Fig. 3.48 *– Sweden buoy WEC (Uppsala University)*

Two body heaven convertors are multi-body convertors in which ocean power is extracted from the relevant motion between two bodies. One of these bodies is float on ocean surface and another is completely submerged.

The wavebob [Fig. 3.49] consists of an inner buoy, submerged body (body2), and floating buoy (body 1) which are axially connected to each other. Additionally a high Pressure oil hydraulic system is implemented extracting power to electric generator.

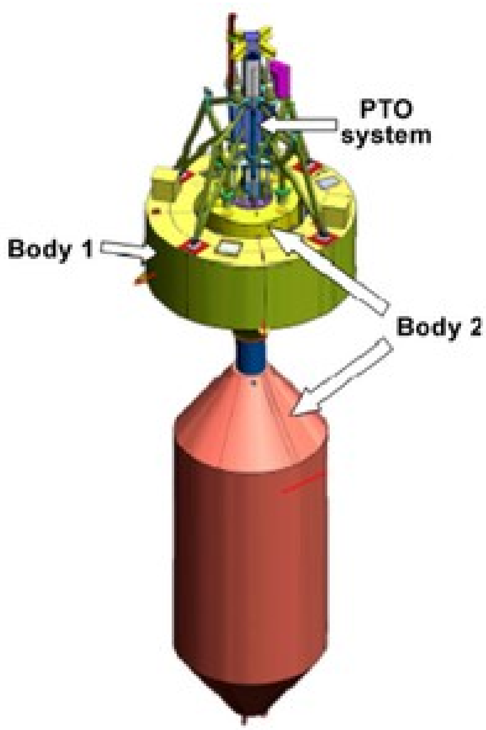

Fig. 3.49 *– Wavebob (Falcão et al., 2010)*

The PowerBuoy [Fig. 3.50] sits below the water's surface. Inside, a piston moves as the PowerBuoy bobs with the rise and fall of the waves. This movement drives a generator, producing electricity which is sent to the shore by an underwater cable.

Fig. 3.50 *– Powerbuoy (www.oceanpowertechnologies.com)*

In the case of heaven buoys, Wave Star Energy company has developed an innovative WEC namely Wave Star WEC. In this device a jack up structure stands on sea bed and provides a reference to the buoys [Fig. 3.51]. A full sized system is consisting of different buoys in which a hinging arm is utilized to transfer each buoy's motion to the PTO. The buoys have ability to be polled up (survival mode) in case of storm condition.

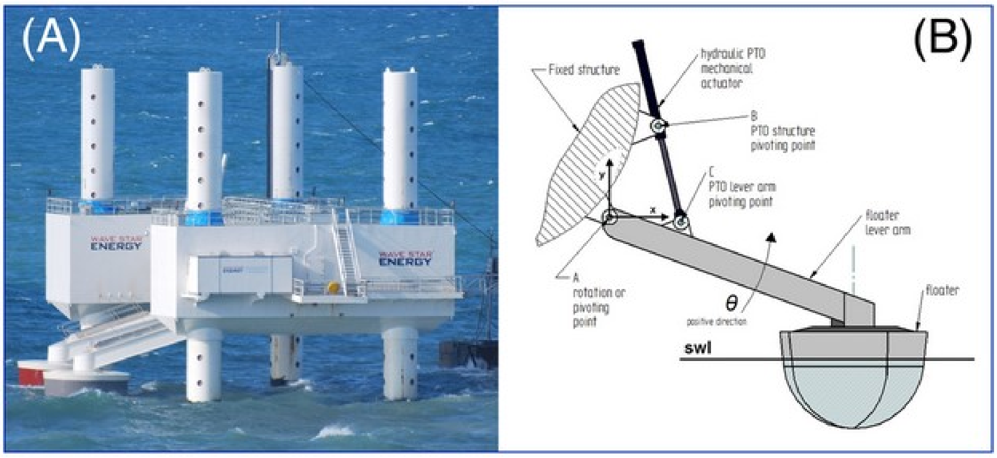

Fig. 3.51 *- Wave Star WEC (www.wavestarenergy.com)*

Pitching oscillators are WECs which extract wave power by hinging motion in wave propagation direction.

Developed in Lancaster University, PS Frog Mk 5 [Fig. 3.52] is the best example of Floating Pitching Convertors. The PS Frog Mk 5 is composed of a large buoyant paddle with an internal ballasted handle below it. It oscillates in pitching mode and is float on sea level. When wave acts on paddle the ballast provides necessary reaction for pitch motion, consequently the wave power is absorbed by partially resisting the sliding of a PTO mass, which moves in guides above sea level. The mechanical motion is transferred via hydraulic circuit to an electrical generator.

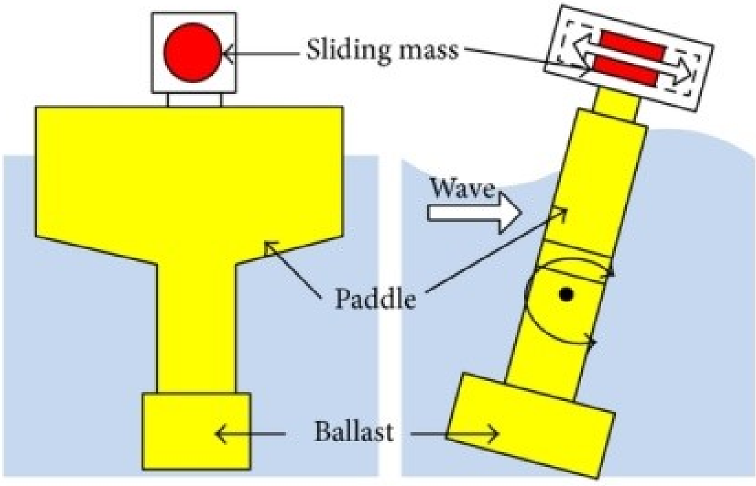

Fig. 3.52 *- PS Frog Mk 5 (Falcão et al., 2010)*

The IPS buoy [Fig. 3.53] was invented by Noren. The device consists of a buoy rigidly connected to a fully submerged vertical tube called "acceleration tube" open at both ends. The tube contains a piston whose motion relative to the floater tube system; this motion is originated by wave action on the floater and by the inertia of the water enclosed in the tube, driving a power take off mechanism.

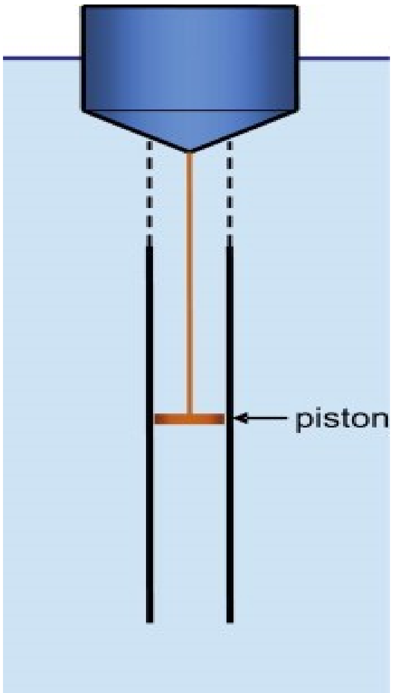

Fig. 3.53 *– The IPS buoy (Falcão et al., 2012)*

The Aquabuoy [Fig. 3.54] follows the same principles of the IPS buoy but at the both ends of the tube there is attached a hose pump, or rather a steel reinforced rubber tube that pressurizes and pumps water as it is stretched and compressed. As the buoy bobs, seawater is pushed up and down the tube causing the piston to move and extend or compress the hose pump. The pressurized water is sent through an electric generator before being returned into the ocean.

Fig. 3.54 *– The Aquabuoy (www.finavera.com)*

The sloped IPS buoy [Fig. 3.55, Fig. 3.56] is another variation of the original IPS buoy studied in 1990 at the University of Edinburgh.

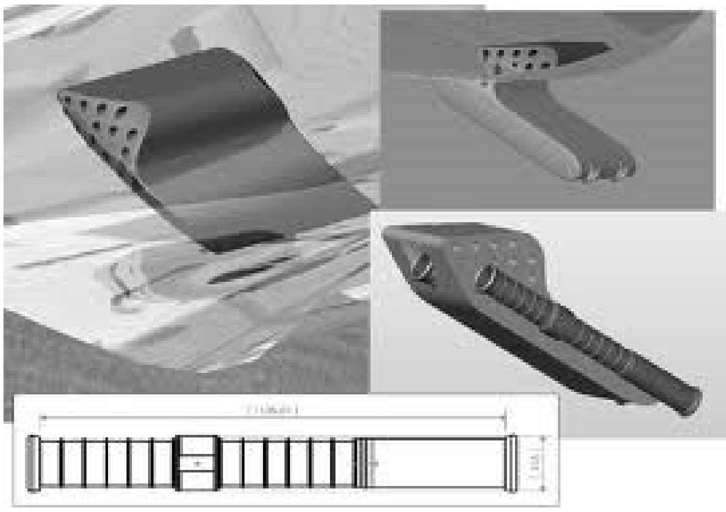

Fig. 3.55 *– The sloped IPS buoy (www.mech.ed.ac.uk)*

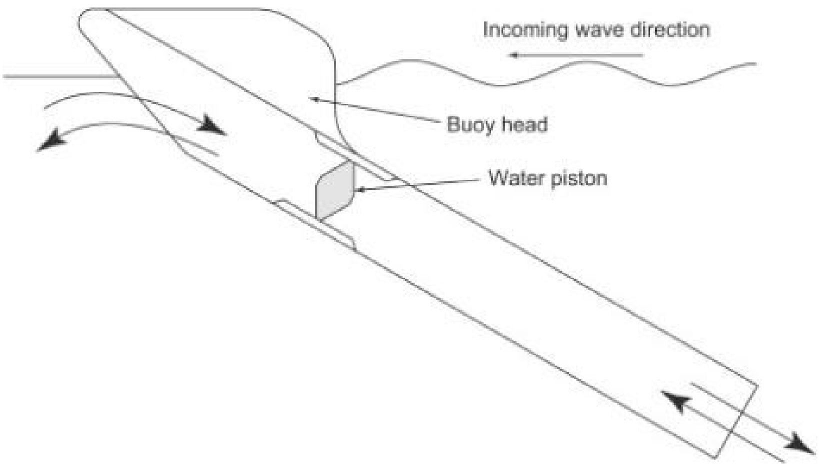

Fig. 3.56 *– The sloped IPS buoy (www.mech.ed.ac.uk)*

3.5 The FlanSea Project

The FlanSea project, launched the 1st September 2010 as the effort and the result of a collaboration of many partners, was aiming to study all aspects of a single point absorber wave energy converter in order to acquire relevant knowledge of this new technology.

An important pillar in this research was the design, construction, testing and analysis of the test results of a prototype point absorber WEC, later called the Wave Pioneer, in Ostend [Fig. 3.57, Fig. 3.58, Fig. 3.59].

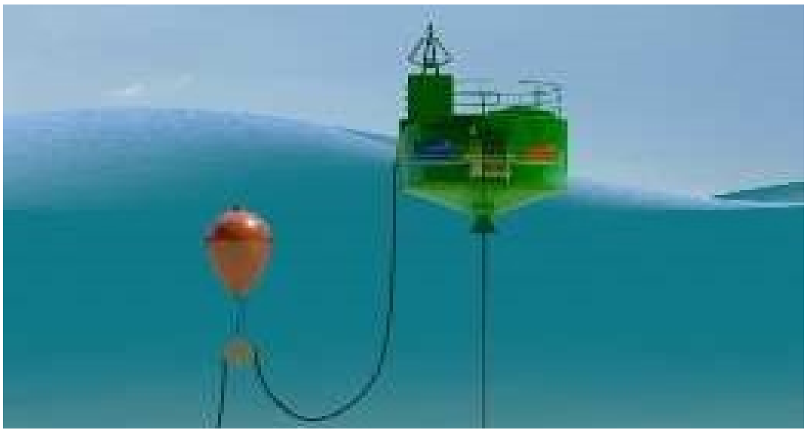

Fig. 3.57 *– The FlanSea project (The FlanSea project, 2013)*

Fig. 3.58 *– Photo of the FlanSea buoy moored at the dock (FlanSea end report, 2014)*

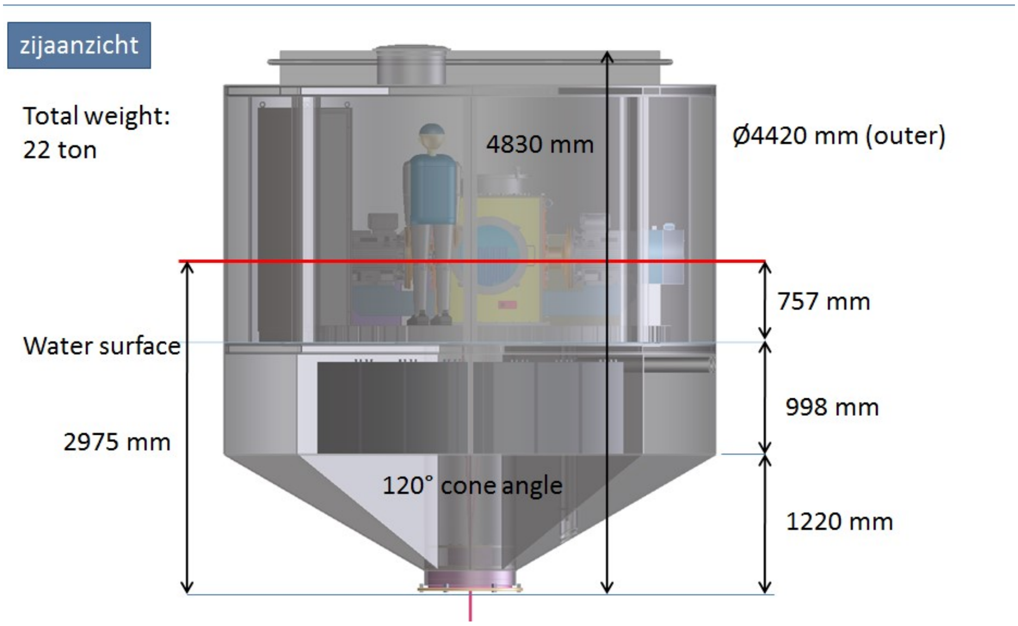

***Fig. 3.59** – Section of the FlanSea buoy (The FlanSea project, 2013)*

The first step involved the design of a concept, which was then tested in a scale of 1:10 at the Borgerhout Hydraulics Lab [Fig. 3.60].

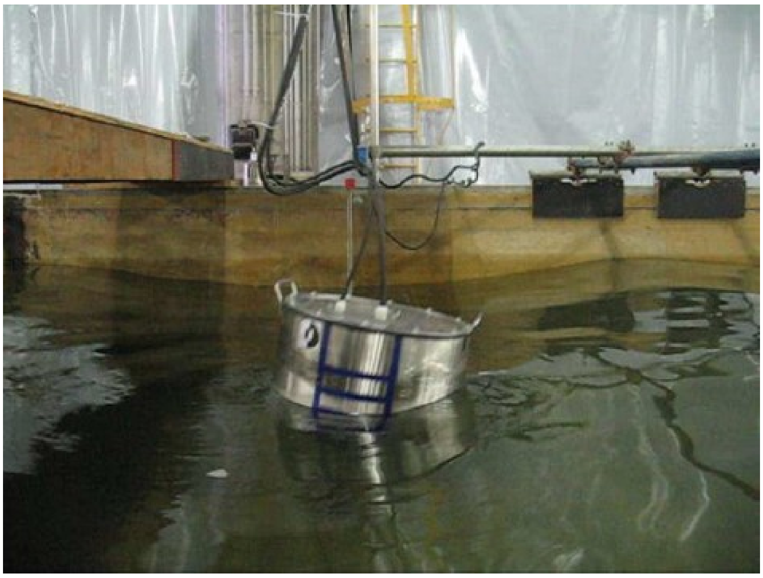

***Fig. 3.60** – The prototype in 1:20 scale during the tests (The FlanSea project, 2013)*

Numerous devices were identified and evaluated for the safe anchoring of the buoy in storm conditions; at last the Wave Pioneer was tested with significant wave height of over 2,5 meters and the anchorage demonstrated good resistance to keep the device in position during the extreme waves [Fig. 3.61, Fig. 3.62]:

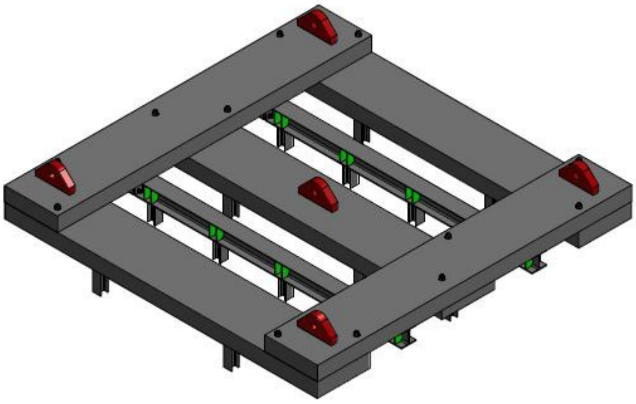

Fig. 3.61 *– 3D illustration of the anchorage (The FlanSea project, 2013)*

Fig. 3.62*– Photo of the anchorage (The FlanSea project, 2013)*

The Wave Pioneer was also equipped with many sensors, ranging from a few temperature sensors to video cameras for recording real life images [Fig.3.63]:

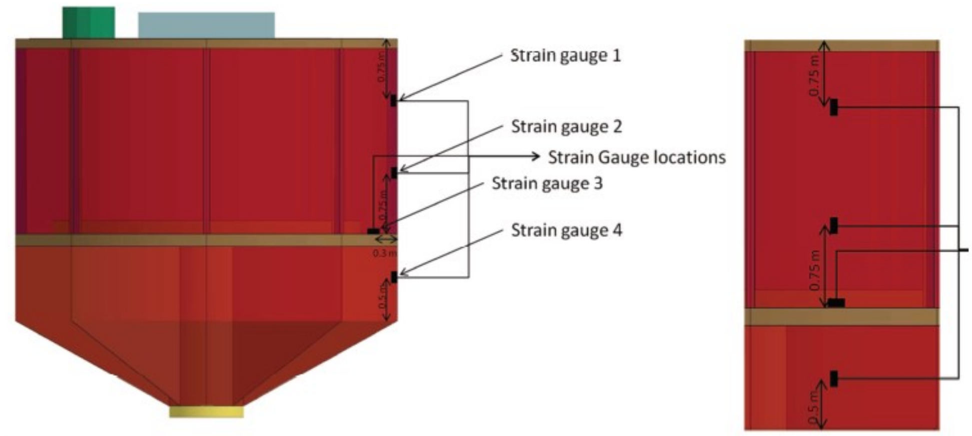

***Fig. 3.63** – Positions of the strain gauges on the buoy (FlanSea end report, 2014)*

Finally the Wave Pioneer Finally, with a rated power of 25 kW, was tested in the port of Ostend from 23rd April to June 26th 2013 [Fig. 3.64] and from June 26th to November 28th 2013 outside the breakwaters [Fig. 3.65, Fig. 3.66]

***Fig. 3.64** – The buoy in the Ostend harbor (The FlanSea project, 2013)*

Fig. 3.65 *– Transport of the buoy out of the dock (FlanSea end report, 2014)*

Fig. 3.66 *– The FlanSea buoy out of the breakwaters (The FlanSea project, 2013)*

As important consequence of its hydrodynamic shape and a redundant survival system the Wave Pioneer proved storm resistant. In the following picture a photo taken during the storm occurred in September 2013 [Fig. 3.67]:

***Fig. 3.67** – The buoy during the storm (September 2013, Hs = 2.5 m) (The FlanSea project, 2013)*

It was a lot of sea experience gained by the project, both during testing in the dock, outdoor the breakwaters and during the various test periods at sea. The main point is that the development, the installation and the maintenance of a wave energy converter in open sea are expensive, and so the economic potential of the concept of Wave Pioneer is even more important. Some important negative aspects met during the tests are the followings:

- Due to the movement of the buoy and the multiple incoming and outgoing movement of the main cable, the entry section of the Wave Pioneer is resulted very susceptible. A reliable alternative is necessary in order to maintain the buoy operational for a longer period of time.
- The tide and in particular the associated flow created significant problems related to the operational behavior; for example the standby behavior buoy induced slack in the rope, and this created issues with the anchorage..
- The average power per float is limited in relation to the relatively high cost for the electrical connection.
- A system with a cable connection to the soil is very simple, but has an higher maintenance costs. Coupled with the higher wear than expected, this provides a high operational cost. Efforts should be made therefore to a design where crucial components of float are accessible to visual inspection.

Visible damages are reported in the following. A first heavy cable damage occurred by the jamming of the cable under the edge of the anchorage [Fig. 3.68]:

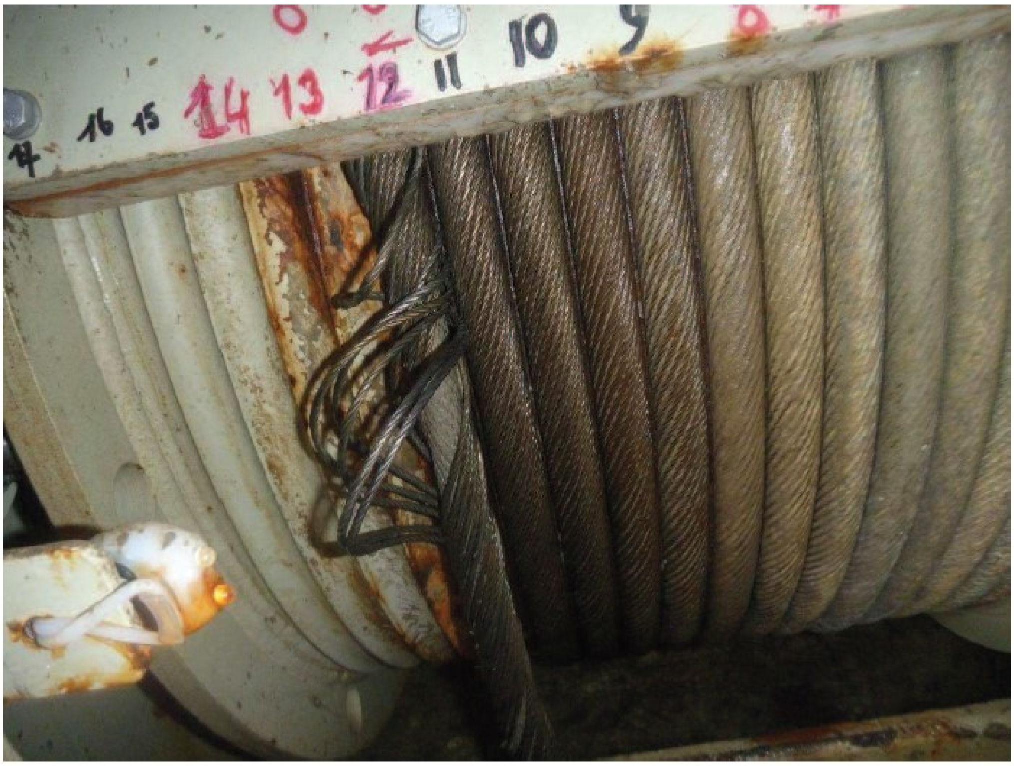

Fig. 3.68 *– The cable damaged (FlanSea end report, 2014)*

A second heavy cable damage occurred after damaging the keel of the buoy, as showed in the photo below [Fig. 3.69]:

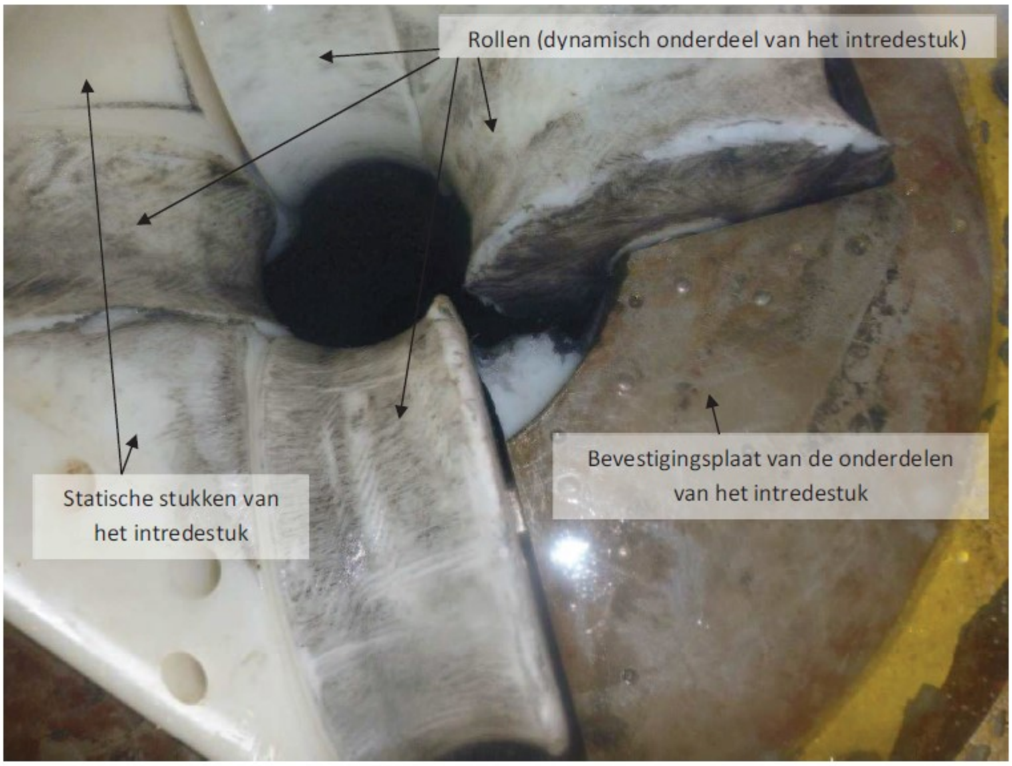

Fig. 3.69 *– Injuries at the buoy's keel (FlanSea end report, 2014)*

By the way, a lot of data have been recorded like the total motor force, the buoy's position, the output power PTO and the net production. In the following table are represented some time series of the precious mentioned parameters [Fig. 3.70]:

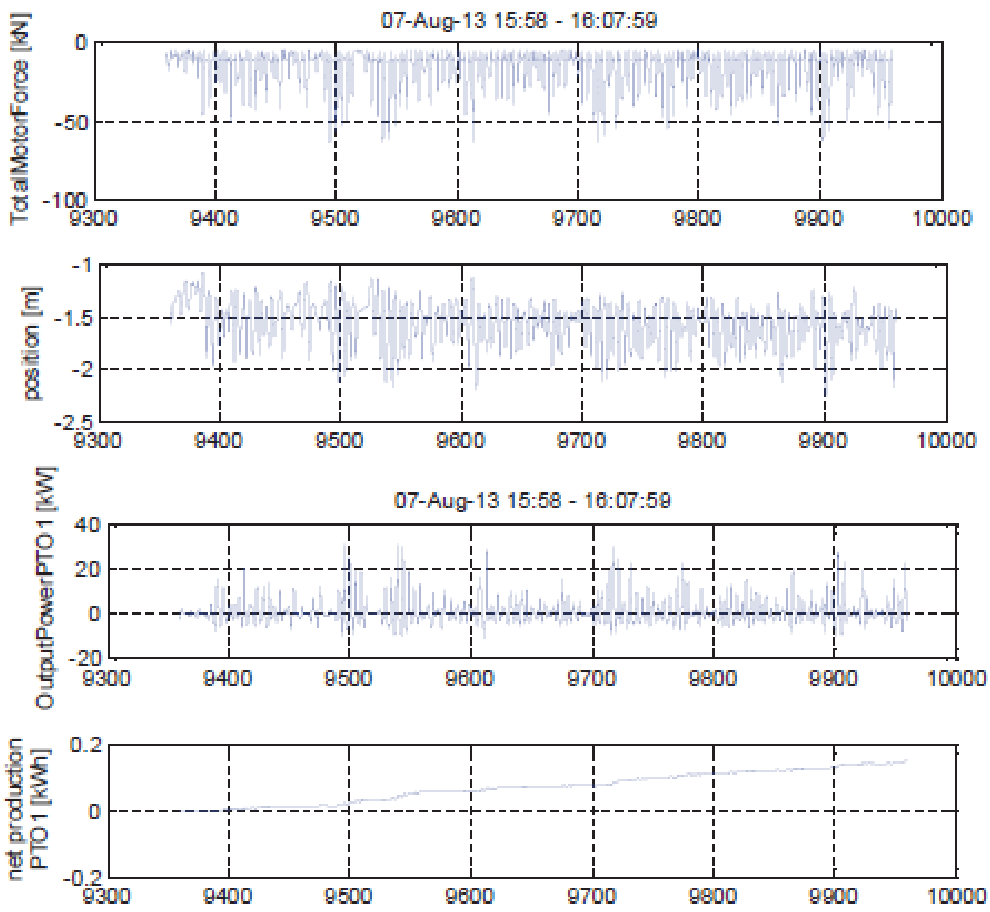

Fig. 3.70 *– In the picture the total motor force [kN], the buoy's position [m], the output power PTO [kW] and the net production PTO [kW/h] for a small time window (FlanSea end report, 2014)*

3.6 PTO

Due to the very small scale used, the power take off (PTO) system is not included in this study; on the other hand it represents one of the most important and critical part of each wave energy device. Talking about point absorber we can find different PTO systems: electrical systems and hydraulic systems.

3.6.1 Electrical PTO with constrained tuning

The Electrical PTO system [Fig. 3.71] is the most studied device and consists of:

- a winch on which the cable winds;
- two gearboxes at both sides of the winch. They upscale the rotational velocity to match better the rpm of the motor/generator.

These machines generate electricity during the upward movement or energy can be invested during part of the downward movement. The motor force consists in four different components: the tuning force, the damping force, the inertia compensation force and pulling force:

- the tuning force is a force used to tune the natural frequency of the buoy;
- the damping force is the force generates power;
- the inertia compensation force is the force that compensates the inertia force of the rotational inertia when the buoy moves down;
- the pulling force is a constant force used to keep tension in the cable.

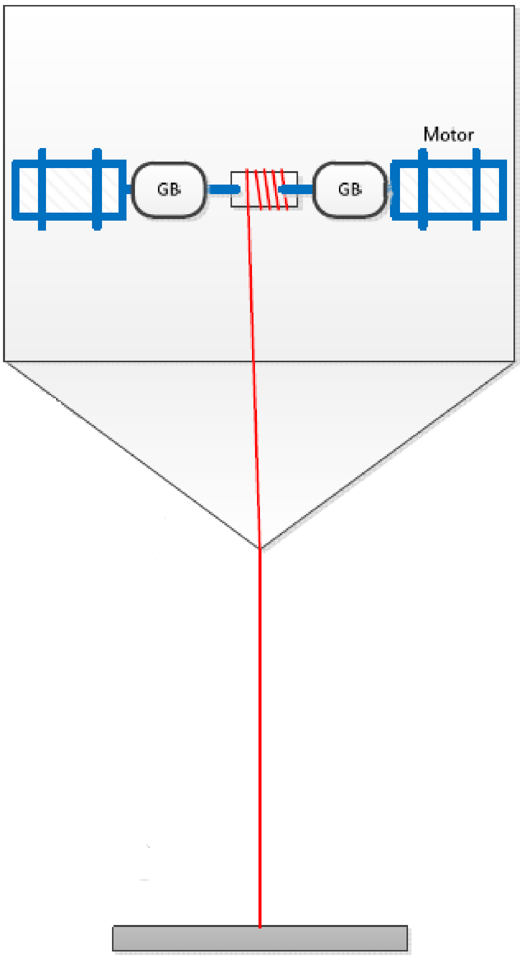

Fig. 3.71 - Device of an electrical PTO with constrained tuning (The FlanSea Project)

3.6.2 Hydraulic PTO system

This system is based on a cylinder that pumps oil into an accumulator. The pressure is then converted in energy by a generator. This system is characterized by:

- a cylinder converts the wave forces through the buoy movement into hydraulic pressure;
- a winch that compensates for tidal height variations;
- a hydraulic system that consists of: a passive one-way valve (for the classical latching system) [Fig. 3.72] or an active valve (for the constant force tuning) [Fig. 3.73], that separates cylinder from high pressure accumulator, an accumulator at high pressure, an hydraulic motor that is connected to a generator, a low pressure reservoir, passive one-way valve that separates the reservoir from the cylinder.

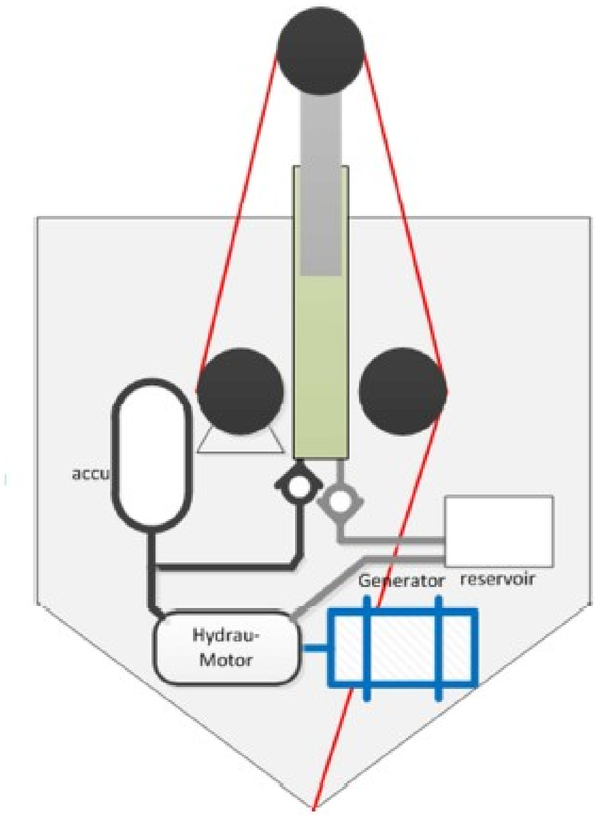

***Fig. 3.72**– Scheme of a hydraulic PTO system with a passive one way valve (The FlanSea Project)*

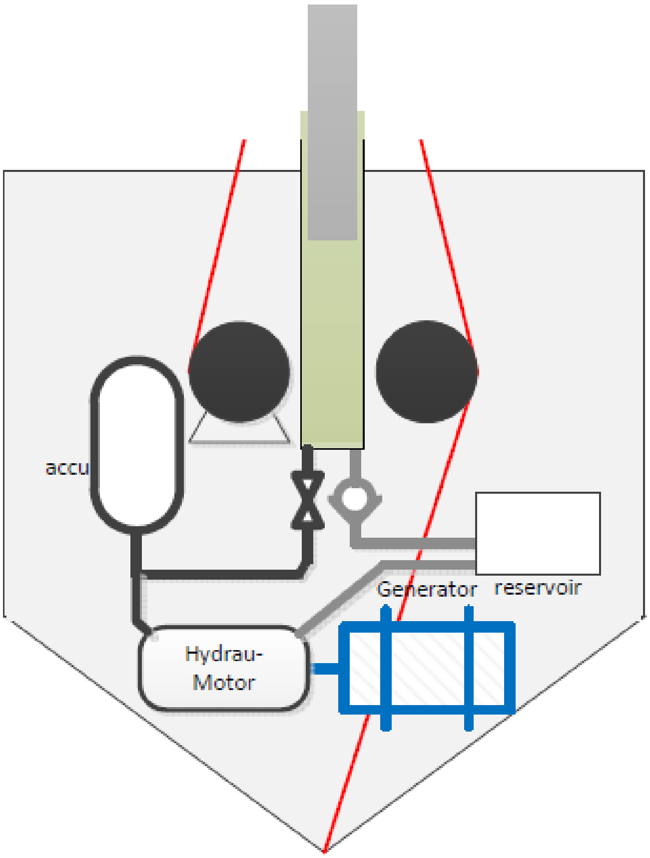

Fig. 3.73 *- Scheme of a hydraulic PTO system with an active valve (The FlanSea Project)*

3.6.3 Absorbed power

The absorbed power depends on the system and can be calculated as:

- for the electrical PTO: rotational speed of the winch multiplied by the machine torque acting on winch.
- for the hydraulic PTO: the piston speed multiplied by the hydraulic force on the piston (pressure times piston surface).

For a quickly overview, below are represented some comparisons between different pto systems in different sea climate, where generally it is evident that the electrical technology is able to harvest more energy than the hydraulic devices[3] [Fig. 3.74, Fig. 3.75]:

[3] Damen, M. & Al.(2011). Electrical vs Hydraulic PTO, *FlanSea project report number: FLA267-175.* Ghent.

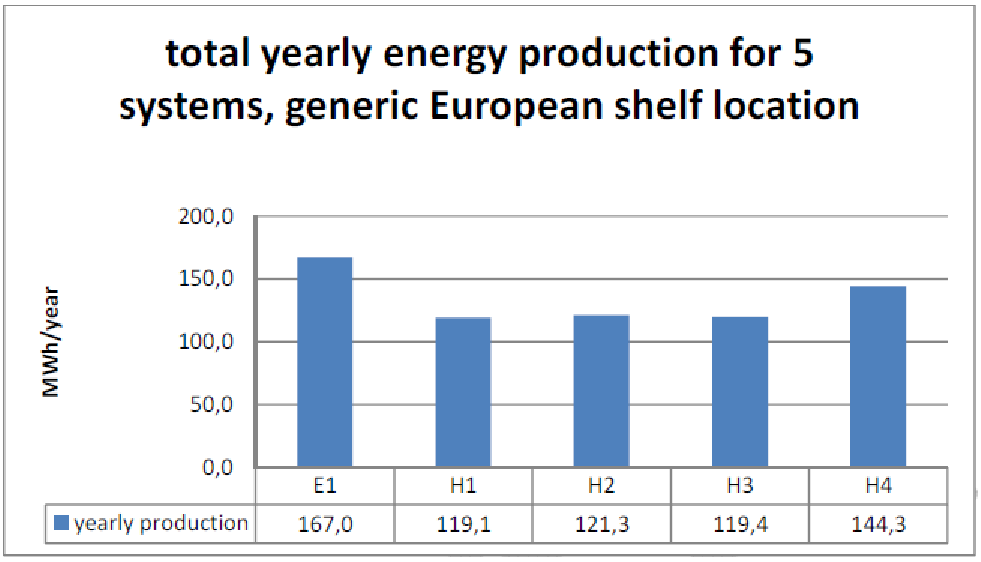

Fig. 3.74 – *Total yearly production for devices with different PTO (The FlanSea Project)*

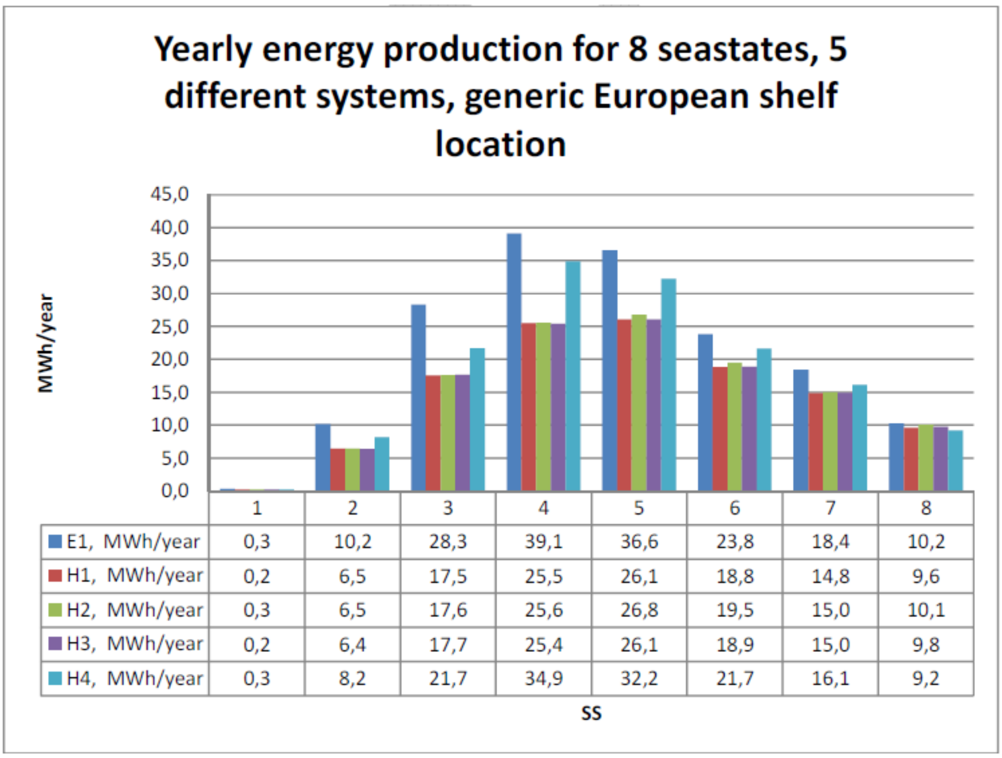

Fig. 3.75 - *Total yearly production in eight Sea states for different devices (The FlanSea Project)*

3.7 Previous experiments

At the bottom of the lab experimental tests, there are previous researches made for the FlanSea buoy. The first part consisted in numerical model tests; only after acquiring data from these, physical tests were performed in Borgerhout.

For what concern the numerical model, the major interest was the research for an optimal buoy configuration; the shape, the center of gravity and the stiffness of the rope are a few elements that govern:

- the power output of the buoy;
- the stability of the buoy;
- the survivability of the buoy.

3.7.1 The geometry of the buoy vs. the power output

The first part is concentrated on the influence of the buoy's geometry on the average power production. The boundary conditions were the wave climate and the maximum motor force; the primary investigated wave climate was Ostend and in a later stage an average power output for an exploitation zone (Westhinder) was also quickly calculated. The six sea states considered are showed in the table [Tab. 3.1]:

Sea states Ostend	*Hs (m)*	*Mean Te (s)*	*Mean Tp (s)*	*Occurrence (%)*
SS1	*0.25*	*4.19*	*4.75*	*49.2*
SS2	*0.75*	*4.6*	*5.28*	*35.9*
SS3	*1.25*	*5.18*	*6.09*	*10.1*
SS4	*1.75*	*5.94*	*7.01*	*3.1*
SS5	*2.25*	*6.59*	*7.71*	*1.2*
SS6	*2.75*	*7.22*	*8.37*	*0.4*

Tab. 3.1 – Wave climate for the six Sea states considered (The FlanSea Project, Dennis Renson)

Regarding the motor forces, they were delivered by the PTO system; four forces taken into account were: 82 kN, 164 kN, 246 kN, 328 kN.

3.7.2 The buoy shape

A first comparison was made by changing the top angle. The considered buoy angles were 90°, 120°, 140° and 160°. The influence on the power gain is showed in the following graph [Fig. 3.76][4]:

[4] Renson, D. (2011). D vs. Seastates: Power output, *FlanSea project report number: FLA267-xx.* Ghent.

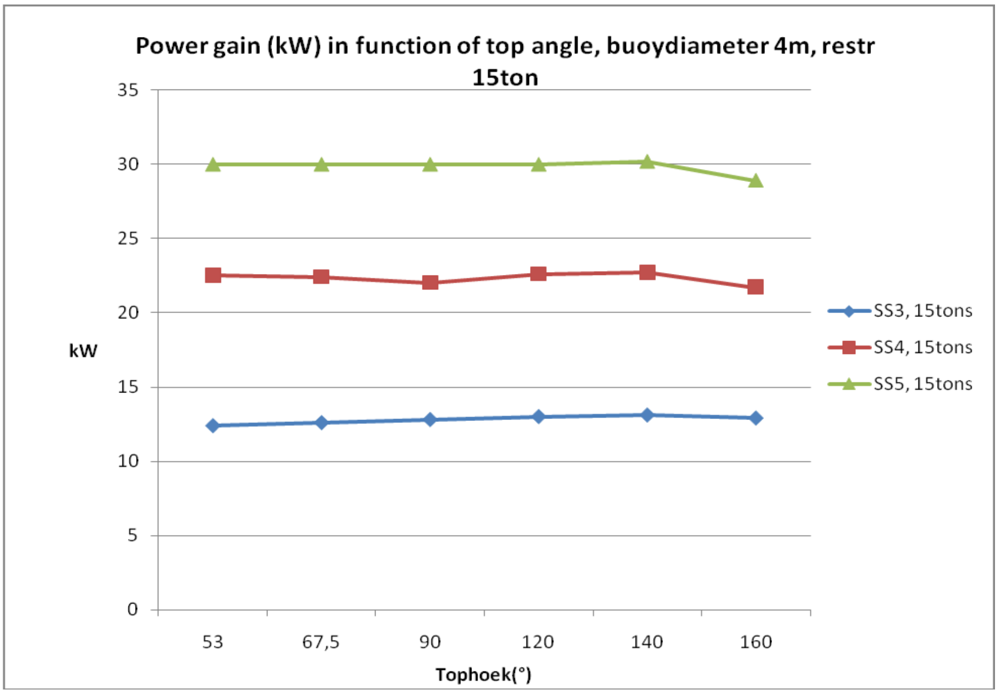

Fig. 3.76– *Power harvesting for different configurations (The FlanSea Project, Dennis Renson)*

There can be concluded that the power output of the wave energy converter is not influenced by the top angle.

Starting from a basis buoy of one meter of height and a straight cylinder, other shapes were investigated [Fig. 3.77]:

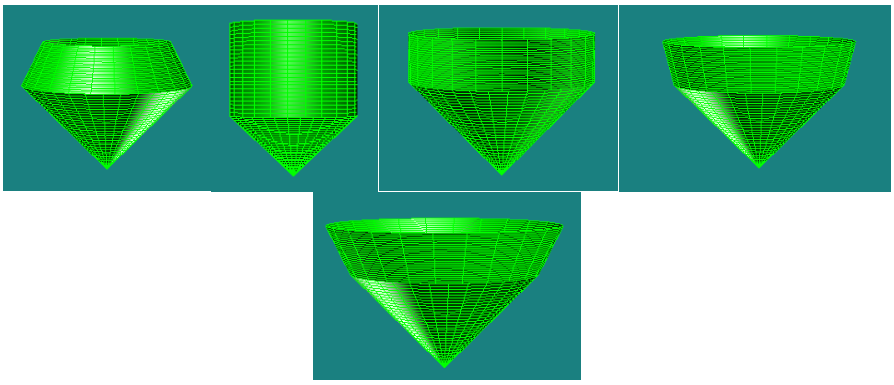

Fig. 3.77 *– Different shapes investigated (The FlanSea Project, Dennis Renson)*

At the end, it is not clear the relations between the changings of the shapes and the power output.

3.7.3 The buoy diameter

At last, the diameter was the only parameter left; fixed the angle at 120° and the cylinder height at one meter, three different buoy diameters were considered: four, five and six meter [Fig. 3.78]:

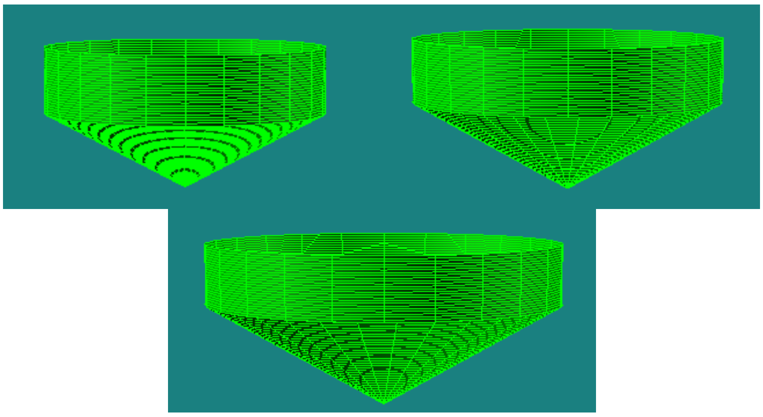

Fig. 3.78 *– The three diameters used for the tests (The FlanSea Project, Dennis Renson)*

Different diameters mean different weight as reported below (diameter, weight and height of the conic part):

- 4m, M 17.8 tons, d 2.15m
- 5m, M 29.8 tons, d 2.44m
- 6m, M 45.7 tons, d 2.73 m

The water depth at the considered location was ± TAW-7m meter (TAW stands for Tweede Algemene Waterpassing, a reference depth) [Fig. 3.79].

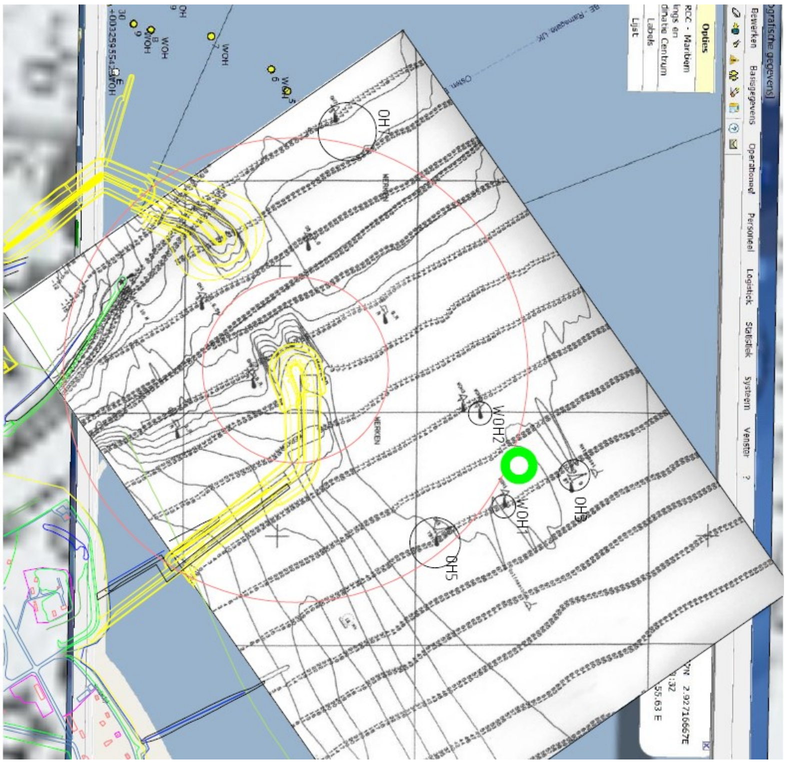

Fig. 3.79 *- Buoy location in the proximity of the harbour of Ostend (green doughnut) (The FlanSea Project, Dennis Renson)*

It was also considered a safety distance from the anchorage. The reasons for a sinkage restriction are considered in order to keep the buoy watertight and avoiding damage by hitting the anchorage [Fig. 3.80]. The sinkage restriction was set at two meter (relative position of the buoy to the wave elevation), for each diameter, despite it was only important for the buoy with four meter of diameter.

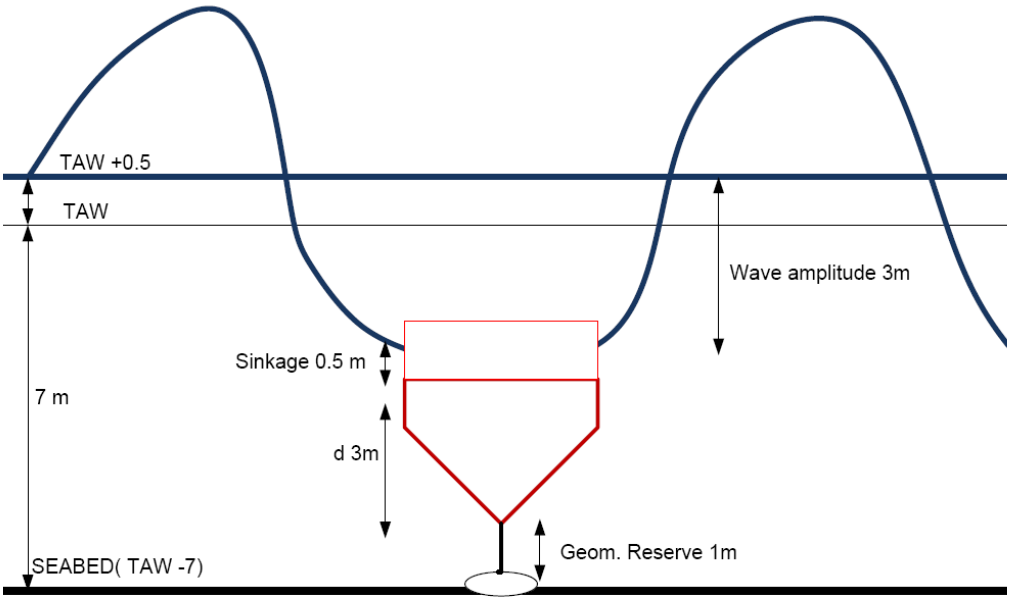

Fig. 3.80 *– Representation of the sinkage (The FlanSea Project, Dennis Renson)*

In order not to burn the engine each engine had its T_RMS max (root mean square of the torques), a parameter that gives an idea of the overheating and overloading of the engine; regarding the analysis, first of all the power output for each buoy was studied separately investigating the sea climate in Oostende [Fig. 3.81, Fig. 3.82, Fig. 3.83][5]

[5] Renson, D. (2011). D vs. Seastates: Power output, *FlanSea project report number: FLA267-xx.* Ghent.

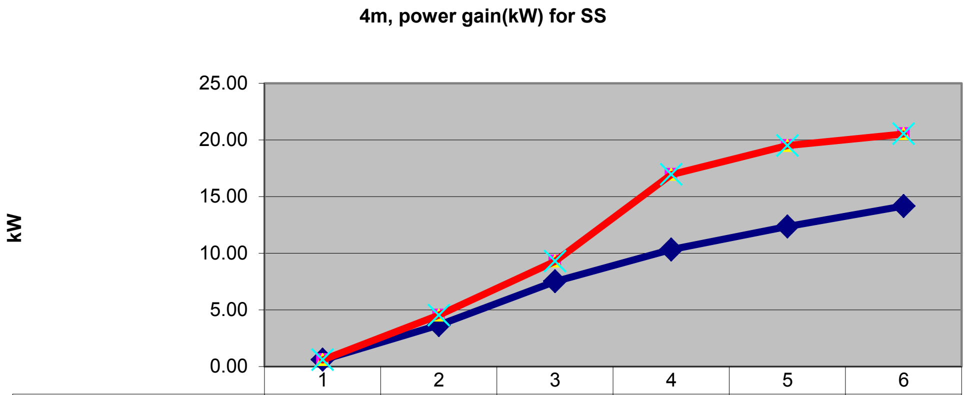

SS	1	2	3	4	5	6
82 kN, T_rms limit	0.57	3.64	7.50	10.32	12.34	14.15
164 kN, sinkage limit	0.57	4.51	9.28	16.94	19.50	20.53
246 kN sinkage limit	0.57	4.51	9.28	16.94	19.50	20.53
328 kN, sinkage limit	0.57	4.51	9.28	16.94	19.50	20.53

SS

Fig. 3.81 *– Power gain of the four meter buoy in different Sea states (The FlanSea Project, Dennis Renson)*

For the forum meter buoy it is clear that the sinkage limit is already reached for 164 kN max force and more. With an installed force of 164 kN the buoy can be optimally controlled and tested.

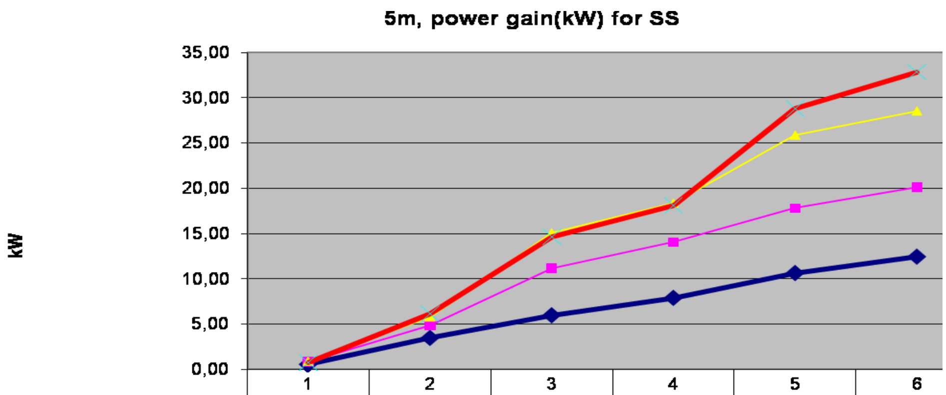

SS	1	2	3	4	5	6
82 kN, T_rms limit	0,59	3,50	6,00	7,92	10,65	12,46
164 kN, T_rms limit	0,86	4,84	11,16	14,07	17,81	20,11
246 kN	0,90	5,80	15,07	18,36	25,88	28,55
328 kN, sinkage limit	0,77	6,14	14,67	18,10	28,83	32,85

SS

Fig. 3.82*– Power gain of the five meter buoy in different Sea states (The FlanSea Project, Dennis Renson)*

About the five meter diameter buoy the power gain for more engines becomes clear and going from three to four engines is useful only for higher sea states.

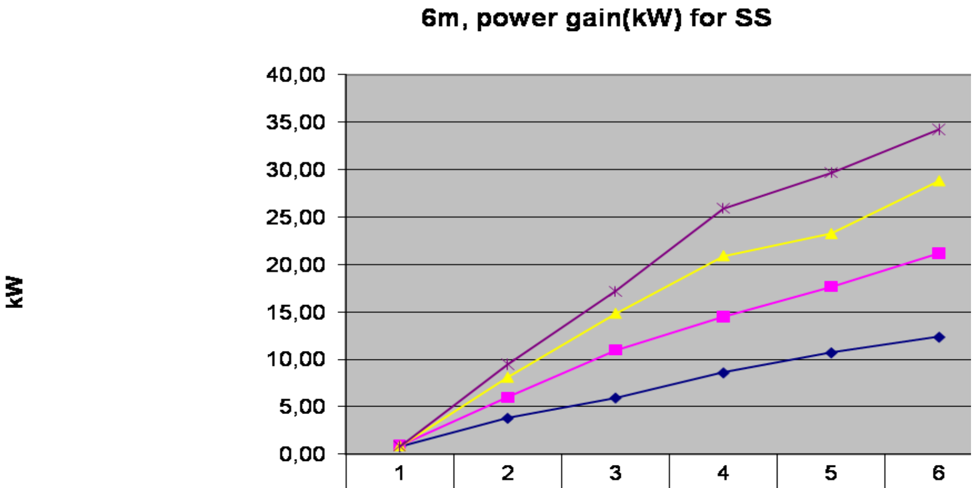

	1	2	3	4	5	6
82 kN, T_rms limit	0,79	3,80	5,95	8,60	10,72	12,37
164 kN, T_rms limit	0,94	6,01	10,97	14,51	17,66	21,20
246 kN	0,86	8,09	14,83	20,90	23,23	28,79
328 kN	0,86	9,48	17,16	25,91	29,65	34,22

ss

Fig. 3.83 *– Power gain of the six meter buoy in different Sea states (The FlanSea Project, Dennis Renson)*

The power gain for more engines becomes clear and going from three to four engines is always useful.

At the end, to compare the 3 buoys on a relevant base, the mean power output of each buoy was also calculated for each sea states at location Westhinder [Fig. 3.84, Fig. 3.85, Fig. 3.86, Fig. 3.87]. To have an yearly energy yield in MWh, the average power needs to be multiplied by 8.76.

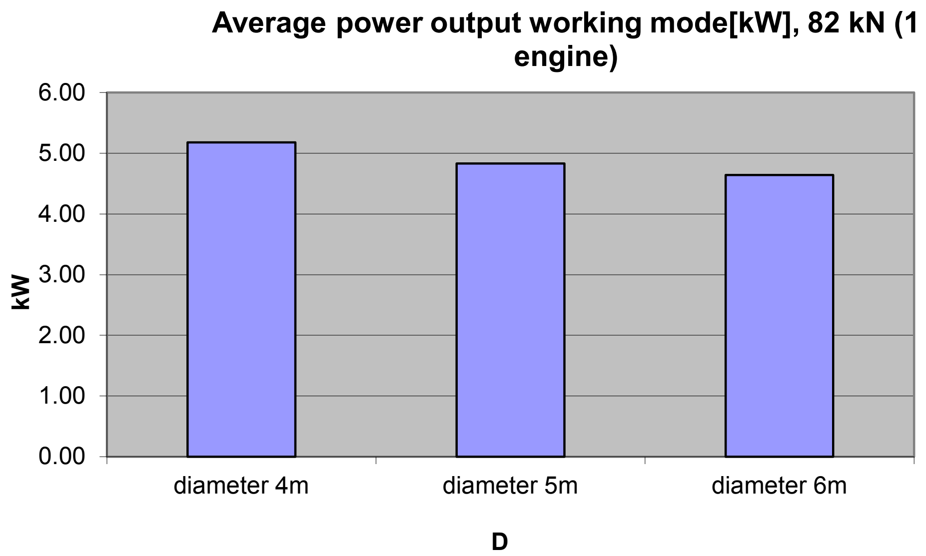

Fig. 3.84 *– Comparison between the three buoys, setting with one engine (The FlanSea Project, Dennis Renson)*

For the lowest sea state, the mean power for the three diameters doesn't show a meaningful difference.

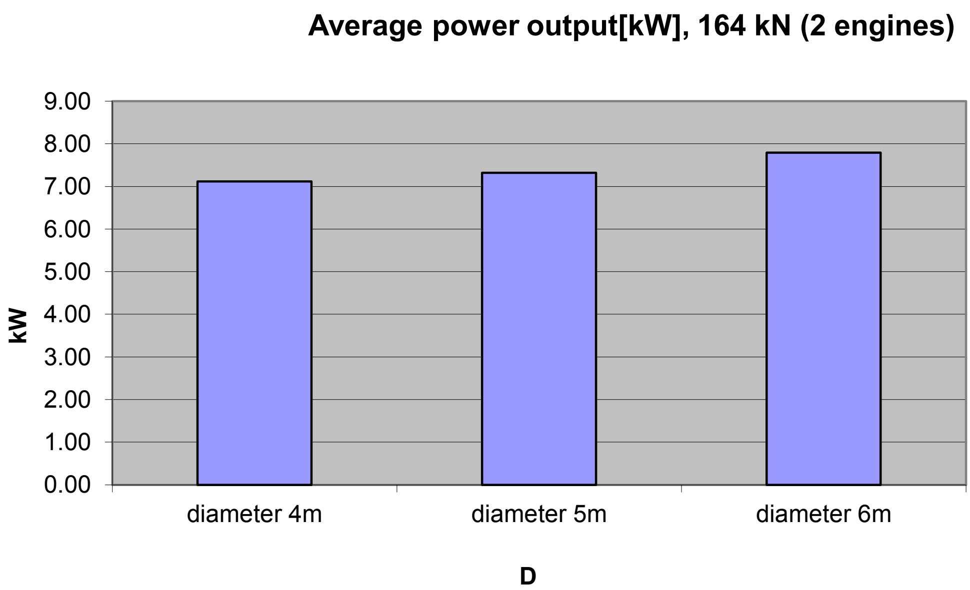

Fig. 3.85 *– Comparison between the three buoys, setting with two engines (The FlanSea Project, Dennis Renson)*

Also in this case, no significant difference between the buoy power outputs is shown.

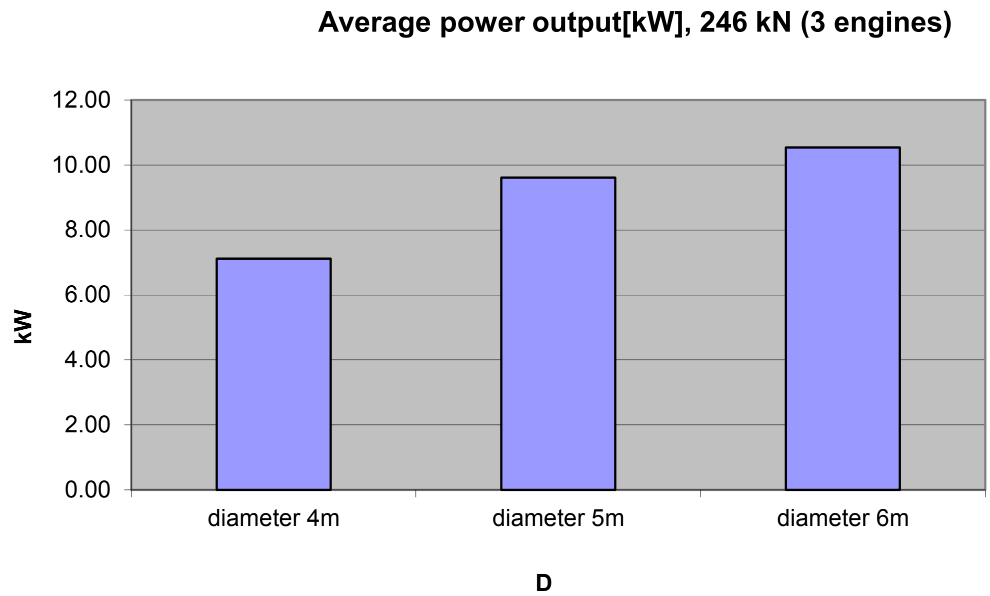

***Fig. 3.86**– Comparison between the three buoys, setting with three engines (The FlanSea Project, Dennis Renson)*

There is a clear power gain for the bigger buoys; the installed forces come close to the needed forces for optimal control of the bigger buoys.

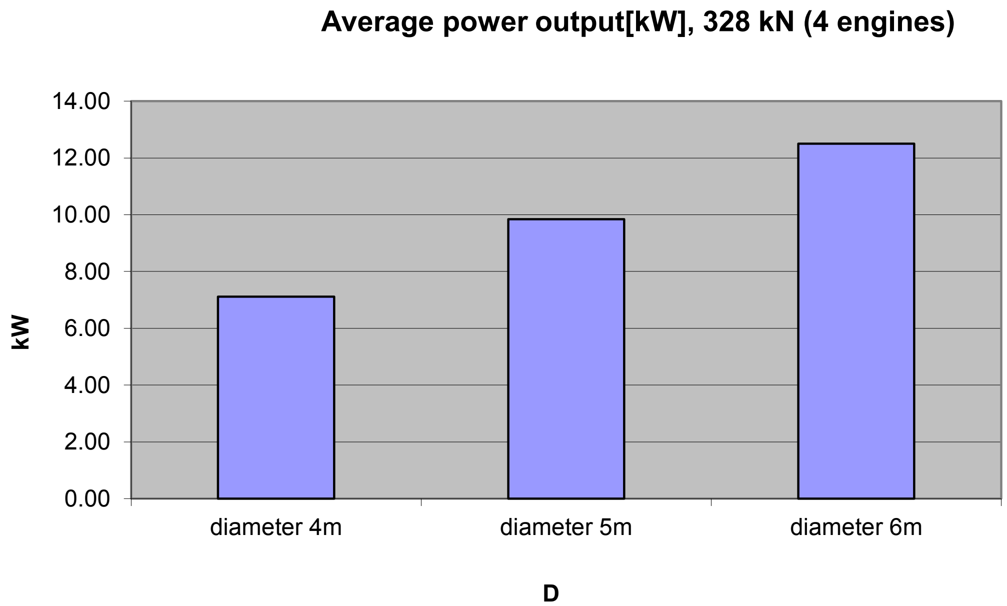

***Fig. 3.87** – Comparison between the three buoys, setting with four engines (The FlanSea Project, Dennis Renson)*

There is an even more clear power gain for the biggest buoys; the installed forces come close to the needed forces for optimal control of the bigger buoys. The power gain for the 5m buoy for three to four engines isn't that big, which means an optimum is almost reached.

It is now clear that when choosing for one or two engines (82 kN or 164 kN), the influence of the diameter on the mean power output is rather small. The output for a small, optimally controlled buoy is almost equals of the output for a big, suboptimal controlled buoy.

3.7.4 Wave Star vs. Flansea

The numerical results of a floater of the WAVESTAR concept was compared for different installed forces with the results of the Flansea buoy [Fig. 3.88, Fig. 3.89][6]:

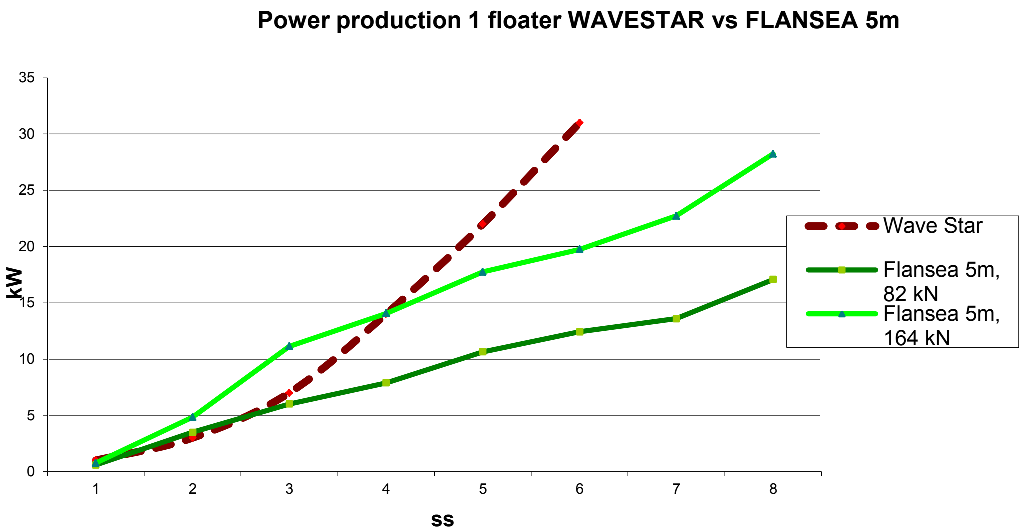

***Fig. 3.88** – Comparison between the FlanSea five meter buoy and one floater WAVESTAR (The FlanSea Project, Dennis Renson)*

[6] Renson, D. (2011). D vs. Seastates: Power output, *FlanSea project report number: FLA267-xx.* Ghent.

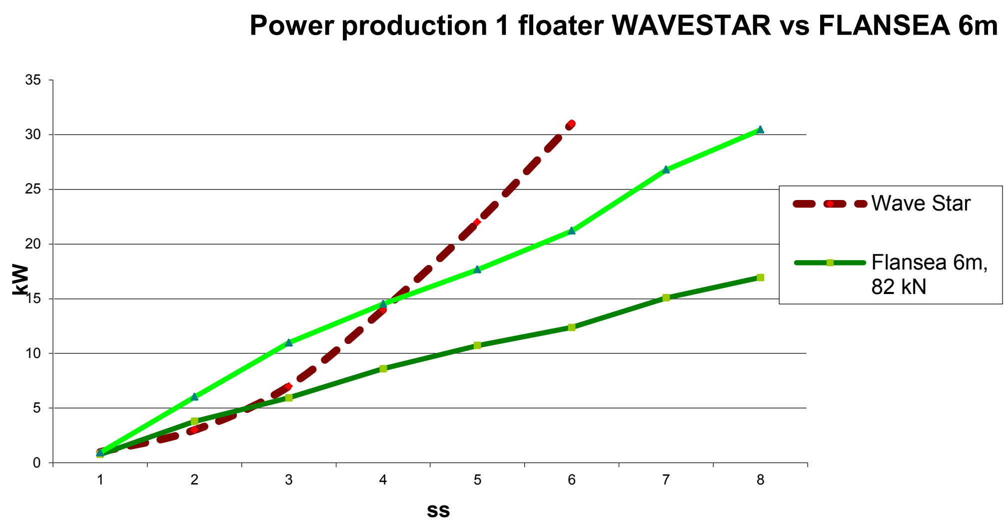

Fig. 3.89 – *Comparison between the FlanSea six meter buoy and one floater WAVESTAR (The FlanSea Project, Dennis Renson)*

The tests show that Flansea simulation results are in comparable with the WAVESTAR.

3.7.5 Hydrostatic stability

Changing the shape, the angle, the center of gravity and a other factors has consequences on the hydrostatic stability. It has an influence on the hydrodynamic coefficients (added mass and hydrodynamic damping), which play an important role in the dynamic behavior. In the previous researches illustrated below, a lot of configurations have been tested through the WAMIT software[7].

For the numerical model, the hydrodynamic parameters which were calculated with WAMIT are the added moment of inertia, the hydrodynamic damping coefficient and the exciting wave moment in the frequency domain. They characterize the response amplitude operator (RAO) in the roll motion. The RAO gives the resulting motion in radians per meter amplitude as a function of frequency for a free-floating buoy without cable. The RAO, however, gives a good indication of how the behavior will be when a

---

[7] Falter, J. (2011). Some notes on stability and geometry, *FlanSea project report number: FLA267- 163*. Ghent.

cable is attached. The effect of the cable will mainly depend on the tuning and power take-off algorithm.

Important parameters in the WAMIT simulations are the location of the center of gravity and the radius of gyration which characterize the mass distribution. Changing these parameters will result in a different behavior.

The difference in behavior when changing the center of gravity is showed in the figure [3.90] in which the reference buoy is compared to geometrical identical buoys with the same radius of gyration but different center of gravity.

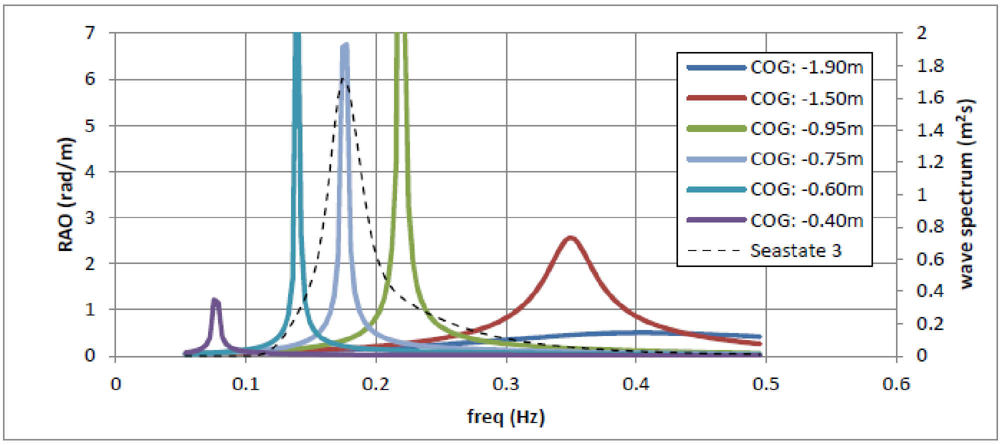

Fig. 3.90 *– Different behaviors obtained changing the COG (The FlanSea Project, Joris Falter)*

The resonance period is not a statistical value, but a theoretical: the resonance frequency is a function of the rotational inertia and the spring constant. The spring constant depends on the location of the center of gravity, the immersed volume and the buoy radius at the waterline. The rotational inertia depends on the mass distribution and the location of the center of gravity.

Since the motion equations are coupled, the theoretical natural frequency only serves to give an indication, and could differ from the real value.

All the geometric shapes used during these tests were based on and compared with the reference buoy illustrated below [Fig. 3.91]:

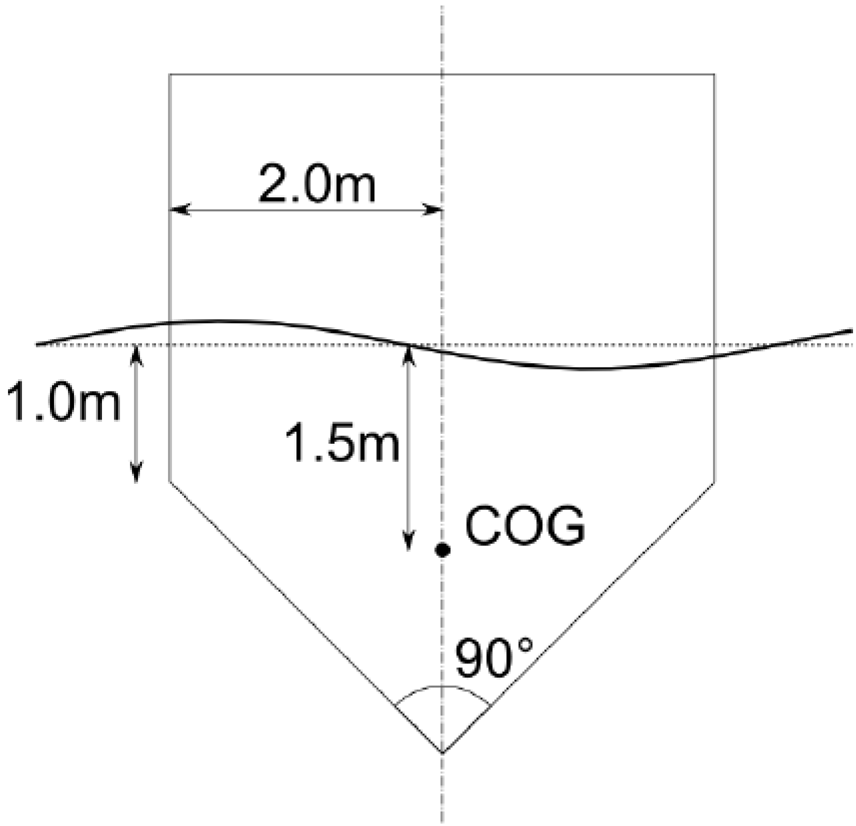

Fig. 3.91 – *Reference buoy (The FlanSea Project, Joris Falter)*

The vertical COG was chosen arbitrarily, but it was the reference on stability and roll behavior.

The coordinate system has its origin on the waterline with the z-axis pointing vertically upwards.

A flatter bottom allows a higher center of gravity with respect to the waterline. On the other hand, there is less volume under the waterline for distributing the weight [Fig. 3.92],

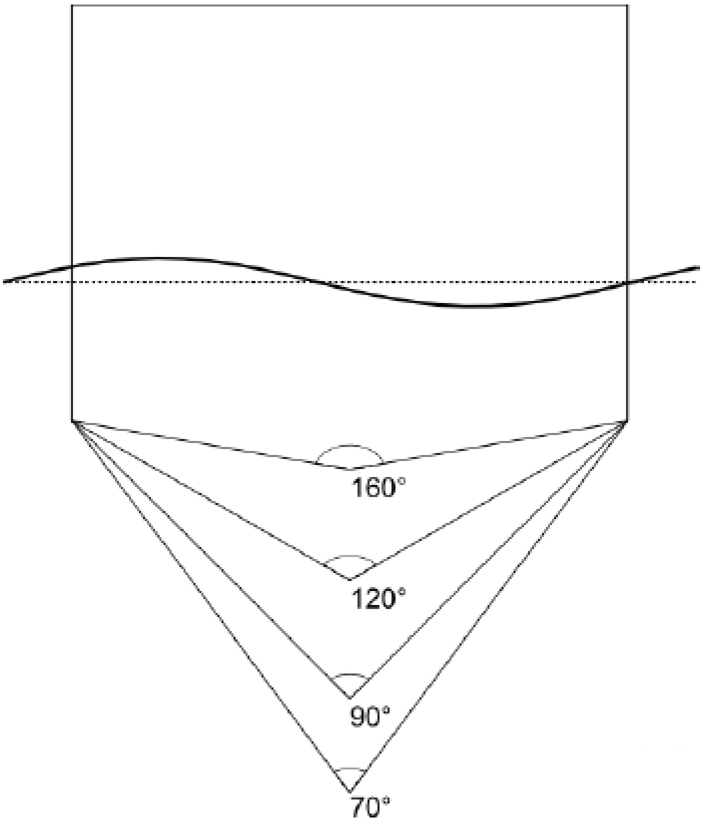

Fig. 3.92 *- The buoy with different cone tip angles (The FlanSea Project, Joris Falter)*

When increasing the cone tip angle and keeping all other values constant, the stability increases [Fig. 3.93]:

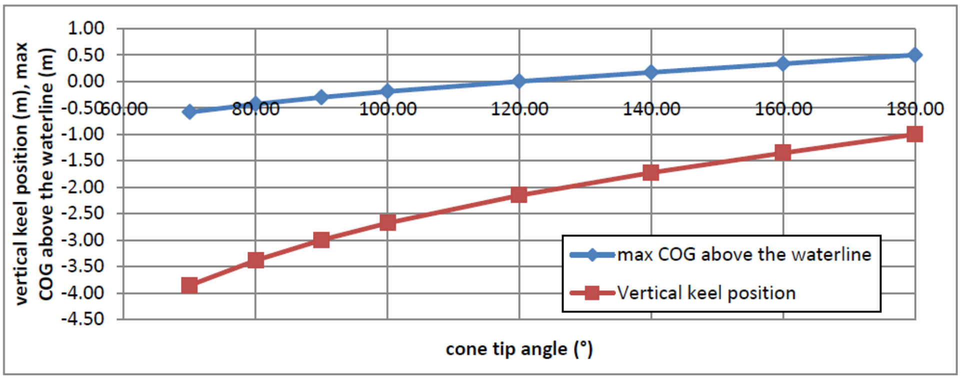

Fig. 3.93*- The vertical position of the keel and the maximum height of the center of gravity (both with respect to the waterline) (The FlanSea Project, Joris Falter)*

In the next figure [3.94] are reported the results considering the 120° and 140° cone tip angle. As can be seen, the resonance frequency increases when the cone tip angle increases, and there is more damping:

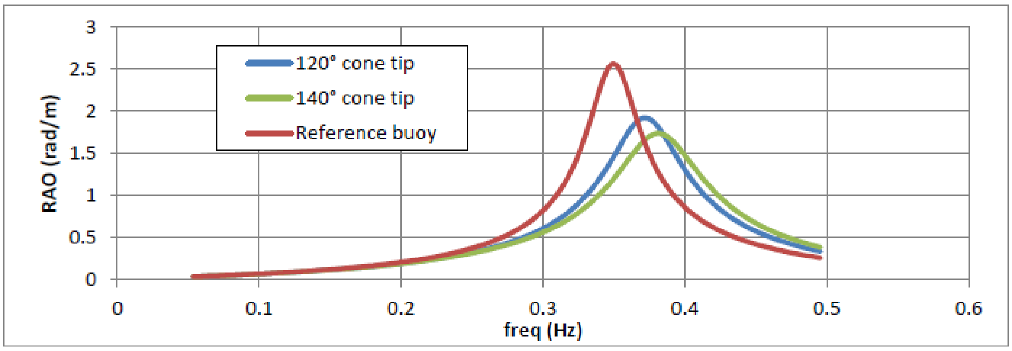

Fig. 3.94 *– Different behaviors obtained changing the cone tip angle (The FlanSea Project, Joris Falter)*

Other numerical tests were performed changing the waterline diameter (the height of the cylindrical part below the waterline remains one meter) [Fig. 3.95]:

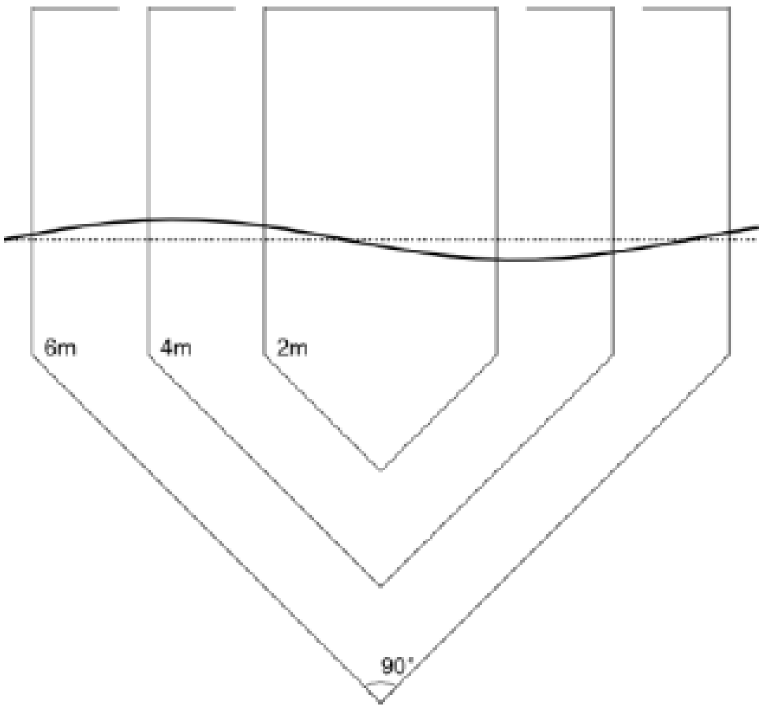

Fig. 3.95 *- The buoy with different diameters (The FlanSea Project, Joris Falter)*

The stability increases with increasing diameter. The following results are for a 90° cone tip angle [Fig. 3.96]:

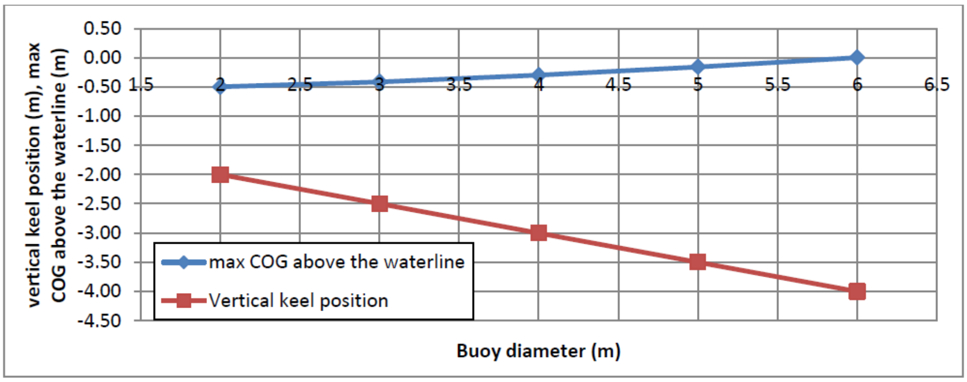

Fig. 3.96 *- The interval in which the vertical center of gravity should be placed (The FlanSea Project, Joris Falter)*

Below it is showed the different behavior between the reference buoy and another buoy with a waterline diameter of five meters [Fig. 3.97]; there is a very small increase in frequency, but more important is the smaller amplitude at the resonance frequency.

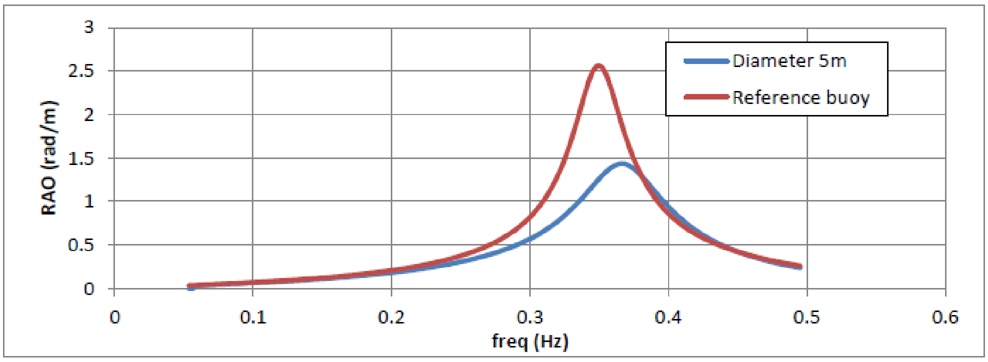

Fig. 3.97 *– Different behaviors obtained changing the diameter (The FlanSea Project, Joris Falter)*

Other shapes investigated took into account different heights of the cylindrical part, fixing the total draft at tree meters [Fig. 3.98] :

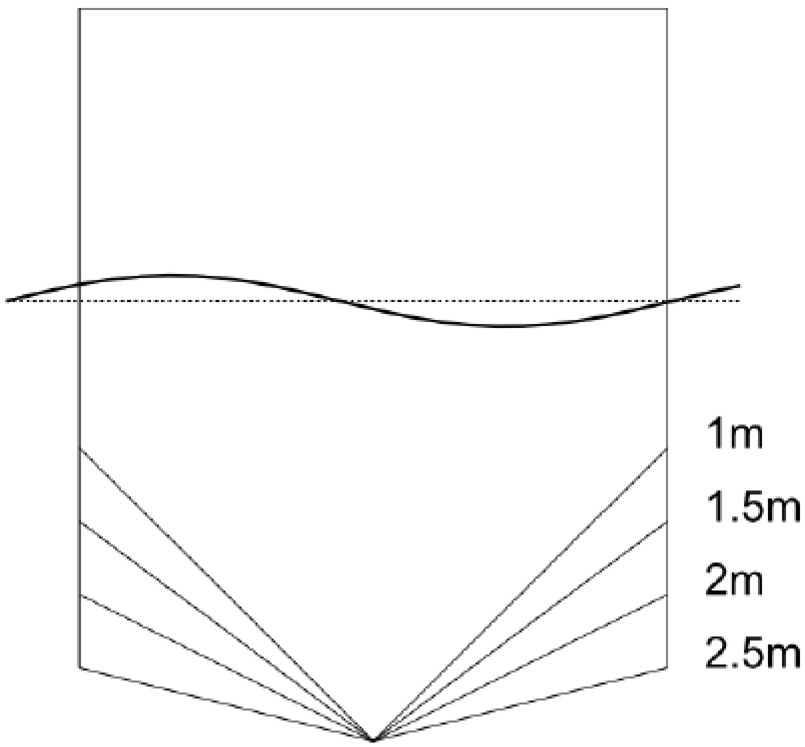

Fig. 3.98- *The buoy with different heights of the cylindrical part (The FlanSea Project, Joris Falter)*

If the height increases the center of gravity moves up decreasing the stability [Fig. 3.99]:

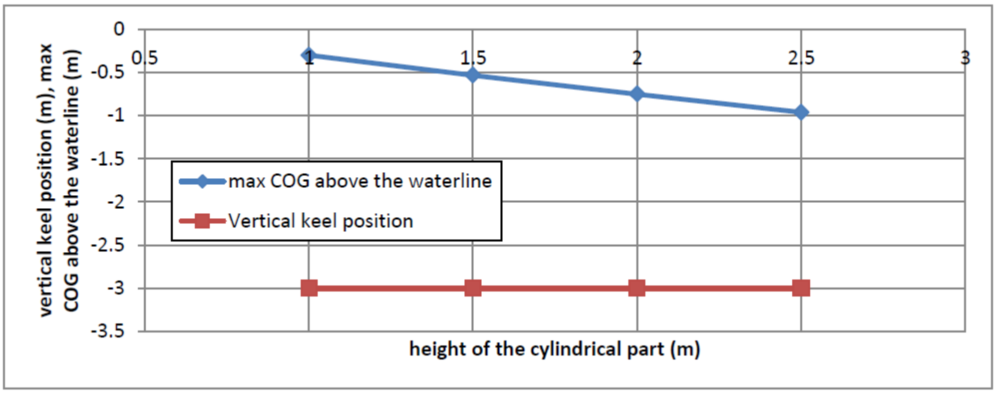

Fig. 3.99 - *The maximum height of the center of gravity with respect to the waterline (The FlanSea Project, Joris Falter)*

As can be seen, the resonance peak for an extended cylinder is at a lower frequency than the reference buoy [Fig. 3.100]:

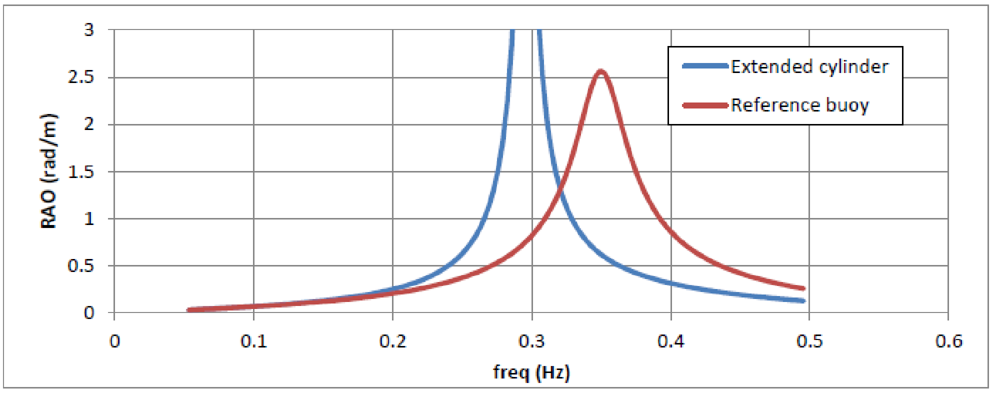

Fig. 3.100 *– Different behaviors obtained changing the height of the cylindrical part (The FlanSea Project, Joris Falter)*

Other configurations were studied changing the waterline radius [Fig. 3.101]:

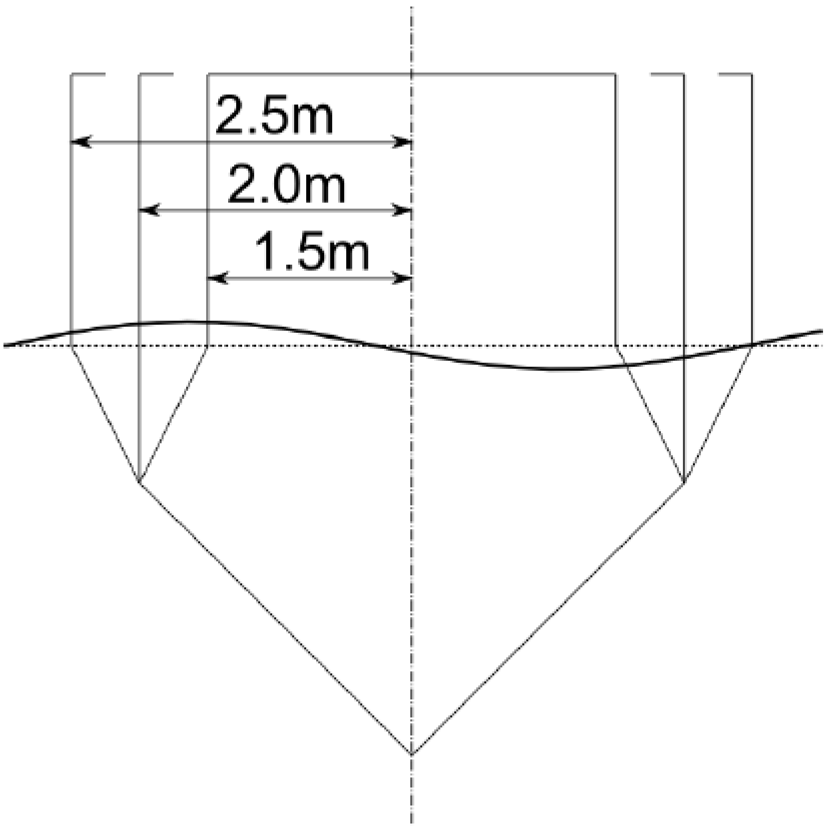

Fig. 3.101*– The buoy with different shapes (The FlanSea Project, Joris Falter)*

In figure [3.102] it is showed that increasing the radius of the waterline will result in increased stability:

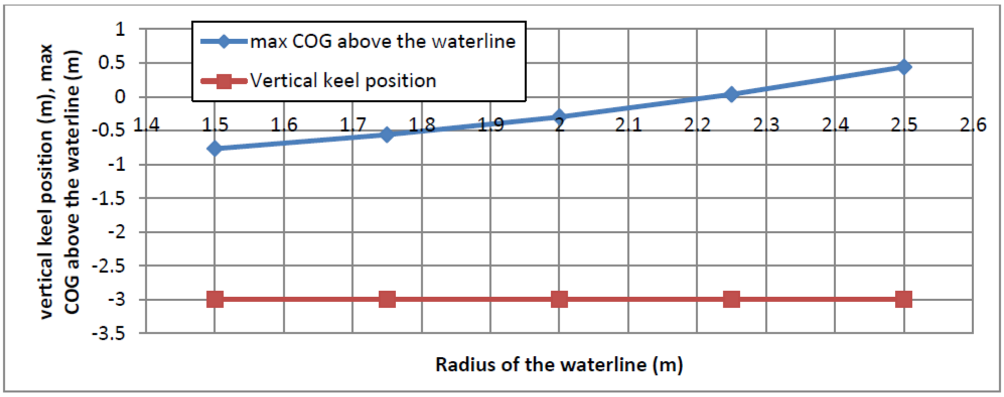

Fig. 3.102 - *The maximum height of the center of gravity changing the shapes (The FlanSea Project, Joris Falter)*

The resonance frequency is higher, and the damping is larger [Fig. 3.103]:

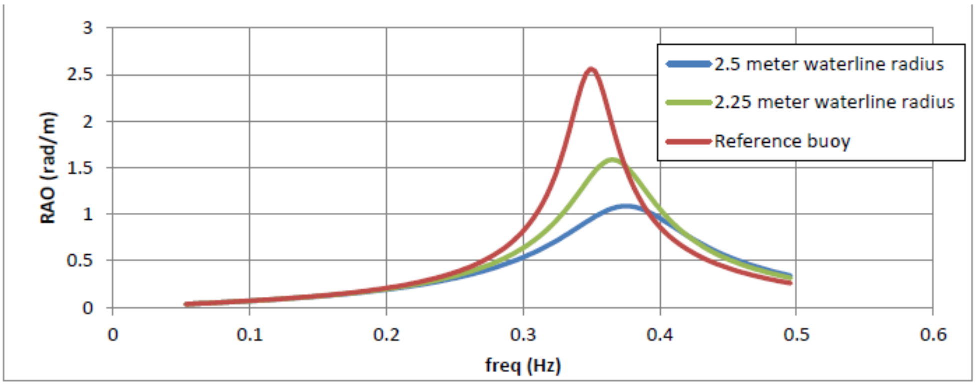

Fig. 3.103 - *The results obtained changing the waterline radius (The FlanSea Project, Joris Falter)*

It is confirmed that the location of the center of gravity and the radius of gyration play the most important role when discussing buoy dynamics.

Concerning the geometry, for the hydrostatics following conclusions for fixed COG and radius of gyration can be drawn:

- the stability improves when the cone tip angle is increased;
- the stability improves when the diameter is increased;
- the stability decreases when the cylinder length is increased;
- the stability increases when the waterline radius increases.

3.7.6 Possible vane configurations

The simulations with the 6DOF simulation code, as well as the stability experiments with a test buoy have pointed out that the pitch motion is significant in certain situations. A possibility exists in putting vanes on the buoy to reduce this motion [Fig. 3.104][8]:

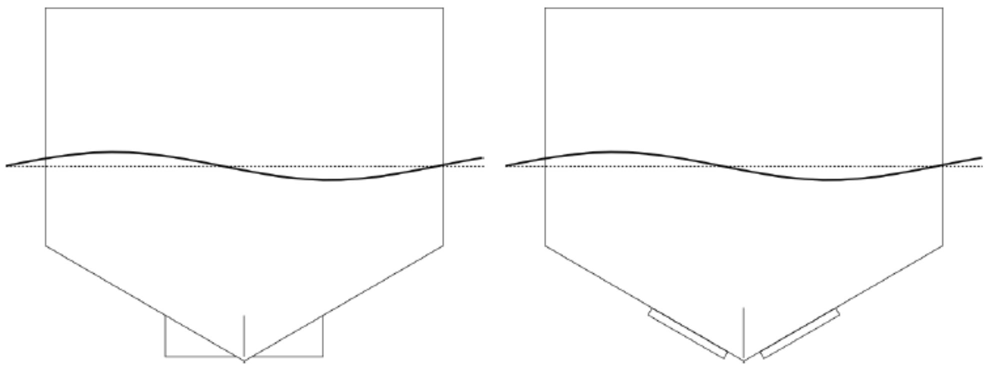

Fig. 3.104 *- Two examples of vane configurations (The FlanSea Project, Joris Falter)*

The vanes surfaces were varied between 0.144 m^2 and 2.309 m^2 (sum of both vanes). The results are represented in the following graph [Fig. 3.105]:

[8] Falter, J. (2011). Reduction of pitch motion by increased damping, *FlanSea project report number: FLA267- 170.* Ghent.

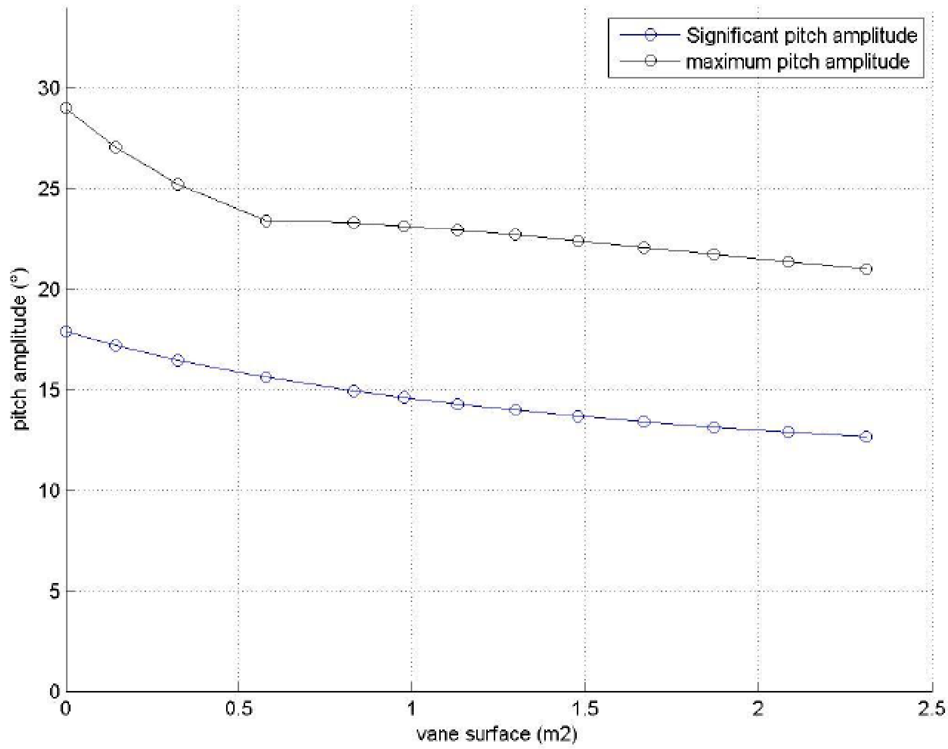

Fig. 3.105 *- Relation between the pitching motion and the vane surface (The FlanSea Project, Joris Falter)*

The largest vane size gives a significant reduction in both significant and maximum amplitude.

3.7.7 Physical tests in the Flanders Hydraulics Research centre

The model which has been agreed to test was similar to the final concept with the PTO located inside the buoy. One of the sketches is showed below [Fig. 3.106]:

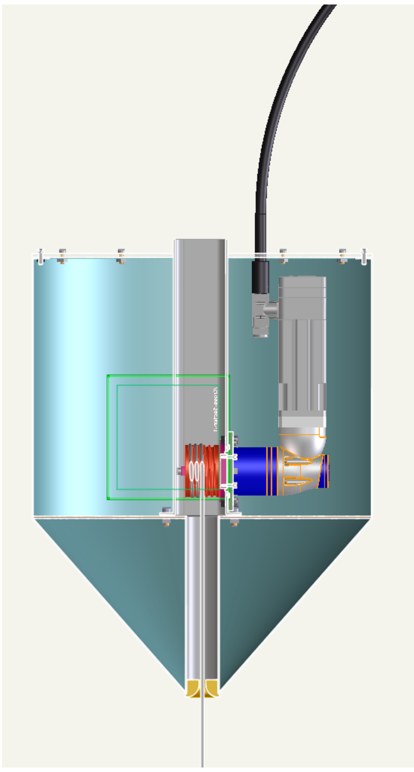

Fig. 3.106 *- Example of the scaled model (The FlanSea project, Scale testing Borgerhout)*

The stability of the buoy was realized by adding extra weights within the buoy. This realistic configuration allowed to study the effect of the balance influence of the PTO on the overall system as well as the reaction of the buoy due to power extraction.

The test setup was composed [Fig. 3.107] by:

- a steel floater;
- a winch;
- a gearbox;
- a motor;
- a cable.

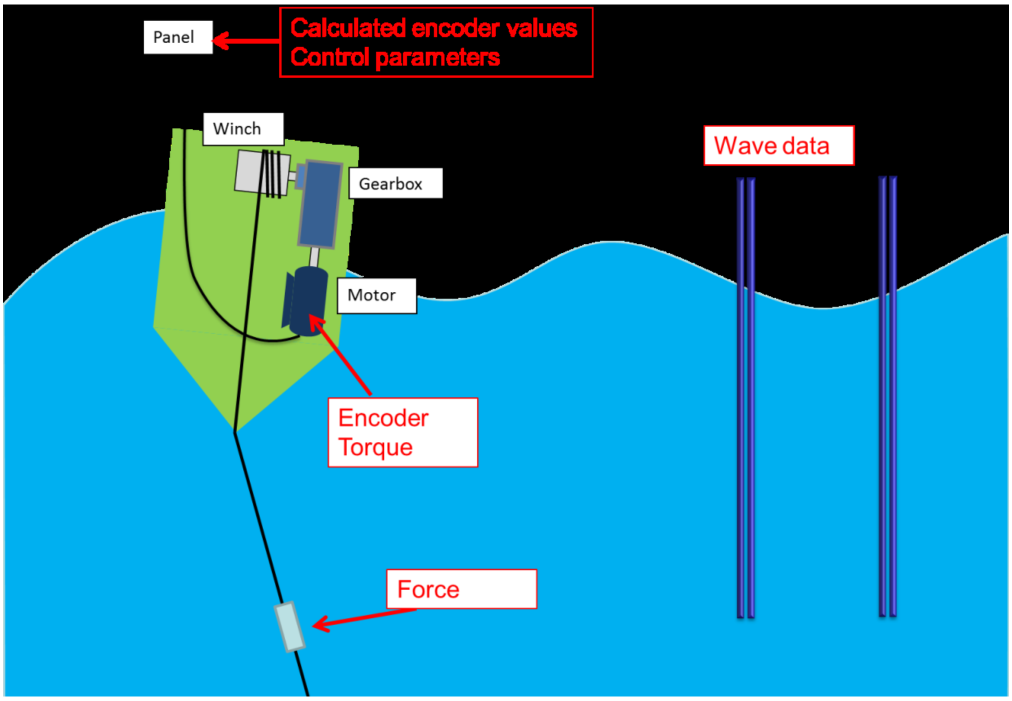

Fig. 3.107 - Schematic representation of the test setup (The FlanSea project, Scale testing Borgerhout)

In order to monitor the situation, the following parameters were logged:

- the encoder position (which also provides velocity and acceleration);
- motor torque measurement
- force transducer in the cable
- wave data
- parameters used in the control
- marker on the buoy: can be used for motion tracking
- for some tests: 3D Acceleration – gyroscope

In the figures below is illustrated the position of the gauges [Fig. 3.108]:

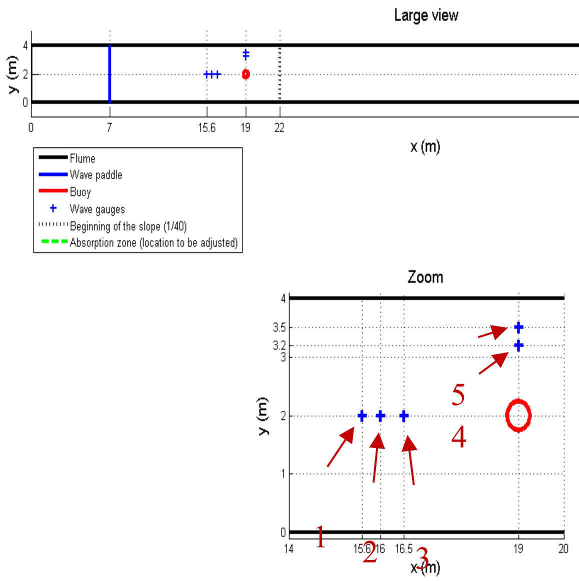

Fig. 3.108 *- Position of the wave gages (indicated as G1 to G5) in the flume (The FlanSea project, Scale testing Borgerhout)*

In the following also some photos taken during the tests [Fig. 3.109, Fig. 3.110]:

Fig. 3.109 *– The scaled model (The FlanSea project, Scale testing Borgerhout)*

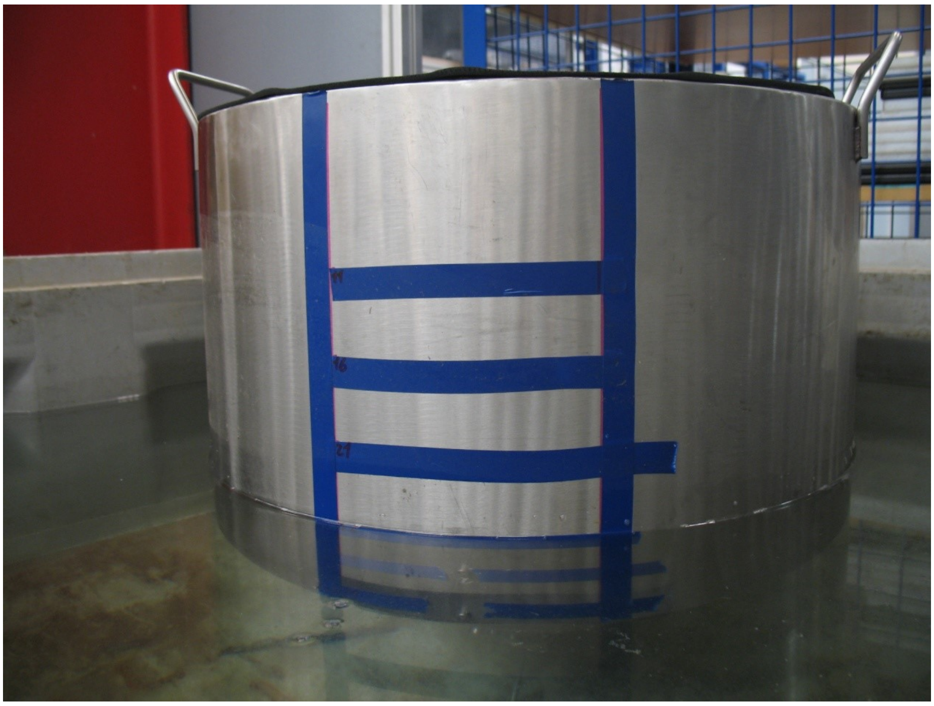

Fig. 3.110 *- The scaled model (The FlanSea project, Scale testing Borgerhout)*

The main objectives of these tests were:

- To check the current concept of the test buoy and gain experience for the final design.
- Gain experience on tuning and its effectiveness
- To provide more realistic inputs on the cable forces and extractable power.
- To quantify the lateral and rotational motions of the buoy and their influence.

Concept check and gain experience

The project allowed to observe various aspects of the overall behavior and gain a lot of experience. It has been noticed that the stability depends on the pulling force and when the pulling force is not high enough, the buoy tends to pitch more.

The problems occurred during the tests were:

- when not enough force is applied the cable gets slack;
- when too much force is applied the buoy oversteers, which results in a very fast and increasing up and down movement;

- when the cable suddenly gets slack, it tends to form a loop at the attachment point. This excess of cable rubs against the bars connected to the winch. After a while the cable starts getting off of the winch and this part of the cable is hanging freely and uncontrolled.

Gain experience on tuning and its effectiveness

First step was to implement the control algorithm, which can be used for tuning; quite some hours were invested in the implementation of the program (Contec, Fig. 3.111), with special care for safety.

Fig. 3.111 - *User interface of the software;* the left pane shows a graphical representation, the right panel is the control panel. *(The FlanSea project, Scale testing Borgerhout)*

The figure below [Fig. 3.112] shows the position measured by the encoder. From this signal velocity and acceleration were derived.

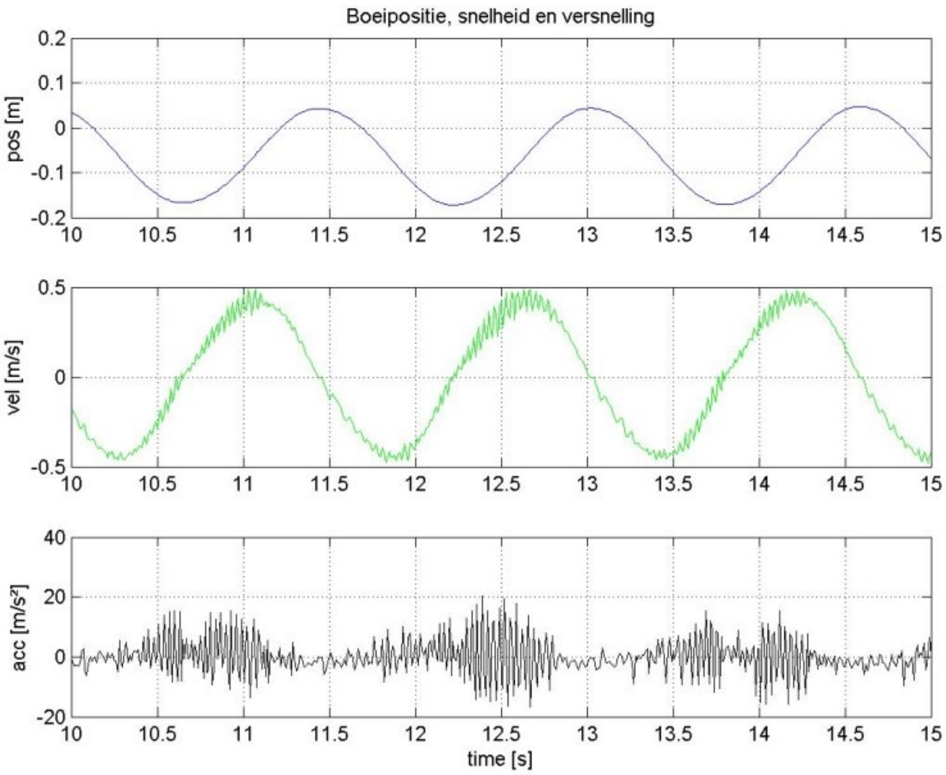

Fig. 3.112- *Encoder position (upper), velocity (middle) and acceleration (down) (The FlanSea project, Scale testing Borgerhout)*

There are two problems for applying tuning:

- acceleration signal quality is not good. By taking a running average, the signal gets better, but there's still too much scatter;
- there is a friction force that mostly originates at the gasket. This friction isn't constant in time. It however defines which part of the motor force reaches the cable.

As the friction force is unknown, damping and tuning are spoiled and the forward way of applying a tuning force and looking what happens doesn't work; because of these problems the effectiveness of tuning wasn't quantified.

Inputs on the cable forces and extractable power

The cable force was constantly measured with a load cell. In order to estimate the power production, a theoretical power has been calculated based on the force and the encoder velocity [Fig. 3.113]:

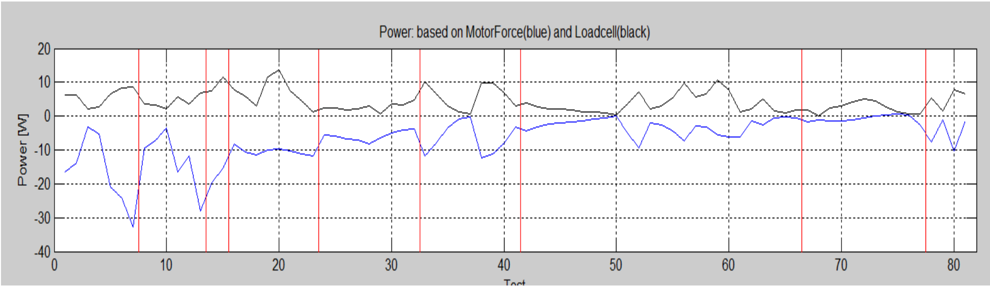

***Fig. 3.113** - Power calculation including friction (blue) and without friction (black) (The FlanSea project, Scale testing Borgerhout)*

Lateral/rotational motions of the buoy and their influence

The buoy movement was quantified based on:

- the 2D buoy motion based on the movies that were made of each test using marker tracking. This gave heave, surge and pitch movement;
- for some tests, an accelerometer was attached to the buoy. This gave the accelerations and rotational velocities in 3 directions.

Below is compared the signal recorded from the physical model and the numerical model [Fig. 3.114]:

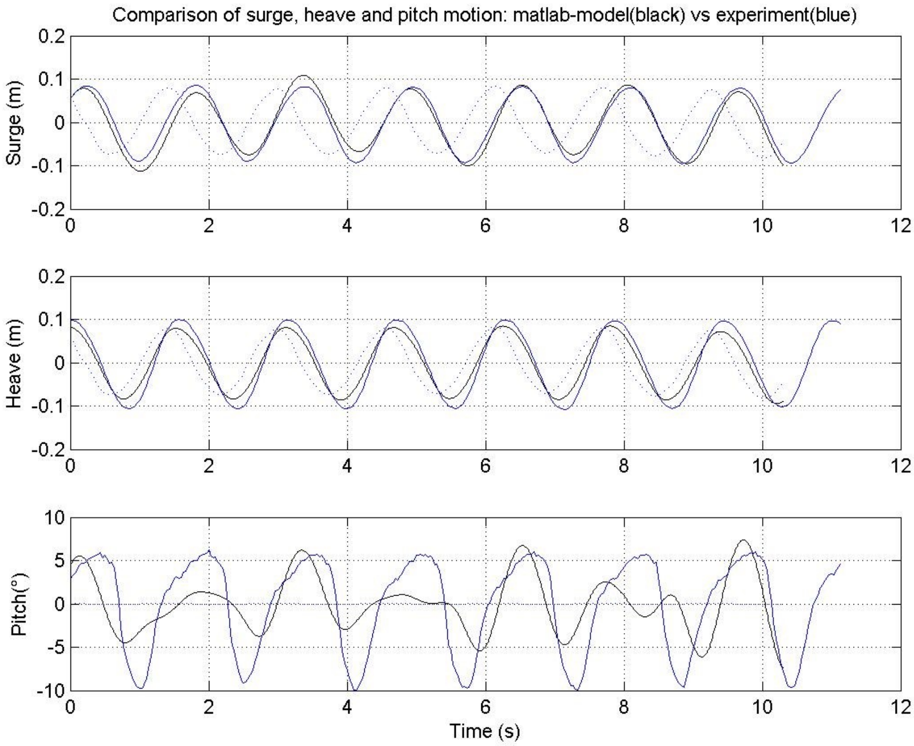

Fig. 3.114 *- Results for the comparison of the 3D motion for regular waves. The dotted line is the wave (The FlanSea project, Scale testing Borgerhout).*

In regular waves, a stable up and down movement couls be established. This means the main movement was a heave movement with limited surge and pitch movements; in irregular waves it was hard to get the buoy into resonance and generally the movement was smaller.

3.8 Theoretical hydrodynamic background

A random Ocean wave can be described as the sum of a large number of harmonic waves[9]; understanding the harmonic waves allows to study properly the irregular waves wave.

The theory used to describe the harmonic wave is the linear theory. The main requirement to apply the linear theory is the amplitudes of the waves that has to be

[9] Holthuijsen, L. H. (2007). Waves in oceanic and coastal waters. Cambridge University Press. UK.

small, in particular small compared with the wave length and small compared with the water depth; it is usually known as the small amplitude approximation.

The water is considered an ideal fluid and for this reason is assumed:

- to be incompressible;
- to have a constant density;
- to have no viscosity;
- the water body is continuous.

The next hypothesis regards the motion of the water particles. It is assumed that the water particles may neither leave the surface or penetrate the fixed bottom. Finally, the only external force is the Earth's gravitational that acts on the particles.

To develop the liner theory the two following equations are used:

- the mass balance equation;
- the momentum balance equation.

In the following is illustrated only the derivation of the mass balance equation because the derivation of these equations is almost identical.

In a x, y, z space is considered a volume of fluid. The fluid density μ per unit volume is transported through a volume $\Delta x\ \Delta y\ \Delta z$

The derivation of the balance equation essentially involves balancing the local storage of the property μ in volume $\Delta x\ \Delta y\ \Delta z$ against the sum of inflow, outflow and local production over a time interval Δt.

The storage is equal to:

$$= \left(\mu\ \Delta x\ \Delta y\ \Delta z + \frac{\partial(\mu\ \Delta x\ \Delta y\ \Delta z)}{\partial t} \Delta t \right) - \mu\ \Delta x\ \Delta y\ \Delta z$$

$$= \frac{\partial \mu}{\partial t}\ \Delta x\ \Delta y\ \Delta z \Delta t$$

Assuming that μ is transported with the velocity of the water particles $\vec{u}= (u_x , u_y, u_z)$, the net import in the x direction, with velocity component u_x during time interval Δt can be written as the difference between the import and the export:

$$= \partial\mu\, u_x\, \Delta y\, \Delta z \Delta t - \left(\mu\, u_x + \frac{\partial \mu u_x}{\partial x}\, \Delta x\right) \Delta y\, \Delta z \Delta t$$

$$= -\frac{\partial \mu u_x}{\partial x}\, \Delta x\, \Delta y\, \Delta z \Delta t$$

net import of μ in the y direction during time interval Δt

$$= -\frac{\partial \mu u_y}{\partial y}\, \Delta x\, \Delta y\, \Delta z \Delta t$$

net import of μ in the z direction during time interval Δt

$$= -\frac{\partial \mu u_z}{\partial z}\, \Delta x\, \Delta y\, \Delta z \Delta t$$

Considering the net import of μ in the x direction during time interval Δt it can be written:

$$\frac{\partial \mu u_x}{\partial x}\, \Delta x \Delta y\, \Delta z \Delta t = S\, \Delta x\, \Delta y\, \Delta z \Delta t$$

where *S* is the production of μ per unit time, per unit volume. Substituting the equations gives:

$$\frac{\partial \mu}{\partial t}\, \Delta x\, \Delta y\, \Delta z \Delta t = -\frac{\partial \mu u_x}{\partial x}\, \Delta x\, \Delta y\, \Delta z \Delta t - \frac{\partial \mu u_y}{\partial y}\, \Delta x\, \Delta y\, \Delta z \Delta t - \frac{\partial \mu u_z}{\partial z}\, \Delta x\, \Delta y\, \Delta z \Delta t + S\, \Delta x\, \Delta y\, \Delta z \Delta t$$

The balance equation for μ per unit volume and per unit time is given simplifying all terms by Δx Δy Δz Δt:

$$\frac{\partial \mu}{\partial t} + \frac{\partial \mu u_x}{\partial x} + \frac{\partial \mu u_y}{\partial y} + \frac{\partial \mu u_z}{\partial z} = S$$

The equation above represents the generation or dissipation of μ per unit of volume per unit of time.

Considering the mass density of water as μ = ρ (≈1027kg/m^3 for sea water) and substitute this the mass balance equation is obtained:

$$\frac{\partial \mathrm{\rho}}{\partial \mathrm{t}}+\frac{\partial \mathrm{\rho u_x}}{\partial \mathrm{x}}+\frac{\partial \mathrm{\rho u_y}}{\partial \mathrm{y}}+\frac{\partial \mathrm{\rho u_z}}{\partial \mathrm{z}}=S_\rho \quad \boldsymbol{mass\ balance\ equation}$$

And if it is assumed that the mass density constant and no production of water (S_ρ = 0) this equation reduces to the following equation, which is known as the continuity equation:

$$\frac{\partial \mathrm{u_x}}{\partial \mathrm{x}}+\frac{\partial \mathrm{u_y}}{\partial \mathrm{y}}+\frac{\partial \mathrm{u_z}}{\partial \mathrm{z}}=0 \qquad \boldsymbol{continuity\ equation}$$

The momentum density of the water is defined as: $\mu = \rho\vec{u} = (\rho u_x, \rho u_y, \rho u_z)$. By substituting $\mu = \rho u_x$ the momentum balance equation for the x component is given:

$$\frac{\partial (\mathrm{u_x \rho})}{\partial \mathrm{t}}+\frac{\partial \mathrm{u_x(\rho u_x)}}{\partial \mathrm{x}}+\frac{\partial \mathrm{u_y(\rho u_x)}}{\partial \mathrm{y}}+\frac{\partial \mathrm{u_z(\rho u_x)}}{\partial \mathrm{z}}=S_x$$

where S_x is the production of momentum in the x direction. Such production of momentum per unit time is by definition a force acting on the volume. The equation may therefore also be written as:

$$\frac{\partial (\mathrm{u_x \rho})}{\partial \mathrm{t}}+\frac{\partial \mathrm{u_x(\rho u_x)}}{\partial \mathrm{x}}+\frac{\partial \mathrm{u_y(\rho u_x)}}{\partial \mathrm{y}}+\frac{\partial \mathrm{u_z(\rho u_x)}}{\partial \mathrm{z}}=F_x$$

where F_x is the body force in the x direction for unit volume. The terms: $\frac{\partial \mathrm{u_x(\rho u_x)}}{\partial \mathrm{x}};\frac{\partial \mathrm{u_y(\rho u_x)}}{\partial \mathrm{y}};\frac{\partial \mathrm{u_z(\rho u_x)}}{\partial \mathrm{z}}$ can be neglected, so the balance equation becomes:

$$\frac{\partial (\mathrm{u_x \rho})}{\partial \mathrm{t}}=F_x$$

Where the horizontal force F_x is due to the horizontal pressure gradient $\partial p/\partial x$ in the water. The total horizontal force on the volume $\Delta x\ \Delta y \Delta z$ is equal to the pressure on the left side of the volume minus the pressure on the right side:

$$p\ \Delta y\ \Delta z - \left(\mathrm{p} + \frac{\partial p}{\partial x}\Delta x\right)\Delta y\ \Delta z$$

Per unit volume this is:

$$F_x = -\frac{\partial p}{\partial x}$$

Considering the mass density of water constant and substituting this force into the momentum balance equation the result is:

$$\boldsymbol{linearised\ momentum\ balance\ equations}$$

$$\frac{\partial \mathrm{u_x}}{\partial \mathrm{t}} = -\frac{1}{\rho}\frac{\partial p}{\partial x}\ ;\frac{\partial \mathrm{u_y}}{\partial \mathrm{t}} = -\frac{1}{\rho}\frac{\partial p}{\partial y}\ ;\frac{\partial \mathrm{u_z}}{\partial \mathrm{t}} = -\frac{1}{\rho}\frac{\partial p}{\partial z} - g$$

Solving the continuity equation and momentum balance equations for specific boundary conditions gives propagation speed of the wave and the wave induced pressure in the water. These boundary conditions are of a kinematic nature and of a dynamic nature.

At the water surface, the kinematic boundary condition is that particles may not leave the surface. In other words, the velocity of the water particle normal to the surface is equal to the speed of the surface in that direction:

$$u_z = \frac{\partial \eta}{\partial t}\quad at\ z = 0$$

where η is the surface elevation, measured vertically upwards from $z = 0$. At the bottom, the kinematic boundary condition is that particles may not penetrate the horizontal bottom:

$$u_z = 0\quad at\ z = -d$$

To ensure that the wave is a free wave subject only to gravity, the atmospheric pressure at the water surface is constant. This is the dynamic surface boundary condition:

$$p = 0 \quad at\ z = 0$$

Finding analytical solutions require the use of a rather abstract function, the velocity potential function φ = φ (x, y, z, t), which is defined as a function of which the spatial derivatives are equal to the velocities of the water particles:

$$\partial\phi(x, y, z, t)\ defined\ such\ that \frac{\partial\phi}{\partial x} = u_x\ ;\ \frac{\partial\phi}{\partial y} = u_y\ ;\ \frac{\partial\phi}{\partial z} = u_z$$

It can exist only if the motion of the water particles is irrotational. In this case, the continuity equation is written in terms of this function φ by substituting the spatial derivatives:

$$\frac{\partial\phi^2}{\partial x^2} + \frac{\partial\phi^2}{\partial y^2} + \frac{\partial\phi^2}{\partial z^2} = 0 \quad \textbf{Laplace equation}$$

The above equation is the Laplace equation. The kinematic boundary conditions at the surface and at the bottom can also be expressed in terms of the velocity potential function:

$$\frac{\partial\phi}{\partial z} = \frac{\partial\eta}{\partial t} \quad at\ z = 0$$

$$\frac{\partial\phi}{\partial z} = 0 \quad at\ z = -d$$

The three momentum balance equations can also be expressed in terms of φ by substituting the spatial derivatives. For the momentum in the x direction, the result is:

$$\frac{\partial}{\partial \mathrm{t}}\left(\frac{\partial\phi}{\partial \mathrm{x}}\right) = -\frac{1}{\rho}\frac{\partial p}{\partial x}$$

$$\frac{\partial}{\partial \mathrm{x}}\left(\frac{\partial\phi}{\partial \mathrm{t}}\right) + \frac{\partial}{\partial x}\left(\frac{p}{\rho}\right) = 0 \quad \rightarrow \quad \frac{\partial}{\partial \mathrm{x}}\left(\frac{\partial\phi}{\partial \mathrm{t}} + \frac{p}{\rho}\right) = 0$$

Finally, the momentum balance equations can be written as:

$$\frac{\partial}{\partial \mathrm{x}}\left(\frac{\partial \phi}{\partial \mathrm{t}}+\frac{p}{\rho}+gz\right)=0$$

$$\frac{\partial}{\partial \mathrm{y}}\left(\frac{\partial \phi}{\partial \mathrm{t}}+\frac{p}{\rho}+gz\right)=0$$

$$\frac{\partial}{\partial \mathrm{z}}\left(\frac{\partial \phi}{\partial \mathrm{t}}+\frac{p}{\rho}+gz\right)=0$$

The sum of terms between brackets appears in all three equations, expressing that this sum is not a function of x, y or z. It can therefore be only a function of the time t: f(t), for which is taken the simplest possible, f (t) = 0:

$$\frac{\partial \phi}{\partial \mathrm{t}}+\frac{p}{\rho}+gz=0$$

This is the linearized Bernoulli equation for unsteady flow. Taking the linearized Bernoulli equation at the surface $z = \eta$ (but in the linear approximation at $z = 0$), with $p = 0$ gives:

$$\frac{\partial \phi}{\partial \mathrm{t}}+g\eta=0 \quad at \quad z=0$$

One of the analytical solutions of the Laplace equation with the above kinematic boundary conditions is a long crested harmonic wave propagating in the positive x direction:

$$\eta(x,t)=a\sin(\omega t-kx) \ \ [Fig.\ 3.115]$$

with the following velocity potential function:

$$\phi=\hat{\phi}\ \cos(\omega t-kx) \quad with \quad \hat{\phi}=\frac{\omega a}{k}\frac{\cosh\big(k(d+z)\big)}{\sinh(kd)}$$

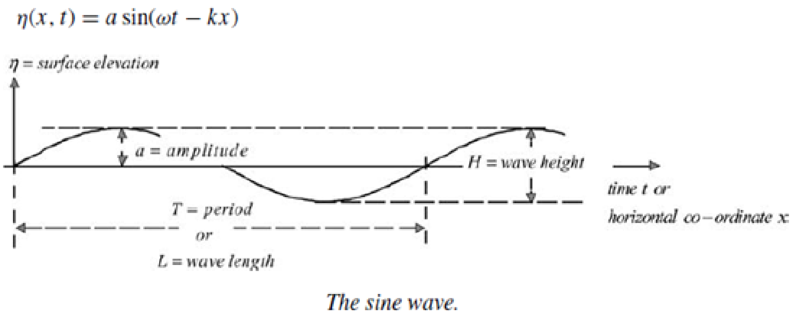

Fig. 3.115 – Indication of the symbols used to describe a sine wave (Holthuijsen, 2007)

The speed of a fixed position in the moving surface profile is by definition the forward speed of the wave; in this position the phase of the wave remains constant:

$$\frac{\partial(\omega t - kz)}{\partial t} = 0 \quad or \quad \frac{\partial \omega t}{\partial t} - \frac{\partial(kz)}{\partial x}\frac{\partial x}{\partial t} = 0 \quad or\ \omega - k\frac{dx}{dt} = 0$$

where x is the position of the point with constant phase, so that the forward speed is:

$$c = \frac{dx}{dt} = \frac{\omega}{k}$$

The particle velocities can be obtained from the velocity potential ϕ, just by using the definition of ϕ: the spatial derivatives of ϕ are the velocity components $\partial\phi/\partial x = u_x$ and $\partial\phi/\partial z = u_z$, so the particle velocities are given by:

$$u_x = \hat{u}\ \sin(wt - kx) \quad with \quad \hat{u}\ = \omega a \frac{\cosh\big(k(d+z)\big)}{\sinh(kd)}$$

$$u_z = \hat{z}\ \cos(wt - kx) \quad with \quad \hat{z}\ = \omega a \frac{\sinh\big(k(d+z)\big)}{\sinh(kd)}$$

Substituting the harmonic surface profile and the corresponding velocity potential function into the expression for the boundary condition of zero atmospheric pressure, gives a relationship between radian frequency ω and wave number k:

$$\omega^2 = gk \tanh(kd)$$

This is called the dispersion relationship; for deep water the dispersion relationship becomes:

$$\omega = \sqrt{gk_0}$$

For very shallow water the dispersion relationship becomes:

$$\omega = k\sqrt{gd}$$

The analytical expression of the pressure is derived by substituting the solution for the velocity potential into the Bernoulli equation, with the result:

$$p = -\rho g z + \rho g a \frac{\cosh\big(k(d+z)\big)}{\cosh(kd)} \sin(wt - kx) \quad z < 0 \; below\ stilll\ water\ level$$

The first term on the right side is the hydrostatic pressure. It is independent of the presence of the wave. The second term is due to the wave and therefore represents the wave induced pressure, denoted as p_{wave}:

$$p_{wave} = \hat{\mathrm{p}}\ \sin(wt - kx) \quad with\ \hat{\mathrm{p}} = \rho g a \frac{\cosh\big(k(d+z)\big)}{\cosh(kd)}$$

This is a propagating pressure wave in the water body, in phase with the surface elevation and with vertically decreasing amplitude [Fig. 3.116]. In deep water the amplitude of the wave induced pressure is ($z < 0$ below the still-water line)

$$\hat{\mathrm{p}} = \rho g a e^{kz} \quad deep\ water$$

In very shallow water the wave induced pressure amplitude is constant along the vertical:

$$\hat{p} = \rho g a \quad very\ shallow\ water$$

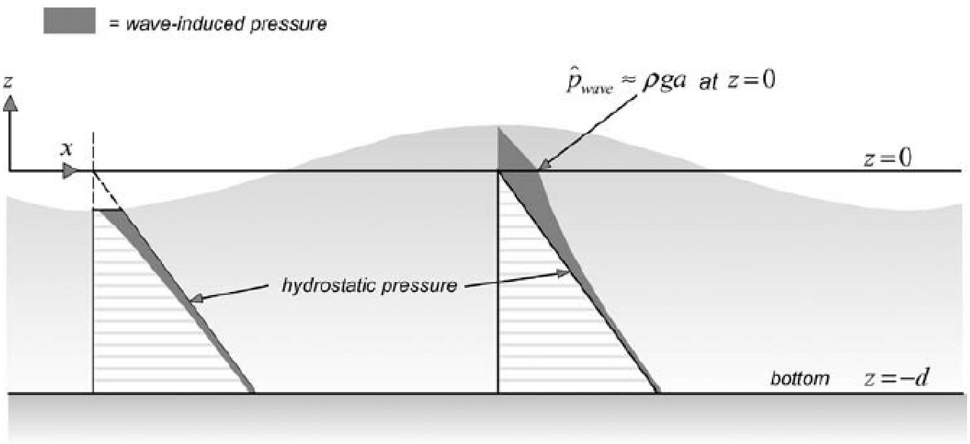

Fig. 3.116 *– Pressure in the water column (Holthuijsen, 2007)*

3.9 Theoretical point absorber background

For an offshore structure that is freely floating, they can be considered six degrees of freedom: three translational and three rotational degrees of freedom[10] [Fig. 3.117]:

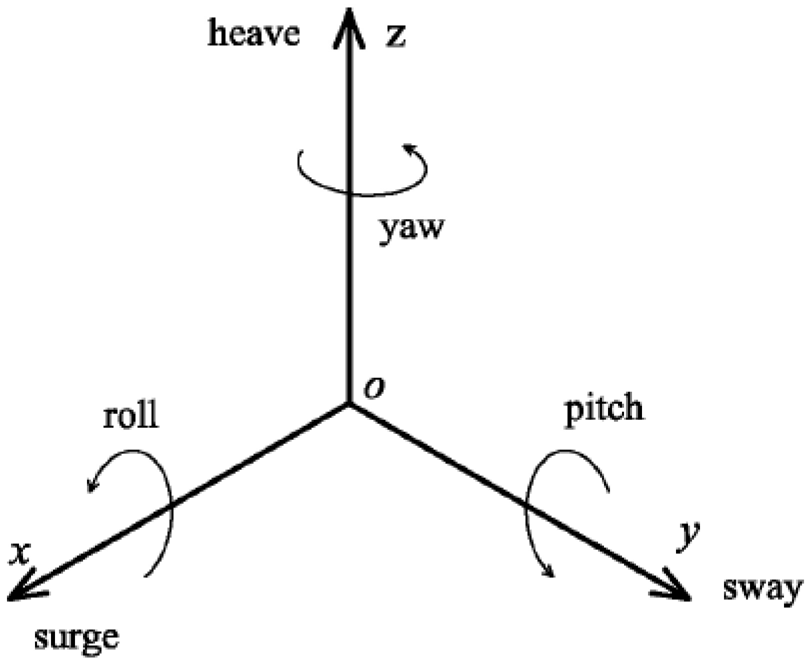

Fig. 3.117 – Coordinates system and degrees of freedom

[10] De Backer, D. (2009). Hydrodynamic Design Optimization of Wave Energy Converters Consisting of Heaving Point Absorbers. *PhD Thesis*. Ghent University, Ghent.

- Surge: horizontal, longitudinal motion along the x-axis.
- Sway: horizontal, transverse motion along the y-axis.
- Heave: vertical motion along the z-axis.
- Roll: angular motion around the x-axis.
- Pitch: angular motion around the y-axis.
- Yaw: angular motion around the z-axis.

Some structures are not freely floating, but are restrained to fewer degrees of freedom. In the following theoretical treatise, it is explained only the heavy motion.

The behavior of a heaving point absorber can be compared to that of a mechanical oscillator, composed of a mass-spring-damper system with one degree of freedom subjected to an external force in the direction of the degree of freedom [Fig. 3.118]

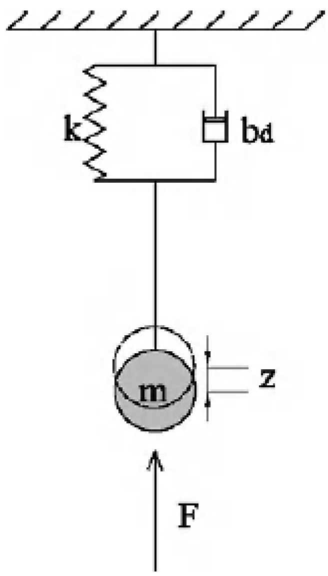

Fig. 3.118 *- A basic mass-spring-damper systems (De Backer, 2009)*

The coefficient b_d is linear and it is the damping coefficient. The external harmonic force is represented by the amplitude F_A and the angular frequency ω.

According to Newton's law, the equation of motion consists of an inertia force $m\frac{d^2z}{dt^2}$, a damping force $b_d\frac{dz}{dt}$, a restoring force kz, and the external force $F_A\sin(\omega t)$:

$$m\frac{d^2z}{dt^2} + b_d\frac{dz}{dt} + kz = F_A\sin(\omega t)$$

Omitting the external force results:

$$m\frac{d^2z}{dt^2} + b_d\frac{dz}{dt} + kz = 0$$

The form of the solution is assumed:

$$z = z_A e^{qt}$$

With z_A and q unknown constants. Substitution of z in the Newton's law gives:

$$(mq^2 + b_d q + k) * z_A e^{qt} = 0$$

The equation above must be valid for all t, so it can be simplified as:

$$mq^2 + b_d q + k = 0$$

And the two solutions for q are:

$$q_{1,2} = -\frac{b_d}{2m} \pm \sqrt{\left(\frac{b_d}{2m}\right)^2 - \frac{k}{m}}$$

When the discriminant D equals zero the oscillation is critically damped, meaning that the systems return to its equilibrium position in the quickest possible way without vibrating around the equilibrium position. The damping coefficient is called the critical damping coefficient b_c:

$$b_c = 2\sqrt{km} = 2m\omega_n$$

With ω_n the natural pulsation frequency given by:

$$\omega_n = \sqrt{\frac{k}{m}}$$

The ratio of the damping coefficient to the critical damping coefficient is called the damping ratio and is denoted by $\zeta_{\mathrm{d}} = \frac{\mathrm{b_d}}{b_c}$

The considered heaving point absorber can generally be considered as an under dumped mechanical oscillator. For an under damped system the value q can be rewritten as:

$$q_{1,2} = -\zeta_{\mathrm{d}}\omega_n \pm i\omega_n\sqrt{1-\zeta_{\mathrm{d}}^2}$$

And the solution of z becomes:

$$z = A_1 e^{q_1 t} + A_2 e^{q_2 t}$$

The constant A_1 and A_2 are determined from the initial conditions. Since $q_{1,2}$ are complex conjugates value, also A_1 and A_2 need to be complex value for z to be real.

$$\begin{cases} A_1 = \frac{1}{2} z_{Af}(\sin(\beta_f) - icos(\beta_f)) \\ A_2 = \frac{1}{2} z_{Af}(\sin(\beta_f) + icos(\beta_f)) \end{cases}$$

$$z = z_{Af} e^{-\zeta_d \omega_n t} \sin\left(\sqrt{1-\zeta_d^2}\ \omega_n t + \beta_f\right)$$

where the index f denotes free oscillation . The exponential function $e^{-\zeta_d \omega_n t}$ is responsible for the decreasing amplitude effect [Fig. 3.119]:

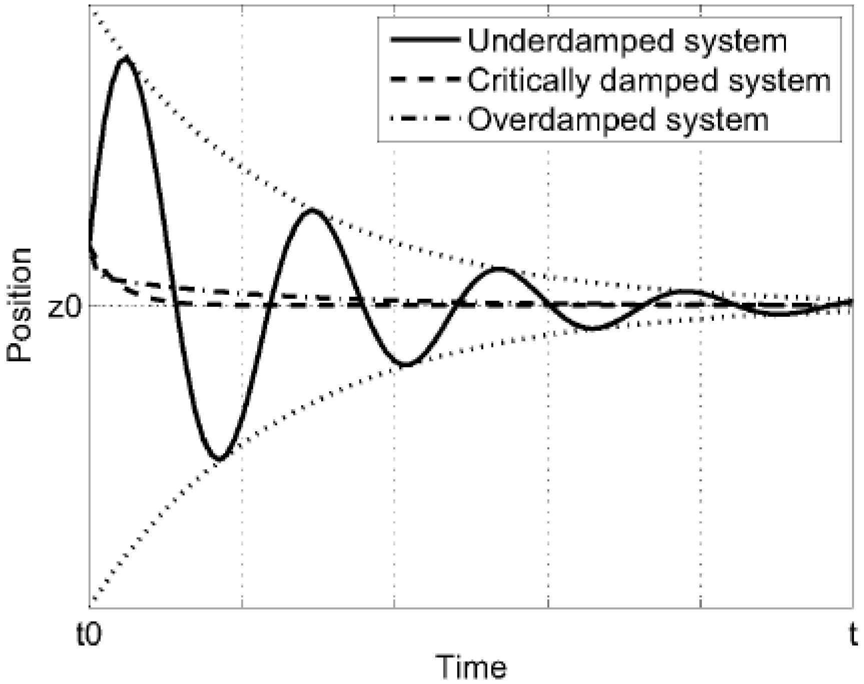

***Fig. 3.119** – In the figure the equation for the decreasing amplitude effect is showed with black dotted lines (De Backer, 2009)*

The sine function causes the oscillations with a frequency equal to the damped natural angular frequency,

$$\omega_d = \sqrt{1 - \zeta_d^2}\ \omega_n$$

The damped free oscillations of a system disappear after a number of oscillations. The number of oscillations depends on the damping in the system. Adopting the following relationships:

$$C_1 = z_{Af} \cos(\beta_f)$$

$$C_2 = z_{Af} \sin(\beta_f)$$

The equation of motion can alternatively be expressed in the form:

$$z = e^{-\zeta_d \omega_n t}(\mathrm{C}_1 \cos(\omega_d t) + C_2 \sin(w_d t))$$

When an external force is applied on the system the complete solution of the equation of motion consists of the sum of the free oscillation and the forced oscillation or steady state oscillation:

$$z = z_{As} \sin(\omega_d t + \beta_s)$$

with z_{As} the amplitude of the steady-state oscillation and β_s the phase angle between the external force and the motion of the system. The index s denotes steady state. The parameters, z_{As} and β_s, can be explained as:

$$z_{As} = \frac{F_A}{((k - m\omega^2)^2 + (b\omega)^2)^{\frac{1}{2}}}$$

And

$$\tan(\beta_s) = \frac{-b_d\omega}{k - m\omega^2}$$

To conclude, the complete response of a mass-spring-damper system subjected to a regular external force is given by:

$$z_{total} = z_{free} + z_{forced} = z_{Af} e^{-\zeta_d \omega_n t} \sin\left(\sqrt{1 - \zeta_d^2}\ \omega_n t + \beta_f\right) + z_{As} \sin(\omega_d t + \beta_s)$$

In the following it is discussed the response of a point absorber, oscillating in a harmonic wave with respect to a fixed reference. The motion of the point absorber is restricted to the heave mode only.

In equilibrium position the floater has a draft d; due to the vertical wave action, the floater has a position z from its equilibrium position [Fig. 3.120].

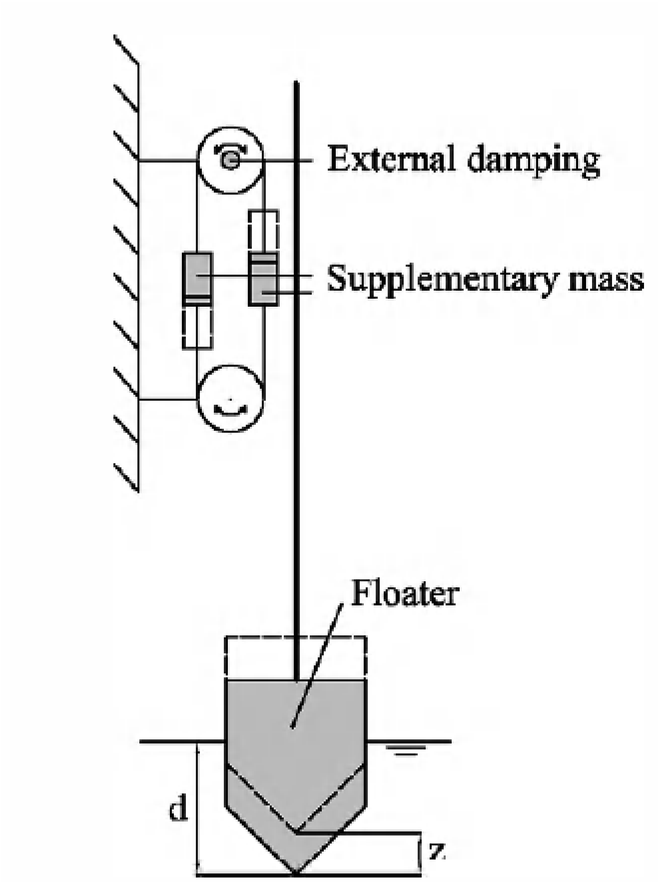

***Fig. 3.120** - A schematic view of the considered point absorber (De Backer, 2009)*

The equation of this motion can be described by the Newton's second law:

$$m\frac{d^2z}{dt^2} = F_{ex} + F_{rad} + F_{res} + F_{damp} + F_{tun}$$

Where m is the mass of the buoy and $\frac{d^2z}{dt^2}$ the buoy acceleration. F_{ex} is the exciting wave force, F_{rad} the radiation force. The radiation force can be decomposed in a linear added mass term plus a linear hydrodynamic dumping term:

$$F_{rad} = m_a(\omega)\frac{d^2z}{dt^2} - b_{hyd}(\omega)\frac{dz}{dt}$$

The hydrostatic restoring force F_{res}, is the Archimedes force F_{arch} minus the gravity force F_g. This force corresponds to the spring force, with a linear spring constant, the hydrostatic restoring force can be expressed as:

$$F_{res} = F_{arch} - F_g = \rho V(t) - mg = kz$$

Where V(t) is the instantaneous volume. The spring constant is expressed as: $k = \rho g A_\omega$where A_ω is the waterline area.

F_{damp} is the external damping force exerted by the Power Take Off and F_{tun} the tuning force for the phase control. Generally these two forces are non-linear; however, for simplicity, they are often assumed linear. In that case the dampi

ng force becomes:

$$F_{damp} = b_{ext}\frac{dz}{dt}$$

with b_{ext} the linear external damping coefficient originating from the PTO and enabling power extraction.

The tuning force can be represented for instance by means of a supplementary mass term. In this case the tuning force is indicated as:

$$F_{tun} = m_{sup}\frac{d^2z}{dt^2}$$

The equation of motion of the presented heaving point absorber can be rewritten as:

$$\left(m + m_a(\omega) + m_{sup}\right)\frac{d^2z(t)}{dt^2} + \left(b_{hyd} + b_{ext}\right)\frac{dz(t)}{dt} + kz(t) = F_{ex}(\omega, t)$$

The steady state solution has been determined previously:

$$z = z_{As}\sin(\omega_d t + \beta_s)$$

Where

$$z_A(\omega) = \frac{F_{ex,A}(\omega)}{\left(\left(\left(m + m_a(\omega) + m_{sup}\right)\omega^2\right)^2 + \left((b_{hyd} + b_{ext})\omega\right)^2 - k\right)^{\frac{1}{2}}}$$

$$\beta_{\mathrm{mot}} = \beta_{\mathrm{Fex}} - \arctan\left(\frac{\left(b_{hyd} + b_{ext}\right)\omega}{\left(m + m_a(\omega) + m_{sup}\right)\omega^2 - k}\right)$$

For what concern the power absorption, it is assumed a harmonically oscillation body with velocity v and subjected to a force $F(t)$:

$$F(t) = F_A \cos(\omega t + \beta_F)$$

$$v(t) = v_A \cos(\omega t + \beta_v)$$

The power average over a period T can be expressed as:

$$P_{av} = \frac{1}{2} F_A v_A \cos(\beta_F - \beta_v)$$

The average absorbed power of a point absorber is equal to the average excited power minus the average radiated power:

$$P_{abs,av} = P_{ex,av} - P_{rad,av}$$

The average exciting power can be expressed as:

$$P_{ex,av} = \frac{1}{2} F_{e,A} v_A \cos(\gamma)$$

$$where\ \gamma = \beta_F - \beta_v\ is\ the\ phase\ shift\ between\ F_{e,A} and\ v_A$$

The average radiation power is given by:

$$P_{rad,av} = \frac{1}{2} b_{hyd} v_A^2$$

Therefore the average power absorbed is:

$$P_{abs,av} = \frac{1}{2} F_{e,A} v_A \cos(\gamma) - \frac{1}{2} b_{hyd} v_A^2$$

Or alternatively can be expressed as the power absorbed by the PTO system:

$$P_{abs,av} = \frac{1}{2} b_{ext} v_A^2 = \frac{1}{2} b_{ext} \omega^2 z_A^2$$

The absorption width, indicated with λ_p, is the crest length over which the total available power corresponds to the absorbed power or the ratio of the absorbed power to the average available power per unit crest length..

$$\lambda_p = \frac{P_{abs}}{P_{avail}}$$

In a regular wave with wave length L, the maximum absorption width of a heaving point absorber is theoretically equal to the wave length divided by 2π.

$$\lambda_{p,max} = \frac{2L}{\pi}$$

For an axisymmetric body with three degrees of freedom: heave, surge and sway, the maximum absorption width is equal to:

$$\lambda_{p,max} = \frac{3L}{2\pi}$$

The maximum power absorption occurs when the equation of the Power absorption derivative to the velocity equals zero. Hence, the optimum amplitude of the velocity is:

$$v_{A,opt} = \frac{F_{ex,A}}{2b_{hyd}}\cos(\gamma)$$

Consequently, the maximum value of the average power absorption is:

$$P_{abs,av,max,} = \frac{F_{ex,A}^2}{8b_{hyd}}\cos^2(\gamma)$$

The optimum phase shift is obtained for $\gamma = 0$. The amplitude of the exciting force is rewritten as:

$$F_{ex,A} = f_{ex}\zeta_A$$

The expression for the maximum average absorbed power becomes:

$$P_{abs,av,max,} = \frac{f_{ex,A}^2}{8b_{hyd}}\zeta_A^2$$

The hydrodynamic coefficient for heavy is:

$$b_{hyd} = \frac{\omega k_\omega}{2\rho g^2 D(k_\omega d_\omega)} f_{ex,A}^2$$

with k_ω the wave number and $D(k_\omega d_\omega)$ the depth factor. The power absorption can be rewritten as:

$$P_{abs,av,max,} = \frac{\rho g^2 D(k_\omega d_\omega)}{4\omega k_\omega} \zeta_A^2$$

The total available average power is given:

$$P_{avail} = \frac{\rho g^2 D(k_\omega d_\omega)}{4\omega} \zeta_A^2$$

A large hydrodynamic damping coefficient at an angular frequency ω indicates that the system has a large capacity to radiate waves at that frequency. In addition the body experiences for that frequency also a large excitation force. Hence, a point absorber that is a good damper at an angular frequency ω is also a good receiver for waves with the same frequency.

3.10 Conclusions

The first conclusion is that a point absorber as a wave energy device can be a good solution if developed for the future. On the other hand, concerning the FlanSea buoy, a lot of work is already done but the problems and some missing points need to be solved with additional research in this field; in fact, despite the goals reached during the numerical and the physical model, some issues are appeared during the tests out of the Ostend's harbor.

The principal aim of the previous lab test was acquire design experience, in order to have an idea about the problems that would be occurred when the buoy would have started to work; especially a lot of experience was learned regarding the waterproofing such as the gaskets for the PTO and other practically aspects.

Important elements like the COG and his influence on the buoy motions was analyzed with numerical model but not on a scaled device in the lab. What we expect is a better motion when the frequencies of the waves get close to the natural frequency for the heavy motion of the buoy; otherwise we don't know how the pitching will influence the buoy movements, so it is very difficult, especially in the irregular waves case, to say what will happen.

In addition, no tests have been done in the hydraulic laboratory regarding the influence of the buoy geometry or the stiffness of the cable on the pitching motion and the biggest problems in the Sea were caused by the roll motion.

For all of these reasons the small-scale laboratory tests are needed.

The experiments campaign will try to find out all of these unknowns to prevent the damages occurred at the FlanSea buoy and get useful information for a new buoy that will be developed in the future; different configurations will be tested (as well explained in the next chapter) and the work will be divided in two phases. In the first time the buoy will be tested only in the heavy motion and in the second part the scaled point absorber will be fixed through a rope at the bottom of the flume and the six degrees of freedom movements will be studied.

4. Hydraulic model tests

4.1 Test facility

The Tests have been carried out in the so called small wave flume at Ghent University.

4.1.1 Wave flume

The flume was built in 1999 and the dimensions are 20,00 x 0,35 x 0,60 m (length x width x high). The design water level is 30 cm (Department of Civil Engineering). All components of the flume (steel construction, step motor, motor steering, software for wave generation, acquisition and analysis) have been designed by Ghent University. The flume consists of independent parts, so that the length can be changed. A picture of the flume is shown in the figure [Fig. 4.1].

Fig. 4.1 *– The wave flume*

4.1.2 Wave generator

The wave generator [Fig. 4.2] consists out of a step motor, which is connected to a wave paddle using a spindle. The wave paddle is piston type with a maximum stroke of 0,40 m. The wave generator is able to generate regular and irregular and solitary waves.

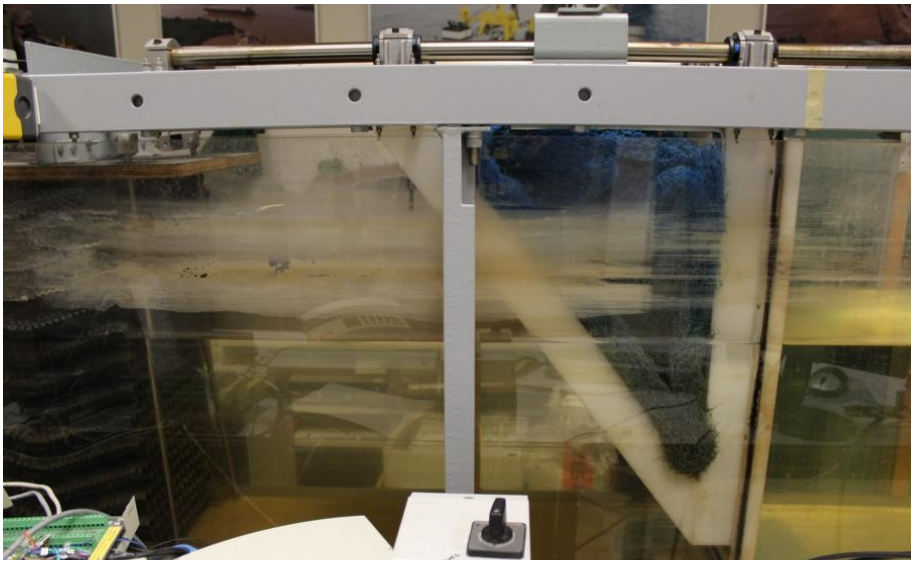

Fig. 4.2 *– The wave generator*

Due to the breaking of the waves and the maximum of the speed and stroke of the wave paddle the maximum wave height and shortest period is limited. The possible regular waves are shown in figure [Fig. 4.3]. For wave periods up to 0.7 s the wave height is limited by the breaking of the waves next to the wave paddle. (Dotted line) For higher periods the speed of the paddle is the limiting factor. (dashed line) The maximum stroke imitates the maximum period of the waves. (P. van Besien, K. Wittebolle 1998)

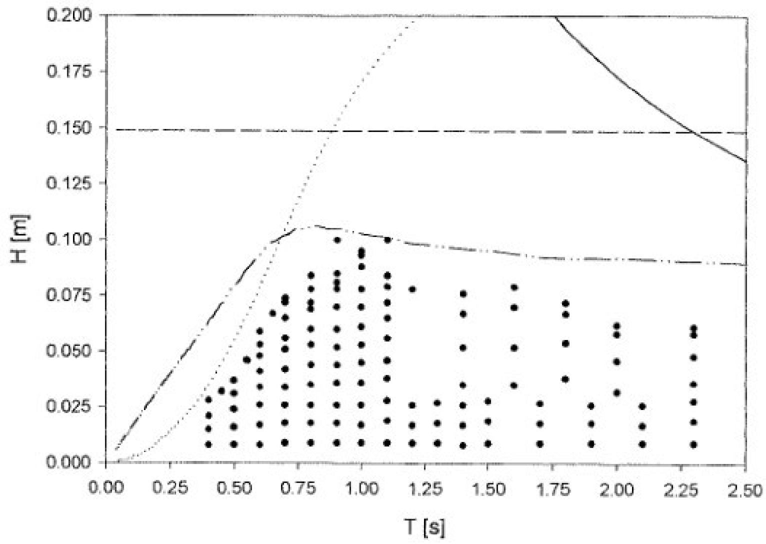

Fig. 4.3 *- Possible Waves*

There is a difference between the theoretical input waves and the real measured waves. This is shown in figure [Fig. 4.4]. In the graph on the left side is the measured wave high over the theoretical wave high. For small wave height are they similar. By increasing the theoretical wave heights the measured wave heights increasing less. This difference need to be regulated by giving higher theoretical input wave heights than the desired wave height. In the right graph of figure 4.4 is shown the measured wave period over the theoretical wave height. It can be seen that the periods are almost the same so that no regulation is needed.

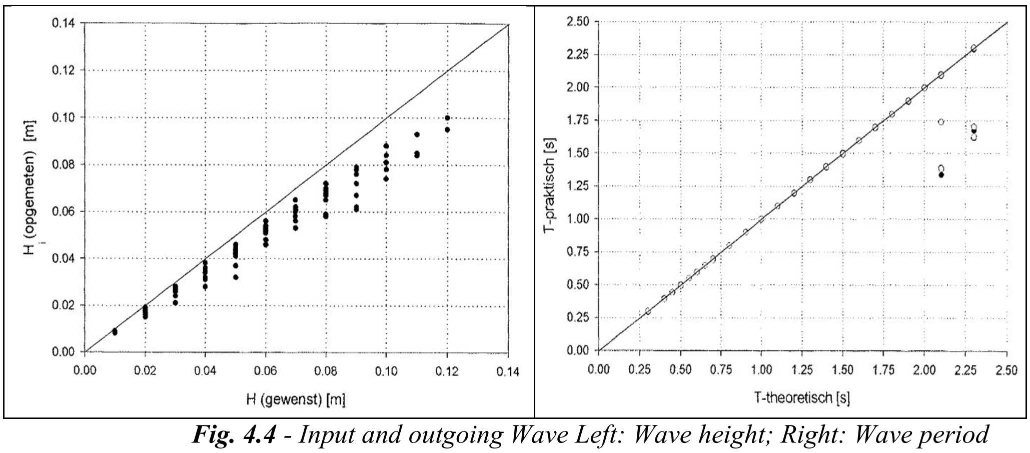

Fig. 4.4 *- Input and outgoing Wave Left: Wave height; Right: Wave period*

4.2 Model scale

To ensure that the physical models are scaled in a meaningful way, some similarities need to be considered. The similarities are: (Wanan Sheng et al. 2014)

- Geometrical similarity
- Kinematic similarity
- Dynamic similarity

For the geometrical similarity the shape of the prototype and the model has to be linear scaled with a fixed factor. Therefor the scaling factor for the length can be defined as:

$$\lambda = \frac{L_p}{L_m}$$

With:

λ: scaling factor

L_p: Length prototype

L_m: Length model

As a result of this definition the scaling for the area and the volume is:

$$\lambda_A = \frac{A_p}{A_m} = \lambda^2$$

$$\lambda_V = \frac{V_p}{V_m} = \lambda^3 .$$

With:

λ_A: scaling factor for an area

A_p: area prototype

A_m: area model

λ_V : scaling factor for a volume

V_p : volume prototype

V_m : volume model

For the kinematic similarity the time needed for motions in prototype needs to be proportional to the time needed in model scale.

The dynamic similarity has two conditions. First the models need to have a geometric similarity and as second condition a similarity between the forces. This means that the ratios between the different forces in prototype have to be the same as in model scale. The most important forces for are:

- Inertia Forces, F_i
- Viscous forces, F_v
- Gravitational forces, F_g
- Pressure forces, F_p
- Elastic forces in the fluid (compressibility), F_e.
- Surface forces, F_s.

The only possibility to reach the complete dynamic similarity is a scaling factor of one. (H. Oumeraci 4/12/2012) Hence this is not meaningful the main force has to be defined and the similarity law has to be chosen. The main laws and the main forces are listed in the table [Tab 4.1]:

Symbol	*Dimensionless Number*	*Force Ratio*	*Definition*
R_e	*Reynolds Number*	$\frac{Inertia}{Viscous}$	$\frac{UL}{\nu}$
F_n.	*Froude Number*	$\frac{Inertia}{Gravity}$	$\frac{U}{\sqrt{gL}}$
M_n	*Mach's Number*	$\frac{Inertia}{Elasticity}$	$\frac{U}{\sqrt{E_v / \rho}}$
W_n	*Weber's Number*	$\frac{Inertia}{Surface tension}$	$\frac{U}{\sqrt{\sigma / \rho L}}$
St	*Strouhall Number*	-	$\frac{f_v D}{U}$
KC	*Keulegan- Carpenter Number*	$\frac{Drag}{Inertia}$	$\frac{U_A T}{D}$

Tab. 4.1 - Similarity laws (S. Steen 8/20/2014)

Waves are mostly affected by Gravity forces. Therefore the Froude scaling law has been chosen for the tests. With the definition of the scaling law the scaling factor for each dimension can be calculated:

$$\frac{U_P}{\sqrt{gL_P}} = \frac{U_M}{\sqrt{gL_M}} \tag{1}$$

By transposing the previous equation arrives at:

$$U_P = U_M \sqrt{\frac{L_P}{L_M}} = U_M \sqrt{\lambda} \tag{2}$$

The main scaling factors are listed below [Tab 4.2]:

Quantity	Scale factor
Acceleration	λ^{0}
Area	λ^{2}
Force	λ^{3}
Length	λ
Mass/Volume	λ^{3}
Power	$\lambda^{3,5}$
Pressure	λ
Time	$\lambda^{0,5}$
Velocity	$\lambda^{0,5}$
Volume flow rate	$\lambda^{2,5}$
Work/ Energy	λ^{4}

Tab. 4.2 - Scale factors

As the prototype the size of the FlanSea buoy has been used. The tests have been carried out with a scaling factor of 1:35. This scaling factor is a result of the circumstances in the test facility. To have less influence by scaling effects the scaling factor should be as big as possible. The main imitating conditions are the width of the wave flume and the generatable waves. Decrease the influence of effects caused by the wall the buoy should have as maximum diameter one third of the width of the flume. To get beneficial results the used wave parameters should be in the same size than the real sea conditions at the Belgium coast. This is a second limitation of the possible scaling factor hence the wave generator has to be able to generate the waves. Summing up these limitations a scaling factor of 1:35 was defined.

4.3 Wave climate

The determination of the waves generated during the physical experiments is an important starting point. The first step is a statistical analysis of the wave heights, which are bigger than a fixed value. Through the regularization of the extreme events, by using well know probabilistic function, it is possible to calculate the wave climate defined as wave heights related to different return periods or the probability of the extreme event occurrence.

The determination of each wave storm inside the historical series is performed introducing a threshold and considering the starting point of each wave storm where the first wave height is bigger than this limit value. It is supposed that the wave storm ends when the wave height is less than the threshold for the first time. At last, for each storm the maximum wave height is taken.

Compatibly with the length of the time series, or rather with the available years, the limit value is chosen in order to have enough events to be analyzed. Due to the copious dates, the matlab script reported in the appendix has been used for this analysis (see appendix A).

Using as a threshold a minimum wave height of 1.50 meter, 1191 events were recorded; after that the data has been organized in an ascend way, from the minimum to the maximum wave height.

The wave heights used during the tests have been determined using the Gumbel distribution and the Weibull distribution.

4.3.1 Gumbel probabilistic distribution

The Gumbel distribution (1935) is:

$$F(x) = e^{-e^{-\frac{x-b}{a}}}$$

Where:

F(x) is the cumulative distribution;

x is the random variable, in this case it is the wave height;

A is the scale parameter;

B is the location parameter.

A and B can be derived from the momentums method through the expressions below:

$B = H_{sm} - 0.5772A$

$A = (6^{0.5}/\pi)\sigma$

With H_{sm} the average of the total amount of the wave heights and σ the standard deviation of the events.

The return period T_r and F(x) are related by the following relation:

$$F(x) = \frac{\lambda_e Tr - 1}{\lambda Tr}$$

Where λ_e is the ratio between the number of the events and the number of the observed years. The parameters founded are reported in the table below [Tab. 4.3]:

Observed years [-]	λ_ε [-]	A [-]	σ [m]	Hsm [m]	B [-]
9.5	120.9	0.4	0.6	2.1	1.8

Tab. 4.3 - Parameters for the Gumbel distribution

Than the significant wave heights has been calculated for each return period using the formula:

$$H_{tr} = B - Aln(-\ln(f(x)))$$

The results are represented below [Tab. 4.4]:

GUMBEL		
Tr [years]	Q [-]	Htr [m]
0.166	0.950	3.159
1	0.992	3.966
2	0.996	4.275
10	0.999	4.991
25	1.000	5.398
50	1.000	5.706
75	1.000	5.886
100	1.000	6.014
125	1.000	6.113
150	1.000	6.194

Tab. 4.4 – Wave heights obtained with the Gumbel distribution

In Figure 4.5 is showed how the Gumbel law approaches the wavedata.

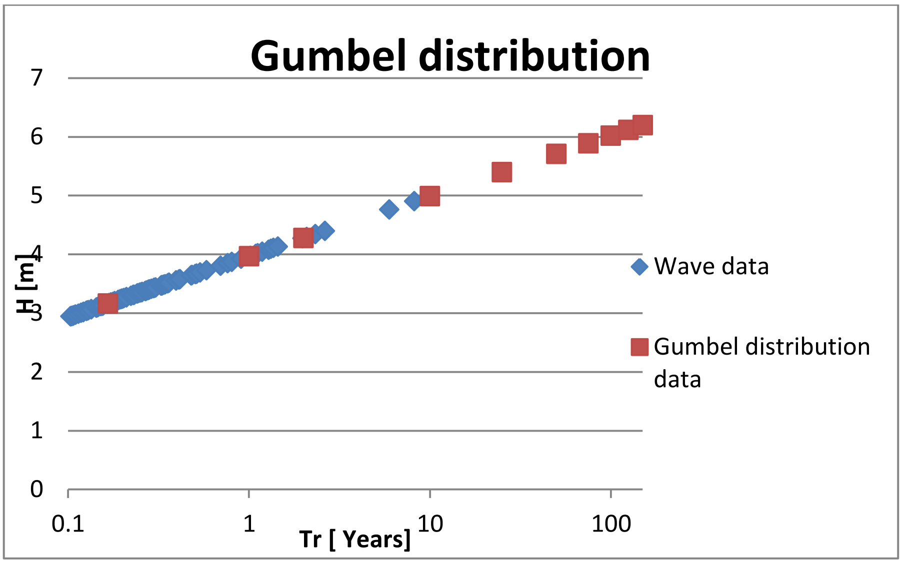

***Fig. 4.5** – Probabilistic Gumbel relation*

4.3.2 Weibull probabilistic distribution

After putting the data in a descending order and categorized each pf them with a "m" index, it has been assigned a non-exceedance probability using the plotting position formula below:

$$\hat{F}(x) = \frac{m}{N+1}$$

Where N indicates the total number of the wavedata.

The Weibull law (1951) is:

$$F(x) = 1 - e^{-(\frac{x-B}{A})^{k_s}}$$

Where:

F(x) is the cumulative distribution;

x is the random variable, in this case the wave height;

A is the scale parameter;

B is the location parameter;

k_s is the shape parameter, chosen approaching the wavedata as good as possible. In this case it is 1.3.

A and B can be derived by linearizing the cumulative distribution; the result is reported below:

$$y = Cx + D$$

Where:

$y(H) = (-LN((1 - \hat{F}(H)))\text{^}(1/k_s)$

x = H, the wave height from the wave data;

A = 1/C;

B = A*D.

After inserting the data in a excel graph, C and D are directly given using a linear interpolation, as showed in the graph below [Fig. 4.6]:

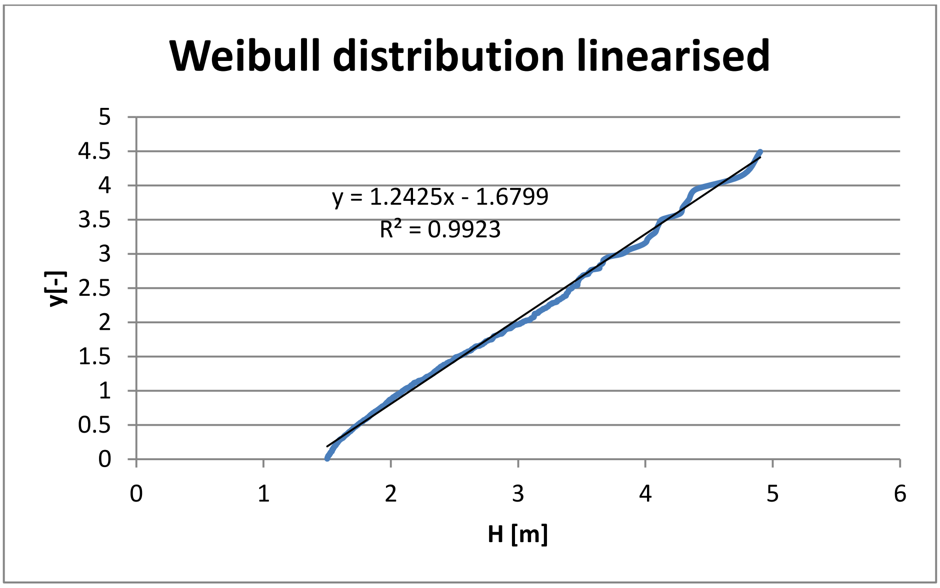

***Fig. 4.6** – In the graph is represented the Weibull distribution, using the plotting position formula.*

The scale parameter, the location parameter and the shape parameter are summarized in the table [Tab. 4.5]:

k_s [-]	A [m]	B [m]
1.300	0.805	1.352

Tab. 4.5 – Parameters of the Weibull distribution

The results are represented below [Tab. 4.6]:

Weibull		
Tr [years]	Q [-]	Htr [m]
0.166	0.950	3.225
1	0.991	4.039
2	0.995	4.334
10	0.999	4.986
25	0.999	5.342
50	0.999	5.605
75	0.999	5.756
100	0.999	5.863
125	0.999	5.945
150	0.999	6.012

Tab. 4.6 – Wave heights obtained with the Weibull distribution

In the next figure [Fig. 4.7] it is showed how the Weibull law approaches the wavedata:

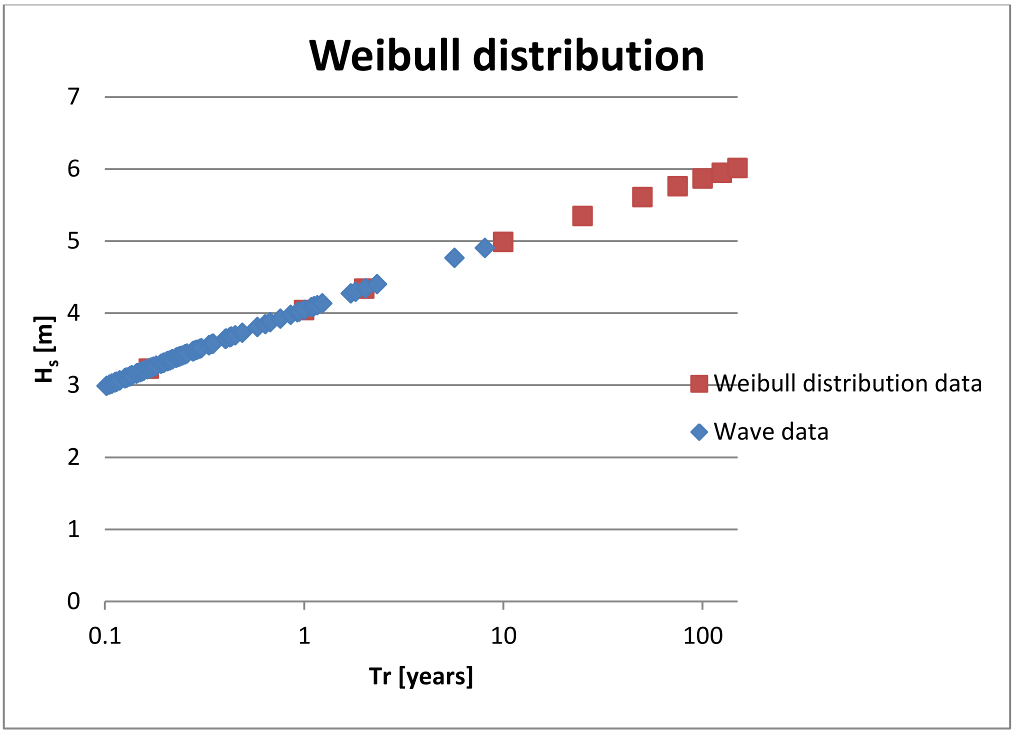

Fig. 4.7 *– Probabilistic Weibull relation*

4.4 Model setup

The physical test is built in order to be able to change the position of the center of gravity; one of the aims of the work is to investigate the behavior of the buoy changing the position of the weight. This objective was achieved building a physical model where it is possible to move a weight in two different positions.

The dimensions of the model, in 1:35 scale, are represented in the next draft [Fig. 4.8]:

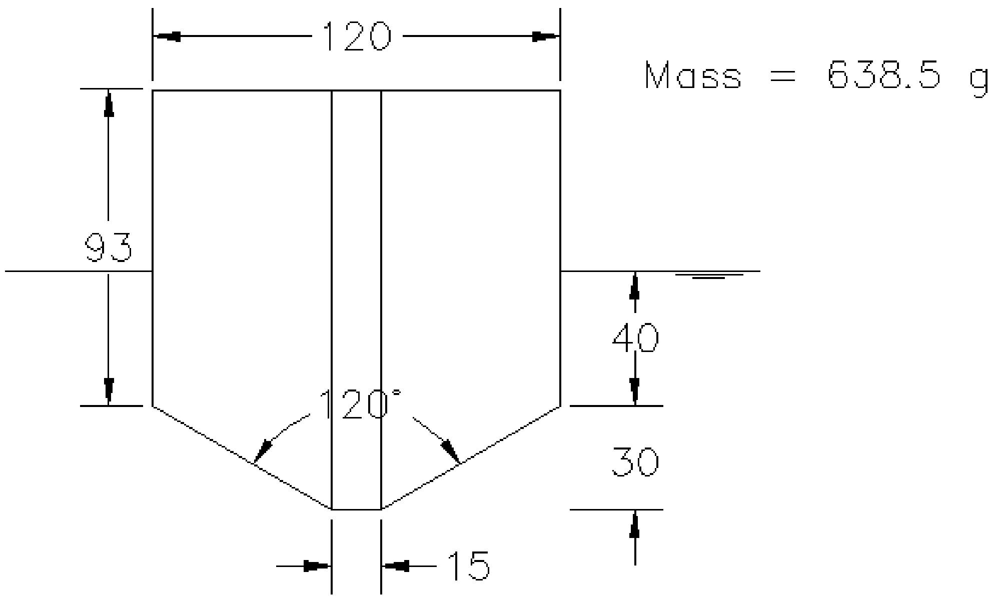

Fig. 4.8 *– Geometry of the buoy; all the dimensions are expressed in millimeters.*

The first step was the study of the metacenter position; the method used is described quickly below. Identifying the metacenter position of the buoy allows calculating the maximum height of the weight keeping the buoy in a stable condition; If the center of gravity is higher than the metacenter, the buoy will be unstable. Indicating [see the Fig. 4.9] the position of the center of gravity with the letter G, the bottom part of the buoy with K (the keel), the position of the center of buoyancy with the letter B and with M the metacenter position, the buoy behaves properly if GM is not negative:

GM = KB + BM – KG

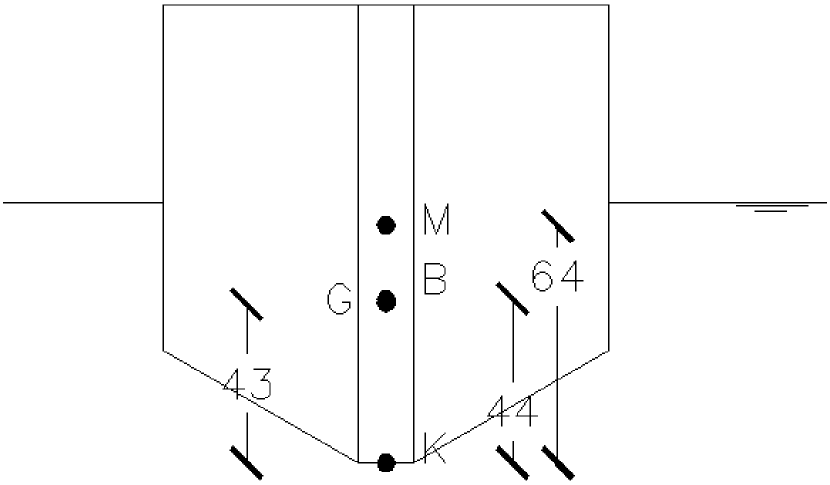

__Fig. 4.9__ – In the picture, the keel, the center of gravity, the center of buoyancy and the metacenter position; all the distance are referred to the keel and are expressed in millimeters.

If the angle of gyration is less, the distance from the buoyancy and the metacenter can be determined with this expression:

$$BM = \frac{I_{xx}}{\nabla}$$

Where:

I_{xx} is the second moment of the area at the waterline;

∇ is the submerged volume.

The physical model is built in order to have a weight able to be displaced in different positions. In particular, the weight has a cylindrical shape whit a hole inside [Fig. 4.10]. The buoy is composed by three parts: a conic part [Fig. xxx], designed with a 3D printer, a cylindrical part made from a PVC pipe and a cover [Fig. 4.11].A bar inside the buoy allows the different displacement of the weight [Fig. 4.12]. At last, two positions of the center of gravity were tested: the first corresponds when weight lays on the conic part. In this configuration the center of gravity is the same as showed above in the figure [Fig 4.13]. The second configuration studied was when the height of G is a bit less than M (if G =M the buoy becomes instable); in this case the height from the keel is 85 millimeters.

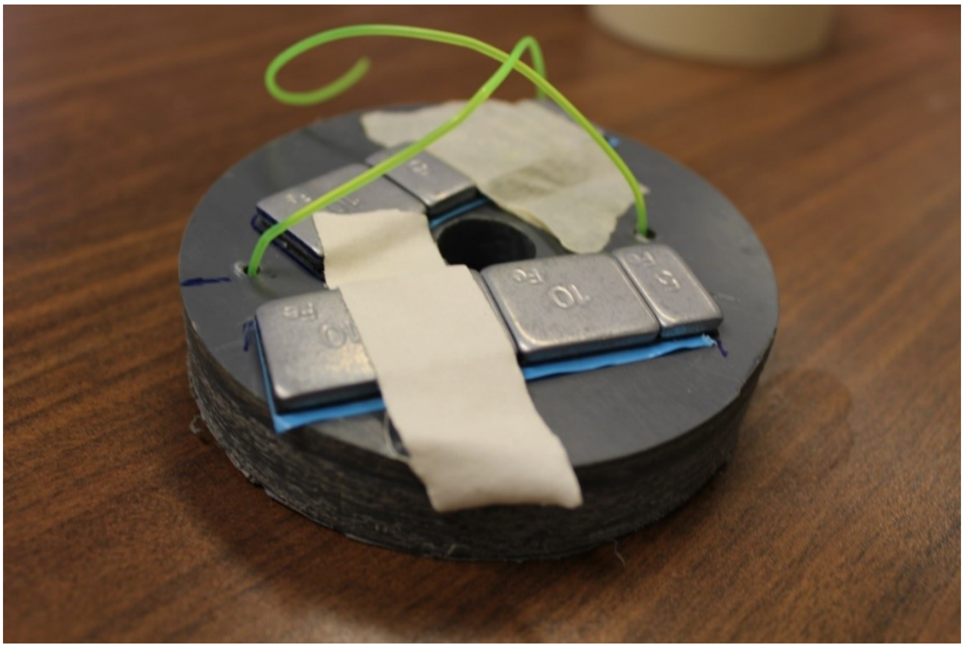

Fig. 4.10 *– The weight used. Some additional weights are also taped on the upper part.*

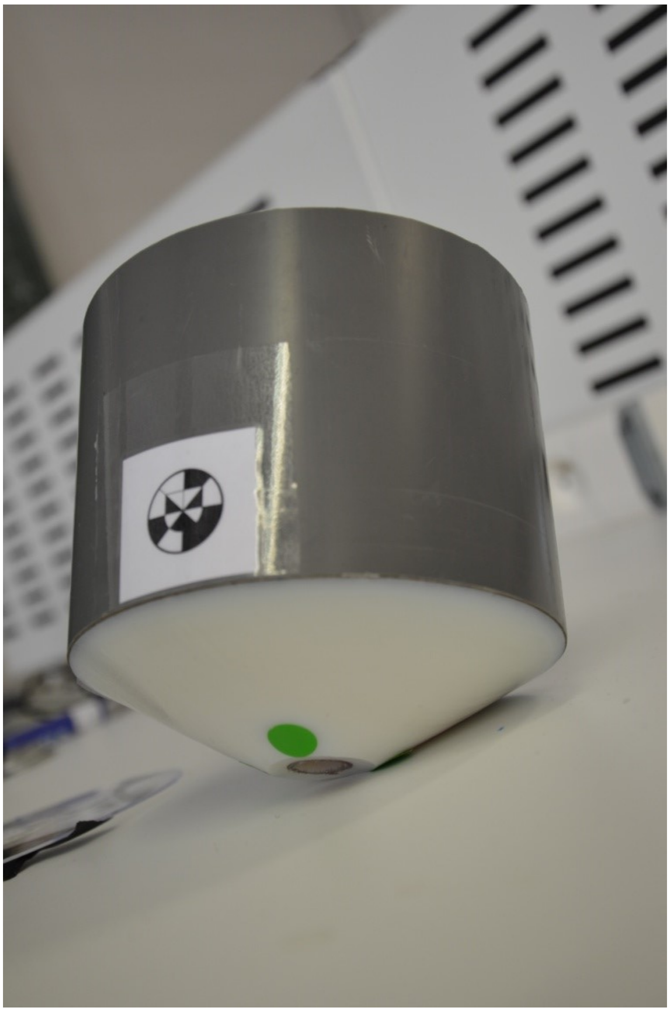

Fig. 4.11 *– Overview of the conic part.*

Fig. 4.12 *– Overview of the cylindrical part and the cover*

Fig. 4.13 *– View of the bar inside the buoy.*

In the tables below [Tab. 4.7] the heights from the keel and the weights of the parts of the buoy are represented:

First configuration		
	distance from the keel [mm]	mass [g]
conic part	22.7	189.3
bar inside	61.5	7.8
cylinder outside	76.5	177.0
weight added	35.0	264.4

Second configuration		
	distance from the keel [mm]	mass [g]
conic part	22.7	189.3
bar inside	61.5	7.8
cylinder outside	76.5	177.0
weight added	85.4	264.4

Tab. 4.7 – Heights and weights of the different parts of the buoy

4.5 Configurations

4.5.1 Degrees of freedom

The first tests have been improved in one degree of freedom configuration. The model is provided with an internal cylindrical hole; it works as a guide, driving the buoy up and down along an external fixed steel bar [Fig. 4.14].

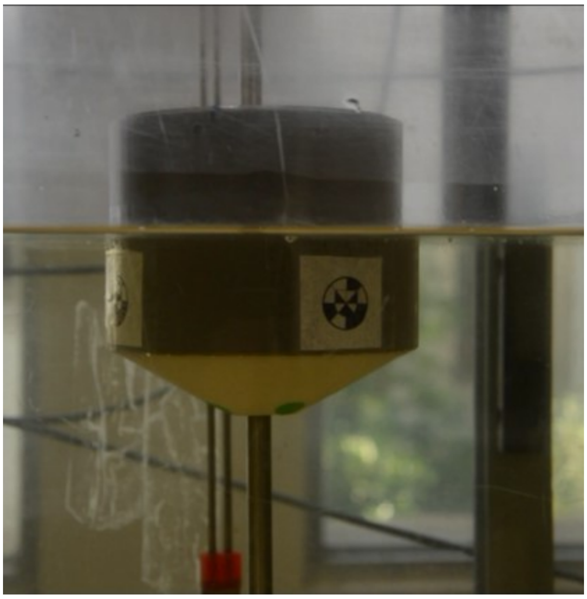

Fig. 4.14 *– One degree of freedom configuration*

Another configuration tested was the six degrees of freedom. In this case, the scaled point absorber was moored at the bottom of the flume through a single line [Fig. 4.15]. The line was connected to a load cell linked to a heavy object on the bed of the flume.

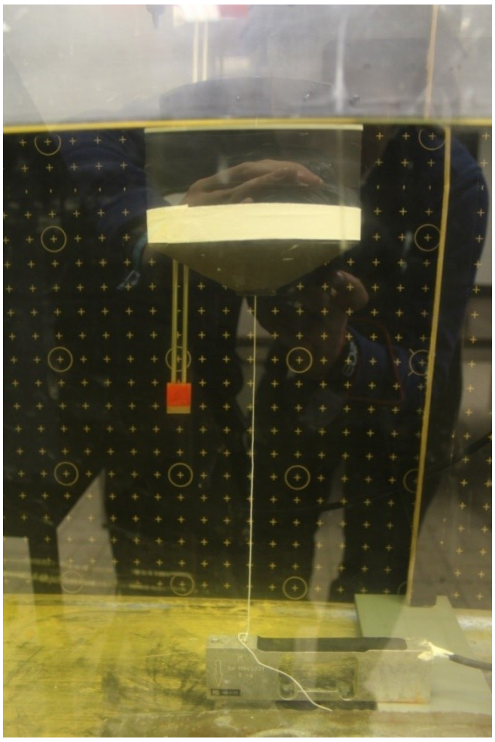

***Fig. 4.15** – Six degrees of freedom configuration*

4.5.2 Cable's stiffness

Three different cables have been used. The first line was stiff; to investigate the stiffness of the other two lines, they have been hanged and different masses have been added [Tab. 4.8] at the edge of each one [Fig. 4.16]. Due to the bigger stiffness of the black cable different masses were used.

white cable	blak cable
gramms	gramms
0	32
15.9	133.3
20.6	230.8
30.3	399

Tab. 4.8 – Weights taped at the lines for the assessment of the stiffness

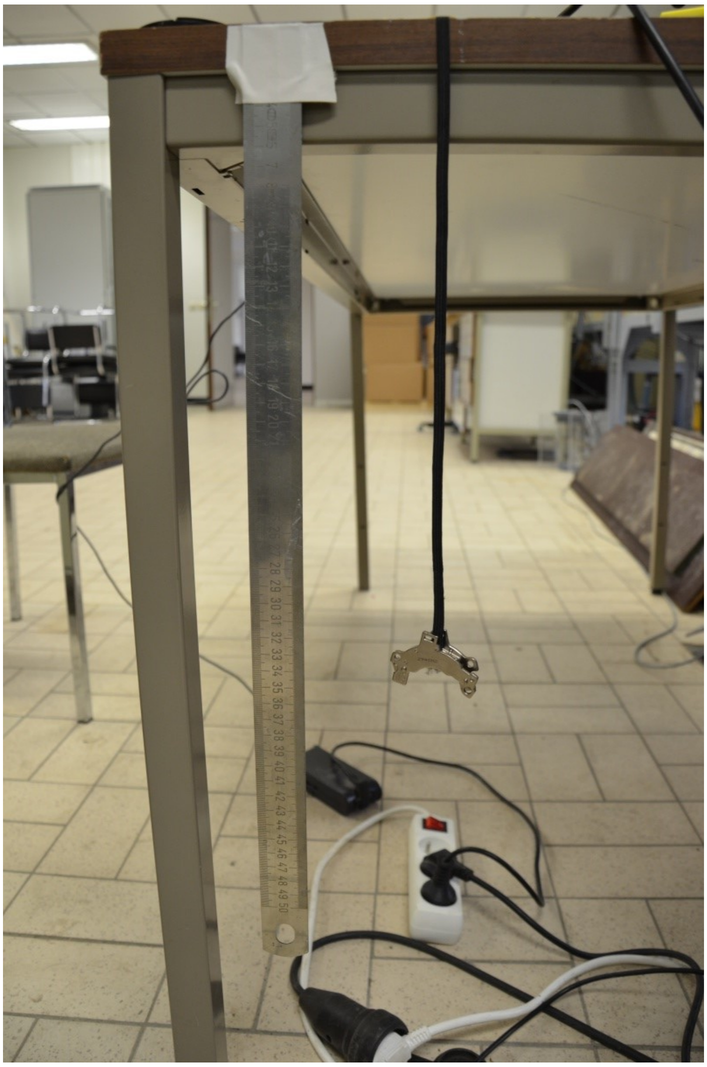

Fig. 4.16 *– Black cable during the test for the estimation of the stiffness*

Than the different lengths were measured to trace the characteristic line in a graph [Fig. 4.17]; the slope of this is the stiffness of the cable. For the white line, the stiffness is resulted 0.71 N/m; for the black cable, that is stiffer than the other, the stiffness is 0.05 N/m.

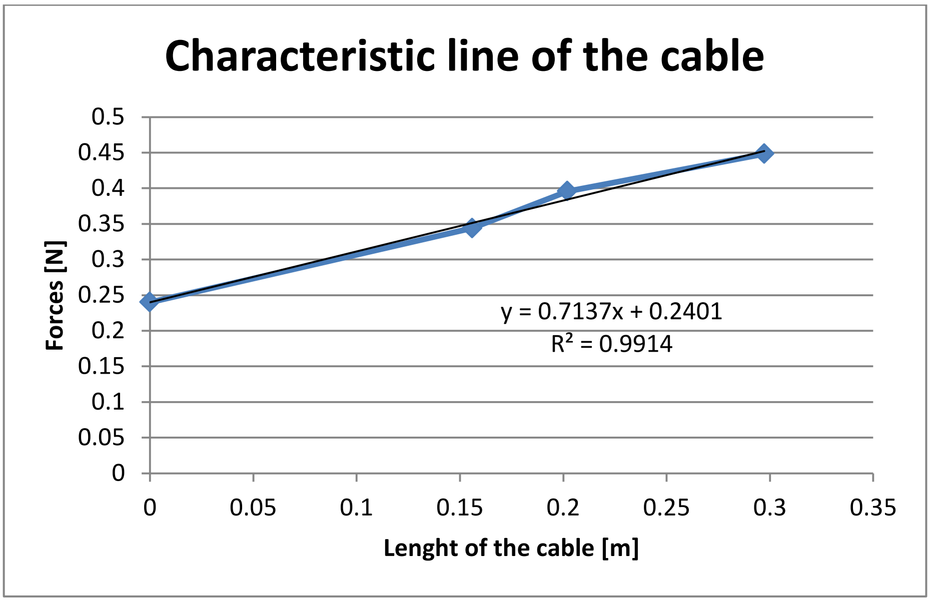

***Fig. 4.17** – Characteristic line for the white cable*

4.6 Measuring devices

In the following chapter the measuring devices that have been used are described.

4.6.1 Wave gauges

Wave Gauges (WG) are installed along the wave flume, to measure the surface elevation. The operation method is based on the measurement of resistance. The flow runs through the two parallel installed steal wired electrodes, which are installed perpendicular to the water surface. The wave gauges are installed, in a way that the electrodes are immersed while the crest and the though of a wave passes the wave gauge [Fig. 4.18]. At the lower end a spacer prevents the electrodes from touching each other. When the wire electrodes are immersed the circuit is closed and a signal is recorded. With increasing water depth the distance the electricity has to travel decreases and therefore the resistance is smaller. A calibration factor is used, which transforms the resistance to the water elevation. The calibration has been done every day before starting the test. A lower pressure is applied onto the moveable fixation of the wave gauges, which is then moving a defined distance upward. After recording the resistance the pressure gets equalise and the wave gauges move back. Knowing the distance and the resistance at the two points allows calculating the calibration factor.

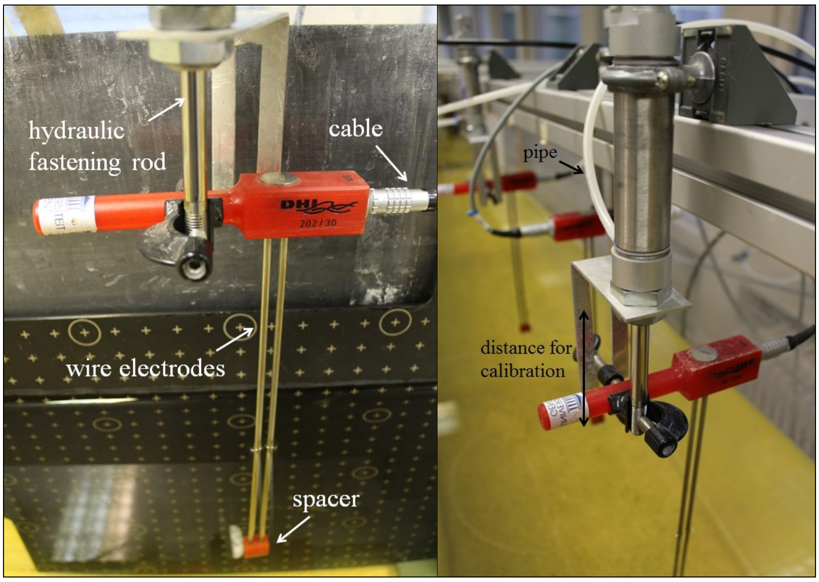

Fig. 4.18 *- Wave gauge left: wave gauge, right: fixation of the wave gauge*

The analysing gives information about the wave characteristic. Therefore it's needed to perform a reflection analyse, to calculate the incident and reflected wave hight. According to Mansard and Funke an array of minimum three wave gauges is needed (Mansard, Funke 1980). The distance between the wave gauges depend on the wave length of the analysed waves. For the model test seven wave gauges in two arrays have been installed in the flume. The positions are shown in figure 4.19 and the distances to the wave generator are given in the next table [Tab. 4.9].

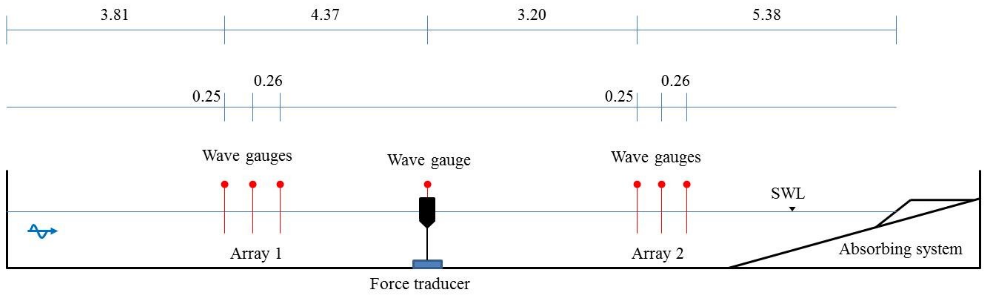

Fig. 4.19 -

Position of the wave gauges

Array	*Wave Gauge*	*Distance to wave generator [m]*
Array 1	*WG 1*	3,81
	WG 2	4,06
	WG 3	4,32
	WG 4	8,18
Array 2	*WG 5*	11,38
	WG 6	11,63
	WG 7	11,89

Tab 4.9 - Position of the Wave gauges

The first two wave gauges are also for the active wave absorption of the wave generator. Two arrays have been installed to be able to see the difference in the wave parameter before and after the buoy. Like this the change of the wave after meeting the buoy can be measured. One wave gauge was installed in the same position as the buoy. Like this the movement of the buoy can be directly compared to the wave in the same position.

4.6.2 Camera

The camera has been used for measuring the displacement of the buoy. For the tests with 1DOF a Canon 100D and for the test with 6 DOF a GoPro has been used. It was required the change the camera due to faster movements of the buoy. The movies made with the Canon have 25 frames per second. This value increased to 100 frames per second for the GoPro.

Both Cameras have been installed on a tripod next to the buoy. The position is shown in the following picture [Fig. 4.20]**Errore. L'origine riferimento non è stata**

trovata.. To avoid reflection the camera was covered with a black plane and the back of the flume was covered with black paper.

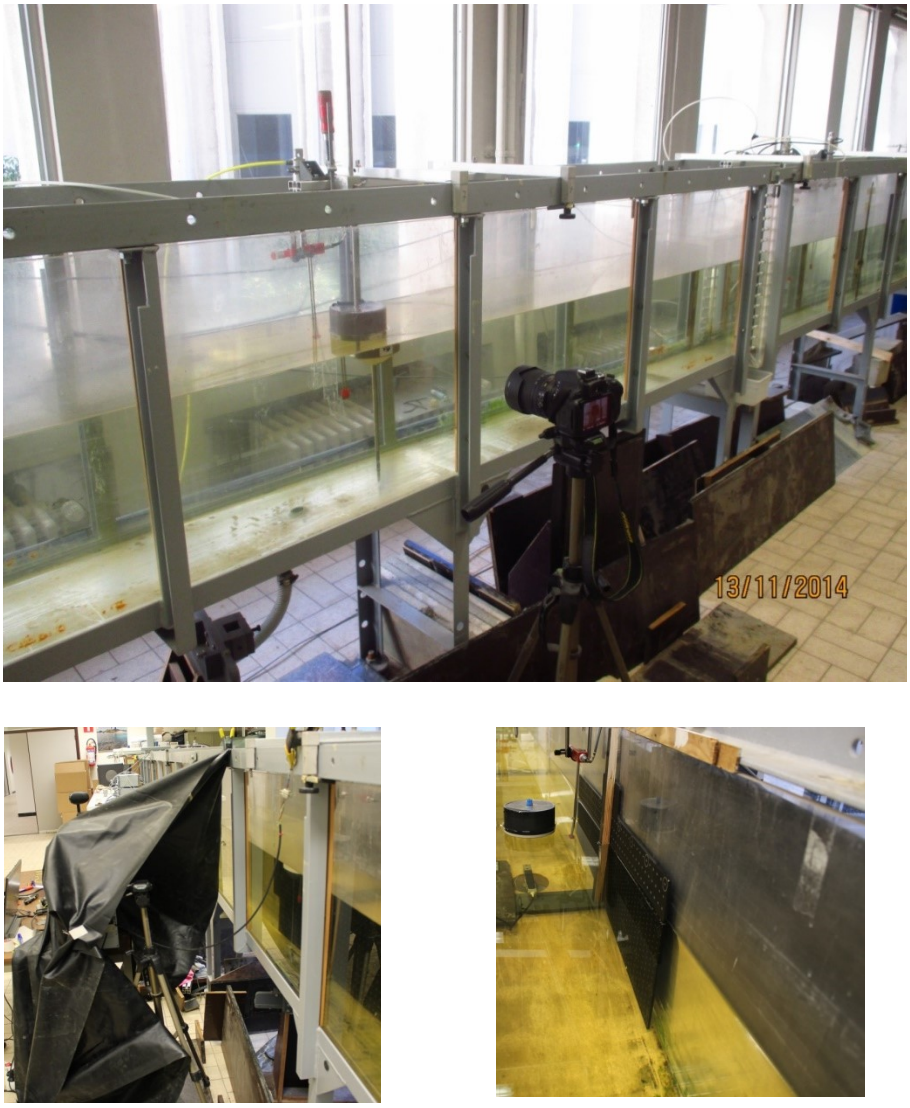

Fig. 4.20 *- Camera*

4.6.3 Linear variable differential transformer (LVDT)

- Smaller wave hights
- 1D
- Core moves causes a voltage, when going down voltage decreases going up increases

4.6.4 Force traducer

Load cell is a passive transducer or sensor which converts applied force into electrical signals. It is made by bonding strain gauges to a spring material. Spring material causes strain due to applied load and strain gage changes its resistance in accordance with the change in strain. The metallic strain gauge consists of a very fine wire. When the stress caused by applied force to an object is below the proportional limit, the strain varies linearly with the stress and the resistance value of the strain gauge varies linearly with the deformation.

During the tests, this device has been used to measure the forces in the line that moored the buoy to the bottom of the flume [Fig. 4.21 and Fig. 4.22]:

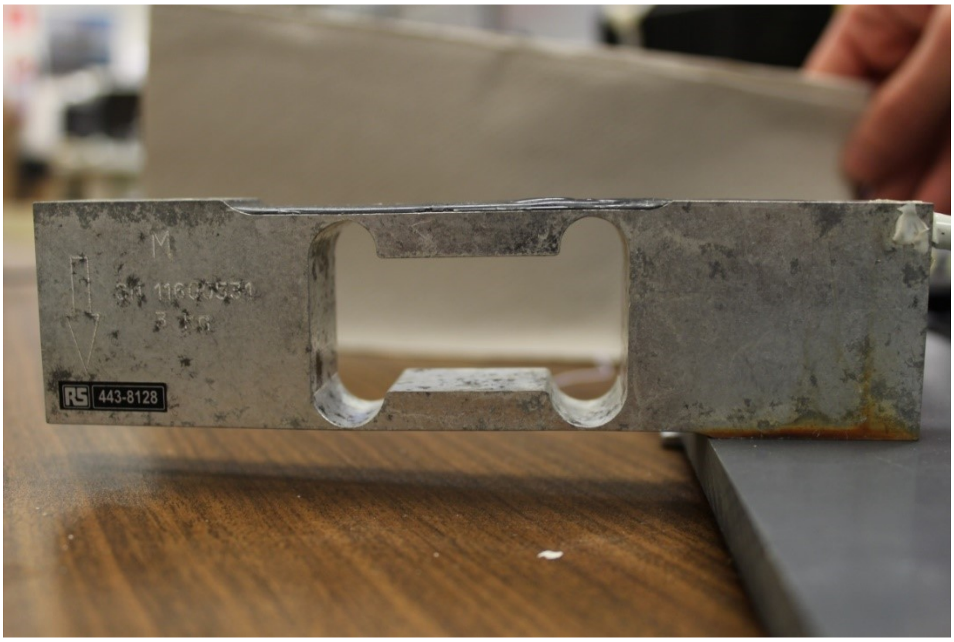

Fig. 4.21 *– The load cell used for the tests out of water*

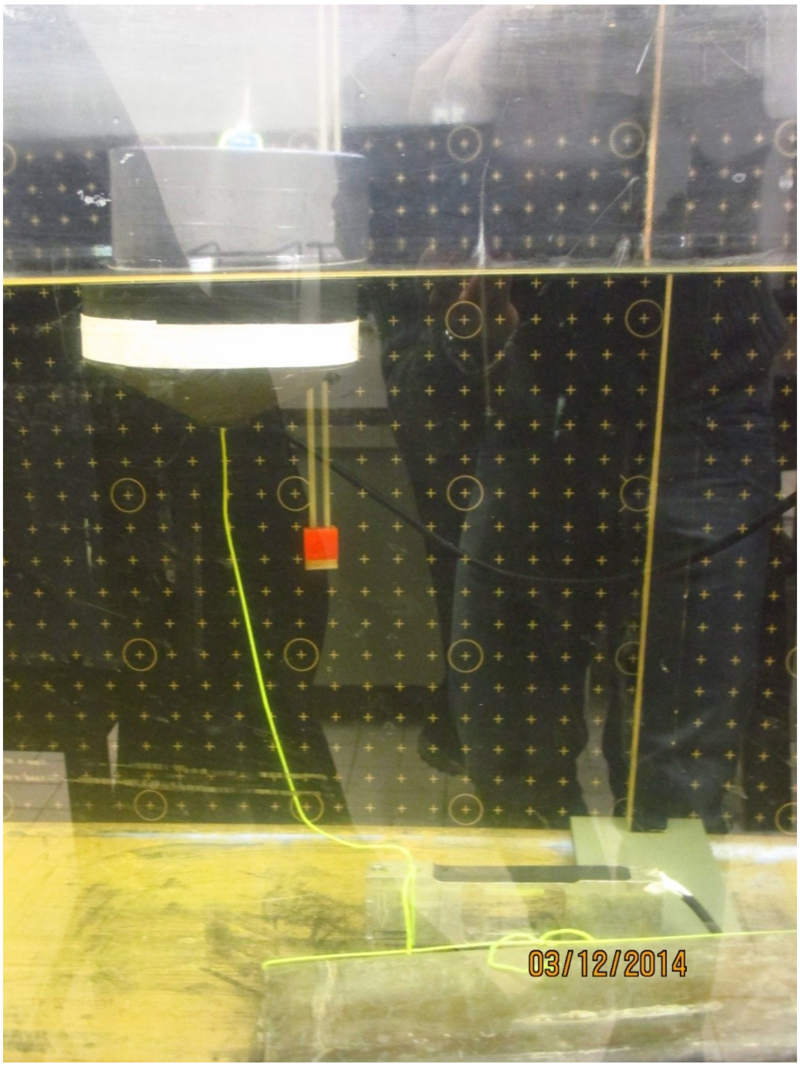

Fig. 4.22 *– In the picture it is showed how the cable is tied to the load cell*

4.7 Test program

In total 115 tests with regular waves and 4 tests with irregular waves have been performed. In table 4.10 the wave parameters and in table 4.11 the test programme with the different configurations is given. The waves included four different wave heights and three different steepness. The different wave heights are 0,113 m, 0,09 m. 0,0179 m and 0,036 m. For the highest wave an event that appears once a year has been chosen. The wave with a wave height of 0,09 m in model scale has a return period of two month. As lowest wave a wave height of 0,036 m has been chosen. Hence it’s not possible to get sufficient data for smaller waves. As medium wave between the extremes a wave height of 0,079 m has been chosen. Because of non-linearity it was not possible to generate higher waves in the wave flume. More details to this effect can be found in chapter 0. The wave steepness can be calculated as

$$s = \frac{H}{L}$$

Due to the longest possible wavelength and the breaking of waves a variability of the steepness is between 0,02 and 0,06. Starting with the steepness the period was calculated. As irregular wave a significant wave height of 0,079 m was chosen. Due to too much overtopping on the buoy it was not possible to perform tests with higher significant wave heights.

The test programme includes test with one and six degree of freedom. For each DOF the centre of gravity of the buoy was changed. For the tests with six degree of freedom three mooring lines with different stiffness have been tested. For the stiff cable the programme included test with different length of the mooring line.

N°	type	Tr [Years]	H/L [-]	Hreal [m]	L_0 [m]	Treal [s]	Hscaled [m]	Tscaled [s]
1	reg	-	0.02	1.250	62.500	6.327	0.036	1.069
2	reg	-	0.04	1.250	31.250	4.474	0.036	0.756
3	reg	-	0.06	1.250	20.833	3.653	0.036	0.617
4	reg	-	0.02	2.750	137.500	9.384	0.079	1.586
5	reg	-	0.04	2.750	68.750	6.636	0.079	1.122
6	reg	-	0.06	2.750	45.833	5.418	0.079	0.916
7	reg	0.166	0.02	3.159	157.950	10.058	0.090	1.700
8	reg	0.166	0.04	3.159	78.975	7.112	0.090	1.202
9	reg	0.166	0.06	3.159	52.650	5.807	0.090	0.982
10	reg	1	0.03	3.966	132.200	9.202	0.113	1.555
11	reg	1	0.04	3.966	99.150	7.969	0.113	1.347
12	reg	1	0.06	3.966	66.100	6.507	0.113	1.100
13	irr	-	0.04	2.750	68.750	6.636	0.079	1.122

Tab. 4.10 – The regular and the irregular waves used during the tests

DOF	COG	Wave types	Cable (lenght)	Sum of the tests	Main parameters analysed
1DOF 1DOF	High Low	reg. reg.	- -	22	Gauge next to the buoy: Hm, Tm Buoy heaving motion: Hm, Tm
1DOF 1DOF	High Low	irr. irr.	- -	2	Gauge next to the buoy: Hs, $T_{H1/3}$,Hmax,$H_{1/10,}$ spectra Buoy heaving motion: Hs, $T_{H1/3}$,Hmax,$H_{1/10}$, spectra
6DOF 6DOF	High Low	reg. reg.	free free	22	Gauge next to the buoy: Hm, Tm heaving motion: Hm, Tm pitching motion: Pm, Tm, Pmax,Pmin
6DOF	High	reg.	stiff (SWL)	6	forces: Peak values (considering/without multiple peaks)
6DOF 6DOF	High Low	reg. reg.	stiff (SWL+WH) stiff (SWL+WH)	25	forces: Peak values (considering/without multiple peaks)
6DOF 6DOF	High Low	reg. reg.	flex. (SWL) flex. (SWL)	25	Gauge next to the buoy: Hm, Tm Buoy heaving motion: Hm, Tm pitching motion: Pm, Tm, Pmax,Pmin forces: Peak values (considering/without multiple peaks)
6DOF 6DOF	High Low	irr. irr.	flex. (SWL) flex. (SWL)	2	Gauge next to the buoy: Hs, $T_{H1/3}$,Hmax,$H_{1/10,}$ spectra Buoy heaving motion: Hs, $T_{H1/3}$,Hmax,$H_{1/10}$, spectra pitching motion: Pm, Tm, Pmax,Pmin forces: Peak values (considering/without multiple peaks)
6DOF	High	reg.	medium stiffness(SWL)	3	forces: Peak values (considering/without multiple peaks)
6DOF	High/Low	reg.	medium stiffness(Various)	12	Gauge next to the buoy: Hm, Tm Buoy heaving motion: Hm, Tm pitching motion: Pm, Tm, Pmax,Pmin forces: Peak values (considering/without multiple peaks)

Tab. 4.11 – Configurations tested and the main parameters analyzed

4.8 Analysis software

4.8.1 L~Davis

As a second analysis programme L~Davis has been used. This program is mainly written and maintained by Matthias Kudella from the Coastal Research Centre in Hannover. The coastal research centre is a collaboration of the TU Braunschweig and the Leibniz University Hannover. L~Davis is mainly developed for the collecting and analysing data for the test facilities in these two universities. Is programme has the following functions (S. Liebisch 5/3/2012):

- Calibration of measuring devices

- Data logging
- Administration of projects
- Display if time series
- Analysing in time and frequency domain
- Reflexion analysing
- Event analysis
- Calculating of forces by integration of pressure measurements

4.8.2 Kinovea

As tracking programme Kinovea has been used. The program is a video analysis software, mainly used for analysing movements in sports. The Project started 2004 as a freeware and became fully open source in 2006. The organization is lead and composed by a team of volunteers. It is a non-profit organization in France. The software can be found on http://www.kinovea.org

4.8.3 Wave Lab 3

Developed at Dept. of Civil Engineering, Aalborg University in 2002, WaveLab is a software for wave data acquisition and analysis; it can provide different types of analyses. During this work, it has been used in particular for the time and frequency domain analysis of regular and irregular waves.

4.8.4 LabView

LabView is a platform software used in the laboratory. Through these a program for the design of regular and irregular waves in the flume has been developed. LabView has been improved by National Instruments company; the asset of this software is the friendly-user interface, obtained by using icons for the logical relations during the program design.

5 Analysis of Model Tests

5.1 Movement of the buoy

In this chapter the analysis of the movement of the buoy will be described.

5.1.1 Buoy with one degree of freedom

For the analysis of the heaving motion of the buoy the movies of the tests have been used. To track the buoy the software Kinovea has been used. First the tracking system gets calibrated by inserting a line with a known length. In this case the diameter of the buoy, which is 12,5cm, was used [Fig. 5.1].

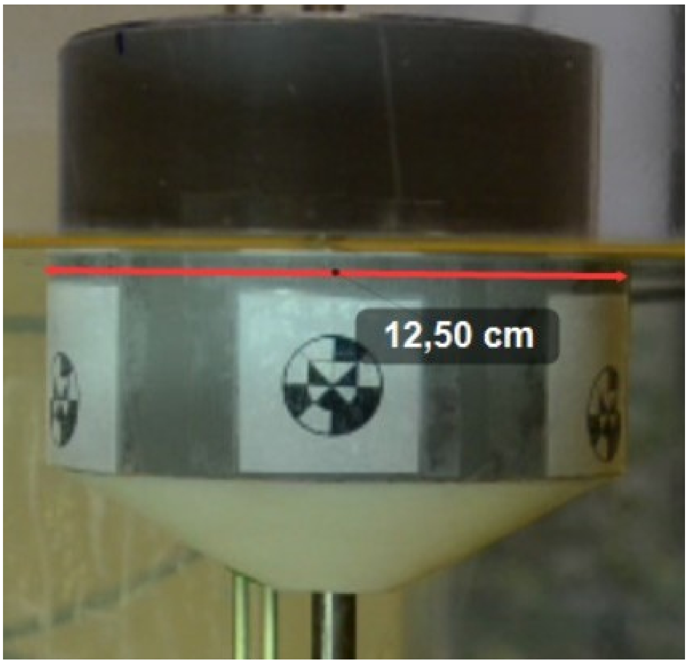

Fig. 5.1 *- Calibration of tracking system*

Afterwards the movement got tracked [Fig. 5.2]. The tracker is put on the marker. When the movie is running, the tracker follows the marker. The software shows the trajectory for the last seconds. If the tracker loses the marker on the buoy the tracker can be handily shifted to another place. This happens mainly if the marker crosses the surface. Also the marker has to be shifted in case that the buoy is rotating. The buoy is rotating and the marker moves to the right side of the movie. At some place it's not anymore filmed and another marker has to been chosen to go on with the tracking.

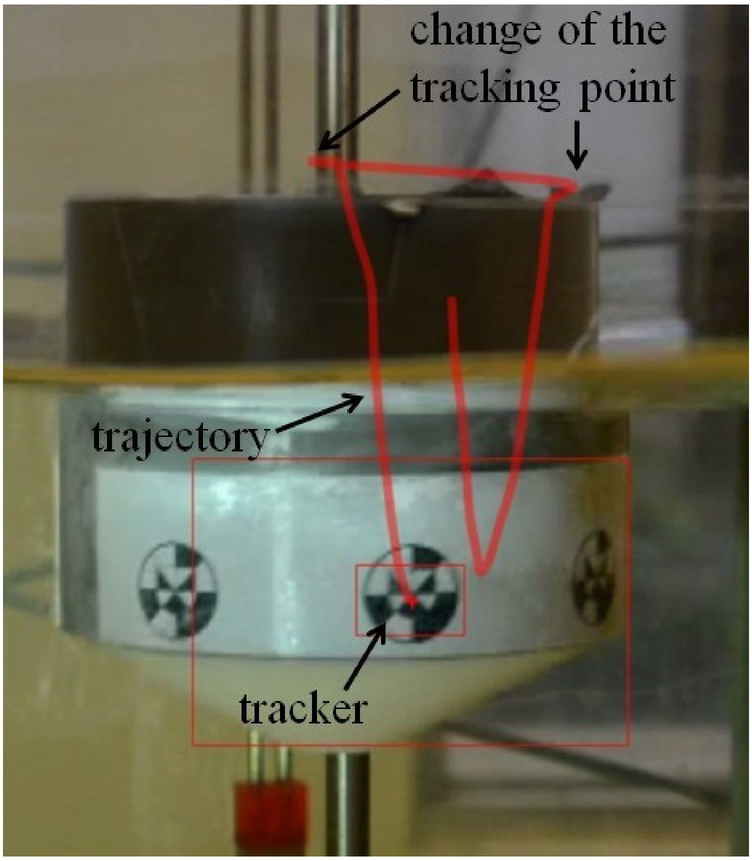

Fig. 5.2 *- Tracking the movement of the buoy*

The software exports the horizontal and vertical position of the tracker for every frame in an excel file. For the following analysis only the vertical position have been consider. For further analysis the excel file has been imported to WaveLab.

5.1.2 Buoy with six degree of freedom

The analysis of the pitching movement is similar to the heaving movement that is described in chapter 0. Again for the tracking Kinovea has been used. The first step is to define the axes. In figure 5.3 is shown that the axes are set to the bottom left corner of the frame. In this way two trackers, with the same origin of coordinate, can be used.

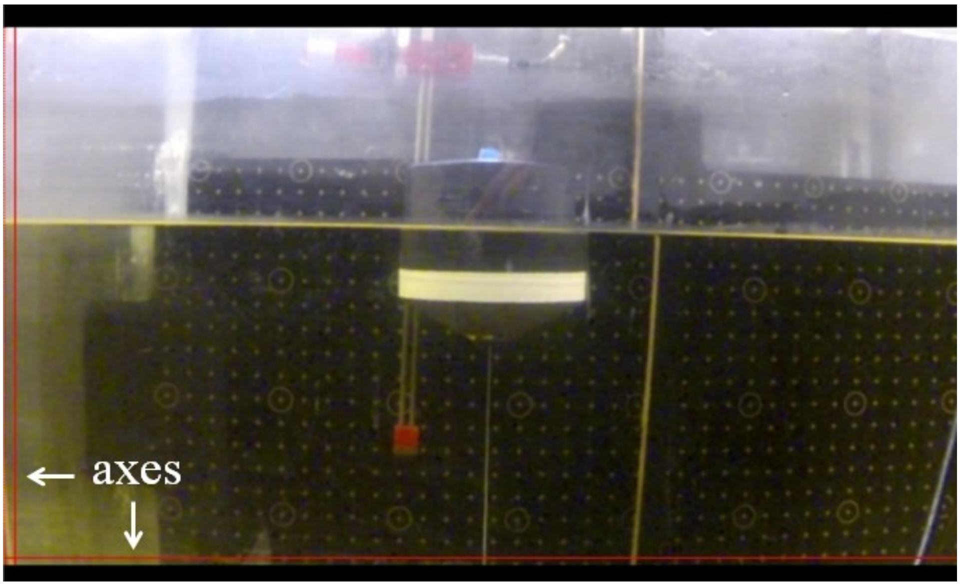

Fig. 5.3 *- Define of the axes in Kinovea*

For the test with six degree of freedom the heaving and the pitching motion has been analysed. Therefore two tracker where needed. The buoy was surrounded with a white line. The two tracking points have been the left and the right bottom corner of this line [Fig. 5.4]. The white line was chosen for having the same reference point for the whole test duration, even if the buoy is rotating.

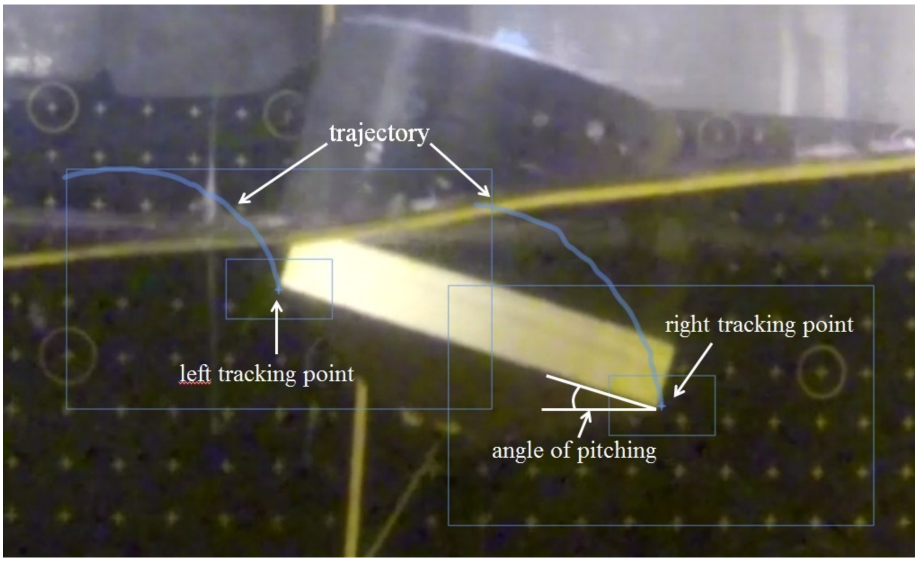

Fig. 5.4 *- Tracking the movement with six degree of freedom*

In the exported excel file the positions of the two tracking points are given. Starting with this information the heaving motion has been calculated out of the mean vertical positions of the two tracking points. The definition of the points is given in figure 5.5.

$$X_b = \frac{x_1 + x_2}{2}$$

x_b: vertical position of the buoy

x_1: vertical position of the left corner

x_2: vertical position of the right corner

The angle between the left and the right tracking point is the angle of the pitching motion [Fig. 5.6]. It can be calculated with:

$$\alpha = \tan^{-1}\left(\frac{y_2 - y_1}{x_2 - x_1}\right)$$

α: pitching angle

x_1: vertical position of the left corner

x_2: vertical position of the right corner

y_1: horizontal position of the left corner

y_2: horizontal position of the right corner

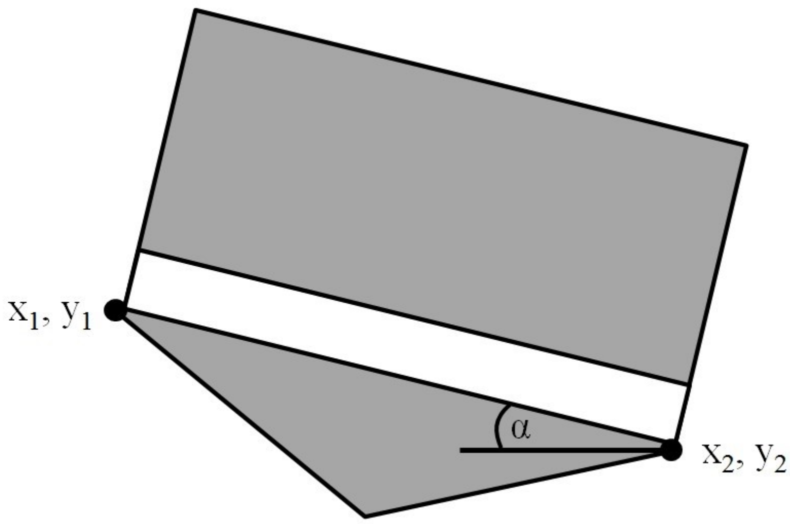

Fig. 5.5 *- Definition of tracking points*

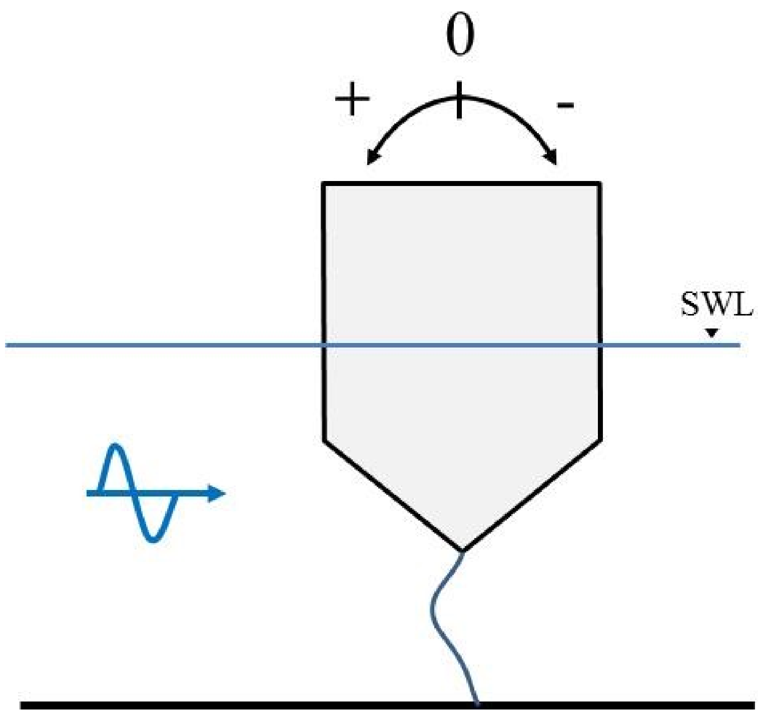

***Fig. 5.6** - Definition of the pitching angle*

The results out of the calculation were saved to a text file and afterwards imported to WaveLab.

5.2 Analysis with L~Davis

The following chapter describes the analysing done with L~Davis. For more information about the program go to chapter 0.

With this programme the analysing of the forces and the pitching has been done. For the analysing of the pitching it is interesting to get information about the minimum and maximum events. Therefore the event analysing of L~Davis has been used. After choosing a test and a timeframe the window shown in figure 5.7 appears. Within this window it was chosen to search for minimums with a distance in time a). As second information the complementary event has been selected b). Now the software searches for maximum within a defined time after the key event c). The selected events can be seen in the time series d).

The results are saved in a text and an Excel file. The file includes general information about the test, statistical values about the time series (mean, maximum, minimum, 10% highest) as well as information about the time and the height of the complementary events. Starting with this data some more characteristic values have been calculated. These are shown in figure 5.8. The mean pitching amplitude was calculated by:

$$\zeta_{mean} = y_{mean,\max} - y_{mean,\min}$$

For the mean period of the pitching motion the time distance of two events has been calculated with:

$$\Delta t = t_2 - t_1$$

For this calculation all located minimum and maximum events have been used and a mean value of the results has been calculated.

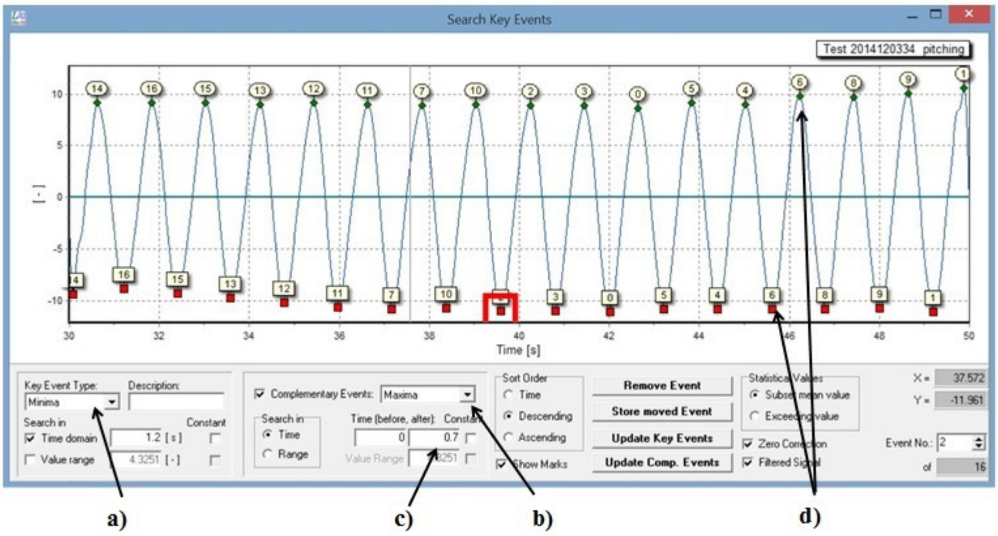

***Fig. 5.7** - Event Analysis with L~Davis; Time series*

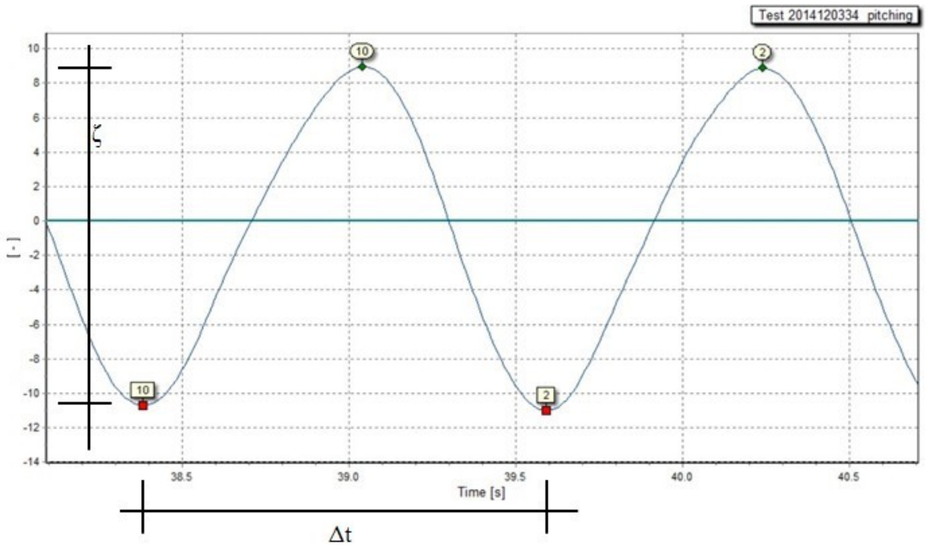

***Fig. 5.8** - Calculated values of the pitching motion*

The same analysing steeps have been used to get the statistical values of the pressure.

5.3 Analysis with WaveLab

The software allows the analysis of the wave parameters. The first step is the definition of the time window to be studied through the component "show signal". The output is the time series [Fig. 5.9]:

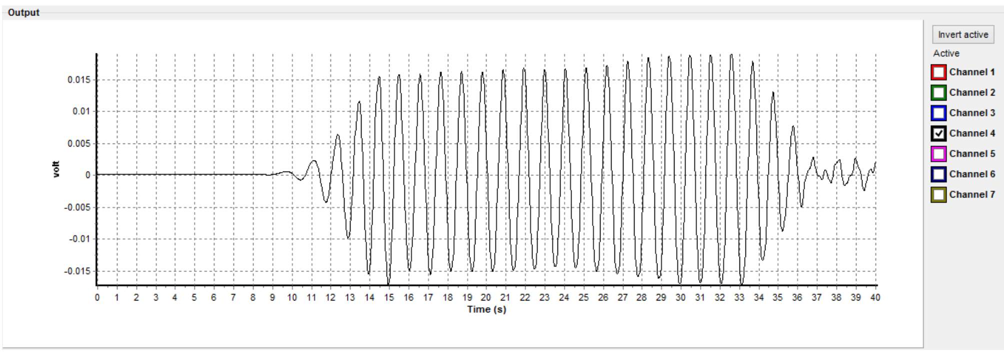

***Fig. 5.9** – The time series; on the right are visible the seven channels that represent the gauges inside the flume.*

The correct start and final points are chosen manually. For the regular waves, this is needed to avoiding analyzing the waves where the signal is not steady. In the next picture the time window for a regular wave is shown [Fig. 5.10]:

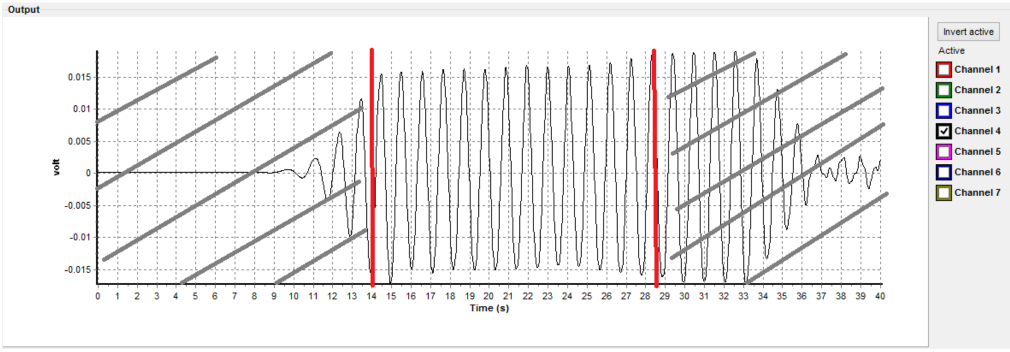

***Fig. 5.10** – Between the two red vertical lines, the time window suitable for the analysis*

For the irregular waves it is almost the same, only the first part and the end of the signal are excluded.

After that, the analysis is performed through the command “Time series analysis”. On the left part of the panel the inputs are the channel to analyze, the water depth, the type of the waves, regulars or irregulars, the scale factor and the point to skip at the start and at the end, or rather the defined time window multiplied by the simple frequency of the channel.

As illustrated in the picture below [Fig. 5.11], the outputs are the mean period, the mean wave height and the variance spectrum, that is a line for regular waves.

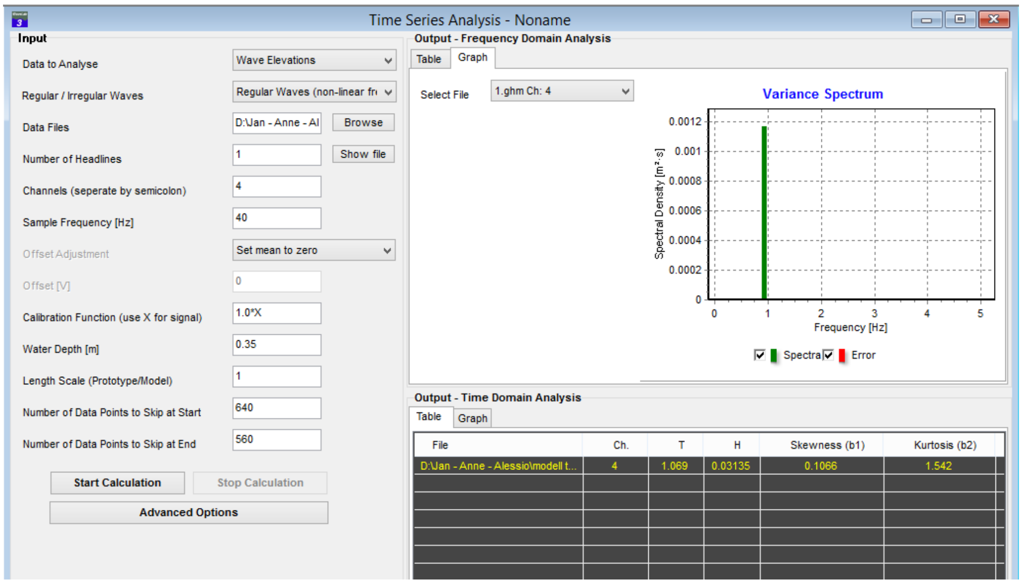

***Fig. 5.11** – Panel of the time series analysis for regular waves.*

For the "Irregular waves" the inputs for the analysis are the same but the output parameters are different: for example the significant wave height, the significant period, the $H_{1/10}$, the variance spectrum etc. [Fig. 5.12]:

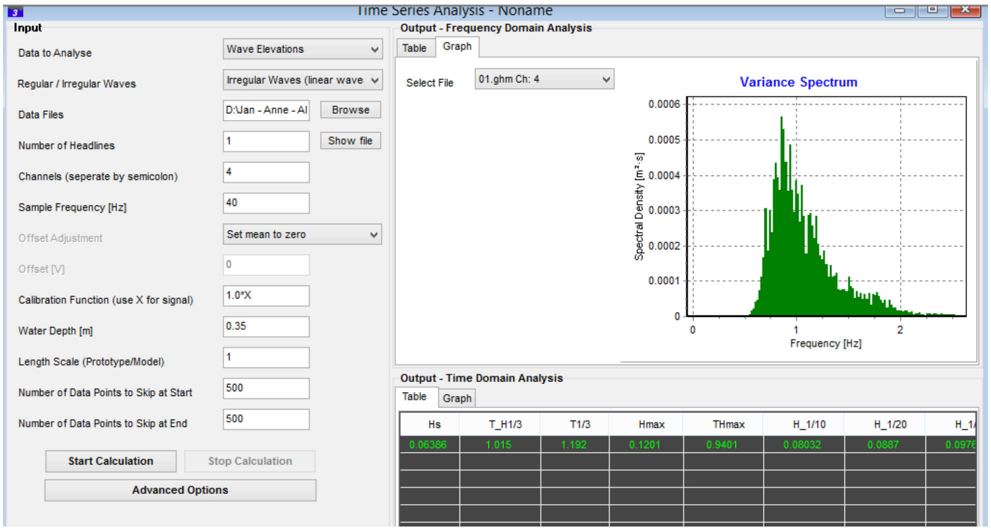

Fig. 5.12 *– Time series analysis panel for the irregular waves*

Other useful components for the assessment of the parameters are the command "compare signal" [Fig. 5.13], that permits the comparison between two signals, and "reflection analysis" [Fig. 5.14]; using a number equal or more than three gauges, to calculate the amplitude reflection coefficient.

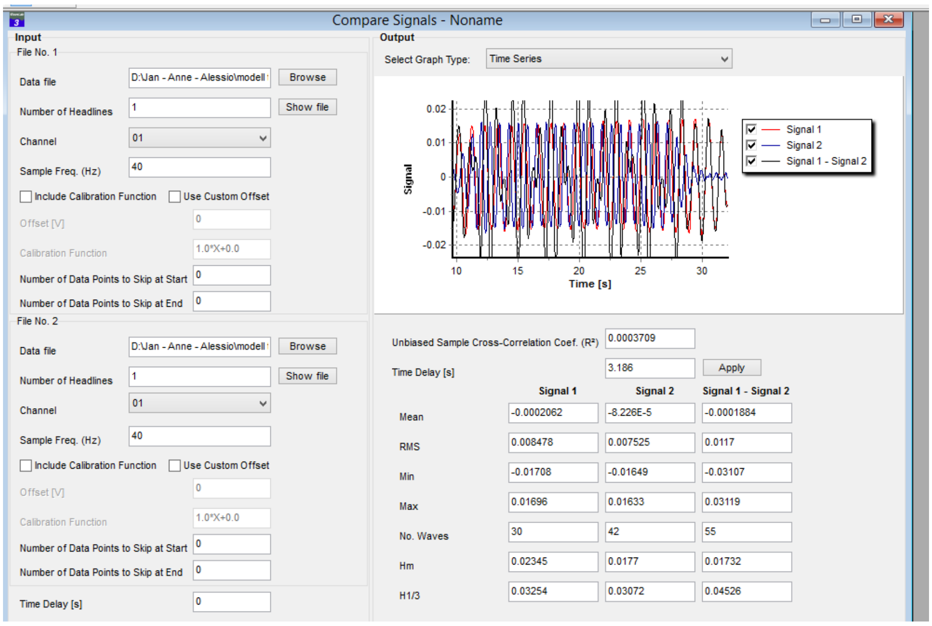

Fig. 5.13 *– Panel "compare signals"*

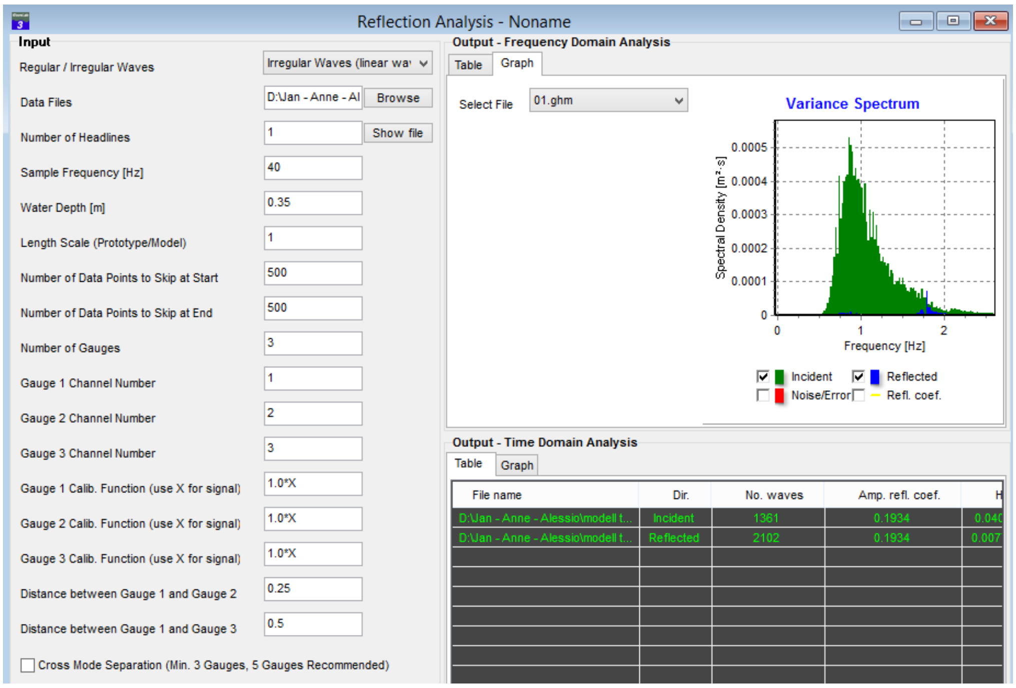

Fig. 5.14 *– View of the component "Reflection analysis"*

5.4 Natural frequency of the buoy

One of the fundamental steps was the reckoning the hydrodynamic parameters of the buoy, in particular:

- the spring constant (c)
- the hydrodynamic damping coefficient (b)
- the damping factor (ζ_d)
- the damped natural frequency (ω_p)
- the natural frequency (ω_n)

The buoy was released at a certain offset height, using the steel bar for the configuration with one degree of freedom, which causes a damped oscillation; this oscillation is damped by the hydrodynamic damping. However it is hard to perform this test in a good way without external influences; for this reason the test was repeated several times and the final results are the average of each test, called "decay test".

5.4.1 Parameters description

Regarding the buoy as a mass-spring-damper the system can be described as:

$$m\frac{d^2z}{dt^2} + b_d\frac{dz}{dt} + kz = f(t)$$

With:

- spring constant : $k = \rho * g * A_w = \rho * g * \frac{\pi D^2}{4}$
- external force: f(t). Which is not existing for the performed tests , so f(t) = 0
- damping constant: b

A general solution of the mass-spring-damper equation is:

$$q_{int} = a * e^{-\zeta_d \omega_n t}\sin(\omega_p t + \varphi)$$

With the damping factor:

$$\zeta_\mathrm{d} = \frac{\mathrm{b_d}}{2\sqrt{km}}$$

5.4.2 Calculation overview

The damping factor is derived from the extreme values of the time series ; than the hydraulic damping is calculated from the average period and damped natural frequency. The period is calculated using the extreme values.

In this case the damped natural frequency equals the measured frequency. It can be calculated from the period:

$$\omega_p = \frac{2\pi}{T}$$

Fitting the extreme values, we can derive ζ_d from the graph, as showed in the following examples [Fig. 5.16]:

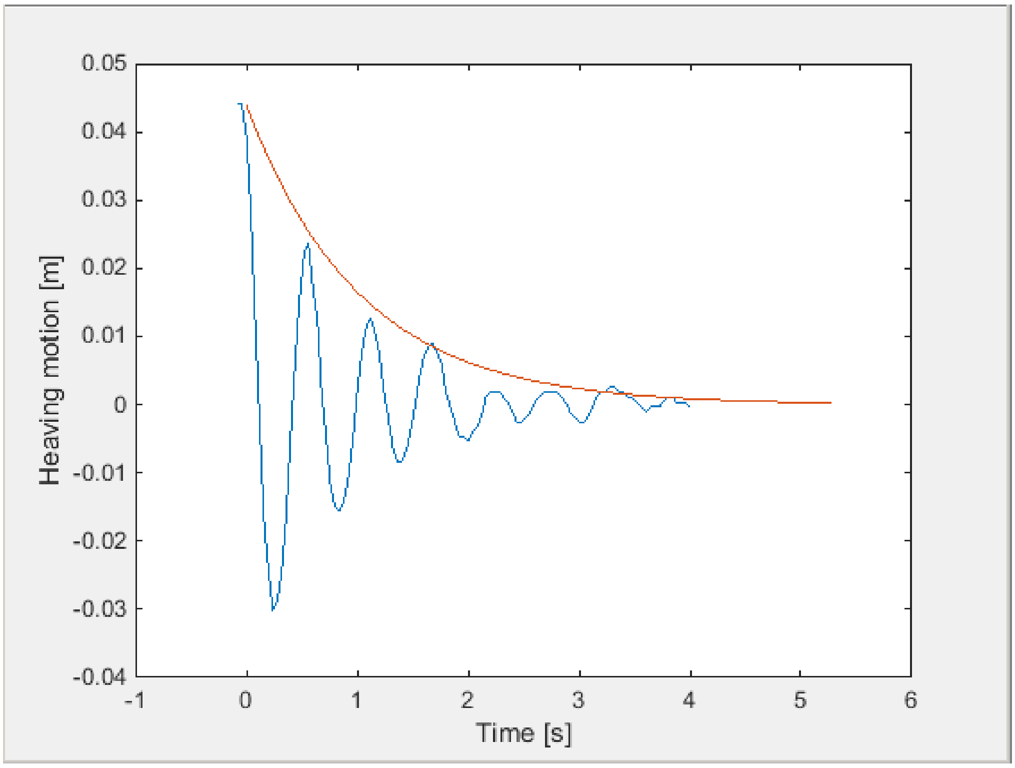

Fig. 5.16 *– With the blue line the time series and in red the exponential fit*

The natural frequency can be derived from the damped frequency and the damping factor:

$$\omega_d = \sqrt{1 - \zeta_d^2}\ \omega_n$$

The added mass represents the mass of the water that moves together with the buoy as if it is part of the buoy. This mass works as an inertia force of the buoy.

Based on the formula of the natural frequency, the added mass (m_{add}) can be derived.

$$\omega_n = \sqrt{\frac{c}{m_{buoy} + m_{add}}}$$

The hydraulic damping can be calculated with:

$$\zeta_d = \frac{b_d}{2\sqrt{c * m_{tot}}}$$

5.4.3 Results

A Matlab script (see Appendix B) has allowed the calculation for the tests done for both positions of the weight. The values are represented in the next table [Tab. 5.1 and Tab. 5.2]:

	Test with weight in high position										
	1	2	3	4	5	6	7	8	9	10	Ave.
c [N/m]	120.38	120.38	120.38	120.38	120.38	120.38	120.38	120.38	120.38	120.38	120.38
ζ [-]	0.053	0.069	0.068	0.078	0.065	0.058	0.060	0.069	0.064	0.054	0.064
ωn [rad/s]	12.870	11.247	9.600	12.533	11.244	10.151	7.584	9.485	11.243	10.424	10.638
Tn [s]	0.488	0.559	0.654	0.501	0.559	0.619	0.829	0.662	0.559	0.603	0.603
fn [Hz]	2.048	1.790	1.528	1.995	1.789	1.616	1.207	1.510	1.789	1.659	1.693

Tab. 5.1 – Hydrodynamic parameters for the weight in high position

	Test with weight in low position										
	1	2	3	4	5	6	7	8	9	10	Ave.
c [N/m]	120.38	120.38	120.38	120.38	120.38	120.38	120.38	120.38	120.38	120.38	120.38
ζ [-]	0.061	0.083	0.061	0.048	0.043	0.042	0.066	0.044	0.063	0.049	0.056
ωn [rad/s]	13.886	11.533	14.052	13.105	14.293	14.037	7.871	13.422	9.636	13.480	12.532
Tn [s]	0.452	0.545	0.447	0.479	0.440	0.448	0.798	0.468	0.652	0.466	0.520
fn [Hz]	2.210	1.836	2.236	2.086	2.275	2.234	1.253	2.136	1.534	2.145	1.994

Tab. 5.2 – Hydrodynamic parameters for the weight in high position

The results remain constant over the different tests; the main differences are for different positions of the weight. It can be explained with the influence of the bar inside the buoy and the handmade tests.

5.4.4 Pitching motions

For what concern the pitching motion, it has been tried to reproduce the free oscillation in a manual way. In addition, another matlab script (reported in appendix C) was written due to the different formula that drive the natural frequency for the pitching motion. However, the results were not correct and this was probably caused by the difficulty to reproduce the lateral gyration manually.

At last, the results have been adopted by the numerical model Nemoh [Fig. 5.17]:

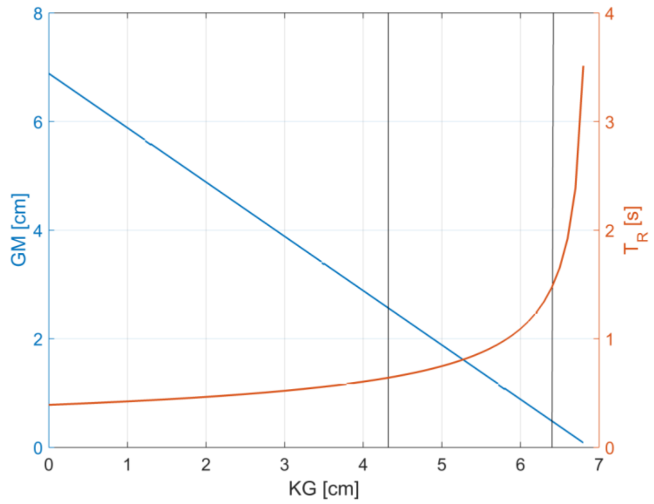

Fig. 5.17 *– In the graph it is represented the relations between the GM (blue line), the pitching natural frequency (red line) and KG on the horizontal axis. The two vertical black lines are the two positions studied.*

5.5 Reflection analysis

The reflection analysis has been carried out with WaveLab. This software is able to perform a reflection analysis for regular and irregular waves in time and frequency domain. It is possible to use different modes. For this test three wave gauges have been used. Therefore the reflection analysis is based on the theory of Mansard and Funke (Mansard, Funke 1980).

5.5.1 Reflection Analysis with Mansard and Funke

The main assumptions of the theory from Mansard and Funke are (Mansard, Funke 1980):

- Irregular waves can be described as a linear superposition of discrete components with their own frequency, amplitude and phase

$$\eta = a_i \cdot \cos(kx - \omega t) + a_r \cdot \cos(-kx - \omega t + \beta)$$

With

a_i: amplitude of incident wave

a_r: amplitude of reflected wave

β: phase angle describing the phase of the reflected waves by accounting for the phase difference between the incident and reflected wave trains at x=0 or t=0 k: wave number

ω: wave angular frequency

- Individual phase velocity can be described by the dispersion relationship

$$\omega^2 = gk \cdot \tanh(kh)$$

h: water depth

g: gravitation constant

The incident wave height H and the reflection coefficient K in terms of a (Isaacson 1991):

$$H = 2a_i$$

$$K = \frac{a_r}{a_i}$$

Performing tests ω and k are known from a measurement of the wave period. So H, K and β have to be determined.

The location of the wave gauges can be written as:

$$x_n = x_1 + \lambda_n$$

With:

x_n: position of wave gauge n

x_1: position of first wave gauge

λ: distance between first and nth wave gauge

or in dimensionless form:

$$kx_n = kx_1 + \Delta_n$$

With:

Δ_n : dimensionless distance between the nth and the first wave gauge that can be described with:

$$\Delta_n = k\lambda_n$$

In this way the equation can be applied at each wave gauge location:

$$\eta_n = a_i \cdot \cos\left(kx_1 + \Delta_n - \omega t\right) + a_r \cdot \cos\left(kx_n + \Delta_n + \omega t - \beta\right)$$

Expressed in terms of an amplitude and phase:

$$\eta_n = A_n^{'} \cdot \cos\left(\omega t - \Phi_n^{'}\right)$$

Than Equation can be used to show that:

$$A_n^{'2} = a_i^2 + a_r^2 + 2a_i a_r \cos\left(2x_n - \beta\right)$$

$$\sin\left(\Phi_n^{'}\right) = \frac{a_i \cdot \sin\left(kx_n\right) - a_r \cdot \sin\left(kx_n - \beta\right)}{A_n^{'}}$$

$$\cos\left(\Phi_n^{'}\right) = \frac{a_i \cdot \cos\left(kx_n\right) - a_r \cdot \cos\left(kx_n - \beta\right)}{A_n^{'}}$$

The measurements at the position of the wave gauges will provide corresponding amplitudes and relative phases. Therefor the surface elevation at the wave gauges can be written as:

$$\eta_n^{(m)} = A_n \cos\left(\omega t - \Phi_1 - \delta_n\right)$$

A_n: measured amplitude

Φ_1: phase angle analogous to $\Phi^{'}_n$

δ_n:measured phase of the nth wave record relative to that of the first record so that:

$$\delta_n = \Phi_n - \Phi_1$$

Now there are different methods to solve these equations. For the performed model tests the least squares methods described by Mansard and Funke has been used. Therefor three wave gauges are needed so that the measured quantities are A_1, A_2, A_3, δ_2 and δ_3.To estimate the quantities H, K and β the equations were rewrite in terms of complex amplitudes as:

$$\eta_n = \left(b_i \cdot e^{i\Delta_n} + b_r \cdot e^{-i\Delta_n}\right)e^{-i\omega t} \quad (n = 1,2,3)$$

$$\eta_n^{(m)} = B_n \cdot e^{-i\omega t}$$

where

$$b_i = a_i e^{ikx_1}$$

$$b_r = a_r e^{-i(kx_1 - \beta)}$$

$$B_n = A_n e^{-i(\Phi_1 - \delta_n)}$$

Starting with the equation and the sum of the squares of the errors between the complex amplitude of the assumed and the measured may be written as:

$$E^2 = \sum_{n=1}^{3}\left[b_i \cdot e^{i\Delta_n} + b_r \cdot e^{-i\Delta_n} - B_n\right]^2$$

This Equation can be minimized with respect to the complex unknowns b_i and b_r by setting $\partial\left(E^2\right)/\partial b_i$ and $\partial\left(E^2\right)/\partial b_r$ in turn to zero. This gives rise to two complex equations for b_i and b_r

$$\sum_{n=1}^{3} e^{i\Delta_n}\left[b_i \cdot e^{i\Delta_n} + b_r \cdot e^{-i\Delta_n} - B_n\right] = 0$$

$$\sum_{n=1}^{3} e^{-i\Delta_n}\left[b_i \cdot e^{i\Delta_n} + b_r \cdot e^{-i\Delta_n} - B_n\right] = 0$$

The solution of these two equations provide b_i and b_r in terms of B_n and a_i, a_r and β in terms of A_n.

$$a_i = |X_i|$$

$$a_r = |X_r|$$

$$\mathrm{X} = Arg(\mathrm{X}_i) - Arg(\mathrm{X}_r)$$

Where

$$\mathrm{X}_i = \frac{s_2 s_3 - 3s_3}{s_5}$$

$$X_i = \frac{s_1 s_4 - 3s_3}{s_5}$$

and

$$s_1 = \sum_{n=1}^{3} e^{i2\Delta_n}$$

$$s_2 = \sum_{n=1}^{3} e^{-i2\Delta_n}$$

$$s_3 = \sum_{n=1}^{3} A_n \cdot e^{i(\delta_n + \Delta_n)}$$

$$s_4 = \sum_{n=1}^{3} A_n \cdot e^{i(\delta_n - \Delta_n)}$$

$$s_5 = s_1 s_2 - 9$$

Now H and K are determined and using a_i, and a_r. β can be determined by using:

$$\beta = 2kx_1 - X \pm 2\pi m$$

Where m is an integer, usually chosen such that $0 \le \beta < 2\pi$.

5.5.2 Determination of wave parameters

The reflection analyse was done with WaveLab. As first step the time window needs to be defined. It is important to take care that there actually is reflection during the time window. The waves have to move along the wave flume, reflect at the end and travel back until the array [Fig. 5.18].

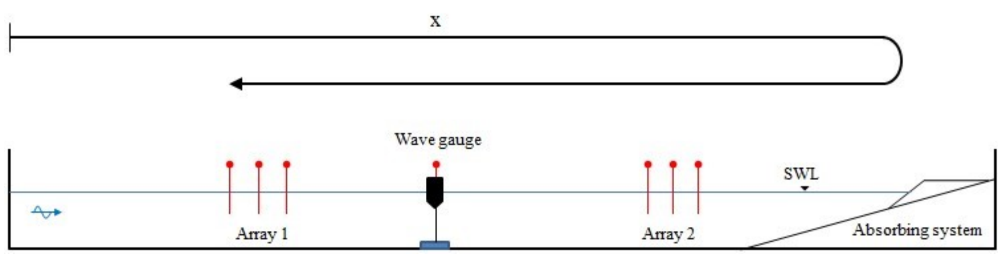

Fig. 5.18 *- Time window for reflection analysis*

He needed time delay can be calculated with:

$$\Delta t = c \cdot x$$

c: wave phase velocity

x: distance that the waves travel

For this experiments is x equal to 30 m.

For calculating the time delay the speed of the waves needs to be calculated. It is defined by:

$$c = \frac{L}{T}$$

The wave length can be calculated by using the dispersion equation:

$$\omega^2 = gh \cdot \tanh(kh)$$

With:

$\omega = \frac{2\pi}{T}$: wave angular frequency

$k = \frac{2\pi}{L}$: wave number

h: water depth

The calculation was done using WaveLab. In figure 5.19 is shown how the window for the reflection analysing looks like. The Number of Data Points to skip at Start can be calculated with:

$$N_{Data\ points} = t_1 \cdot f$$

with:

$N_{\text{Data points}}$: Number of data points to skip at the start

t_1: starting time of the time window

f: Sample Frequency

The Number of data points to skip at end can be calculated with:

$$N_{Data\ points} = \left(t_{tot} - t_2\right) \cdot f$$

t_{tot}: Test duration

t_2: Ending time of the time window

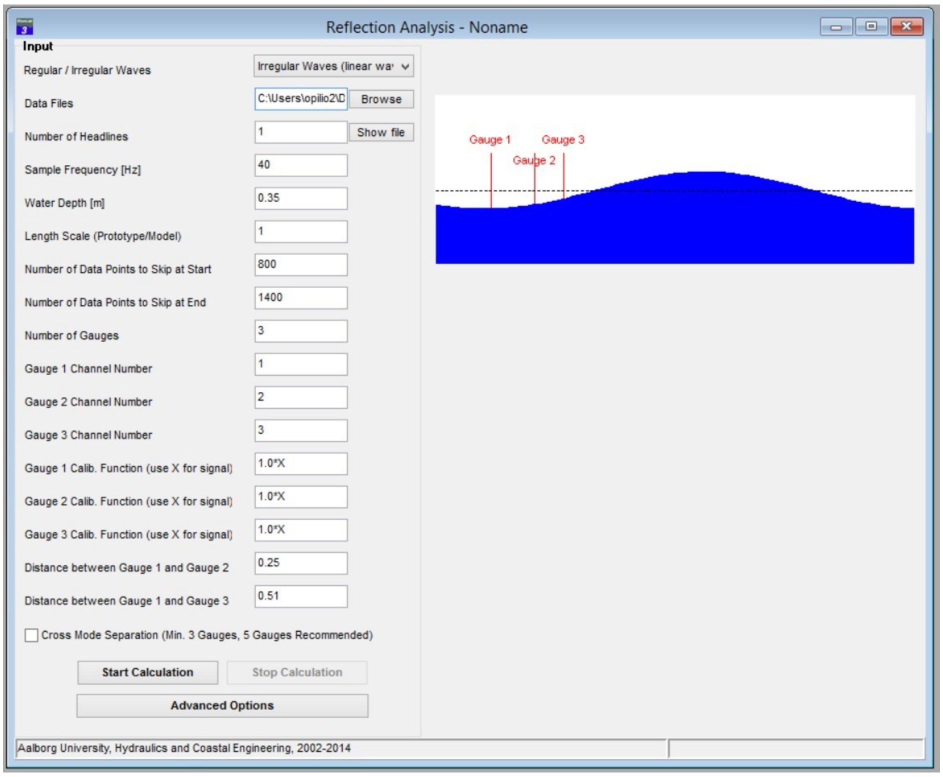

***Fig. 5.19** - Reflection analysis with WaveLab*

The result is a table with the wave characteristics from the incident and reflected waves as well as the reflection coefficient.

6 Lessons learned

Doing Experiments is sometimes a try and error. In this chapter the errors will be described. First the lessons for the model, afterwards the lessons for the wave flume and the Modell tests are considered. In the end the lessons learned from the analysis will be described.

6.1 Experience gained with the line

Regarding the length of the cable it is very important to annotate that the results are depending by its length. It was proved that big changes can be caused by very negligible variations of the length or on other factors which weren't considered; for example, the same test repeated with the same line increased by two millimeters generates as result a decreasing of the forces on the line around the 50%.

For this reason it was necessary changing the position of the center of gravity before the length of the cable, in order to have comparable results.

Particular attention is also necessary for the setting of the total length; a cable too short causes the movement of the buoy also into the lateral walls. This phenomenon should be avoided to have a fine tracking. On the other hand, a long line means a big shifting of the buoy to the edge of the "camera window", becoming impossible the tracking of the device.

6.2 PTO

The PTO system is important for the behavior of the buoy. In the previous tests for the FlanSea buoy, it was simulated rolling the cable moored to the flume bad around a winch connected with a gearbox and a motor. For these tests it was not possible to build a system like this due to the small model scale.

The investigation of the minimum scale that allows the recreation of a PTO system inside the model should be taken into account for the next laboratory experiments.

6.3 Singular waves generating

In order to have a wave comparable with in the numerical model, a lot of time was spent generating singular waves; it has required a matlab script developed considering the displaced volume under a wave crest in the wave period.

The issues found are related to some waves after the transit of the crest; the noise is due to the interaction between the paddle and the water. Despite this, for the numerical model comparison only the first crest was necessary; so it is not needed to improve this aspect.

6.4 Tracking of the buoy

For Tracking the buoy different ways have been tried. For the test with on Degree of Freedom only the heaving movement had to be tracked. In figure [Fig. 6.1] the first development is shown. The Dots on the Buoy are clearer if they are submerged. The dots are as low as possible to avoid that they surface while the heaving motion of the buoy.

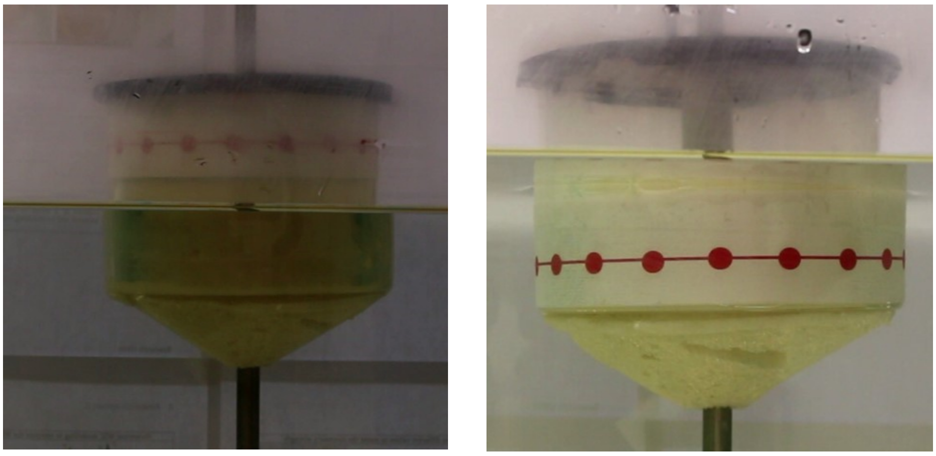

Fig. 6.1 *- Buoy with one DOF*

For the 6 DOF the pitching motion has to be tracked. The movement of the buoy is more complex than with only one Degree. The movements of the different degrees are interference with each other, which results in a faster movement. The frames of the camera are often blurred. First a method which was already implemented in Wavelab was used. The program tracks the pitching out of a special kind of dot [Fig. 6.2]. The result was very inexact because of the fast movement of the buoy and the rotating of the buoy. The frames are blurred and the software is not able to track it. Because of the rotating different dots had to be used. For tracking the pitching the dots had to stay in the same place. Otherwise there will be different results if the dot is rotating to one side of the movie. To avoid this, the buoy got marked with a line. A second focus was on the contrast of the line and the buoy. By testing different colours the best results have been made with a black buoy and a white line. Like this it is possible to track the buoy like on the tests for one DOF. To get better results the contrast between the tracked point and the surrounding had to be increased. The best contrast is with a completely black buoy with a white stripe. To prevent blurred pictures a camera with more frames per second was chosen.

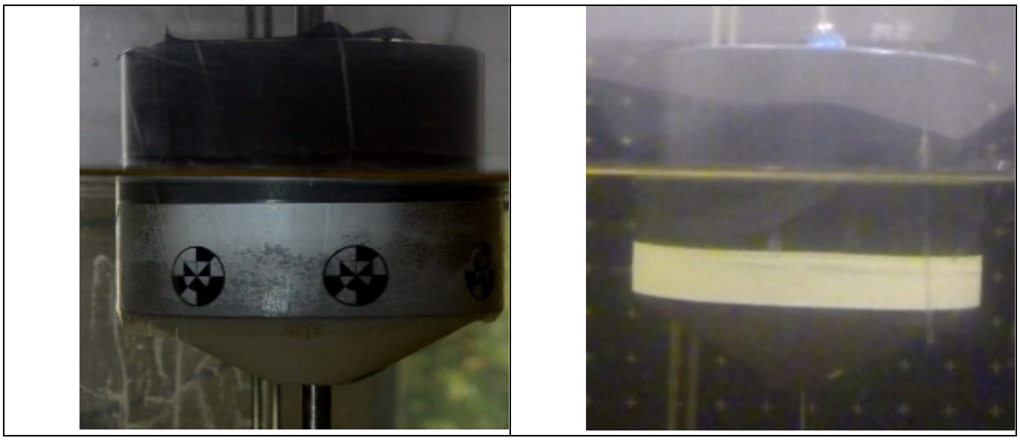

Fig. 6.2 *- Buoy for 1 DOF on the left and 6 DOF on the right side*

6.5 Tracking Software

- Kinovea
- Tracker
- Matlab
- Blender

6.6 Length of the line

- Tested different length
- Pushed under water
- Caused overtopping if to short
- Difference in Forces

6.7 Stability of the buoy

The swim stability of the buoy is very sensitive against weight. Small changes caused high differences in the horizontal axes of the buoy. This causes problems especially for the tests with a high centre of gravity. In the upper left picture of figure 6.3 is shown that there have been holes in the bottom part of the buoy. These holes affected the horizontal axis of the buoy if there are overtopping events. In this case some of the water enters the buoy and is gathering in the holes. Therefor the centre of mass changed in a non-axial way. For changing the centre of gravity some extra masses have been added on different positions of the buoy. These added masses are shown in the upper right picture of figure 6.3. The masses have been fixed on a plastic plate, which was moveable. The weights of the masses are not in cycles around the axes of the buoy. Thus the masses have been rearranging until a position which lead to a stable. When the buoy is swimming small changes on the cover of the buoy influence the position. Therefore some tape has been used for the vernier. The position of the cap was marked as well as the position of the plastic disk. In this way the buoy had a horizontal position when the test are started. During the tests the initial position changed if there was overtopping. This causes variances especially for long tests.

Fig. 6.3- Stability of the buoy

6.8 Overtopping on the buoy

- With stiff cable pushed down
- High waves
- high pitching

6.9 Body of the buoy

- Avoid not symmetric holes inside
  - Overtopping water stays inside this holes
- More safe against overtopping
  - Submerged path changes if water is inside

6.10 Generated waves in the flume

- Unlinearity with higher waves

6.11 LDTV

For evaluating the tracking of the buoy a linear variable differential transformer (LDTV) has been used for some tests [Fig. 6.4]. Due to the limited range of 8 cm the LDTV this was only possible for small waves. The LDTV was fixed on the buoy for one DOF. In this way the movement of the buoy was measured. The main Part of the LDTV is a metal core. When this core moves it causes a voltage, which decreases when the core moves down and increases when the core moves up.

***Fig. 6.4** – LDTV*

In figure 6.5 a time series is given. It includes the measurements of the LDTV (red), the camera (green) and the wave gauge next to the buoy (blue). It can be seen that the minima and maxima values of the camera are about 3 mm higher that the values from the LDTV. This variance is still acceptable. The time series also shows that there is a delay between the movement of the buoy and the wave. It is not possible to get information about this delay out of the existing movie data. For this information the starting time of the movie needs to be the same as the wave gauges. This can be investigated in further tests.

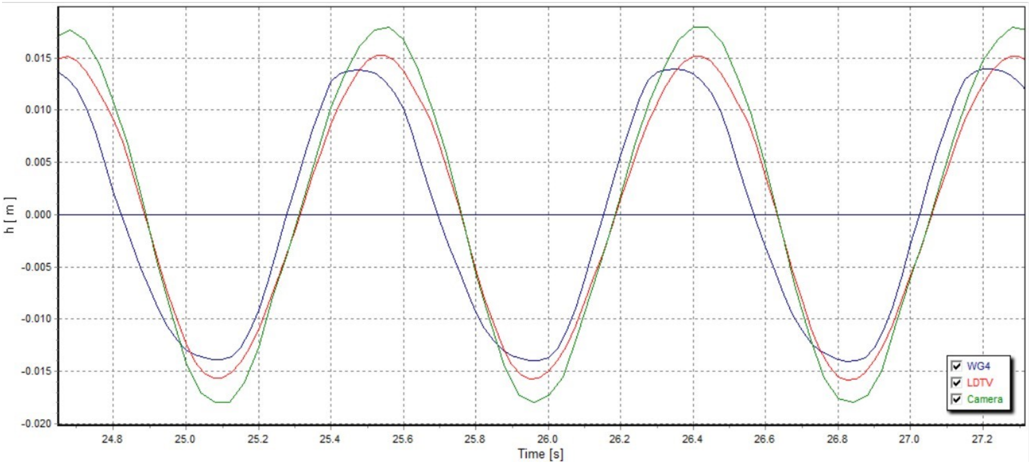

Fig. 6.5 *- Time series of LDTV*

6.12 Reflection on the window

For tracking the Buoy it is important to have clear and sharp frames. Therefore it is important that the reflection at the window is at low as possible. For this reason the camera has been covered with a tarpaulin. One side of the flume is covered with black paper at the backside and with black wood from the inside [Fig. 6.6].

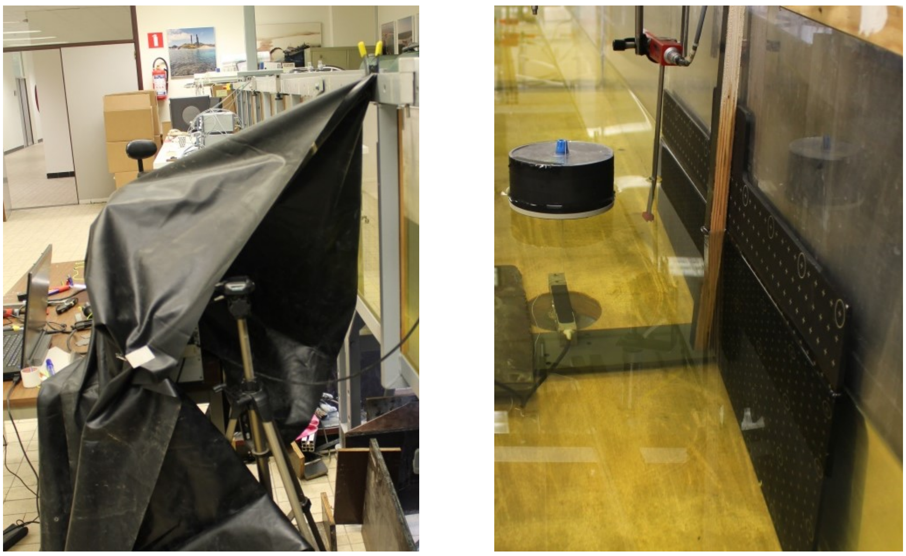

Fig. 6.6 *- Reflection on the window*

7. Results

7.1 One degree of freedom, regular waves

7.1.1 Results

In this configuration, a steel bar inside the buoy constrains the buoy in a up and down motion, avoiding the other degrees of freedom. The comparisons made regard different regular waves for the two positions of the weight inside the buoy.

In the figure below [Fig. 7.1], it is showed that the results for the high and low positions are almost the same; the differences are caused probably by the friction between the buoy and the bar. It seems that in the low position the buoy is more stable, especially for the highest waves. On the vertical axis it is reported the mean value of the buoy heaving motion and in the horizontal axis the mean value of the wave measured by the wave gauge next to the buoy.

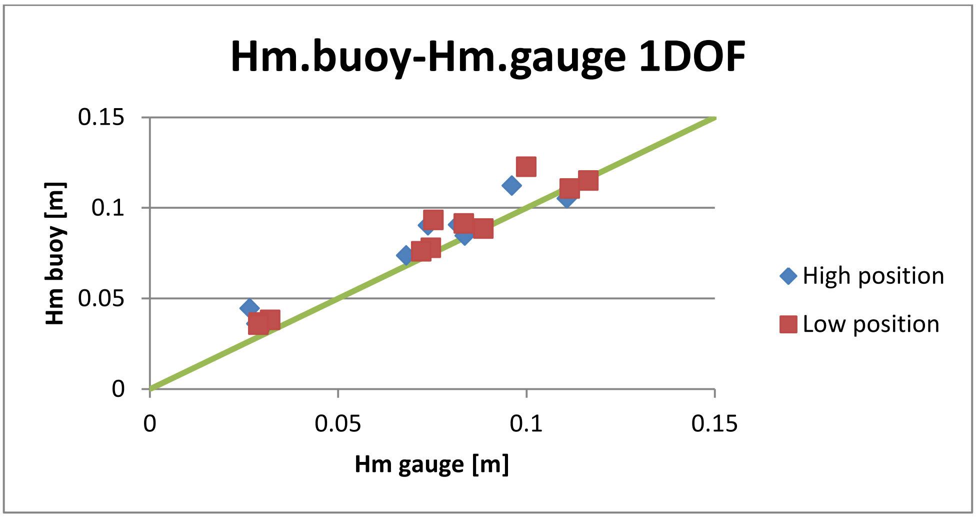

Fig. 7.1 *–Displacements of the buoy for various wave heights with the weight fixed in the low (red dots) and high position (blue dots).*

The periods of the motions with the two different weight positions of the buoy are identical to the wave periods [Fig. 7.2]:

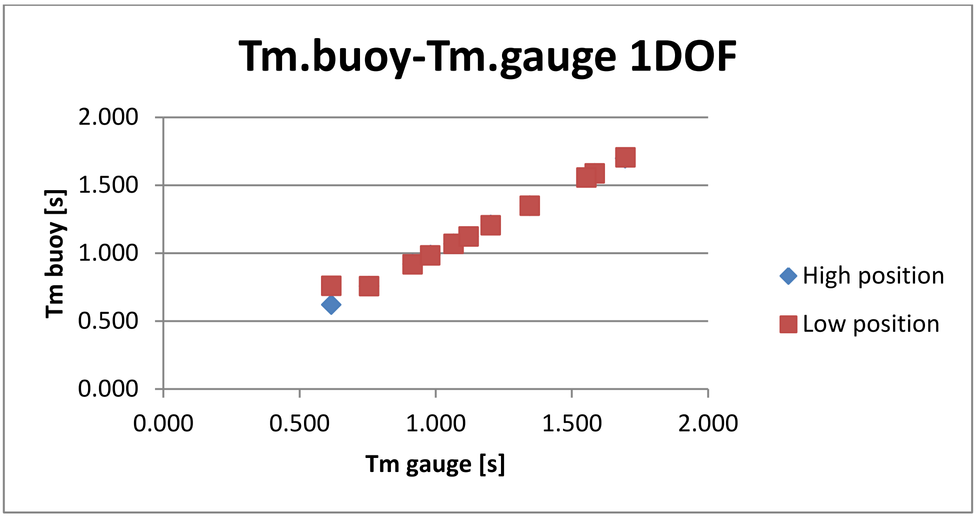

***Fig. 7.2** – Mean period of the heaving motions of the buoy (Tm buoy) and the mean period of the regular waves measured to the gauge next to the buoy (Tm gauge); with the blue dots it is indicated the weight in the high position and in red the low position.*

Putting the ratio between the buoy vertical motion and the wave height with the wave frequency gives an idea about the behavior of the model. Generally, the ratio is more than the unit, but a significant rise is near the natural frequency [Fig. 7.3]:

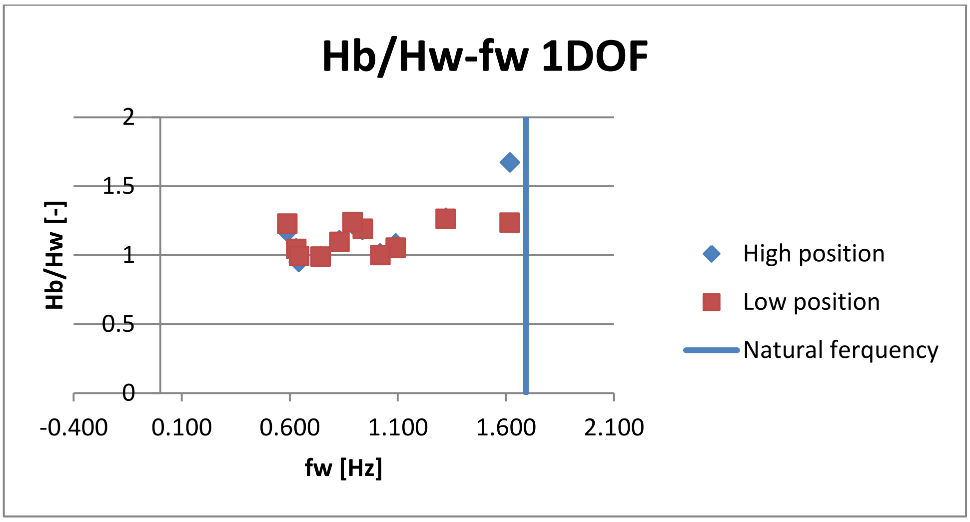

***Fig. 7.3 -** Ratio between the buoy vertical motion and the wave height compared with the wave frequency.*

7.1.2 Conclusions

No relevant differences have been found in this phase. The motions are almost identical both for the high and the low position. A visual response can be given showing the signal for the same waves with the weight displaced in the two ways [Fig. 7.4]; considering also the errors caused by the tracking software, the signals are equals.

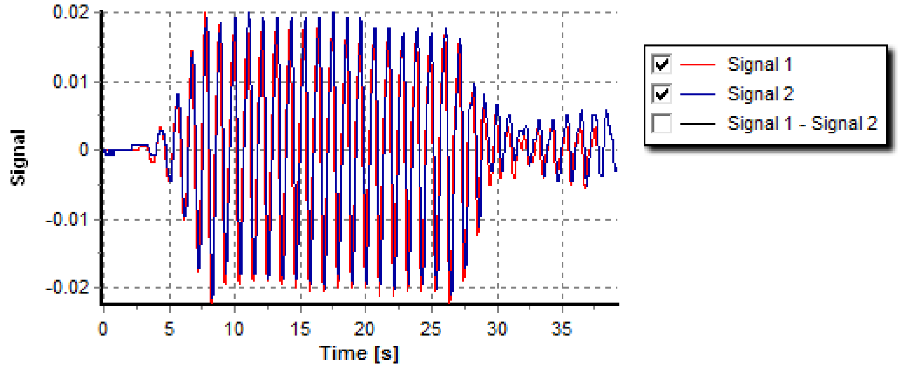

Fig. 7.4 *– Time series with the weight in the high position (blue line) and in low position (red line) for the same waves (Hm = 0.031 m; Tm = 1.067 s). On the vertical axis the motion of the buoy in meter.*

The only difference seems to be in the motion amplification when the signals approach the natural frequency as it is figured previously [Fig. 7.3]; in this case when the device has the center of gravity higher, the amplification is greater.

7.2 One degree of freedom, irregular waves

7.2.1 Results

Starting from the results obtained for the regular waves, it was tested the device in one degree of freedom for a significant sea state; the wave spectrums are represented below [Fig. 7.5]; they confirm that the buoy in the two configurations has been submitted by the same waves.

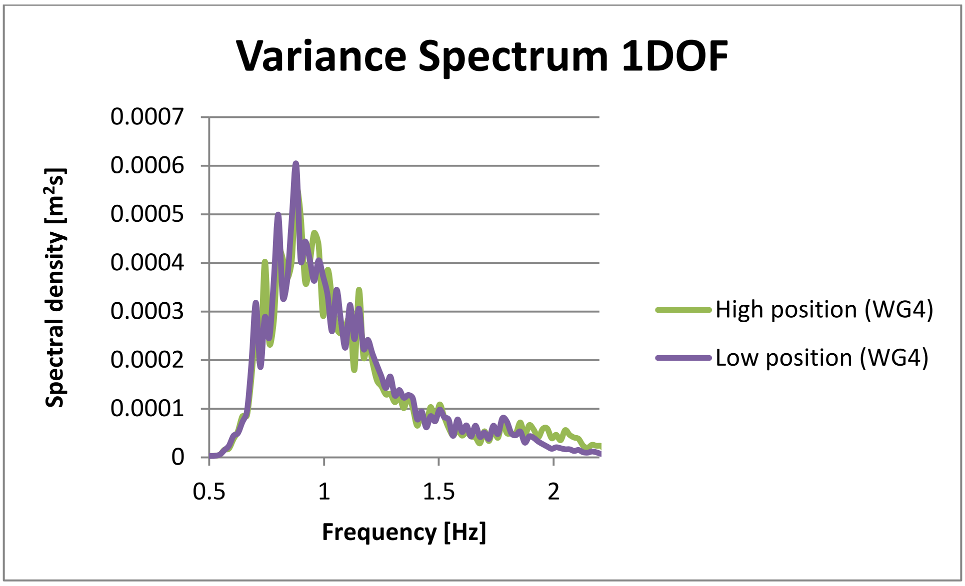

Fig. 7.5 – *Variance spectrums of the waves registered at the gauge next to the buoy in the two different configurations.*

The graph below confirms what was expected looking the results for the regular waves [Fig. 7.6]: there aren't important differences between the two positions of the weight. Using the buoy's motions for the high and the low displacement of the mass like wave heights, they have been extracted the "Variance spectrums" for the device.

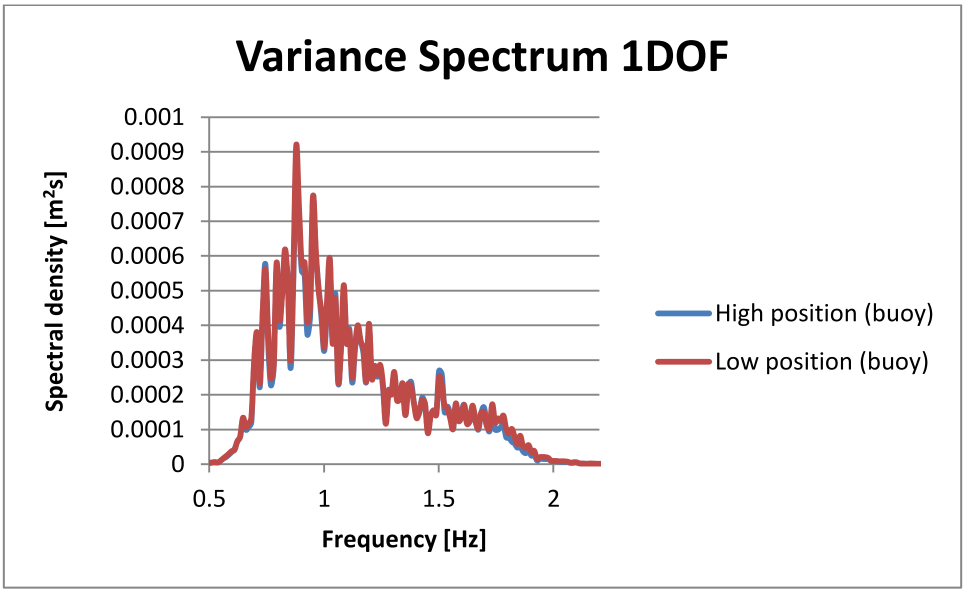

Fig. 7.6 – *Comparison of the two spectrums obtained from the movements of the buoy with different center of gravity.*

7.2.2 Conclusions

At last, what can be said from these tests is that if the buoy had moved only in one degree of freedom condition it would not have mattered the position of the weight.

Interesting is the motion amplification. As it is happened for the regular waves, also for the irregular waves the movement amplitude of the buoy is bigger than the wave amplitude. It seems to be related by two factors:

- the wave height: higher is the wave and bigger is the motion amplification of the buoy; it is showed in the figures [Fig. 7.7 and Fig. 7.8] as the principal peak of the buoy's spectrum around the peak frequency of the irregular waves;
- the wave frequency: a secondary peak is recognizable near the natural frequency for the heaving motion of the buoy [Fig. 7.7 and Fig. 7.8], that was calculated to be 1.69 Hz.

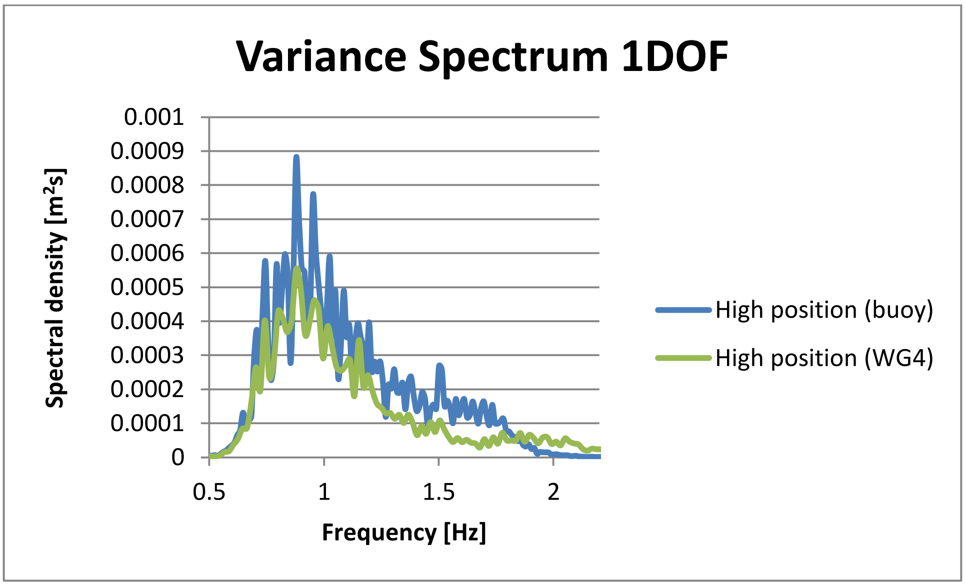

Fig. 7.7 *– Comparison of the wave variance spectrum and the spectrum obtained from motions of the buoy with the mass in the high position.*

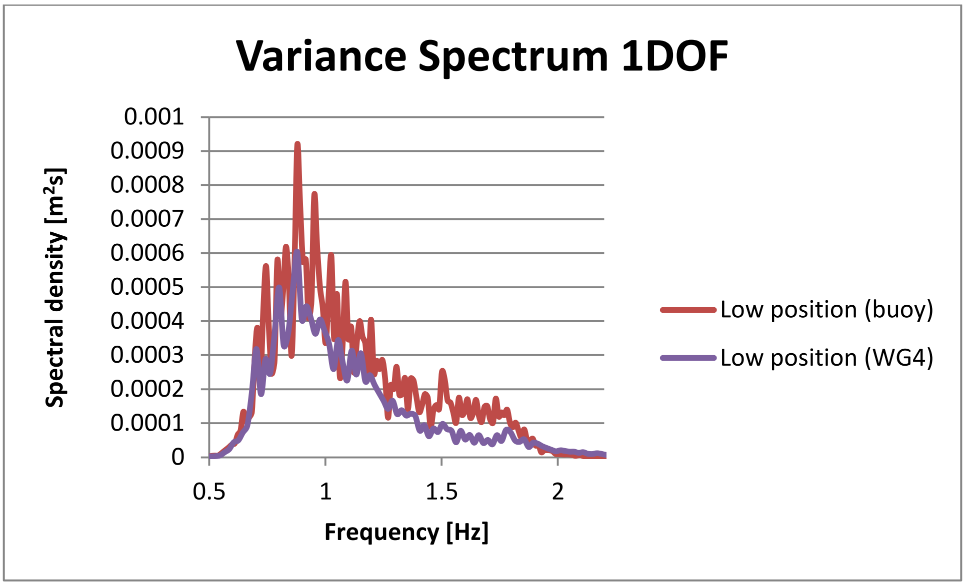

Fig. 7.8 *– Comparison of the wave variance spectrum and the spectrum obtained from motions of the buoy with the mass in the low position.*

7.3 Six degrees of freedom, regular waves: free motion

7.3.1 Results

With the buoy in "free floating" condition, several tests with regular waves have been performed. In this configuration, changing the weight inside the device, they have been analyzed the first waves, or rather the waves before the buoy reached the edge of the camera window; generally less than ten waves.

The results acquired by the heaving motion analysis are the same than the results discovered during the tests with the regular waves in one degree of freedom configuration:

- the heaving motion period is identical to the wave period [Fig. 7.9];

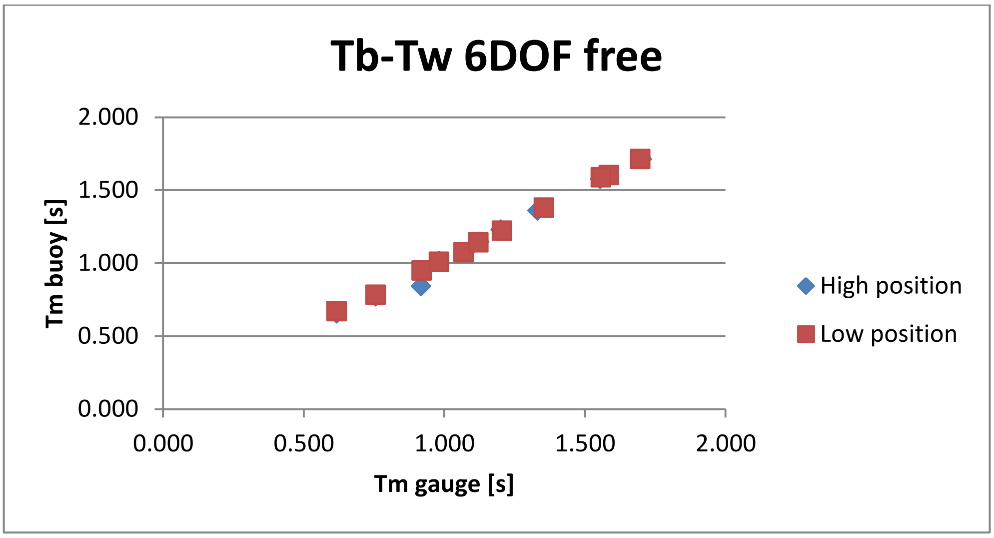

Fig. 7.9 *– Mean period of the heaving motions of the buoy (Tm buoy) and the mean period of the regular waves measured to the gauge next to the buoy (Tm gauge); with the blue dots it is indicated the weight in the high position and in red the low position.*

- the buoy motion is bigger than the wave amplitude [Fig. 7.10];

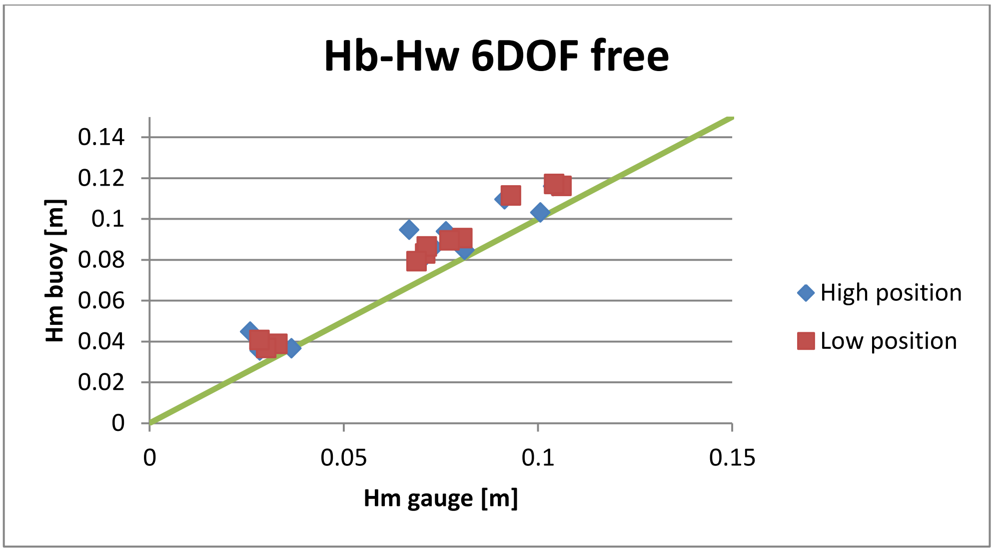

Fig. 7.10 *–Displacements of the buoy for various wave heights with the weight fixed in the low (red dots) and high position (blue dots).*

- the amplification increases approaching the natural frequency of the heaving motion [Fig. 7.11];

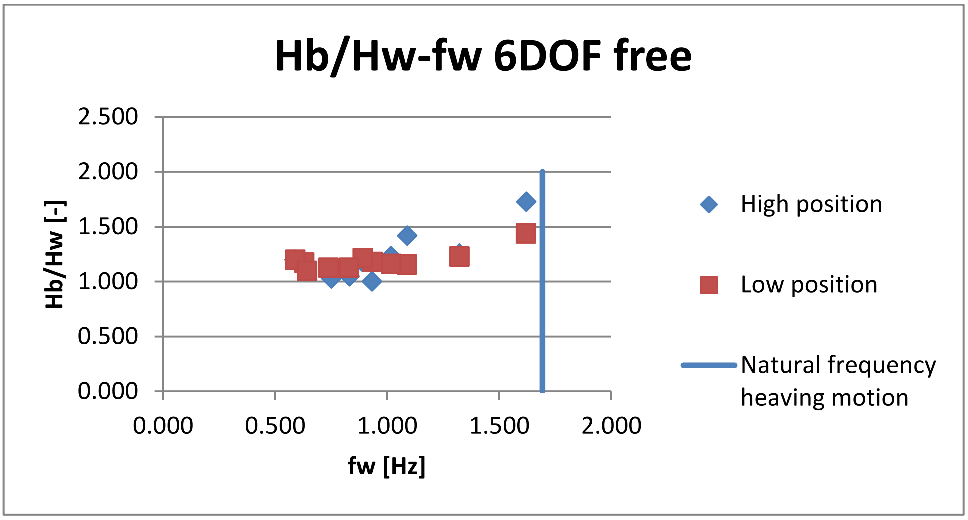

Fig. 7.11 *- Ratio between the buoy vertical motion and the wave height compared with the wave frequency.*

Regarding the pitching motion it has been taken positive the clockwise direction and negative the counterclockwise direction.

The first difference with the heaving motion regards the pithing period that results independent by the wave period [Fig. 7.12]:

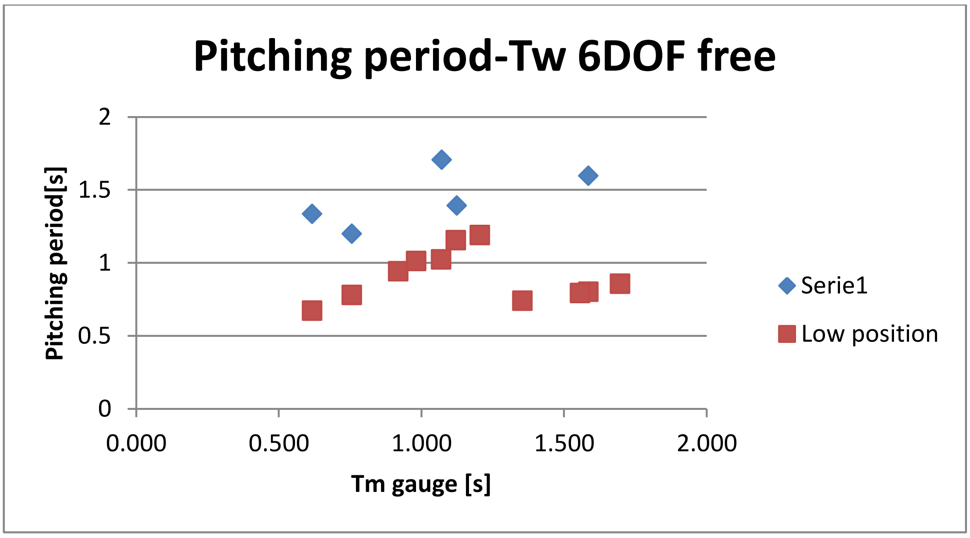

Fig. 7.12 *– Pitching period (on the vertical axis) compared with the wave period recorded at the gauge next to the device.*

In the graph representing the total amplitude of the pitch compared with the regular waves recorded by the wave gauge [Fig. 7.13] it is showed that the results are completely different for the two configurations; in particular, when the buoy has an high center of gravity is more stable independently by the wave height.

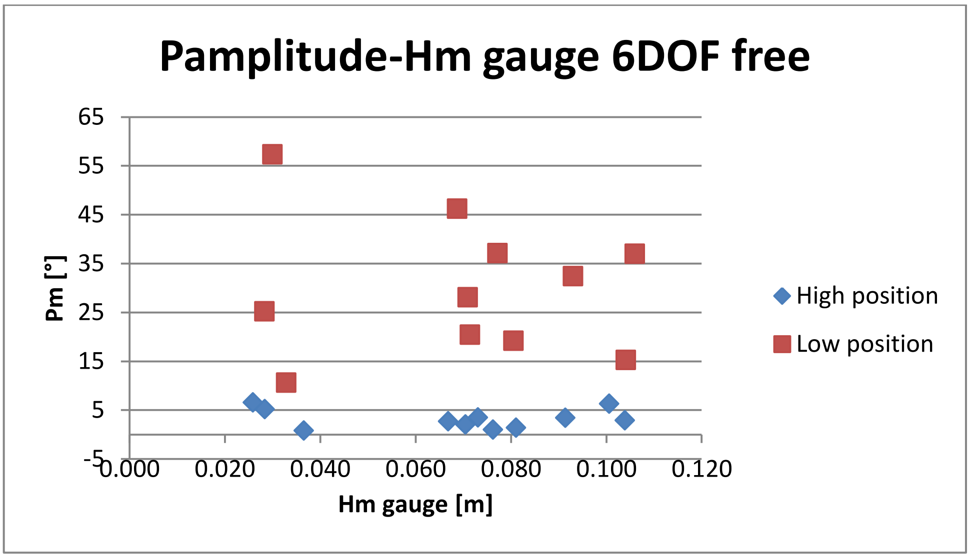

Fig. 7.13 – Comparison between the mean pitching amplitude on the vertical axis and the wave height.

The figure below [Fig. 7.14] highlights the relation between the amplification of the pitching motion and the wave frequencies. For the high position of the mass, a little peak is visible near the relative natural frequency; in the low position the buoy's behavior is hard to be described. Despite of the predictable and visible peak around the natural frequency for the low position, an increasing of the oscillation and the reducing of the wave frequency involves an instable condition for the device.

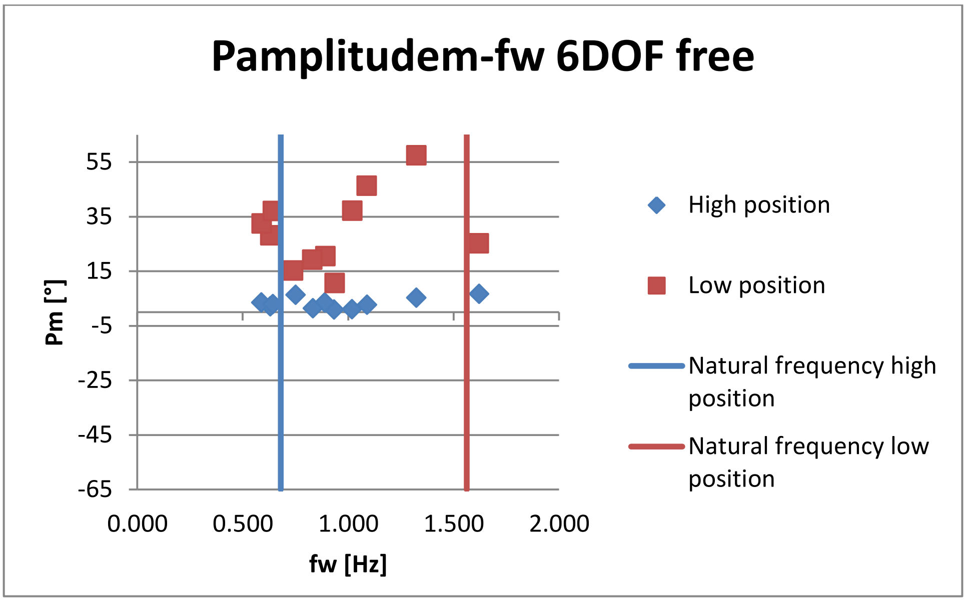

Fig. 7.15 *- Comparison between the mean pitching amplitude on the vertical axis and the wave frequency on the horizontal one.*

Other graphs which show the maximum positive pitching amplitude value related to the wave parameters can be found in the Appendix D.

7.3.2 Conclusions

These tests show that the response of the device is better when the weight is displaced in the high position. A comparison of the two signals for the highest wave (Hm = 0.101 m: T = 1.331 s) gives the same conclusion [Fig. 7.16]; as it can be observed, the vertical motion is bigger when the center of gravity is high:

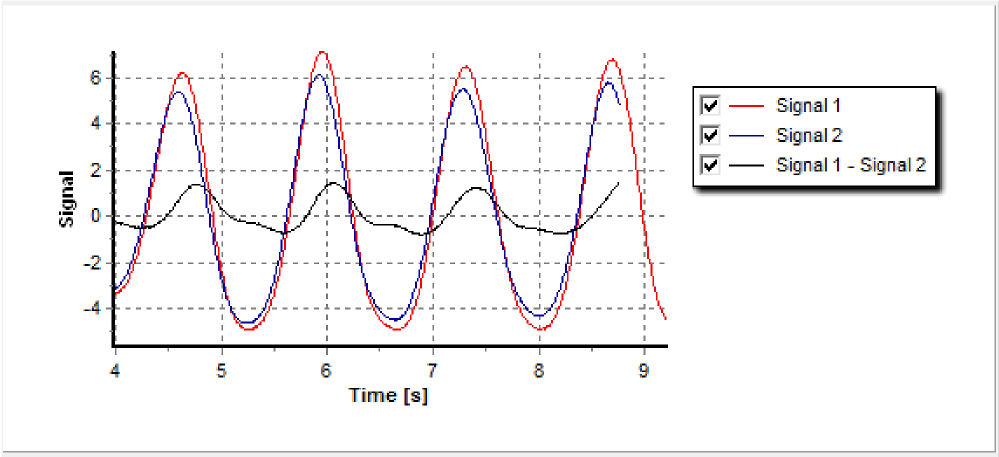

Fig. 7.16 *– Comparison of the heaving motion time series with the weight in the high position (red line) and the weight in the low position (blue line); the black line represents the difference. On the vertical axis is reported the motion in centimeters.*

An acknowledgment of this behavior might be the major energy converted in the oscillation of the device when the mass inside the buoy is dislocated down; this difference, analyzing for example the same wave used before (Hm = 0.101 m: T = 1.331 s), is considerable [Fig. 7.17]:

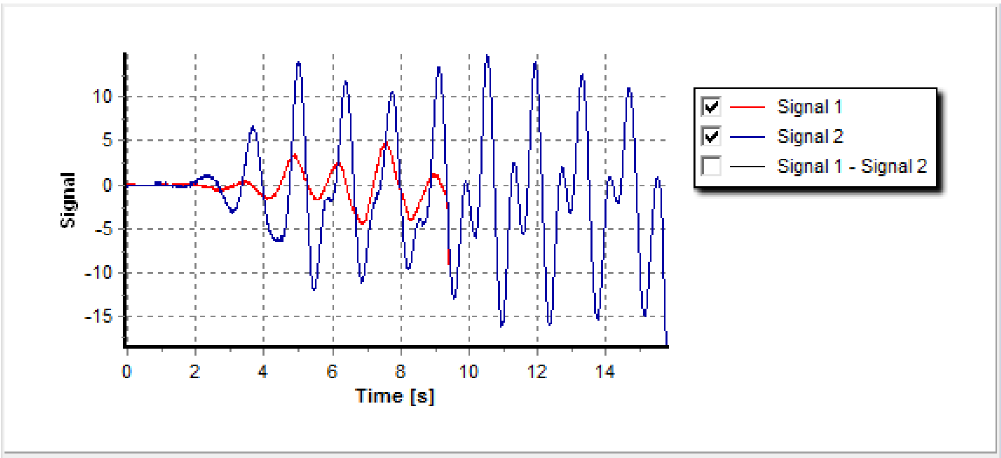

Fig. 7.17 *– Comparison of the pitching motion time series with the weight in the high position (red line) and the weight in the low position (blue line). On the vertical axis is reported the motion in degrees.*

7.4 Six degrees of freedom, regular waves: stiff cable

7.4.1 Results

In the following step the device was tested introducing a stiff line that moored the buoy at a load cell capable to recorder the pressure undergone by the cable.

The principal issue found during this phase was the impossibility to track the motions of the buoy; as it is showed in the photogram [Fig. 7.18] in this condition when the buoy is pushed, it starts rolling around the axis orthogonal to the glass window and making the tracking not possible.

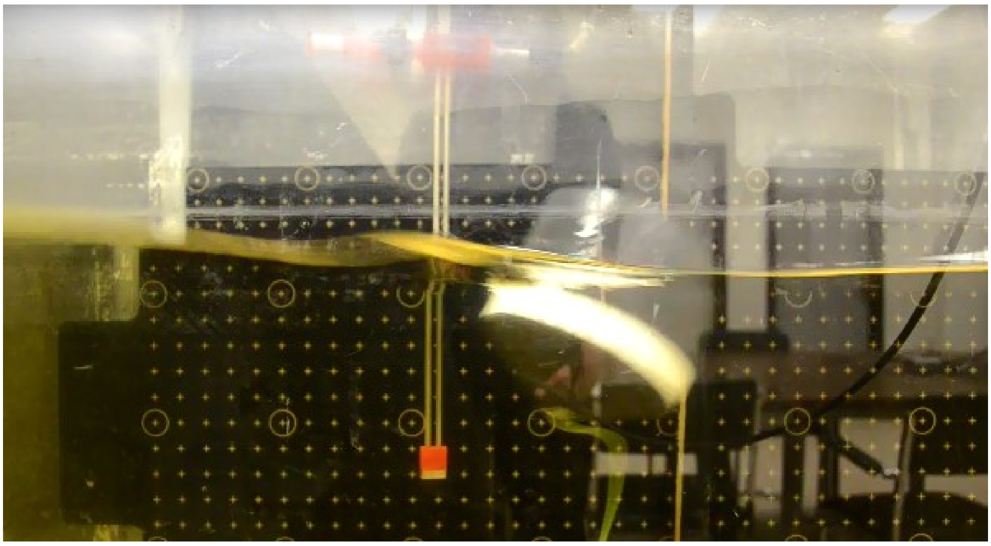

Fig. 7.18 *– Photogram taken during the recording of a test; it is possible to perceive the wrong tilt angle.*

For this reason the data achieved from these tests regard only the forces and the signal measured by the load cell.

Keeping the length of the line equal to the still water level plus the wave height, they were carried out various experiments with the mass in the high and low position.

The forces exercised seems to be not depended by the wave heights as it is underlined in the graph [Fig. 7.19].

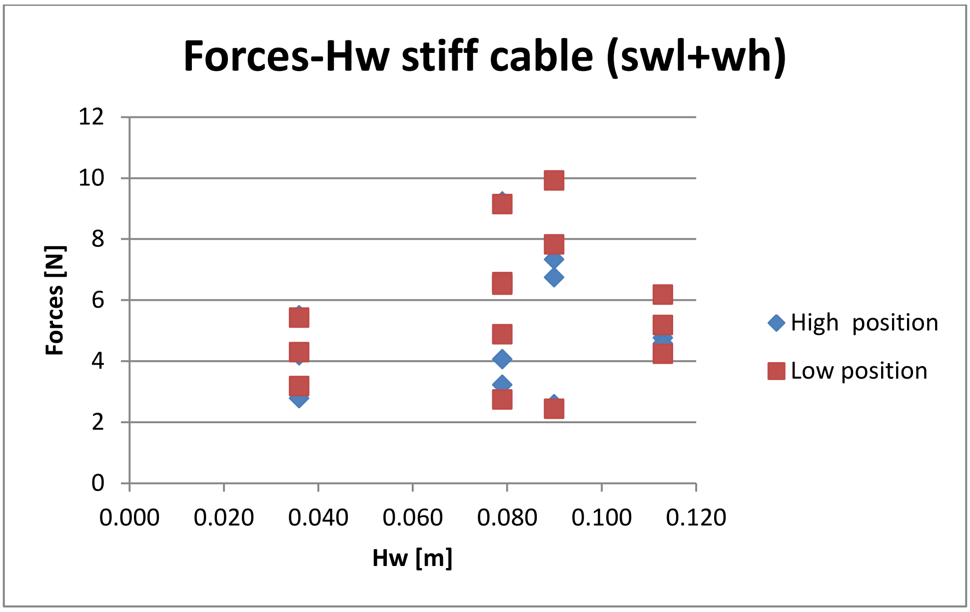

Fig. 7.19 *– Forces compared with the wave heights.*

More useless results are acquired relating the forces undergone by the device and the wave frequencies [Fig. 7.20]; for both configurations, the loads look to decrease if the wave frequency increases.

For the high center of gravity, maximum value is recognizable around a frequency of 0.6 Hz, that is also the natural pitching frequency for the high position.

When the weight is down, the force trend is the same like the high position, with the difference of a peak around 1 Hz.

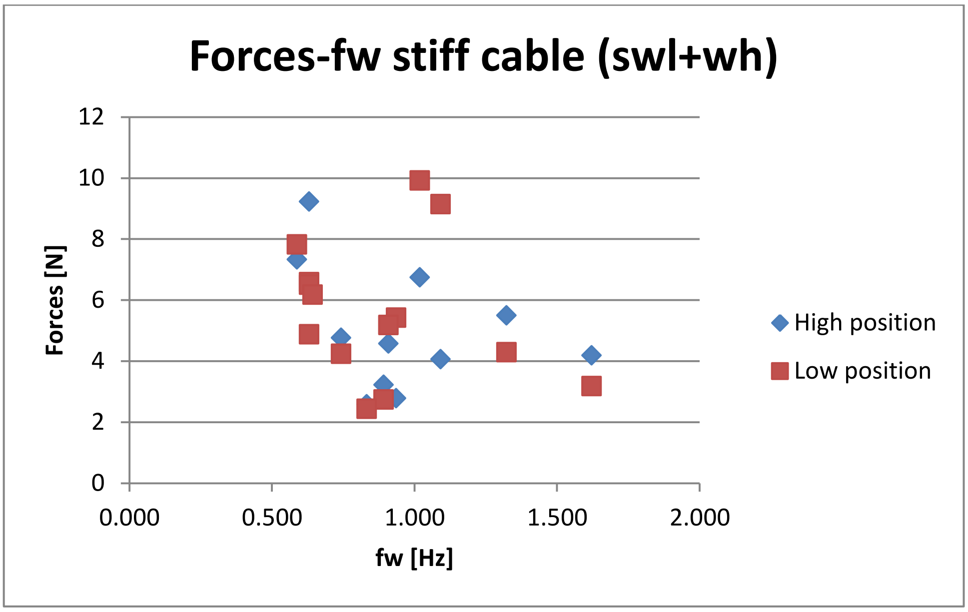

Fig. 7.20 *– Relation between the forces and the wave frequencies.*

An interesting characteristic discovered during the analysis of the signals is the presence of multiple peaks [Fig. 7.21].

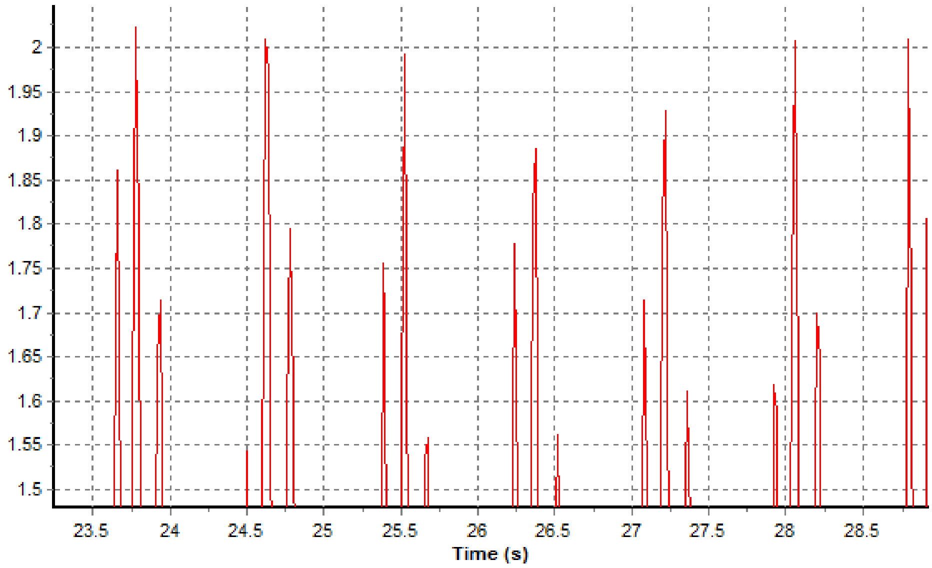

Fig. 7.21 *– Time series of the forces recorded by the load cell; on the vertical axis the Force [N] and on the horizontal axis the Time [s]. They are evident the triple peaks.*

Unfortunately, this particularity of the signal doesn't seem to have relation with the wave frequency [Fig. 7.22] or with the wave height [Fig. 7.23 and Fig. 7.24].

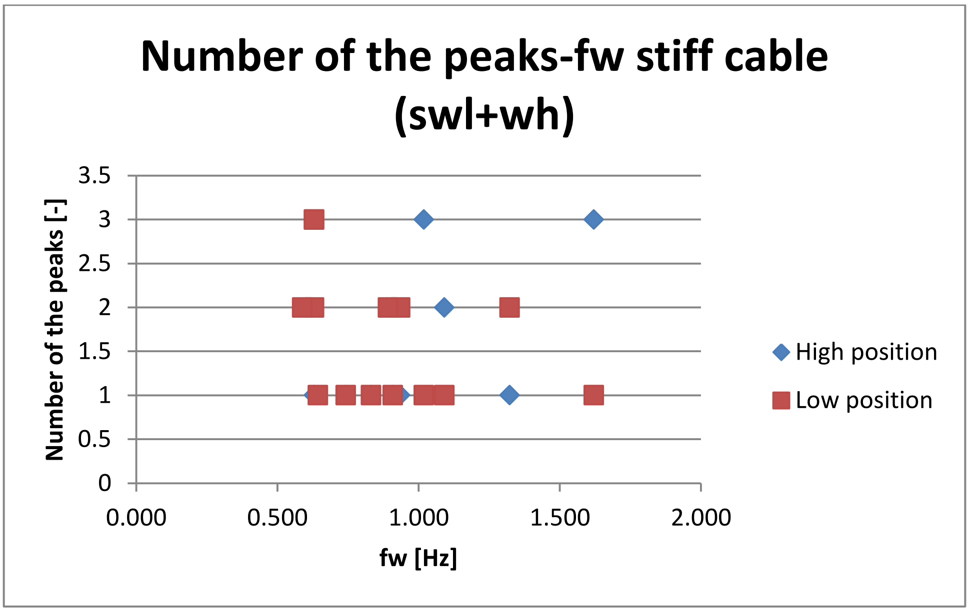

Fig. 7.22 *– Relation between the multiple peaks and the frequencies.*

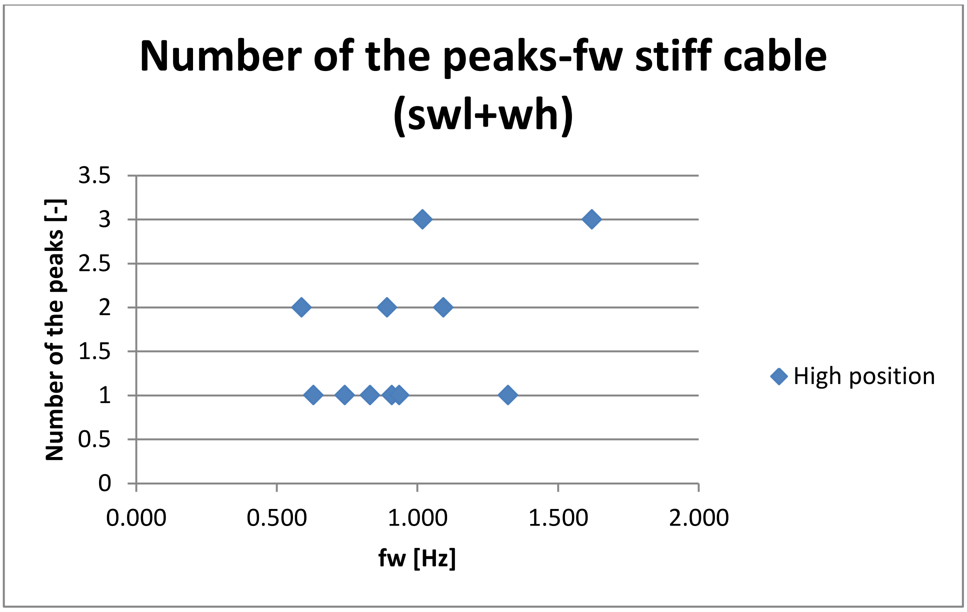

Fig. 7.23 *– Relation between the multiple peaks and the frequencies for the high position of the center of gravity*

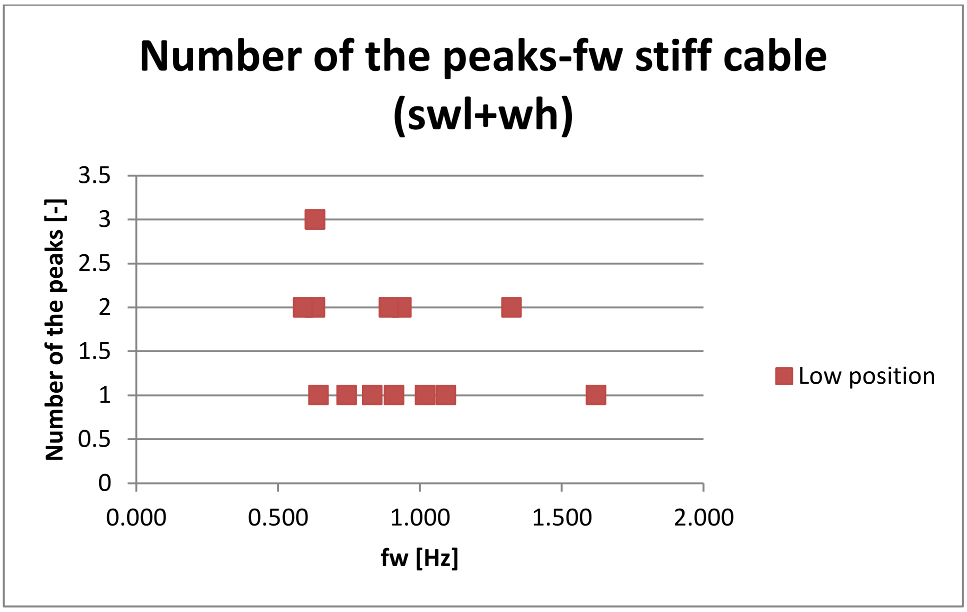

***Fig. 7.24** – Relation between the multiple peaks and the frequencies for the low position of the center of gravity*

7.4.2 Conclusions

These tests don't give a real idea about the influence of the stiff line, the frequency and the wave heights on the forces and the multiple peaks present in the signal recorded by the load cell.

In the Appendix E there are reported some graphs that show the results of few tests conducted on the buoy with the weight displaced in the high position and with the length of the line equal to the water level; but also in these cases the results are the same.

7.5 Six degrees of freedom, regular waves: flexible cable

7.5.1 Results

In this phase, the buoy is moored through a very flexible cable and tested with regular waves. The results, illustrated in the following, denote the same conclusions found beforehand. Regarding the heaving motion:

- the heaving motion period is identical to the wave period [Fig. 7.25];

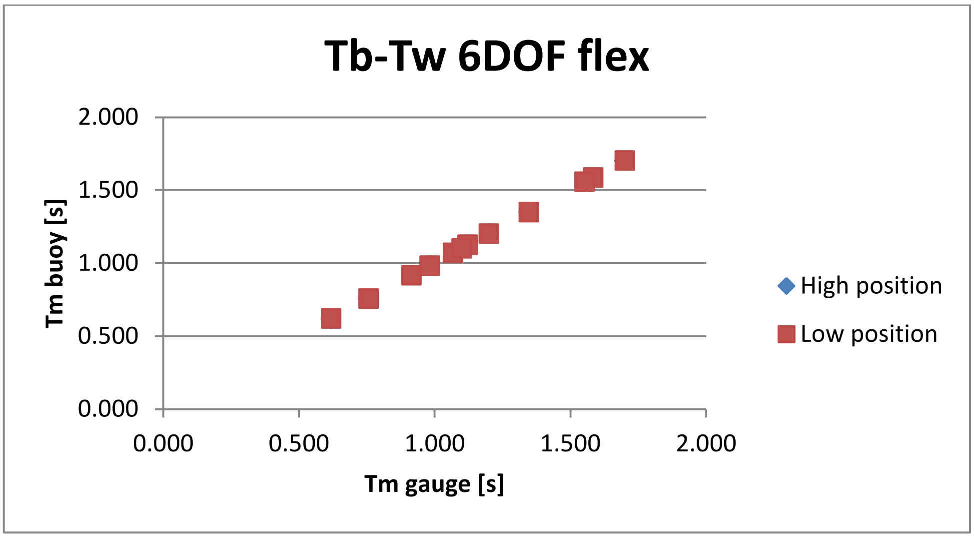

Fig. 7.25 *– Mean period of the heaving motions of the buoy (Tm buoy) and the mean period of the regular waves measured to the gauge next to the buoy (Tm gauge); with the blue dots it is indicated the weight in the high position and in red the low position.*

- the buoy motion is bigger than the wave amplitude [Fig. 7.25];

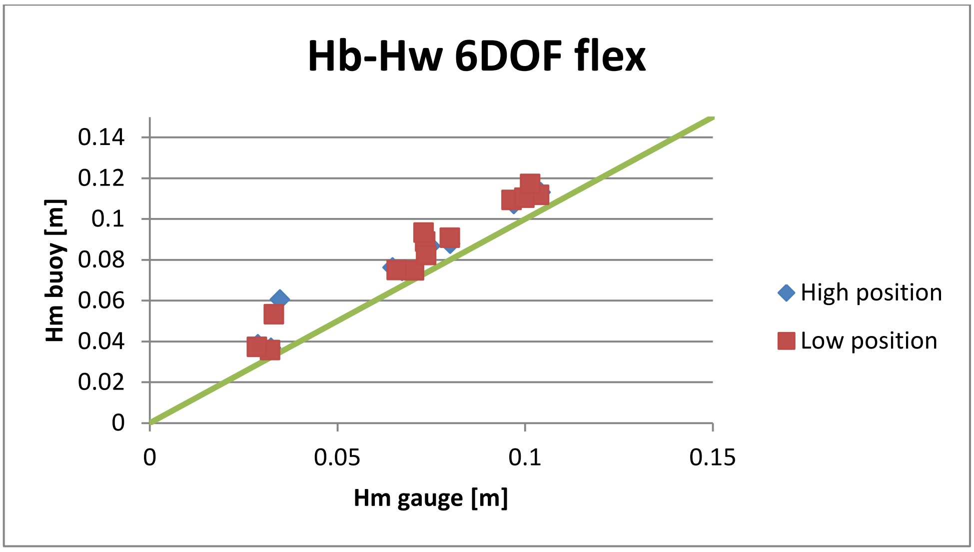

Fig. 7.25 *–Displacements of the buoy for various wave heights with the weight fixed in the low (red dots) and high position (blue dots).*

- the amplification increases approaching the natural frequency of the heaving motion [Fig. 7.26];

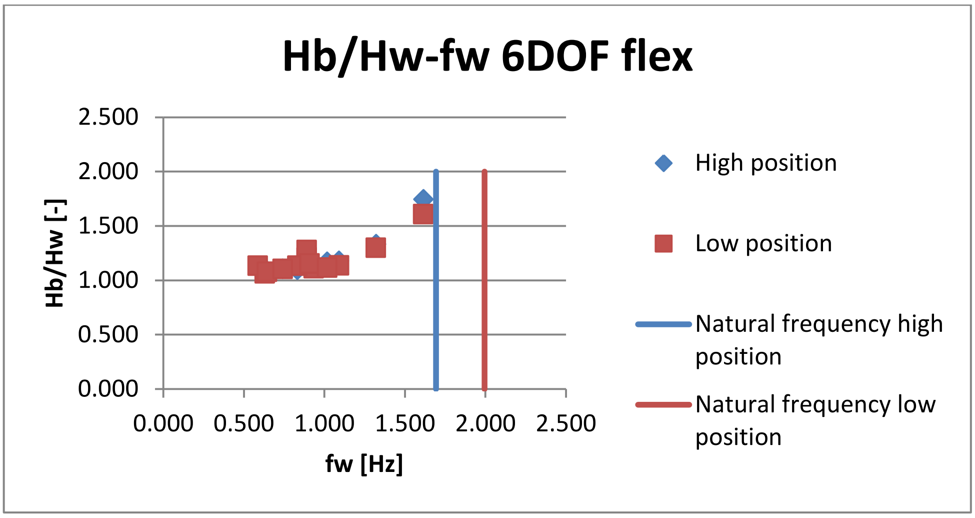

Fig. 7.26 *- Ratio between the buoy vertical motion and the wave height compared with the wave frequency.*

Talking about the pitching motion, like in free condition, the pitching period results quite different from the wave period [Fig. 7.27].

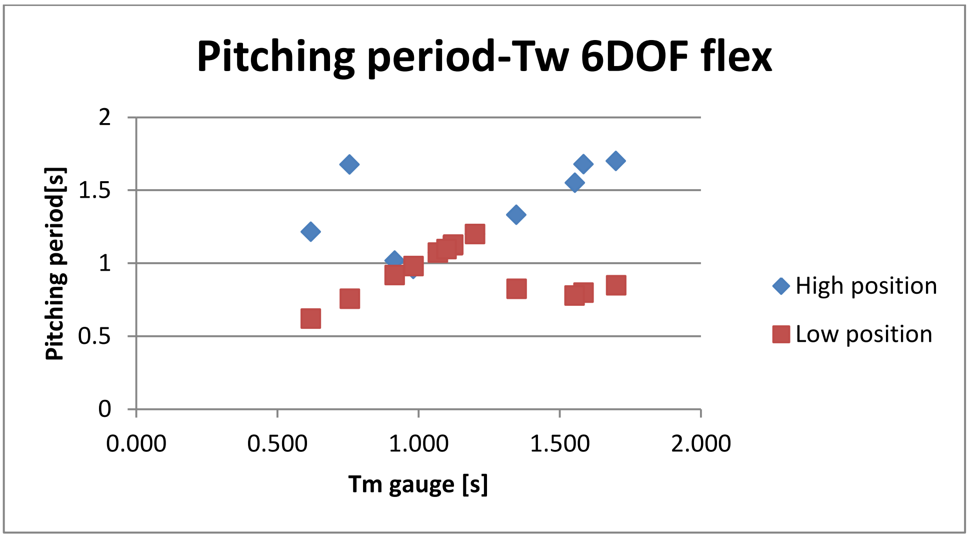

Fig. 7.27 *– Pitching period on the vertical axis compared with the wave period recorded at the gauge next to the device.*

The pitching amplitude is usually less when the mass is positioned up, but for the highest waves the oscillations in this configurations increase quickly [Fig. 7.28].

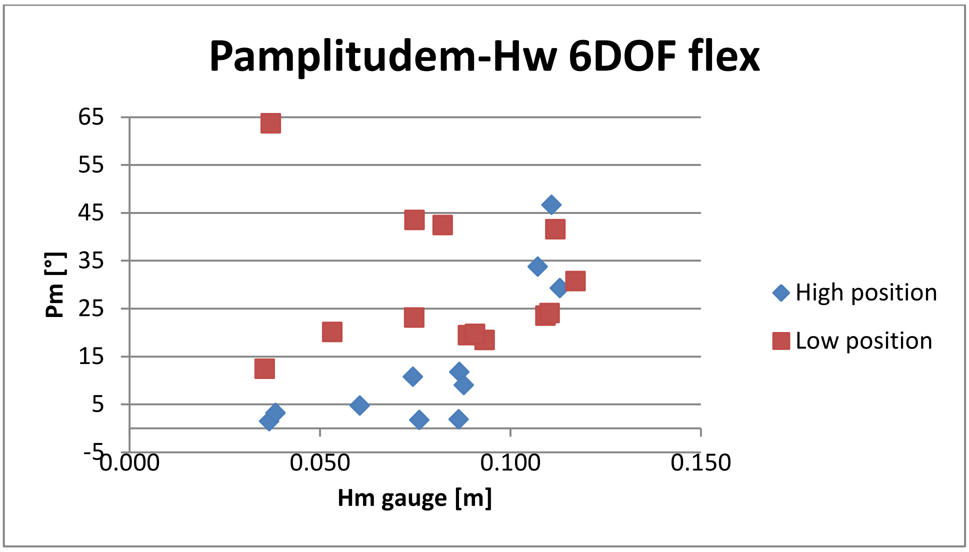

Fig. 7.28 – *Comparison between the mean pitching amplitude on the vertical axis and the wave height.*

This behavior is described as a peak around the natural pitching frequency in the high position [Fig. 7.29]. Other graphs (Appendix F) showing different relations confirm this tendency.

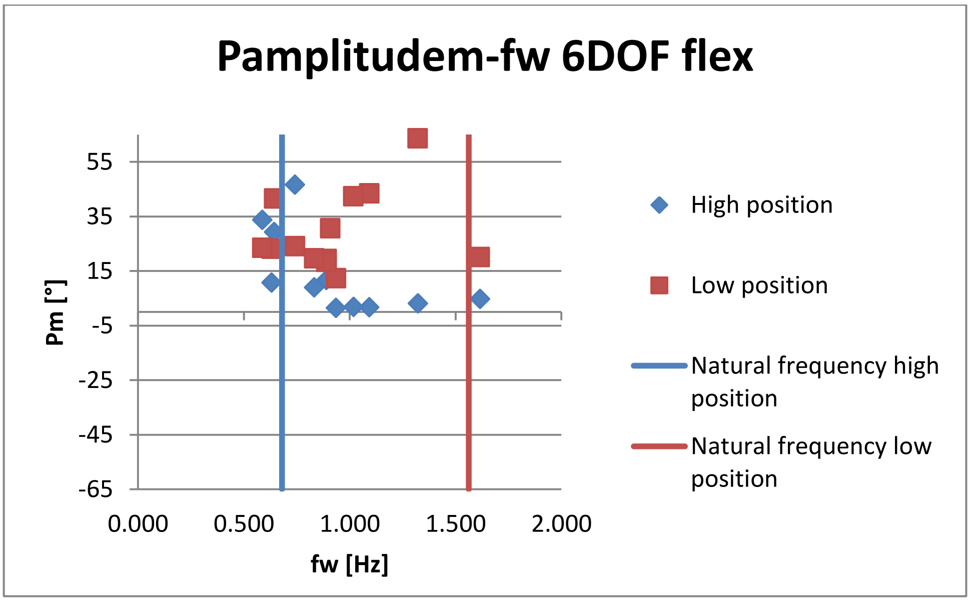

Fig. 7.29 – *Comparison between the mean pitching amplitude on the vertical axis and the wave height*

7.5.2 Conclusions

Even now the heaving motion for the two configurations are quite identical for all waves tested [Fig 7.30 and Fig. 7.31].

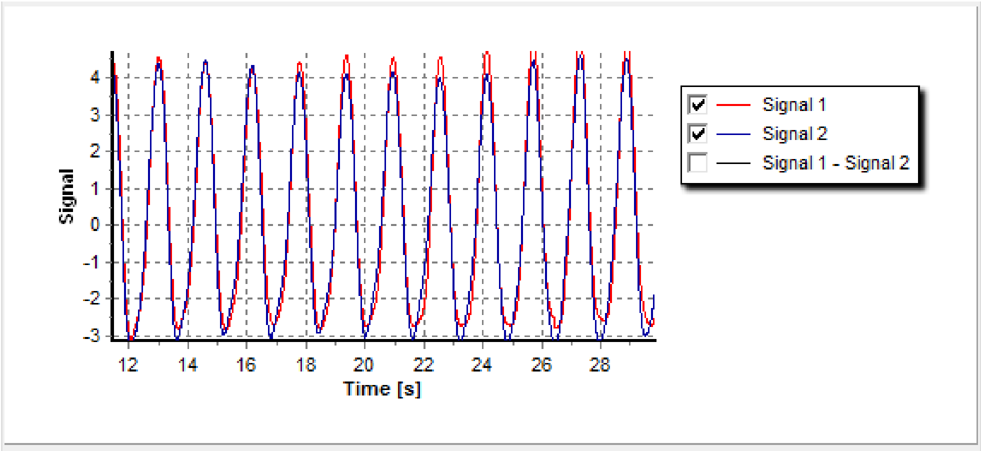

***Fig. 7.30** – Comparison of the heaving motion time series of the same waves (Hm =0.07 m, Tm = 1.585) with the weight in the low position (red line) and the weight in the high position (blue line); the black line represents the difference. On the vertical axis is reported the motion in centimeters.*

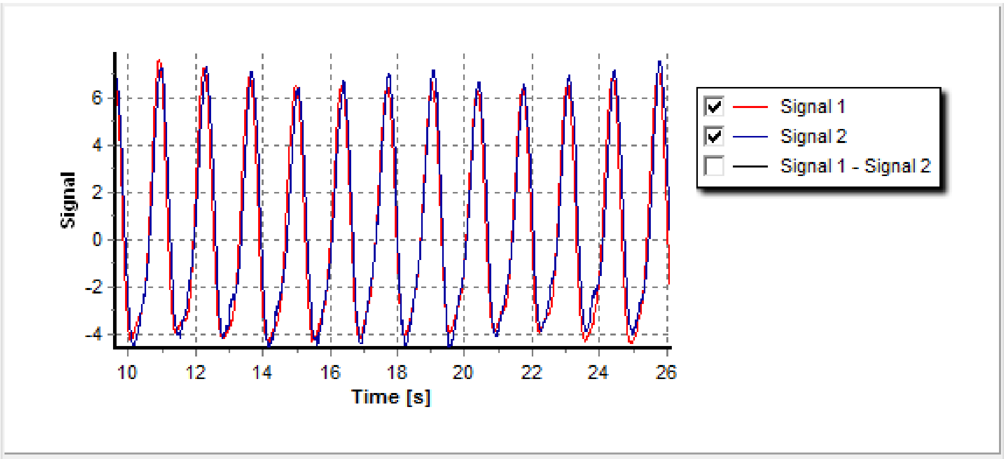

***Fig. 7.31** – Comparison of the heaving motion time series of the same waves (Hm =0.10 m, Tm = 1.348) with the weight in the low position (red line) and the weight in the high position (blue line); the black line represents the difference. On the vertical axis is reported the motion in centimeters.*

The differences are in the pitching motion: depending by the frequency of the waves generated, the gyrations are comparable when the frequency of the waves are close to the natural pitching frequency for the high position of the center of gravity [Fig 7.32 and Fig. 7.33].

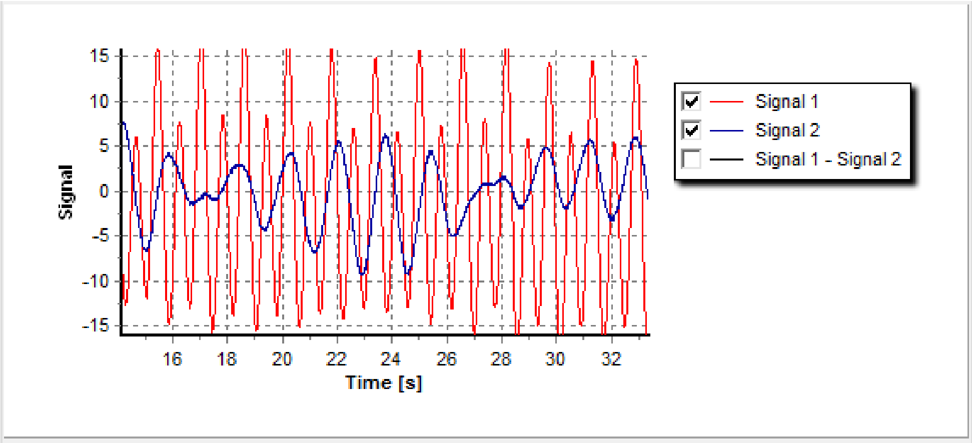

Fig. 7.32 *– Comparison of the pitching motion time series of the same waves (Hm =0.07 m, Tm = 1.585) with the weight in the low position (red line) and the weight in the high position (blue line). On the vertical axis is reported the motion in degrees.*

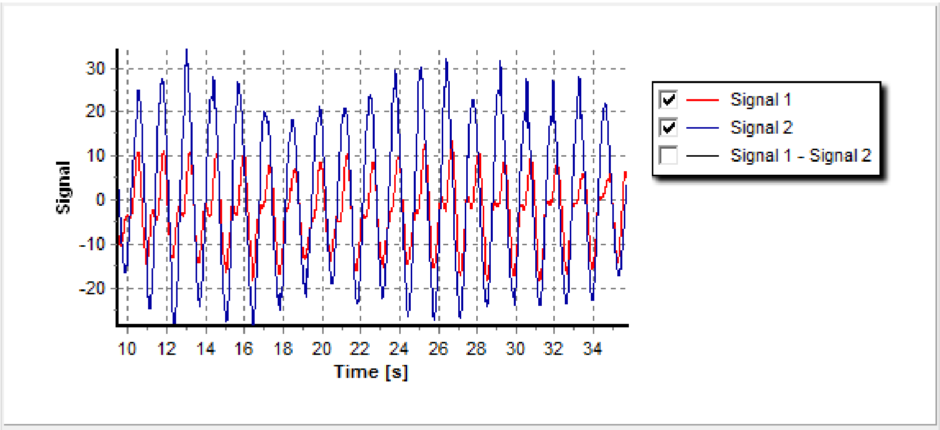

Fig. 7.33 *– Comparison of the pitching motion time series of the same waves (Hm =0.10 m, Tm = 1.348) with the weight in the low position (red line) and the weight in the high position (blue line). On the vertical axis is reported the motion in degrees.*

Despite of what was discovered for the stiff cable, with the flexible line the loads acting on the cable increase simultaneously at the wave heights [Fig. 7.34].

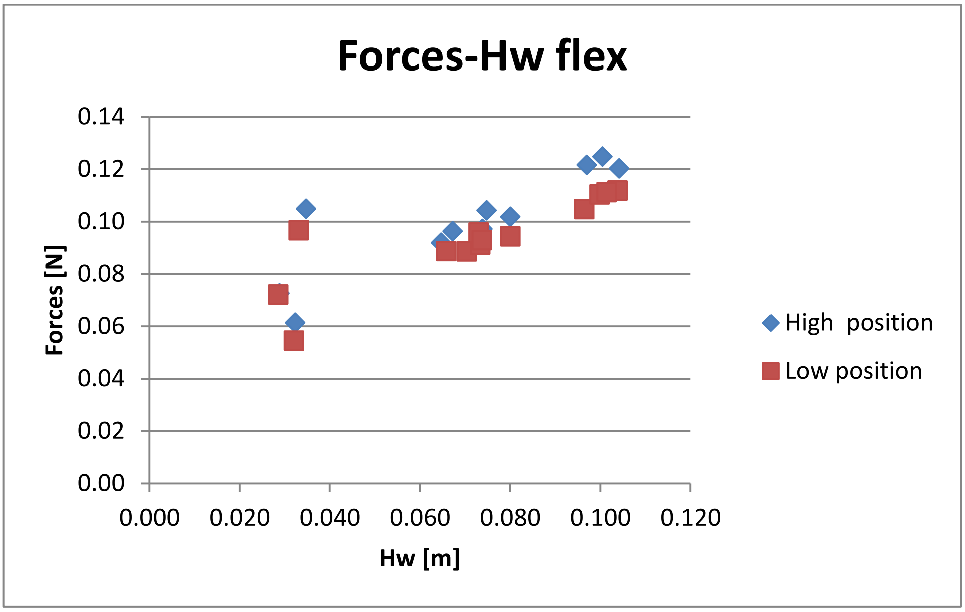

Fig. 7.34 *– Forces compared with the wave heights.*

7.6 Six degrees of freedom, irregular waves: flexible cable

7.6.1 Results

The results for the configuration with the buoy connected at the bottom of the flume with a flexible line and tested with irregular waves are the same obtained on the one degree of freedom; in fact for the same waves [Fig. 7.35] the heaving motions are alike [Fig. 7.36].

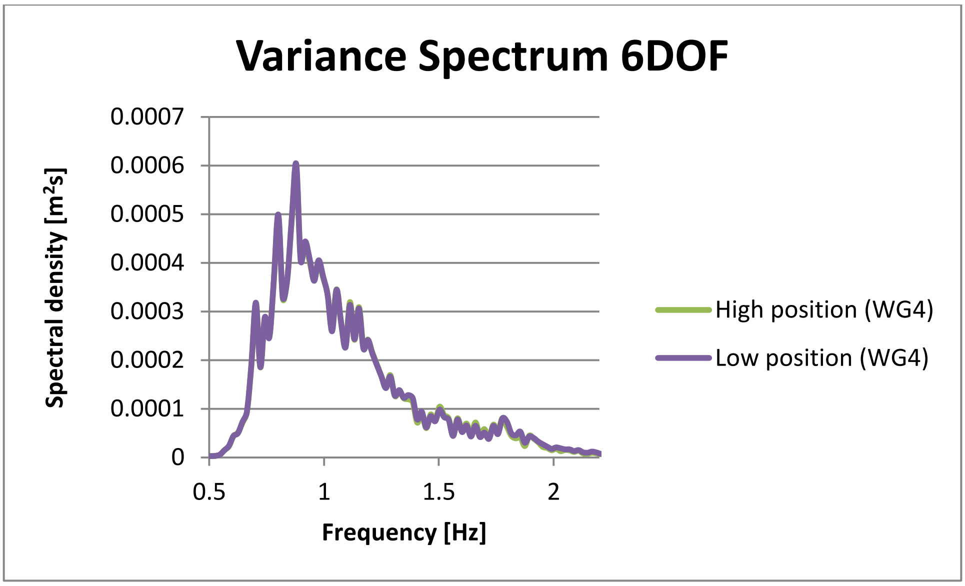

Fig. 7.35 – *Variance spectrums of the waves registered at the gauge next to the buoy in the two different configurations.*

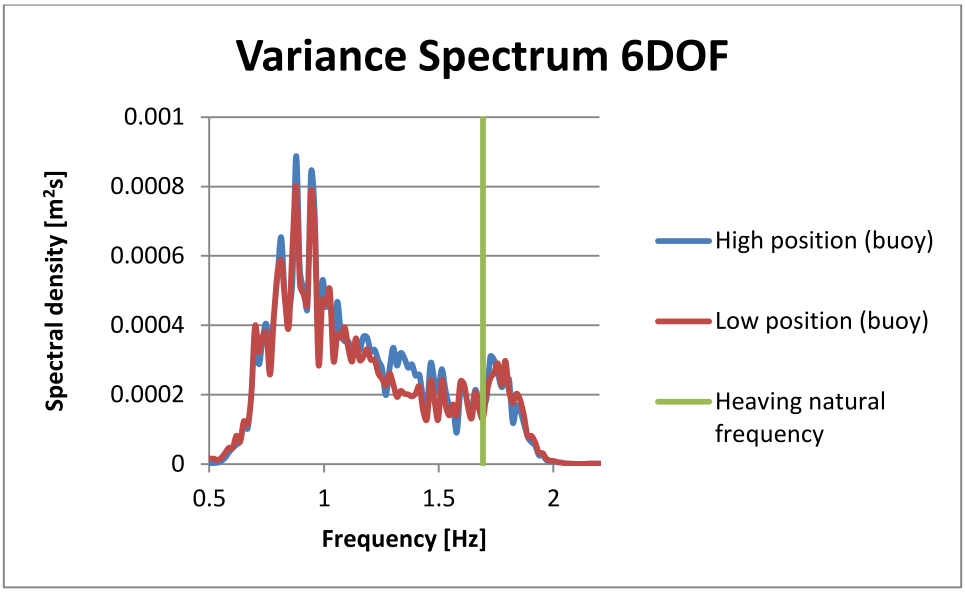

Fig. 7.36 *– Comparison of the two spectrums obtained from the movements of the buoy with different center of gravity.*

7.6.2 Conclusions

Both spectrums extracted from the heaving motions show a general amplification of the buoy's movements with a peak at the peak frequency of the waves variance spectrum and another one close to the heaving natural frequency [Fig. 7.37 and Fig. 7.38].

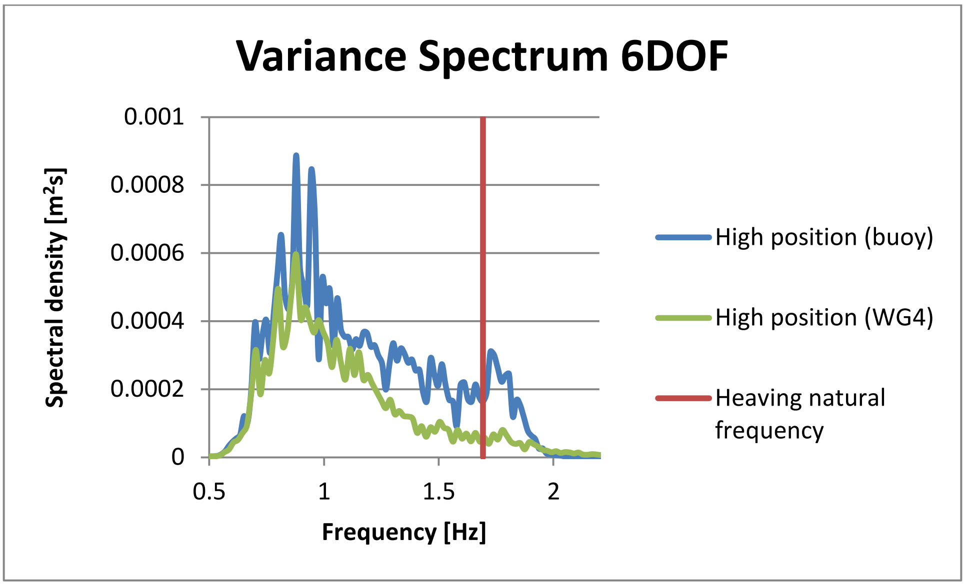

Fig. 7.37 *– Comparison of the wave variance spectrum and the spectrum obtained from motions of the buoy with the mass in the high position.*

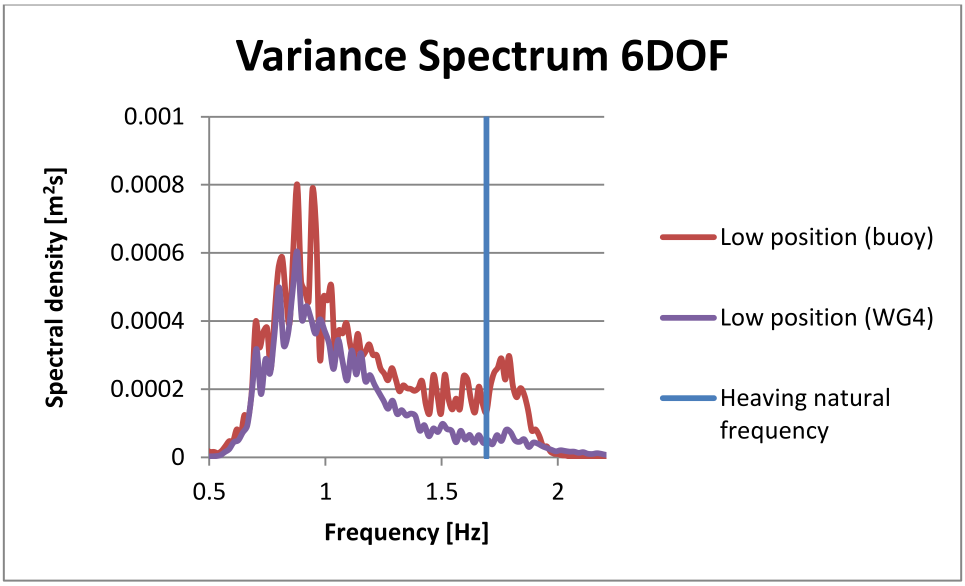

Fig. 7.38 *– Comparison of the wave variance spectrum and the spectrum obtained from motions of the buoy with the mass in the low position.*

7.7 Six degrees of freedom, regular waves: medium stiff cable

7.7.1 Results

For the last tests, the buoy was moored at the load cell through a medium stiff cable. Then, for both configurations, chancing for three times the length of the cable two regular waves have been tested.

No logical relations can be described for the pitching motion. Putting in the graph the amplitude, with before the wave heights and next the wave frequency, sometimes the gyrations are bigger for the high center of gravity, other times not [Fig. 7.39 and Fig. 7.40]. It might be due to the proximity of the wave frequency to the natural one, but the tests are not many to say something in this sense.

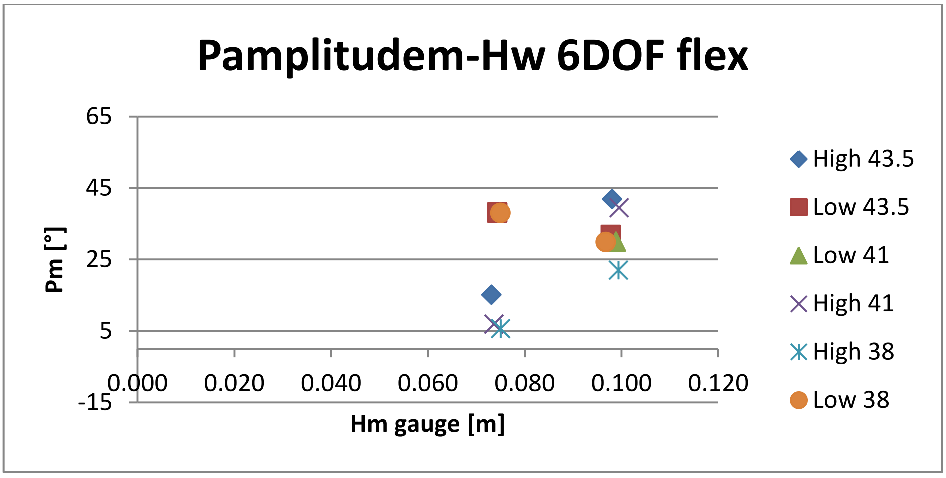

Fig. 7.39 – *Pitching amplitude compared with the wave height.*

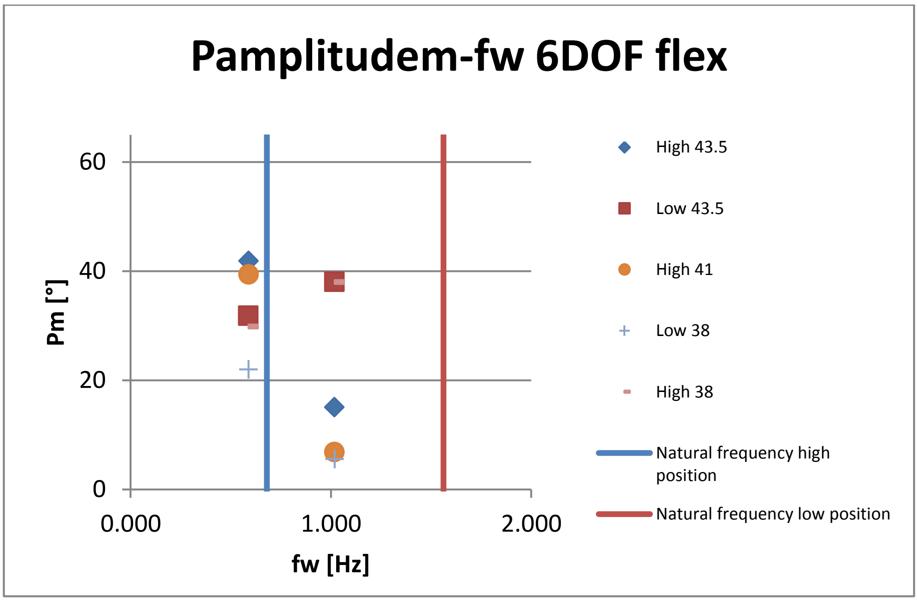

Fig. 7.40 *– Pitching amplitude compared with the wave frequency.*

An expected result for the heaving motion is obviously the increased motions when the line is longer [Fig. 7.41].

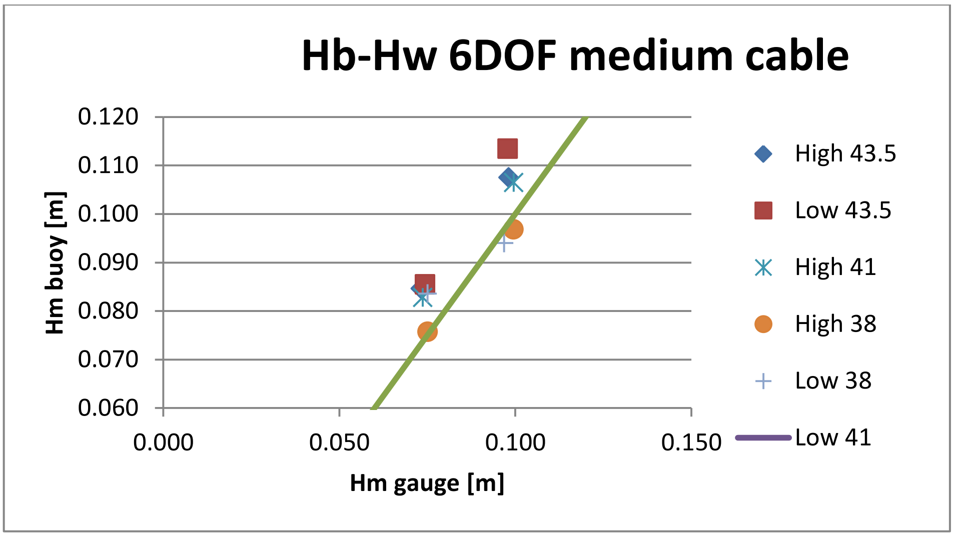

Fig. 7.41 *–Displacements of the buoy for various wave height.*

7.7.2 Conclusions

For these experiments, the information acquired are less, as observed in some results, or not useless.

The forces recorded, due probably to the high sensibility of the load cell, don't show a rational distribution when they are compared with the wave heights [Fig. 7.42] as well as are related to the wave frequencies [Fig. 7.43].

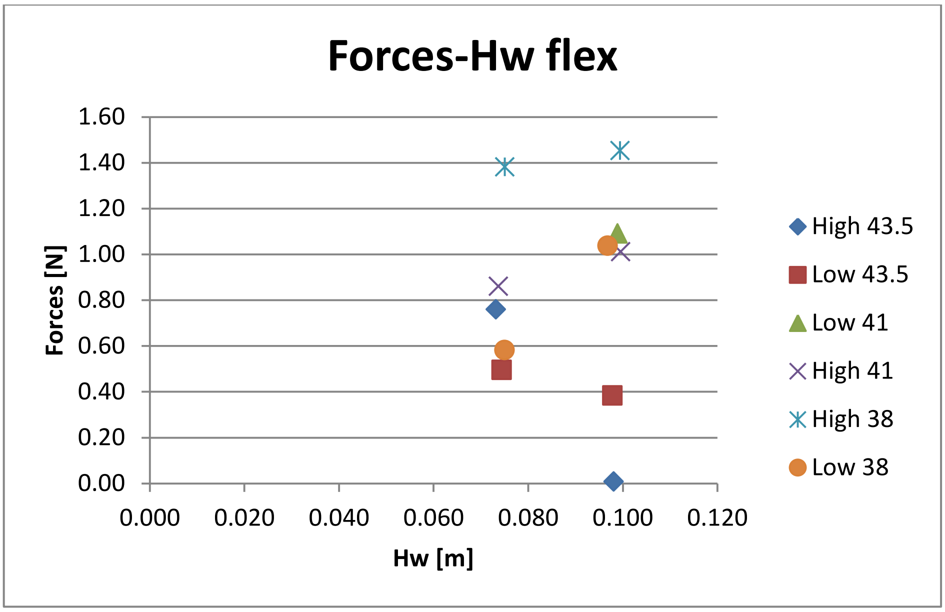

Fig. 7.42 – *Forces compared with the wave heights.*

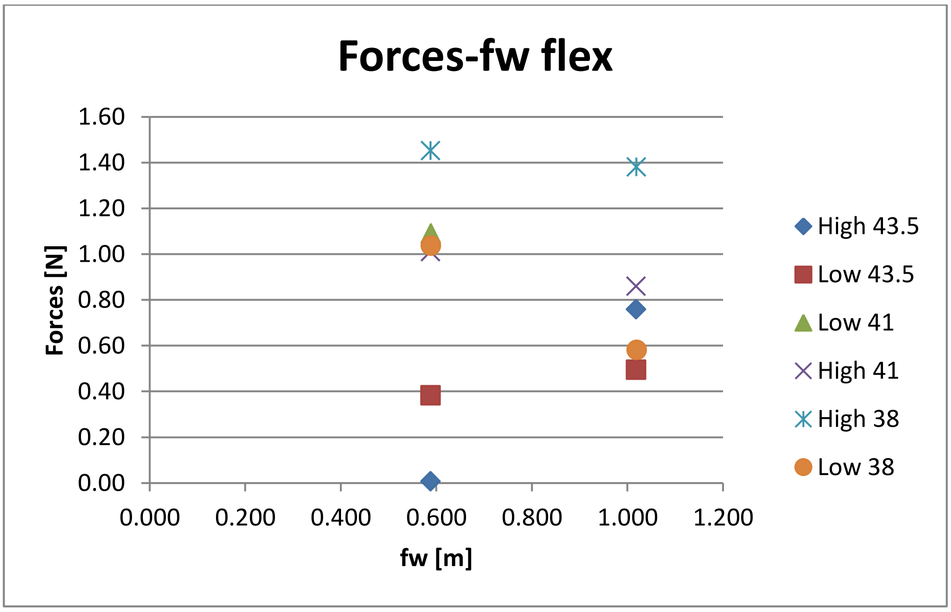

Fig. 7.43 – *Forces compared with the wave frequencies*

8. Conclusions

8.1 1Dof vs 6DOF Regular Waves

Comparing the configurations tested in the two kind of tests is the starting point to understand some important information on the behavior of the buoy and the influence of the geometry device on the motions.

Particularly interesting in this case is how the buoy reacts if it is constrained to move only up and down, if it is free of floating or it is moored with a flexible line to the bottom of the flume. The first considerations regard the amplitudes of the movements if the device undergoes the same waves [Fig. 8.1].

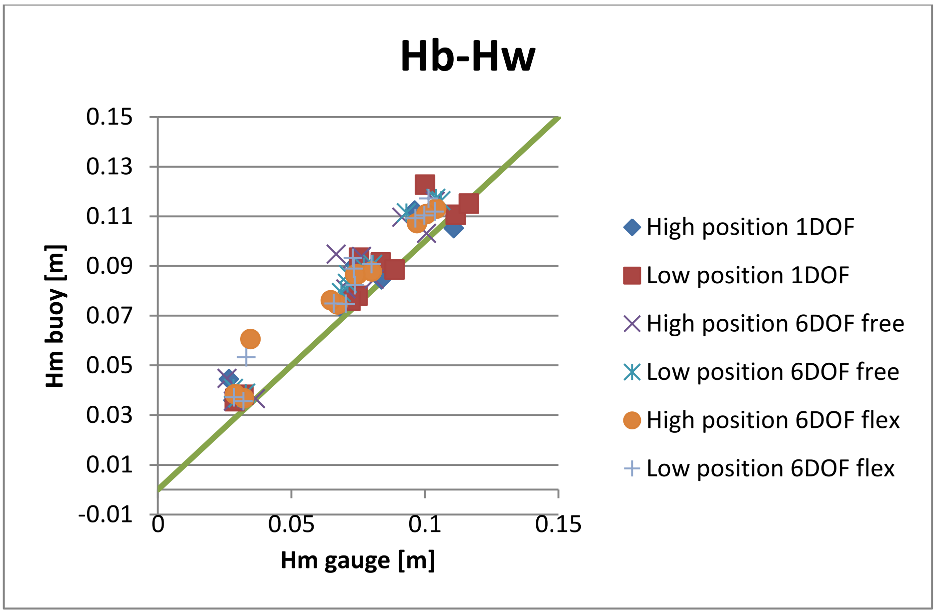

Fig. 8.1 *– Amplitudes of the buoy's motion for different configurations compared with the related wave heights.*

What can be deduced is that the amplitude of the heaving motion is not so influenced by the energy burnt off by the pitching motion, indeed the movements are quite alike.

Other significant information can be deducted analyzing the heaving motion amplifications connected to the wave frequencies [Fig. 8.2].

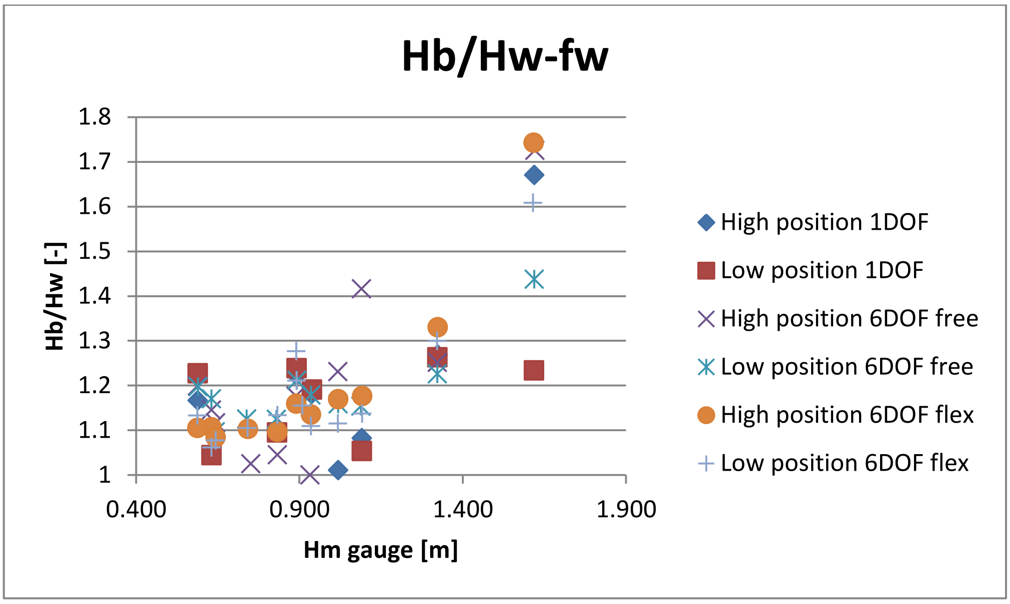

Fig. 8.2 *– Amplifications of the buoy's motion for different configurations compared with the related wave frequencies.*

The behavior seems to be characterized in two different ways. Close to the natural frequency (= 1.67 Hz) the amplification is more relevant when the center of gravity of the device is in the high position. However an opposite tendency is possible to identify for low frequencies, when the low center of gravity shows a better response.

About the pitching motion no results are obviously available from the tests conducted in one degree of freedom; but as seen in the previous chapter, the functioning of the buoy is markedly depending on the vertical position of the mass.

The analysis of the sea climate assumes a principal rule, in particular about the most probably wave frequencies in the working condition of the device.

8.2 1Dof vs 6DOF Irregular Waves

The comparisons between the spectrums acquired from the motion of the buoy represent an additional source to investigate the response of the device; the first step consists on the evaluation of the wave spectrums in order to assure that the experiments are performed under the same conditions [Fig. 8.3]. In detail, four spectrums have been analyzed: two for the one degree of freedom and two for six degrees of freedom, with the buoy moored with the flexible line to the load cell.

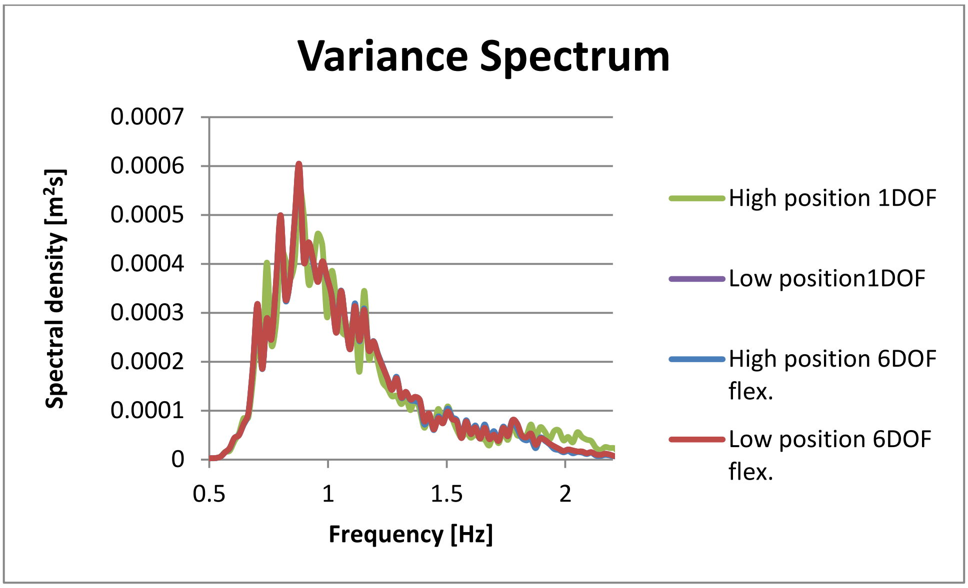

Fig. 8.4 *– Variance spectrums acquired from the waves recorded at the wave gauge next to the model during the tests.*

The graph above illustrates that the spectrums are comparable, confirming that the buoy in the various tests is undergone at the same waves; the next phase regards the comparison between the different heaving motions of the buoy. It is done like for the waves extracting a "spectrum" from the vertical movements of the buoy [Fig. 8.5].

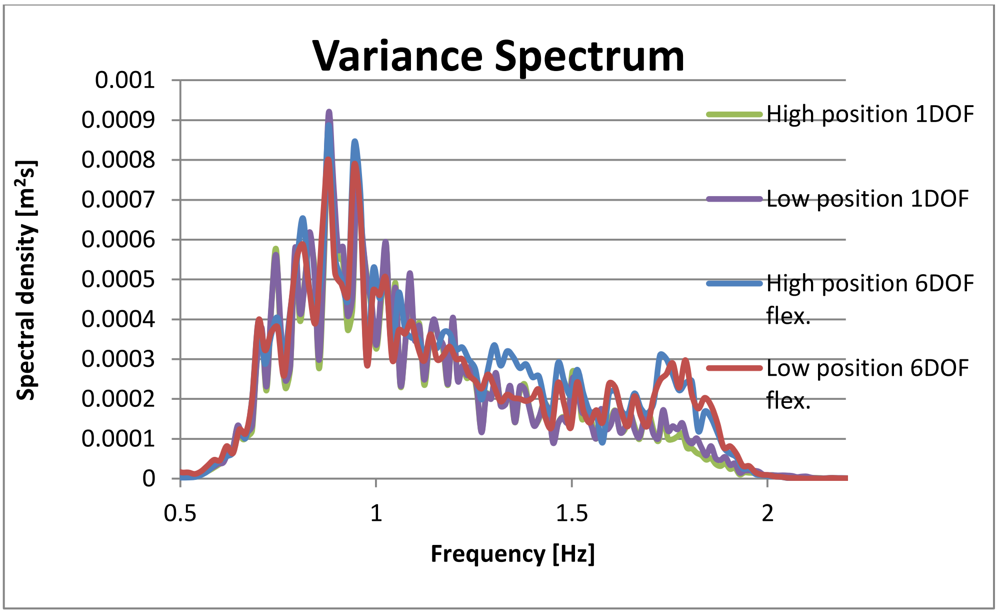

Fig. 8.4 *– Variance spectrums obtained from the buoy heaving motions for different configurations.*

The variance spectrums are alike, but the two peaks detectable around the natural frequency of the heaving motion are really interesting. The signals show the importance, how already discovered during the analysis of the regular waves, of the resonance conditions of the device; in fact bigger is the amplification of the motion, bigger is the energy harvested from the sea.

A better behavior is possible changing the buoy geometry and making a device with the same natural frequency as the characteristic frequency of the sea climate.

8.3 The pitching motion

From the results discovered in the chapter before it is clear the central role played by the wave frequency in the efficiency of the model; this is confirmed especially when the buoy is connected with the bottom. So it has sense to study a wide range of frequency.

For the irregular waves, exactly how made for the heaving motion, it is possible to create a variance spectrum for the pitching substituting the amplitude in degrees at the vertical motion of the buoy.

In the graph below are represented the two spectrums obtained for the pitching motion with the weight in low and high position and the wave spectrum [Fig. 8.5]:

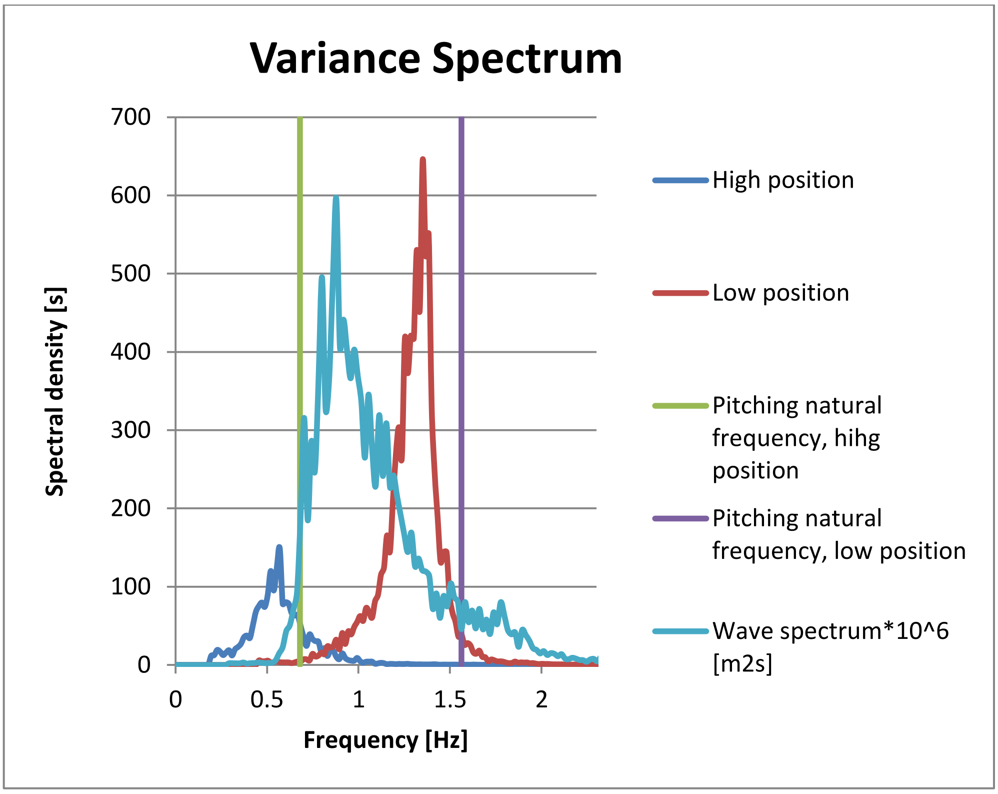

Fig. 8.5 *– Variance spectrum for the pitching motion.*

The results are interesting and repeat in a certain way what was found for the regular waves. First of all the different heights of the two peak are evident. This fact might be caused by two factors:

- The better general response of the device when it has the center of gravity displaced in the high position, as also a validation acquired with the regular waves;
- As detectable looking the wave spectrum, the characteristic frequency of the wave spectrum is in the middle of the two natural frequencies, but the waves that act near the natural frequency for low center of gravity are bigger than the waves close to the other natural frequency. This might be an explanation for this relevant difference.

Anyway, the irregular waves generated are representative of the sea climate in the area where the FlanSea buoy was installed, and probably where it will be collocated the next prototype if developed.

The tests demonstrate that for this buoy geometry, for this flexibility of the line and without power take off system connected, the buoy has a better response, both for the heaving and pitching motion, when the center of gravity is higher as possible, compatibly with the limit of stability of the buoy.

8.4 How the geometry influences the buoy motion

At last, for what concern the tests done, the center of gravity in the high position represents the best choice.

The heaving motion takes usually advantage when the frequencies of the waves approach the heaving natural frequency of the model.

The study of the pitching motion represents the principal aim of this work; interesting is the response in terms of gyration of the device undergone at the characteristic sea state; the results discovered in the subchapter before illustrate a relevant difference between what was analyzed during the preliminary tests of the FlanSea buoy [Fig.8.6] .

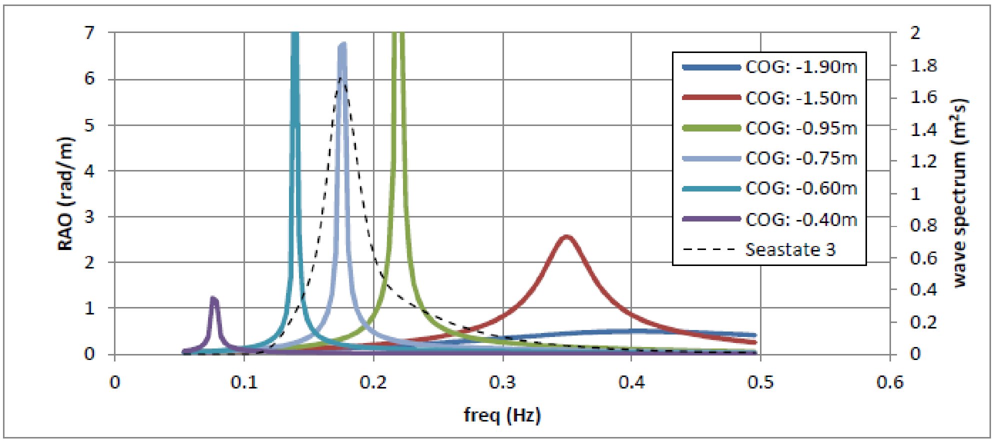

Fig. 8.6 *– Different behaviors obtained changing the COG (The FlanSea Project, Joris Falter)*

The studies done in the small flume [Fig. 8.5] demonstrate that the amplifications of the signal for devices with the natural pitching frequency immediately on the right or on the left of the characteristic wave frequency are not alike as showed in the graph above.

Surely the sea states and the geometry are not the same, but if confirmed, this different behavior might be the basis for the next studies, adopting new solutions to have a center of gravity higher as possible.

8.5 New model proposed

As already said the pitching motion plays an important role in the behavior of the buoy; representing a motion to avoid for a better workings of the device. The proposals evaluated below follows both the results obtained in the previous numerical model comparisons and during this work.

The principal aim is decreasing the pitching natural frequency and if possible reducing the pitching motion amplification.

The changes, relatively to the buoy tested, regard:

- The angle of the conic part, reduced from 120 degrees to 90 degrees; this modification shifts the center of gravity up, giving as the consequence the dropping of the pitching frequency.
- A second conic part that keeps the buoy's waterline radius.

- The additions of four symmetric vanes to increase the general stability of the device.

At last, it has been developed a new proposal for the keel completely integrated in the new geometry.

In the next figure a visual representation of the changes produced [Fig. 8.7]:

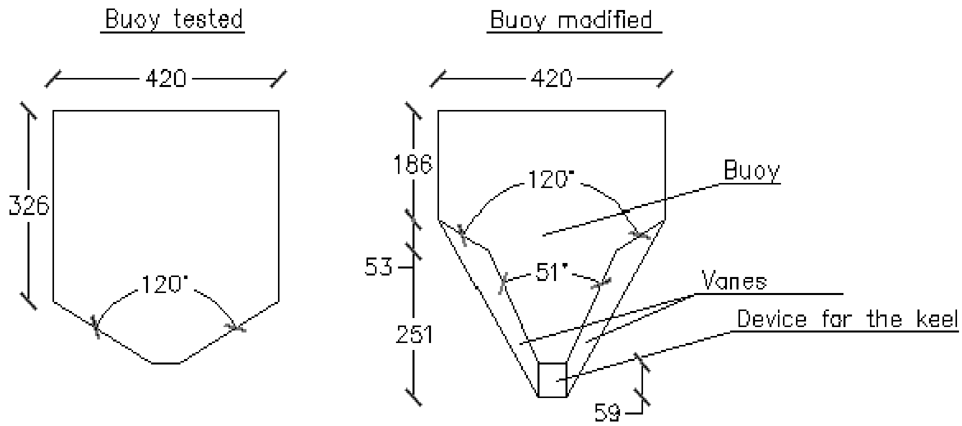

***Fig. 8.7** – The buoy tested on the left and the new proposal on the right; the dimensions in centimeters represent the real size*

The following figures show the new device drawn in three dimensions from different point of views; the prototype is not designed, but it has been supposed the buoy built in fiberglass (blue) and the vanes in steel (grey) [Fig. 8.8]:

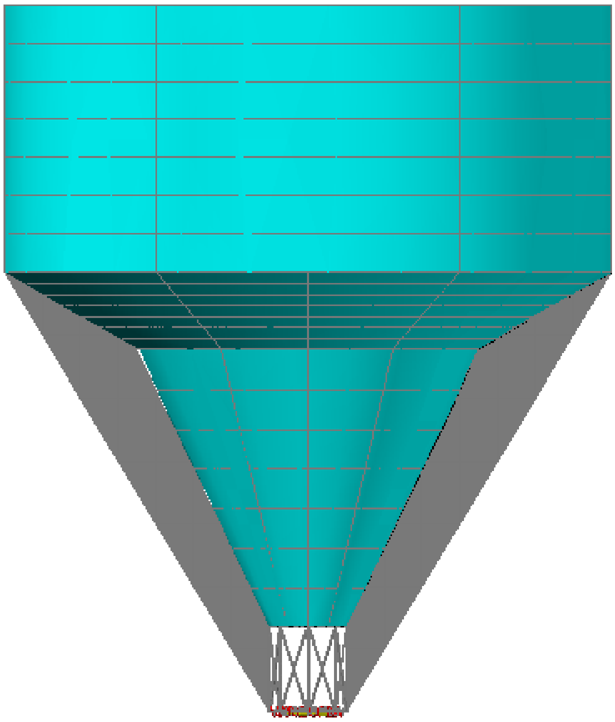

Fig. 8.8 *– Front view of the buoy.*

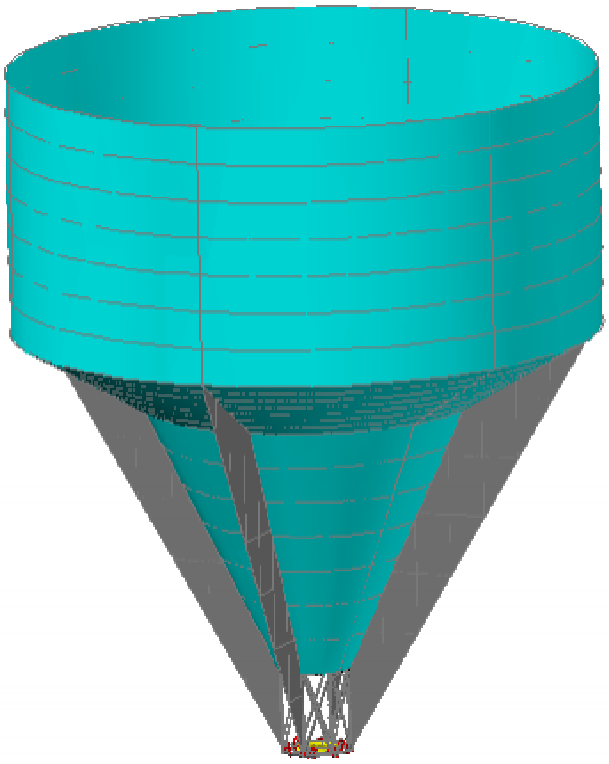

Fig. 8.10 *– Perspectival view of the buoy .*

The new bottom is thought to be more strong than the previous one. It is composed by a steel framework connected to the buoy through the vanes and a keel similar to the original. At the edge, a system of springs supports a plastic ring [Fig. 8.11 and Fig. 8.12]:

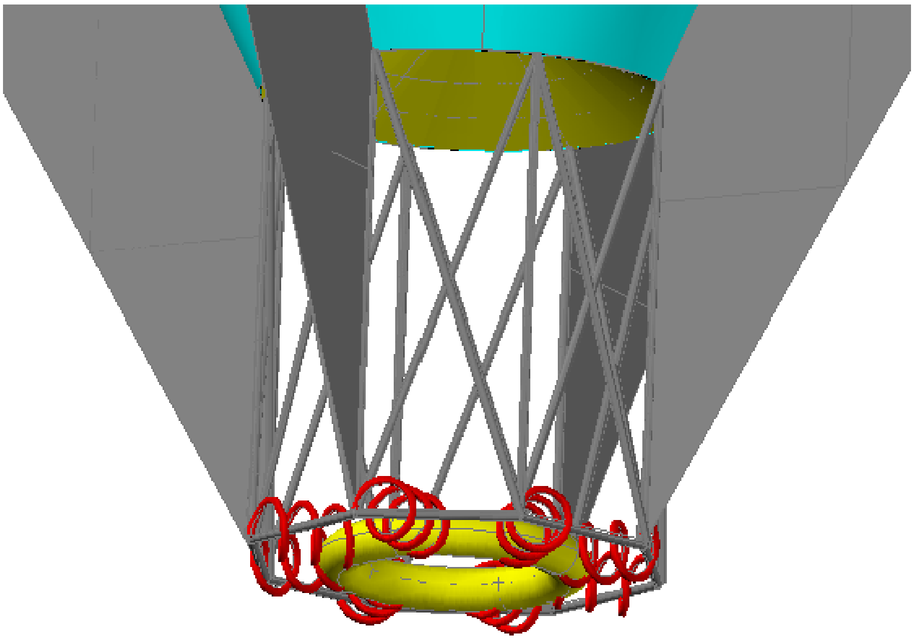

Fig. 8.11 *– Perspectival view of the keel; there are colored in yellow (plastic) the ring and the keel, in red the springs and in grey the steel framework.*

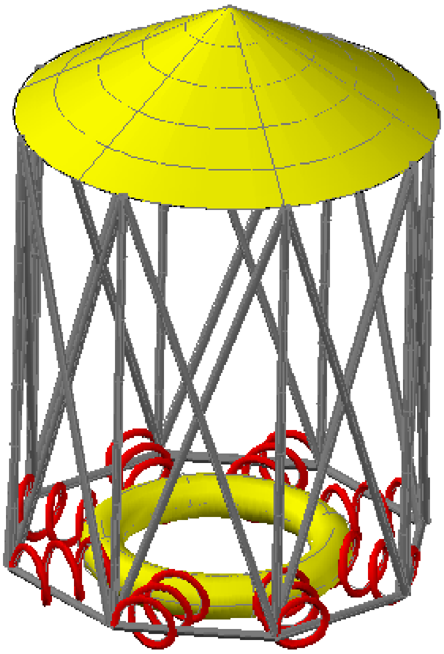

Fig. 8.12 *– The keel system in detail.*

The system is designed to allow small pitching motion without interferences. If the oscillations increases, the line pushes the external ring and the loads are absorbed by the springs. The bottom of the buoy is protected, and possible damages would concern only the external part, easier to inspect and repair directly on the site.

8.6 Future research and remarks

The first consideration concerns the impossibility to have a predictable behavior of the model without the forces produced on it by the power take off system. As already written, the size of the buoy used for the experiments was too small for the installation of a system able to replicate the same effects.

A valid mechanism might be to installing a gear with a spring inside where roll up the line that moors the buoy at the bottom of the flume. With an idea of the dimensions of these, the next step should be the minimum scale that allows to insert it inside the buoy.

The following efforts on the buoy geometry should be also concentrate on the validation on the data acquired for the same buoy using the two different centers of gravity for different sea states. In fact, the irregular waves tested represent the characteristic wave climate; especially the critical events like the annual storms should be tested to confirm or not the better behavior of the buoy with the mass displaced in the high position.

Finally, other configurations should be tried, keeping in mind that devices with a geometry similar to the model tested should have a natural pitching frequency less than the typical wave frequency.

Some useful information concerning the buoy motion have been acquired through the tests; a new proposal, designed as the result of all previous experiments together with the experience gained, lays the foundations for future projects. For all of these reasons, the aims proposed have been successfully achieved.

My work represents a small step forward in the research of point absorber wave energy converter. Surely there are still many unknowns, but through this thesis the way to drive to develop an economic and worthwhile device is shorter.

Appendices

Appendix A. Matlab function used to identify the maximum wave heights for each storm from the time series.

```
function [H,N ] = peaks(v,h )
%INPUT
%v : Hs data
%h : threeshold value
%OUTPUT
%H : Hs values bigger than h
%N : H lenght
i = length(v);
j = 1;
Z(j) = 0;
for k = 1:i
    if v(k)<= h
        if Z(j)>=h
            j=j+1;
            Z(j)=0;
        end
    else
        if v(k)>Z(j)
             Z(j)=v(k);
        end
    end
end
N=j-1;
for k=1:N
    H(k)=Z(k);
end
```

Appendix B. Matlab script used to calculate the heaving hydrodynamic parameters

```
%input
D=0.125;
rho=1000;
g=9.81;
freq=25;
limit=0.005;
limit2=0.008;
% read the xlm file

M=xlsread('2014112504.xml');


% define the x, y positions of the points

x1=M(:,1);
y1=M(:,2);
x2=-M(:,3);
```

```
t=numel(x2);
% define buoy motion
time=[0:1/freq:t/freq-1/freq];
for i=1:t;

    heaving(i)=(x2(i));

end


mean=0;
for y=numel(heaving)-2:numel(heaving)-1
    mean=mean+heaving(y);
end
mean=mean/2;
heaving=abs(heaving-mean);
x2=x2-mean;

i = length(heaving);
j = 1;
Z(j) = 0;
bibu(j)=0;

for k = 1:i
    A(k)=k;
    if heaving(k)<= limit
        if Z(j)>=limit
           j=j+1;
           Z(j)=0;
          bibu(j)=0;
        end
    else
        if heaving(k)>Z(j)
            Z(j)=heaving(k);
            bibu(j)=k;
        end
    end
end
if Z(j)==0
    N=j-1;
    for k=1:N
    p(k)=Z(k);
    T(k)=bibu(k)/freq;
    end
else
    T=bibu/freq;
    p=Z;
end
k=numel(T)-1;
for s=2:k;
    Period_peak(s-1)=-2*(T(s)-T(s+1));

end
k=numel(T);
for s=1:k;
    Tpeak(s)=T(s);
```

```
    peak(s)=p(s);
end
k=numel(T);
Pmean=sum(Period_peak)/(k-1);
wp=2*pi./Pmean;
j=1;
zazu(j)=0;
for k=1:i-1
    if heaving(k)-heaving(k+1)>limit2
        zazu(j)=k;
        j=j+1;
        zazu(j)=0;
    end
end
Tstart=zazu(1)/freq;

%Exponential fit

Tpeak=Tpeak(1:end-1);
peak=peak(1:end-1);
pol = polyfit(Tpeak, log(peak), 1);
tau = -pol(1);
a=Tpeak(1)*freq;
plo=x2(a:end-1);
time=[Tpeak(1):1/freq:t/freq-1/freq]-Tstart;
Tm =0:0.01:i/freq;
T0=peak(1);
peak_t = T0*exp(-(Tm)*tau);

figure
plot(time, -plo, Tm, peak_t)
% Hdrodynamic parameters
c=rho*g*pi.*(D/2)^2;
zeta=sqrt(1/tau^2/(1+wp^2));
wn=wp/sqrt(1-zeta^2);
Tn=wn/2/pi;
parameters(1)=c;
parameters(2)=zeta;
parameters(3)=wn;
parameters(4)=Tn;
parameters=parameters';
```

Appendix C. Matlab script used to calculate the pitching hydrodynamic parameters

```
%input
D=0.125;
rho=1028;
g=9.81;
freq=100;
Ixx=0.000011984224905356 6;
GM=0.02091057655;
```

```
limit2=1;

% read the xlm file

M=xlsread('GOPR0365.xml');


% define the x, y positions of the points

x1=M(:,1);
y1=M(:,2);
x2=M(:,3);
y2=M(:,4);
t=numel(x1);
% define buoy motion
time=[0:1/freq:t/freq-1/freq];
for i=1:t;
    H_buoy(i)=y1(i)+((y1(i)-y2(i))/2);
    a(i)=atan((y2(i)-y1(i))/(x2(i)-x1(i)))*360/2/pi;
    pitching(i)=abs(atan((y2(i)-y1(i))/(x2(i)-x1(i)))*360/2/pi);

end
limit=7.5;

i = length(pitching);
j = 1;
Z(j) = 0;
bibu(j)=0;
for k = 1:i
    A(k)=k;
    if pitching(k)<= limit
        if Z(j)>=limit
           j=j+1;
           Z(j)=0;
          bibu(j)=0;
        end
    else
        if pitching(k)>Z(j)
            Z(j)=pitching(k);
            bibu(j)=k;
        end
    end
end
if Z(j)>Z(j-1)
    N=j-1;
    for k=1:N
    p(k)=Z(k);
    T(k)=bibu(k)/freq;
    end
else
    T=bibu/freq;
    p=Z;
end

au=numel(T)-2;
for s=1:au;
    Period_peak(s)=2*(T(s+1)-T(s));
```

```
end

k=numel(T);
for s=1:k;
    Tpeak(s)=T(s);
    peak(s)=p(s);
end

Pmean=sum(Period_peak)/(au);
wp=2*pi./Pmean;
%Exponential fit
Tpeak=Tpeak(1:end-1);

for k=1:i-1
    if pitching(k)-pitching(k+1)>limit2
        zazu(j)=k/freq;
        j=j+1;
        zazu(j)=0;
    end
end

peak=peak(1:end-1);
p = polyfit(Tpeak, log(peak), 1);
tau = -p(1);
T0 = peak(1);
paf=Tpeak(1)*freq;
plo=pitching(paf:end-1);
time=[0:1/freq:t/freq-1/freq-Tpeak(1)];
Tm =0:0.01:i/freq;
peak_t = T0*exp(-(Tm)*tau);
zeta=sqrt(tau^2/(wp^2+tau^2));

plot(time, plo, Tm, peak_t)
% Hdrodynamic parameters
c=rho*g*Ixx*GM;

wn=wp/sqrt(1-zeta^2);
Tn=2*pi/wn;
parameters(1)=c;
parameters(2)=zeta;
parameters(3)=wn;
parameters(4)=Tn;
parameters=parameters';
```

Appendix D. Six degrees of freedom, additional graphs acquired by the tests done in free floating condition.

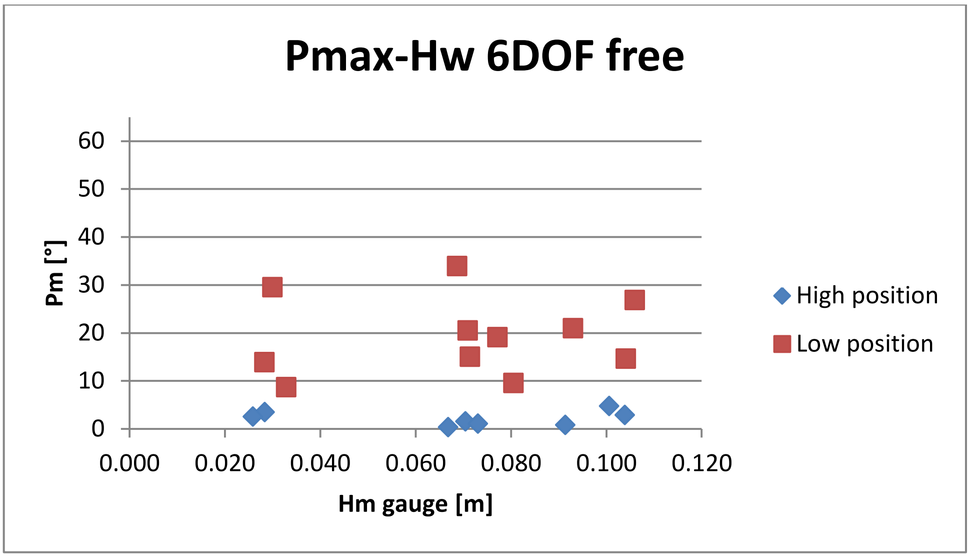

Fig. D.1 – Maximum positive pitching value related with the wave height.

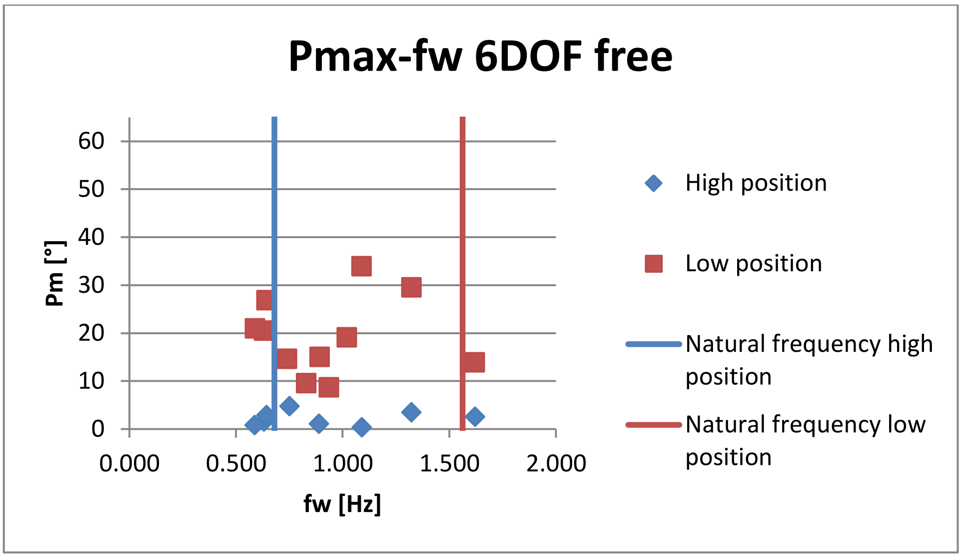

Fig. D.2 – Maximum positive pitching amplitude compared with the wave frequency.

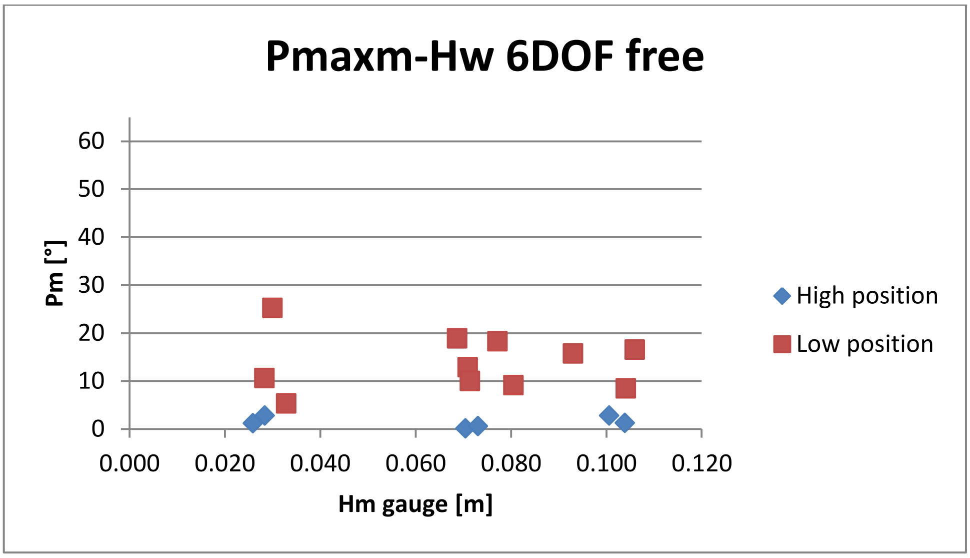

Fig. D.3 – *Mean positive pitching value related with the wave height.*

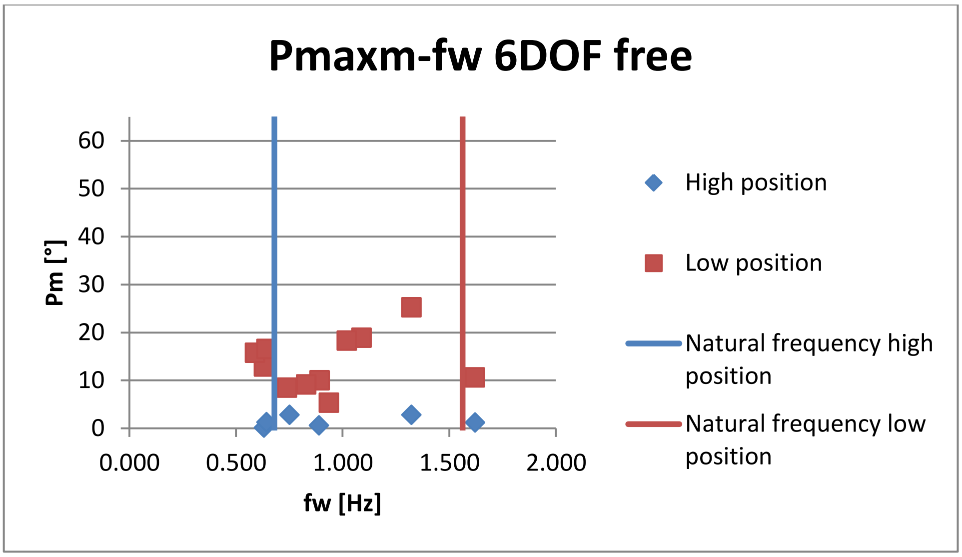

Fig. D.4 – *Mean positive pitching amplitude compared with the wave frequency.*

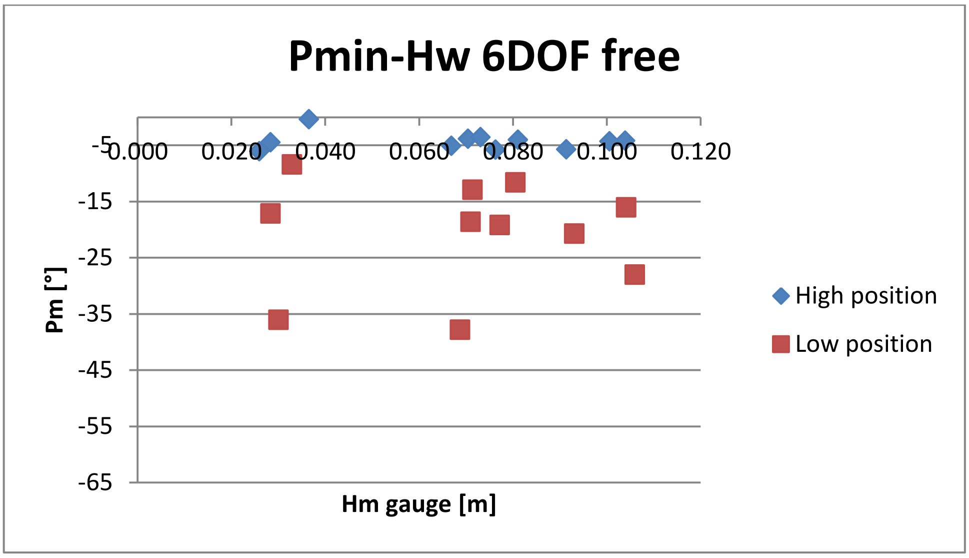

Fig. D.5 – *Maximum negative pitching value related with the wave height.*

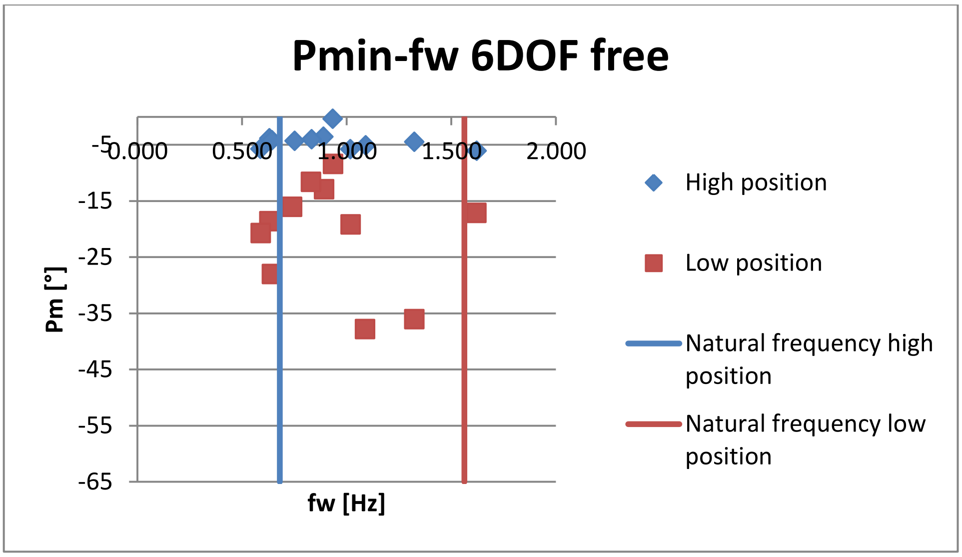

Fig. D.6 – *Maximum negative pitching amplitude compared with the wave frequency.*

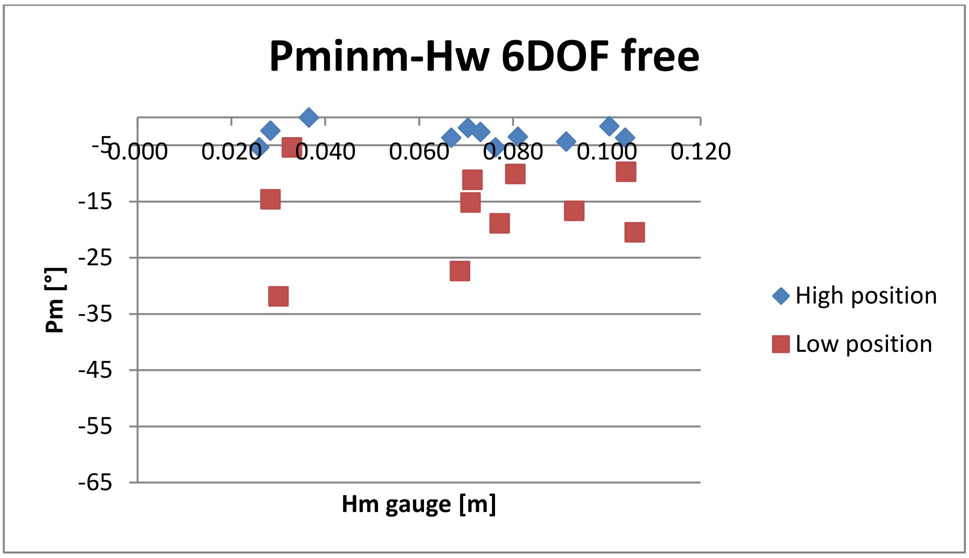

Fig. D.7 – *Mean negative pitching value related with the wave height.*

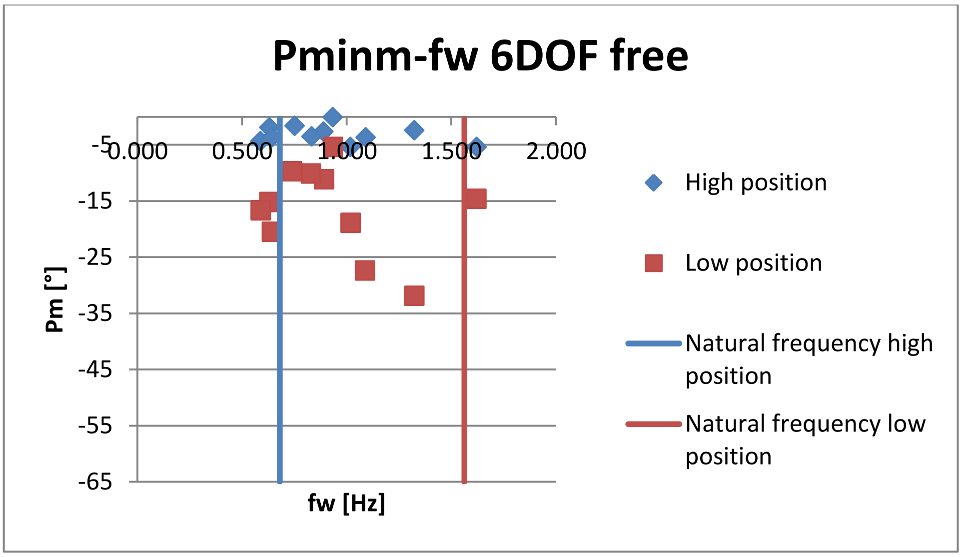

Fig. D.8 – *Mean negative pitching amplitude compared with the wave frequency.*

Appendix E. Six degrees of freedom, additional graphs acquired by the tests done with the stiff cable.

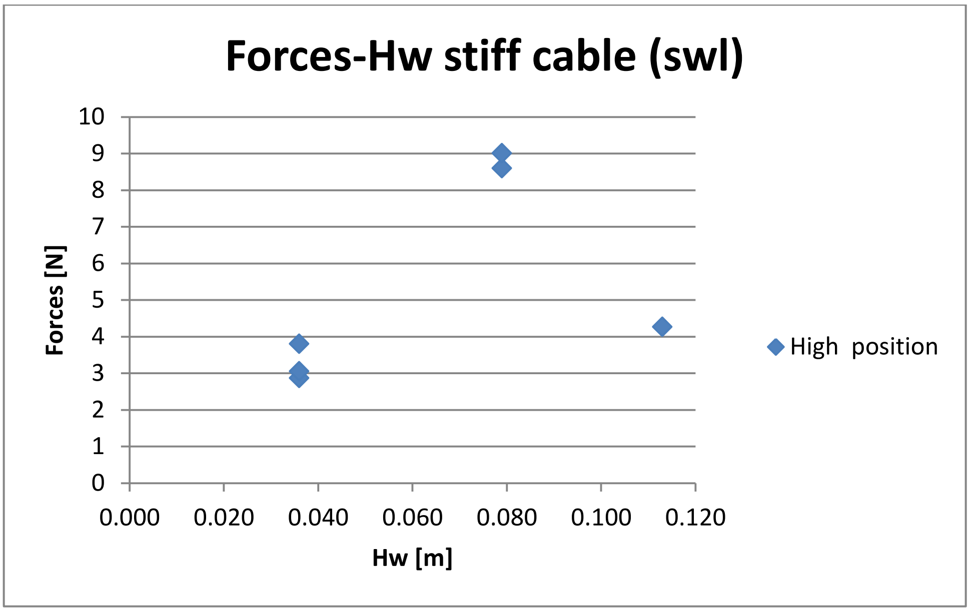

Fig. E.1 – Forces compared with the wave heights.

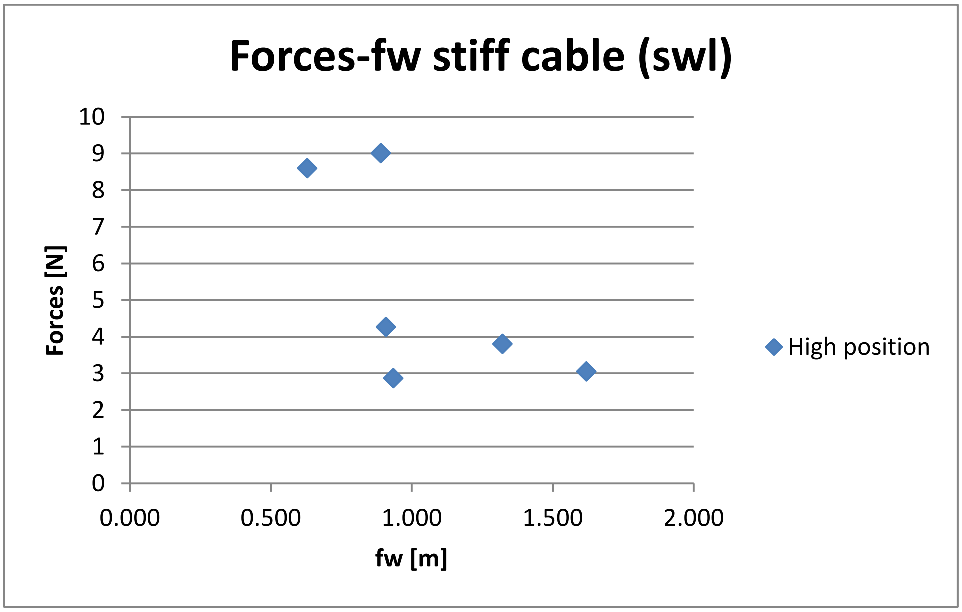

Fig. E.2 – Forces compared with the wave frequencies.

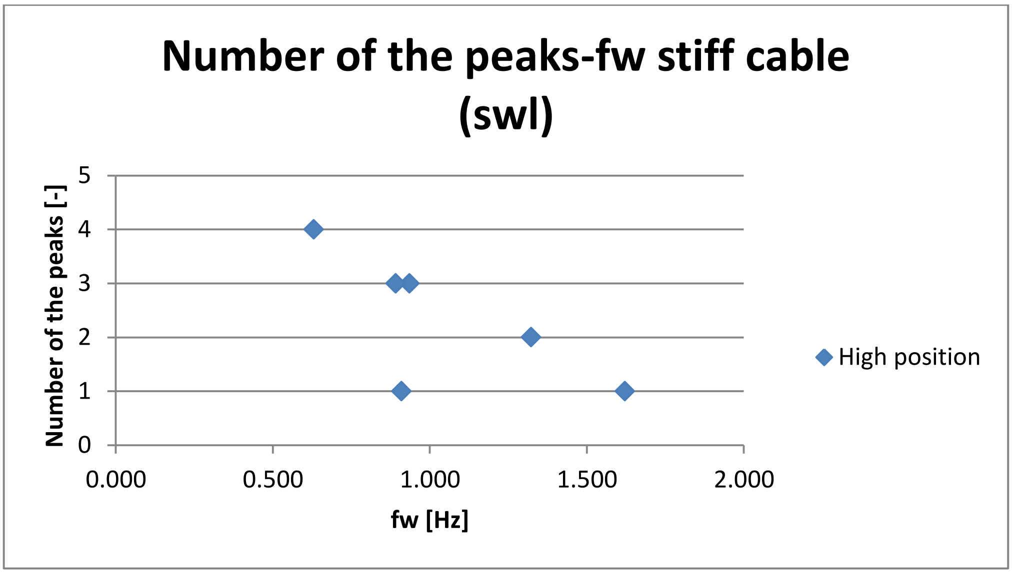

Fig. E.3 *– Relation between the multiple peaks and the frequencies for the high position of the center of gravity*

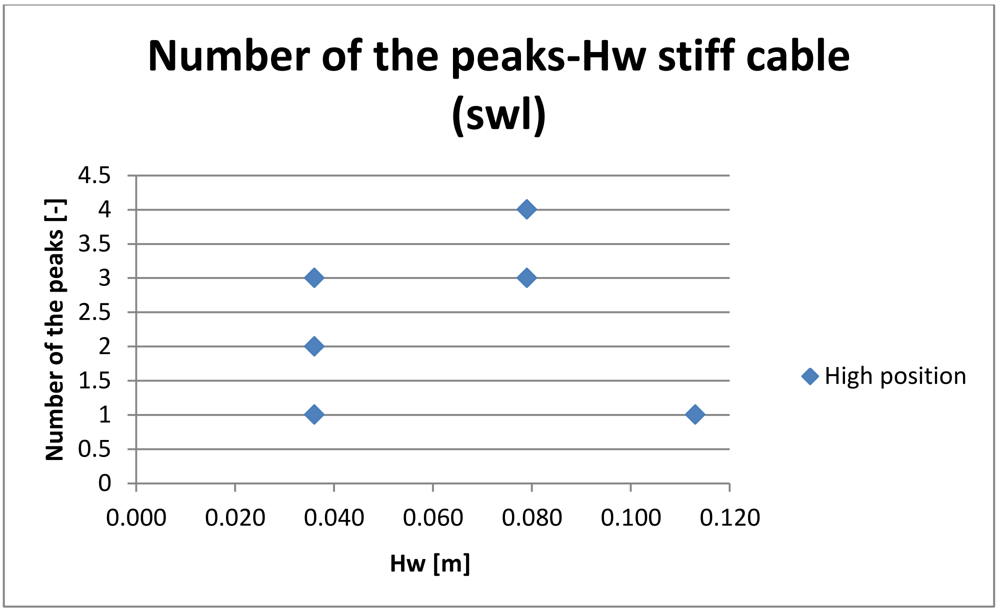

Fig. E.4 *– Relation between the multiple peaks and the wave heights for the high position of the center of gravity*

Appendix E. Six degrees of freedom, additional graphs acquired by the tests done with the flexible cable.

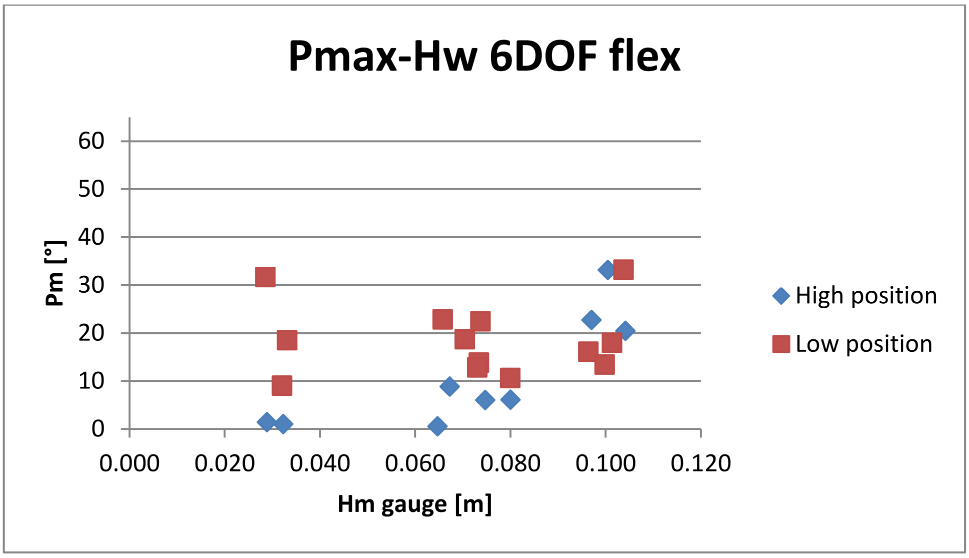

Fig. F.1 – *Maximum positive pitching value related with the wave height.*

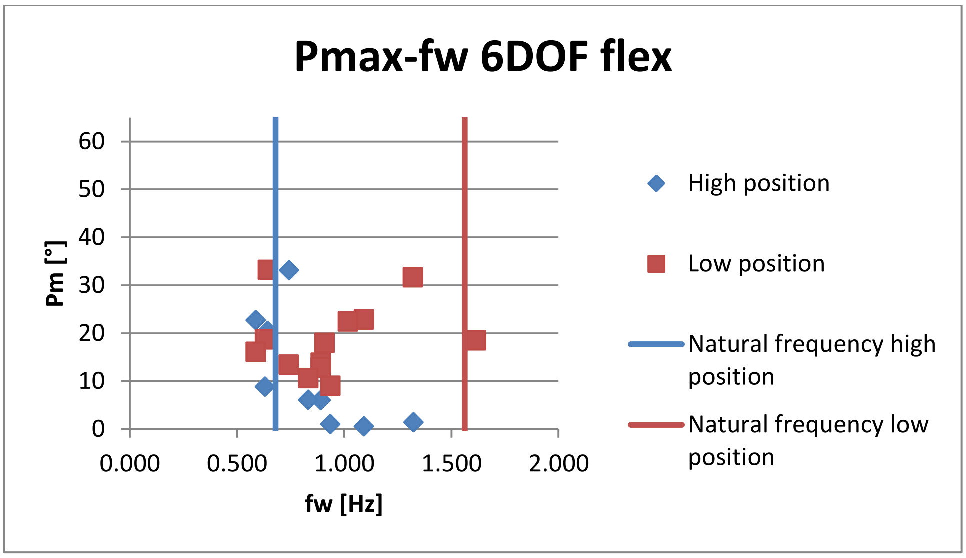

Fig. F.2 – *Maximum positive pitching amplitude compared with the wave frequency.*

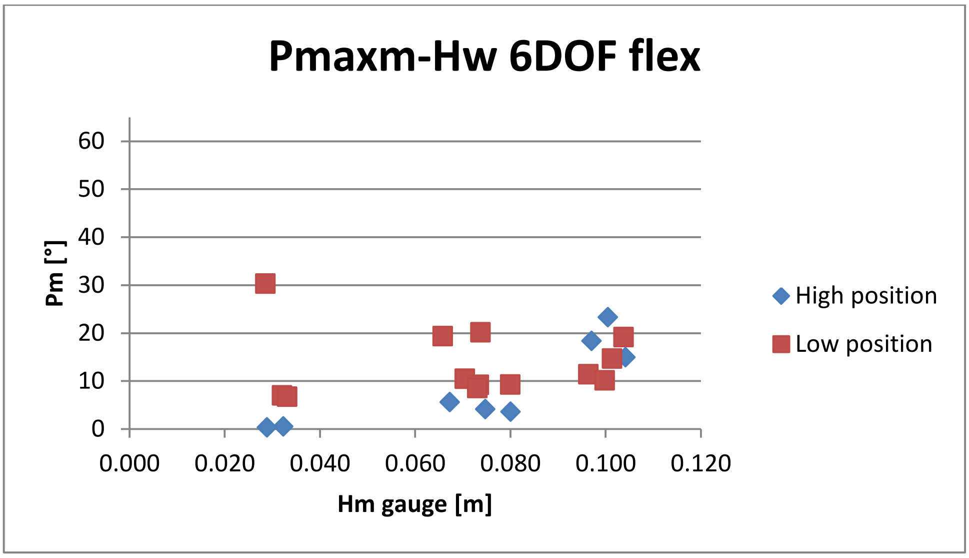

Fig. F.3 *– Mean positive pitching value related with the wave height.*

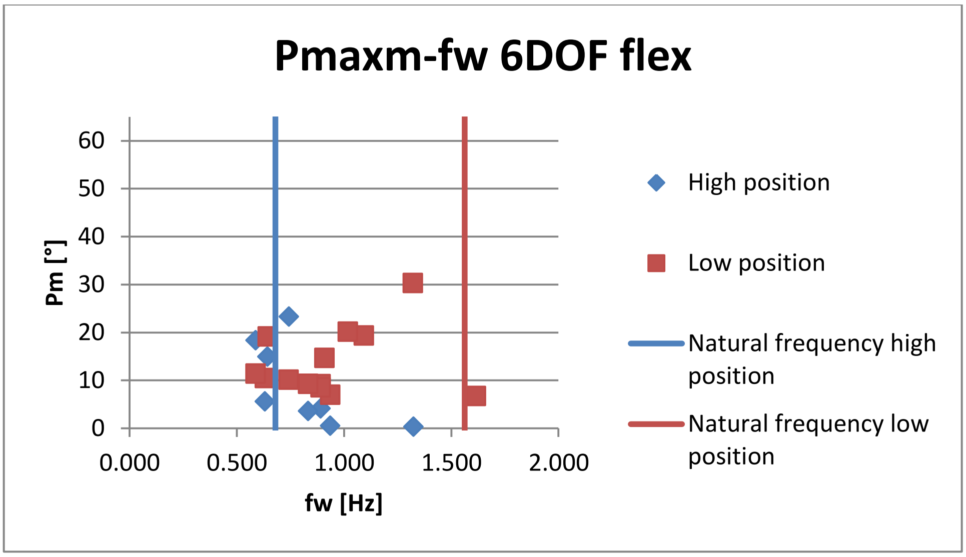

Fig. F.4 *– Mean positive pitching amplitude compared with the wave frequency.*

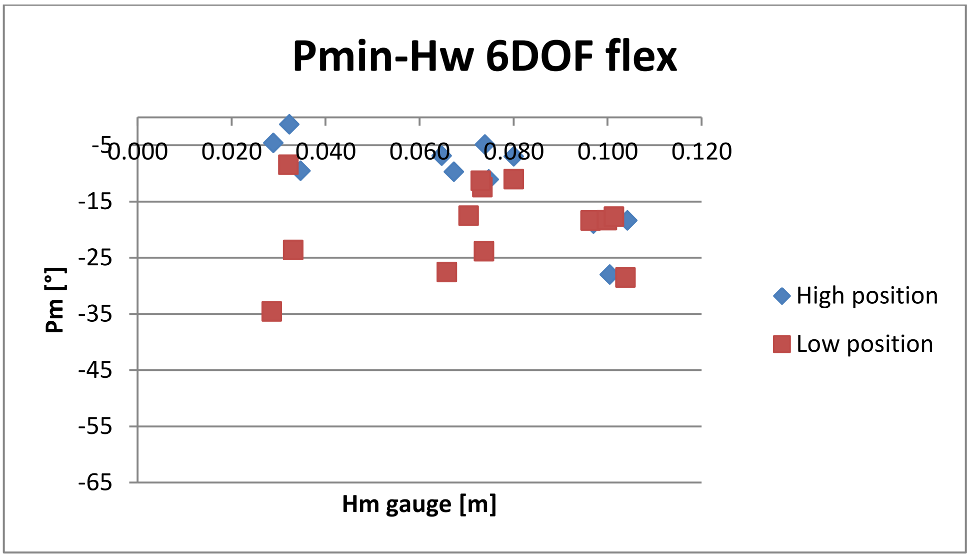

Fig. F.5 *– Maximum negative pitching value related with the wave height.*

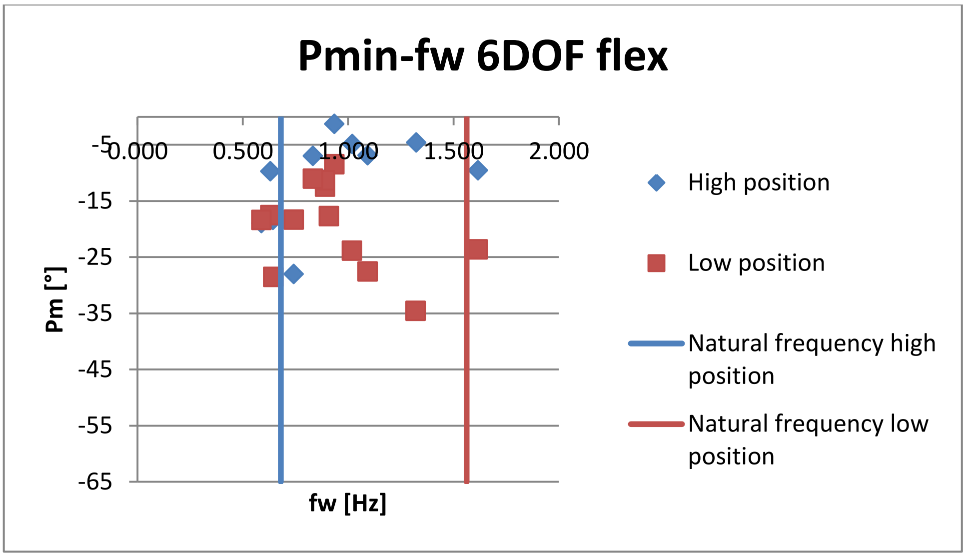

Fig. F.6 *– Maximum negative pitching amplitude compared with the wave frequency.*

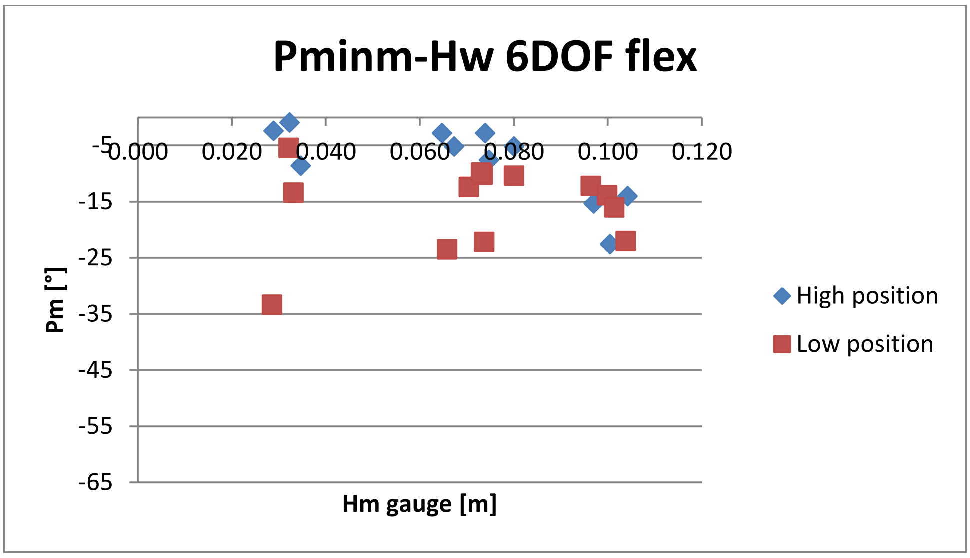

Fig. F.7 – Mean negative pitching value related with the wave height.

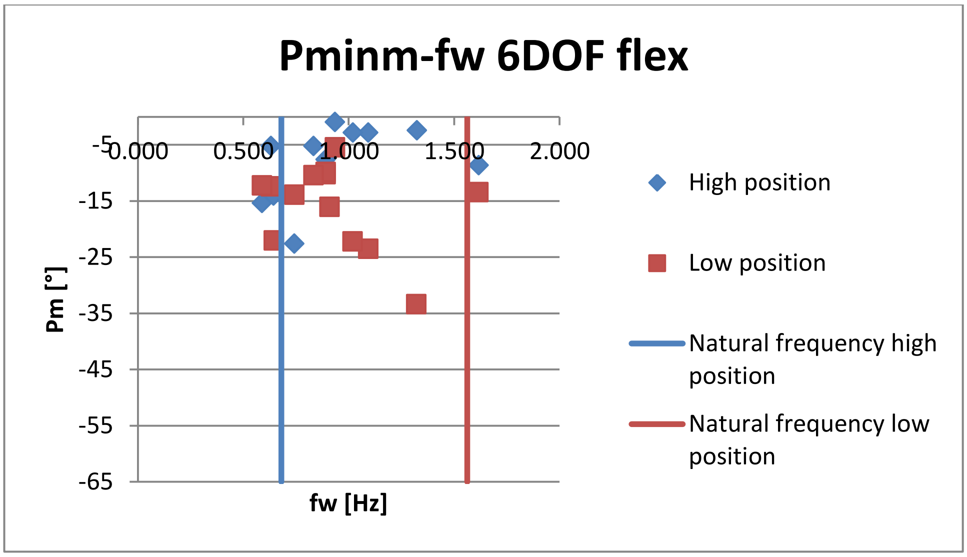

Fig. F.8 – Mean negative pitching amplitude compared with the wave frequency.

References

(n.d.) Retrieved from Pelamis Wave Power: http://www.pelamiswave.com/

(n.d.) Retrieved from VOITH - Wave Power Plants: http://www.voith.com/en/products-services/hydro-power/ocean-energies/wave-power-plants-590.html

(n.d.) Retrived from WaveStar Energy: http://wavestarenergy.com/

(n.d.). Retrieved from Aalborg University Software for Wave Laboratories: http://www.hydrosoft.civil.aau.dk/wavelab/

(n.d.). Retrieved from National Instruments: http://www.ni.com/labview/i/

(n.d.). Retrieved from EngineersGarage: http://www.engineersgarage.com/articles/load-cell

Boyle, G. (2004). Renewable Energy. Oxford University Press. Oxford.

Barstow, S., & Al. (2010). Assessing the global wave energy potential. *Proceedings of OMAE2010.* China.

Cornett, A. M. (2008). A global wave energy resource assessment. *National Research Council.* Ontario, Canada.

Damen, M. & Al.(2011). Electrical vs Hydraulic PTO, *FlanSea project report number: FLA267- 175.* Ghent.

De Backer, D. (2009). Hydrodynamic Design Optimization of Wave Energy Converters Consisting of Heaving Point Absorbers. *PhD Thesis*. Ghent University, Ghent.

Dean & Darlymple. (1991). Engineering Wave Properties. In D. Darlymple, *Water Wave Mechanics for Engineers and Scientists*. World Scientific.

Drew, B., & Al. (2009, 16 June). A review of wave energy converter technology. *IMechE.*

Ehsan Enferad, E. & Nazarpour, D. (2013). Ocean's Renewable Power and Review of Technologies: Case Study Waves. *New developments in renewable energy.* Iran

Falcao, A. (2012). Wave Energy Utilization. *Lesson for the International PhD Course University of Florence- Tu-Braunschweig, XXVII Cycle* . Florence.

Falcao, A. (2010). Wave energy utilization: A review of the technologies. *Renewable and Sustainable Energy Reviews.*

Falter, J. (2011). Reduction of pitch motion by increased damping, *FlanSea project report number: FLA267- 170.* Ghent.

Falter, J. (2011). Some notes on stability and geometry, *FlanSea project report number: FLA267- 163.* Ghent.

Flemish Ministry of Transport and Public Works: Haecon, Probabilitas, Hydro Meteo Atlas Measurement grid Flemish banks. sea stated, scatter diagramm.

Griet De Backer (2009), Hydrodynamic Design Optimization of Wave Energy Converters Consisting of Heaving Point Absorbers. *PhD Thesis*. Ghent University, Ghent.

Hans Op het Veld (2011), Hydrodynamic parameters, *FlanSea project report number: FLA267-XX*

Holthuijsen, L. H. (2007). Waves in oceanic and coastal waters. Cambridge University Press. UK.

Mansard, E.P.D.; Funke, E. R. (Eds.) (1980): The measurement of incident and reflected spectra using a least square method. Proceedings 17th International Conference Coastal Engi-neering (ICCE). Sydney, Australia. ASCE. Volume 1.

McCormick, M. (2007). Ocean Wave Energy Conversion. Dover. New York.

Ophetveld, J. (2011). Hydrodynamic parameters, *FlanSea project report number: FLA267-196.* Ghent.

Oumeraci H. (2012): Küsteningenieurwesen II. Wasserbauliches Versuchswesen und Dimen-sionsanalyse. TU Braunschweig. Braunschweig, 4/12/2012.

P. van Besien; K. Wittebolle (1998): Ontwerp en Kalibratie von een Golfgoot. Thesis. Uni-versiteit Gent. Faculteit Toegepaste Wetenschappen. Vakgroep Civiele techniek.

Pelc, R., & Fujita, R. (2002). Renewable energy from the ocean. *Marine Policy.*

Troch, P. (2000). Experimentele studie en numerieke modellering van golfinteractie met stortsteengolfbrekers. *PhD Thesis*. Ghent University, Ghent.

Renson, D. (2011). D vs. Seastates: Power output, *FlanSea project report number: FLA267-xx.* Ghent.

Renson, D. (2011). Max draught vs. storm conditions for Ostend, *FlanSea project report number: FLA267-xx.* Ghent.

Steen S. (2014): Experimental Methods in Marine Hydrodynamics. General Modelling and Scaling Laws. NTNU. Trondheim, 8/20/2014.

Suroso, A. (2005). Hydraulic Model test of Wave Energy Conversion. *Jurnal Mekanika.*

Thorpe, T.W. (1999) An overview of wave energy technologies. *Wave Power: Moving towards Commercial Viability*. Broadway House. London

Twidell, J. & Weir T. (2006). Renewable Energy Resources. E&FN Spon. London

Vantorre M. (2009), Manoevreer- en Zeegangsgedrag van Maritieme Constructies. Universiteit Gent, Gent.

Verbrugghe Tim (2012/2013): Ontwerp van een point-absorber golfenergieconvertor met hy-draulische Power Take Off. Master Thesis. Universiteit Gent, Gent.

Wanan Sheng; Raymond Alcorn; Tony Lewis (2014): Physical modelling of wave energy converters. In Elsevier (84).

Wave Flume Manual. Department of Civil Engineering, Ghent University.

Westwood A. (2004). Ocean Power: Wave and tidal energy review. Retrieved from: http://www.renewableenergyfocus.com/